Università degli Studi di Siena

Dipartimento di Biotecnologie, Chimica e Farmacia

DOTTORATO DI RICERCA IN CHEMICAL AND PHARMACEUTICAL SCIENCES

XXXV CYCLE (2019-2022)

A multidisciplinary approach to the development of innovative tools for pharmaceutical and technological applications

Coordinator: **Prof. Maurizio Taddei**

Tutor: **Prof. Andrea Cappelli**   *Ph.D. Candidate:* **Mario Saletti**

To my precious family.
To Ettore and Eugenio.
To Carmen.

Contents

Contents

Contents

List of abbreviations

AA = Arachidonic Acid

API = Active Pharmaceutical Ingredient

BABP = Bile Acid Binding Protein

BBHC = Biocompatible and Biomimetic Hyaluronic Coating

BF = Benzofulvene monomer

CBP = Choline-binding proteins

cGMP = Cyclic Guanosine Monophosphate

COX-2 = Cyclooxygenase-2

CuAAC = Copper(I)-Catalyzed Azide Alkyne 1,3-dipolar Cycloaddition

DDS = Drug Delivery System

ECM = Extracellular Matrix

FA = Ferulic Acid

GFP = Green Fluorescent Protein

GI = Gastrointestinal

HA = Hyaluronic Acid

HPLC = High-Performance Liquid Chromatography

LDMS = Light-Driven Molecular Switch

MMLCT = Metal-Metal-to-Ligand Charge Transfer

MPS = Mononuclear Phagocyte System

Mw = Molecular Weight

NEG = Nona(ethylene glycol)

NHIP = N-protonated Indanylidene Pyrroline Schiff Bases

NMR = Nuclear Magnetic Resonance

NO = Nitric Oxide

NP = Nanoparticle

OA = Osteoarthritis

OLED = Organic Light-Emitting Diode

PAMAM = Poly(amidoamine)

PBF = Polybenzofulvene

PEG = Poly(ethylene glycol)

PG = Prostaglandin

Pg = Propargyl

PL = Phospholipase

p-HBDI = *p*-hydroxybenzylidenedimethylimidazolidinone

PLQY = Photoluminescence Quantum Yield

PPI = Poly(propylene imine)

PYP = Photoactive Yellow Protein

RA = Rheumatoid Arthritis

sGC = Guanylate Cyclase

SUV = Small Unilamellar Vesicle

TCPB = Tri-component Polymer Brush

*t*NSAID = Traditional Non-Steroidal Anti-inflammatory Drug

Tx = Thromboxane

UV = Ultraviolet

VDHs = Vicinal Diaryl-substituted Heterocycles (VDHs)

WOLED = White Organic Light-Emitting Diode

Chapter 1

Aims and outline of the thesis

1.1. Aims and outline of the thesis.

The research activity carried out during the Ph.D. period has been dedicated to the design, synthesis, and characterization of innovative tools relevant to both pharmaceutical and technological fields. Ranging from medicinal to pharmaceutical-applicative chemistry, this thesis work has been divided into four main research topics. Great interest has been devoted to the investigation of aggregation/polymerization behavior of innovative benzofulvene-based derivatives. The experience acquired with this study has been then employed for the design, synthesis, and characterization of a novel visible-light-sensitive biomimetic molecular switch inspired by the benzofulvene scaffold and the Green Fluorescent Protein (GFP) chromophore. In the framework of material chemistry, the well-known *click-chemistry* reaction of hyaluronic acid (HA) derivatives bearing propargylated ferulic groups has been exploited to obtain biomimetic and biocompatible materials useful in different biopharmaceutical fields. Lastly, the knowledge in medicinal chemistry has guided the design and synthesis of innovative bioactive compounds such as novel Cyclooxygenase-2 (COX-2) inhibitors containing Nitric Oxide (NO) donor moiety (CINODs) endowed with vasorelaxant properties.

After a brief general outline in this current **Chapter 1**, the following chapters introduce the above-mentioned research topics and present the Ph.D. candidate's contribution to them. Particularly, **Chapter 2** describes the *"affinity polymerization"* mechanism in the formation of polymeric materials based on repetitive monomeric units of the 3-phenylbenzofulvene that spontaneously polymerize by simple removal of the solvent. The Ph.D. candidate's contribution has been focused on the synthesis of novel benzofulvene-based derivatives bearing complexed and non-complexed pyridine rings in different positions of the benzofulvene scaffold, to evaluate the effects generated by the insertion of a bulky substituent in the aggregation/polymerization behavior.

Chapter 3 begins with the presentation of light-sensitive molecules called Light-Driven Molecular Switches (LDMSs). In this context, the Ph.D. candidate's contribution has regarded the chemical-structural manipulation of the benzofulvene structure to develop a novel set of biomimetic photoswitches inspired by the supramolecular properties of the 3-phenylbenzofulvene scaffold (i. e. self-assembling by π-stacking interactions) and the molecular features of the GFP chromophore.

Chapter 4 shows two different applications of HA in the field of materials chemistry. The first one describes the development of a technological platform for coating the

surfaces of low-generation (1-3) poly(propylene imine) (PPI) dendrimers with low molecular weight HA to obtain a biomimetic and biocompatible coating. In particular, HA has been anchored on the surface of PPI dendrimers by the *click-chemistry* reaction between their azido-functionalized surfaces and the HA derivatives bearing propargylated ferulic groups. The resulting materials have been proposed as biocompatible drug delivery systems (DDSs) of Doxorubicin. The second application is related to hyaluronane-based graft copolymers showing low (8.7 kDa) and medium (270 kDa) molecular weight values that have been exploited in cross-linking by the *click-chemistry* reaction. Interestingly, the interaction of resulting HA materials with water led to the formation of hydrogels, and the tunable rheological behavior of these materials led to their applicability in different biomedical fields.

Finally, **Chapter 5** describes the design of new bioactive compounds such as COX-2 inhibitors containing a Nitric Oxide donor moiety (CINODs) endowed with vasorelaxant properties. In this regard, the Ph.D. candidate's contribution has been dedicated to the synthesis, Nuclear Magnetic Resonance (NMR) characterization, Mass Spectrometry (MS), and High-Performance Liquid Chromatography (HPLC) analysis of these new hybrid molecules.

The outcomes of these studies would provide fertile ground for future projects that will hopefully contribute to accelerate the research in several fields. Indeed, the increased knowledge on the behavior of these innovative tools, by means of a multidisciplinary approach, is the key for boosting the development of novel materials for pharmaceutical and technological applications.

Chapter 2

Investigation of aggregation/polymerization behavior of innovative benzofulvene-based derivatives

2.1. π - Stacked benzofulvene polymers.

For years now, Cappelli and coworkers have been involved in the design, synthesis, and characterization of innovative polymeric materials, so-called benzofulvene polymers, based on repetitive monomeric units based on the 3-phenyl-1*H*-indene structure. Interestingly, the 3-phenylbenzofulvene monomers (e. g. **BF1**) polymerize spontaneously following a simple removal of the solvent, in the apparent absence of catalysts or initiators (Figure 2.1).
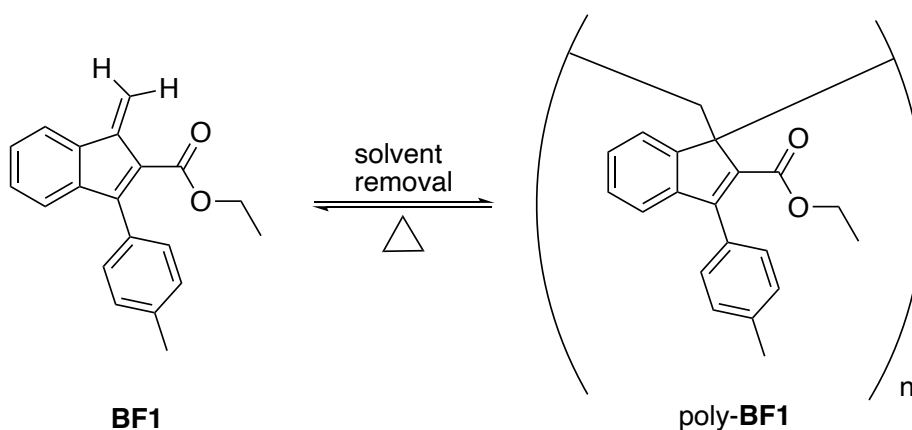
Figure 2.1. Synthesis of the prototypical polybenzofulvene derivative poly-**BF1**.

The polybenzofulvene derivatives (PBF, e. g. poly-**BF1**) obtained show peculiar features such as high molecular weight, thermoreversible polymerization/depolymerization behavior, high π-stacking, tendency to generate macromolecules nanostructures, high solubility in the most common organic solvents combined with interesting optoelectronic features.[1,2] Improving organic materials for optoelectronic applications represents a very attractive current topic owing to the importance of organic microelectronics in producing modern electronic devices. In this direction, Cappelli and coworkers have recently described a class of highly emissive polymeric supramolecular assemblies based on phenylbenzofulvene scaffold (e. g. poly-6-DMFL-**BF3k**)[3] useful in optoelectronic applications such as optical displays, sensors, and organic light-emitting diodes (OLEDs).[4-9]

2.2. "Affinity polymerization": a peculiar topochemical spontaneous polymerization mechanism.

The topochemical polymerization mechanism has been extensively investigated through structure-activity relationship studies of the prototype monomer **BF1** and it was named "*affinity polymerization*".[10] In particular, benzofulvene derivatives have shown a strong propensity to make π-stacking interactions, which have been considered to be responsible for the spontaneous polymerization of monomeric units of **BF1** and derivatives. Thanks to these π - π interactions, benzofulvene monomers organize in columnar aggregates, which are compacted up to the critical distance of polymerization (Figure 2.2).
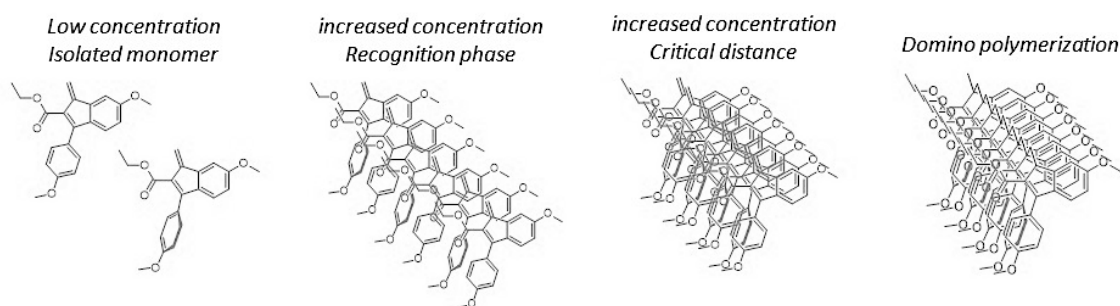
Figure 2.2. Hypothetic mechanism responsible for spontaneous polymerization of benzofulvene monomers following removal of the solvent.

Concerning the "*affinity polymerization*" process, it is worth considering that the number of monomeric units and the position of the substituents affect the number of aggregated monomers needed to reach the critical polymerization distance. It has been brought to light that the phenyl substituent in position 3 of the indene ring (Figure 2.3) plays a *key role* in the polymerization process since it establishes π-stacking interactions that are able to influence the recognition phase and subsequent aggregation between monomers.
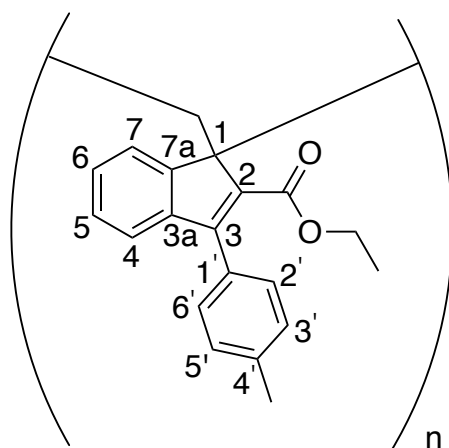
Figure 2.3. Conventional numbering of the 3-phenylindene nucleus of poly-**BF1**. The phenyl substituent in position 3 of the indene ring establishes π-stacking interactions.

In order to study the effect of the substitution on the structure-property relationships of polybenzofulvene derivatives, several specific substituents endowed with appropriate steric and electronic features have been introduced in different positions of the 3-phenylindene nucleus of poly-**BF1**. Interestingly, it has been observed that the presence of relatively bulky groups in the carbon C_2 of indene nucleus, such as -COOEt, favor the vinyl (1,2) polymerization, while smaller functional groups (-H, -F, -Cl, -Br, -CN) lead to the formation of (1,2) and (1,4) polymer chain (Figure 2.4). Furthermore, sterically encumbering groups on the carbon C_2 (-CON(CH$_3$)$_2$ or -C(CH$_3$)$_3$) hamper spontaneous polymerization. Thus, the spontaneous polymerization process involving benzofulvene derivatives appears to be very sensitive to the presence of bulky substituents near the polymerization center (carbon C_2).

1,2-enchained   1,4-enchained
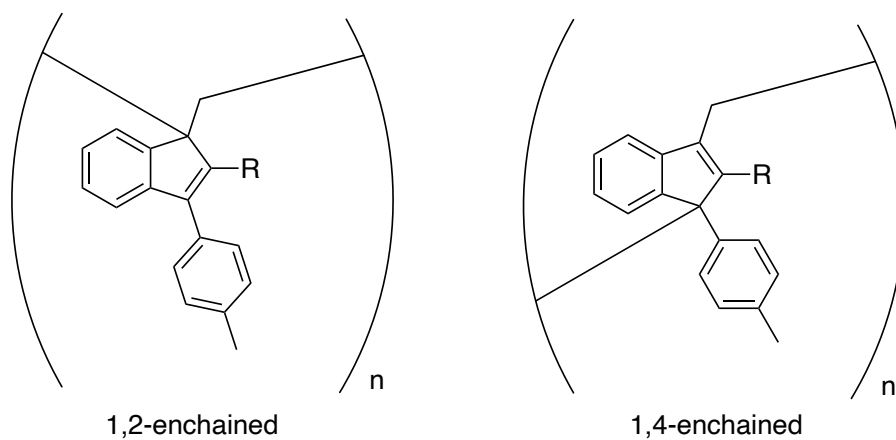
Figure 2.4. The *3*-phenylbenzofulvene monomer can undergo either vinyl (1,2) or diene (1,4) polymerizations, each leading to different polymer backbones.

2.3. Benzofulvene-based derivatives bearing a pyridine ring.

As mentioned above, the spontaneous polymerization process involving benzofulvene derivatives appears to be very sensitive to the presence of bulky substituents in the close proximity of the polymerization center. On the contrary, the spontaneous polymerization process is not affected when the voluminous substituents are located far from the "*key point*", as in the case of the 6-DMFL-**BF3k** derivative.[3] Based on these studies, the research group of Cappelli has designed and synthesized the compound 2-Pyr-**BF3a** bearing a bulky pyridine ring in position 2 of the 3-phenylbenzofulvene moiety to evaluate its propensity towards solid-state spontaneous polymerization. Among the several aromatic rings, pyridine has attracted researchers' attention due to its electronic distribution generated by the presence of the heteroatom. The studies have shown that the presence of a pyridine ring in position 2 of the 3-phenylbenzofulvene scaffold depressed the spontaneous solid-state polymerization and the corresponding benzofulvene derivative 2-Pyr-**BF3a** was found to organize into an ordered crystalline solid state apparently incompatible with the spontaneous polymerization.[11]

2.4. Phosphorescent neutral platinum(II) complexes.

Encouraging results in the design of high-performance organic materials and smart architecture have made organic light-emitting diode (OLED) technology an important competitor for the existing liquid crystal displays. Particularly, the development of phosphorescent materials based on transition metals plays a crucial role in this success. In this direction, the coordination-unsaturated nature of d^8 transition metal complexes with square-planar structures, such as platinum(II), has been found to provide attractive spectroscopic and luminescence properties.[12] In this way, different classes of luminescent platinum(II) complexes have been investigated to date, ranging from nanowires to nanosheets, nanowheels, and nanohelices.[13,14] Due to their peculiar square-planar geometry, the resulting complexes show a notable tendency to stacking, which often gives rise to supramolecular aggregates with interesting optical properties. However, the establishment of several intermolecular interactions is often considered as being disadvantageous for applications where color purity is desirable, but they have also been exploited for broad-band emission and fabrication of white organic light-emitting diodes (WOLEDs).[15] Intermolecular interactions can occur both in the excited state and in the ground electronic

state, and in the latter case occur through the establishment of both π - π and $dz_2 \cdots dz_2$ metallophilic interactions producing a low emissive excited state with triplet metal-metal-to-ligand (^{3}MMLCT) character. Consequently, the photoluminescence quantum yield (PLQY) of the resulting aggregates is also affected as a bathochromic shift of the absorption and emission wavelength occurs.[16]

2.5. References.

1. Cappelli, A.; Anzini, M.; Vomero, S.; Donati, A.; Zetta, L.; Mendichi, R.; Casolaro, M.; Lupetti, P.; Salvatici, P.; Giorgi, G. *J. Polym. Sci. A* **2005**, *43*, 3289-3304.

2. Cappelli, A.; Paolino, M.; Grisci, G.; Giuliani, G.; Donati, A.; Mendichi, R.; Boccia, A. C.; Botta, C.; Mroˊz, W.; Samperi, C.; Scamporrino, A.; Giorgi, G.; Vomero, S. *J. Mater. Chem*. **2012**, *22*, 9611-9623.

3. Cappelli, A.; Villafiorita-Monteleone, F.; Grisci, G.; Paolino, M.; Razzano, V.; Fabio, G.; Giuliani, G.; Donati, A.; Mendichi, R.; Boccia, A. C.; Pasini, M.; Botta, C. *J. Mater. Chem. C* **2014**, 7897-7905.

4. Cappelli, A.; Razzano, V.; Fabio, G.; Paolino, M.; Grisci, G.; Giuliani, G.; Donati, A.; Mendichi, R.; Mroˊz, W.; Villafiorita-Monteleone, F.; Botta, C. *RSC Adv*. **2015**, 101377-101385.

5. Villafiorita-Monteleone, F.; Cappelli, A.; Paolino, M.; Colombo, M.; Cariati, E.; Mura, A.; Bongiovanni, G.; Botta, C. *J. Phys. Chem. C* **2015**, 18986-18991.

6. Mroˊz, W.; Villafiorita-Monteleone, F.; Pasini, M.; Grisci, G.; Paolino, M.; Razzano, V.; Cappelli, A.; Botta, C. *Mater. Lett*. **2015**, 197-200.

7. Villafiorita-Monteleone, F.; Kozma, E.; Pasini, M.; Paolino, M.; Cappelli, A.; Bongiovanni, G.; Mura, A.; Botta, C. *Appl. Phys. Lett*. **2017**, 183301.

8. Villafiorita-Monteleone, F.; Kozma, E.; Giovanella, U.; Catellani, M.; Paolino, M.; Collico, V.; Colombo, M.; Cappelli, A.; Botta, C. *Dye. Pigment*. **2018**, 331-335.

9. Paolino, M.; Reale, A.; Razzano, V.; Giorgi, G.; Giuliani, G.; Villafiorita-Monteleone, F.; Botta, C.; Coppola, C.; Sinicropi, A.; Cappelli, A. *New J. Chem*. **2020**, 13644-13653.

10. Cappelli, A.; Galeazzi, S.; Giuliani, G.; Anzini, M.; Donati, A.; Zetta, L.; Mendichi, R.; Aggravi, M.; Giorgi, G.; Paccagnini, E.; Vomero, S. *Macromolecules* **2007**, *40*, 3005-3014.

11. Paolino, M.; Reale, A.; Magrini, G.; Razzano, V.; Giuliani, G.; Donati, A.; Giorgi, G.; Samperi, F.; Canetti, M.; Mauro, M.; Villafiorita-Monteleone, F.; Fois, E.; Botta, C.; Cappelli, A. *Eur. Polym. J.* **2020**, *137*, 109923.

12. Tang, M. C.; Chan, A. K. -W.; Chan, M. Y.; Yam, V. W. -W. *Topics in Current Chemistry Collections. Springer, Cham*. **2017**.

13. Wong, V. C. -H.; Po, C.; Leung, S. Y. -L.; Chan, A. K. -W.; Yang, S.; Zhu, B.; Cui, X.; Yam, V. W. -W. *J. Am. Chem. Soc*. **2018**, *140*, 657-666.

14. Yuen, M. -Y.; Roy, V. A. L.; Lu, W.; Kui, S. C. F.; Tong, G. S. M.; So, M. -H.; Chui, S. S. -Y.; Muccini, M.; Ning, J. Q.; Xu, S. J.; Che, C. -M. *Angew. Chemie Int*. **2008**, 9895-9899.

15. Murphy, L.; Brulatti, P.; Fattori, V.; Cocchi, M.; Williams, J. A. G. *Chem. Commun*. **2012**, *48*, 5817-5819.

16. Yam, V. W. -W.; Au, V. K. -M.; Leung, S. Y. -L. *Chem. Rev*. **2015**, *115*, 7589-7728.

2.6. Research article: "Synthesis and UV-light induced oligomerization of a benzofulvene-based neutral platinum(II) complex".

Authors: Marco Paolino, Annalisa Reale, Giulia Magrini, Vincenzo Razzano, **Mario Saletti**, Germano Giuliani, Alessandro Donati, Filippo Samperi, Andrea Scamporrino, Maurizio Canetti, Matteo Mauro, Francesca Villafiorita-Monteleone, Ettore Fois, Chiara Botta, Andrea Cappelli.

Contribution: The Ph.D. candidate's contribution to this work refers to the synthesis, preliminary characterization of compounds, and formal analysis.

Based on previous studies, the newly benzofulvene derivative 2-PTPC-**BF3a** has been designed to show a square-planar neutral platinum(II) complex in position 2 of the 3-phenylbenzofulvene moiety. The resulting complex 2-PTPC-**BF3a** has been easily prepared to start from the corresponding benzofulvene derivative 2-Pyr-**BF3a** to evaluate the effects in the aggregation/polymerization behavior generated by introducing a bulky substituent in the proximity of the putative polymerization center. It has been found that the complex based on platinum(II) did not appear to be able to spontaneously polymerize in the solid state, but it organized itself in microcrystalline films that showed notable differences in their architectures, depending on the conditions in which the aggregation occurred. Intriguingly, the UV-light irradiation of the chloroform dispersions of the complex allowed its photopolymerization, giving rise to a polymer that has been characterized by NMR spectroscopy. On the other hand, the UV irradiation of the solid-state complex produced different results, probably owing to its different architecture.

Synthesis and UV-light induced oligomerization of a benzofulvene-based neutral platinum(II) complex

Marco Paolino [a], Annalisa Reale [a], Giulia Magrini [a], Vincenzo Razzano [a], Mario Saletti [a],
Germano Giuliani [a], Alessandro Donati [a], Filippo Samperi [b], Andrea Scamporrino [b],
Maurizio Canetti [c], Matteo Mauro [d], Francesca Villafiorita-Monteleone [c], Ettore Fois [e],
Chiara Botta [c], Andrea Cappelli [a,*]

[a] *Dipartimento di Biotecnologie, Chimica e Farmacia (Dipartimento di Eccellenza 2018-2022), Università degli Studi di Siena, Via Aldo Moro 2, 53100 Siena, Italy*
[b] *Istituto per i Polimeri, Compositi e Biomateriali (IPCB) U.O.S. di Catania, CNR, Via Gaifami 18, 95126 Catania, Italy*
[c] *Istituto di Scienze e Tecnologie Chimiche "G. Natta" – SCITEC (CNR), Via A. Corti 12, 20133 Milano, Italy*
[d] *Université de Strasbourg, CNRS, Institut de Physique et Chimie des Matériaux de Strasbourg (IPCMS), UMR 7504, 23 rue du Loess, 67000 Strasbourg, France*
[e] *Dipartimento di Scienza e Alta Tecnologia, Università degli Studi dell'Insubria, and INSTM, Via Valleggio 11, 22100 Como, Italy*

ARTICLE INFO

ABSTRACT

Neutral platinum(II) complex 2-PTPC-**BF3a** was easily prepared from benzofulvene derivative 2-Pyr-**BF3a** in order to evaluate the effects in the aggregation/polymerization behavior of a bulky substituent capable of establishing intermolecular metal–metal interactions in the close proximity of the putative polymerization center. Complex 2-PTPC-**BF3a** was found to aggregate into an ordered crystalline solid-state without significant spontaneous polymerization, but the UV-light irradiation of its dispersions in chloroform produced corresponding oligomers, which were characterized by NMR spectroscopy and MALDI-TOF mass spectrometry. On the other hand, the UV-irradiation of the platinum complex in the solid-state produced different results probably depending on the aggregate architecture. Notably, the crystalline films deposited from THF solutions on quartz substrates showed weak emissions, which progressively increased upon irradiation with the formation of oligomers devoid of the aggregation-induced quenching sites that seemed to affect the emission of poly-2-PTPC-**BF3a**. Finally, DFT calculations were performed on platinum complex 2-PTPC-**BF3a** in the aim of rationalizing the observed photophysical features.

1. Introduction

Phosphorescent complexes based on platinum(II) have attracted a great deal of interest in the last two decades from both academic and industrial point of views [1–5]. Owing to their square-planar geometry, these closed-shell complexes with d^8 electronic configuration display remarkable tendency towards stacking, which often gives rise to supramolecular aggregates and excimers with interesting optical properties. In particular, these intermolecular interactions occur either at the electronic ground or excited state, and in the former case take place through establishment of both π- π and d_{z2}···d_{z2} metallophilic interactions that yield to a low-lying emissive excited state with triplet metal–metal-to-ligand (^{3}MMLCT) character. As consequence, bathochromic shift of both absorption and emission wavelength occur also

affecting the photoluminescence quantum yield (PLQY) of the resulting aggregates [3,6–9]. Different classes of luminescent Pt(II) systems have been investigated to date, which are able to form a large variety of supramolecular structures, including nanowires [10–12], nanosheets [13], nanowheels [14], and mesophases [15–18], nanohelices [19] and metallogels [20,21]. Nevertheless, establishment of intermolecular interaction is often seen as being disadvantageous for applications where color purity is desirable, but they have also been exploited for broadband emission and fabrication of white organic light emitting diodes (WOLEDs) [22]. In this regard, nitrogen-containing charge-neutral *tris*-chelating ligands (NˆNˆN type), such as terpyridines, have been the most investigated coordinating scaffolds by far, resulting in cationic complexes showing interesting self-assembly properties, but with moderate PLQY [23]. On the other hand, cyclometalating NˆCˆN and NˆNˆC

---

* Corresponding author.
 E-mail address: andrea.cappelli@unisi.it (A. Cappelli).
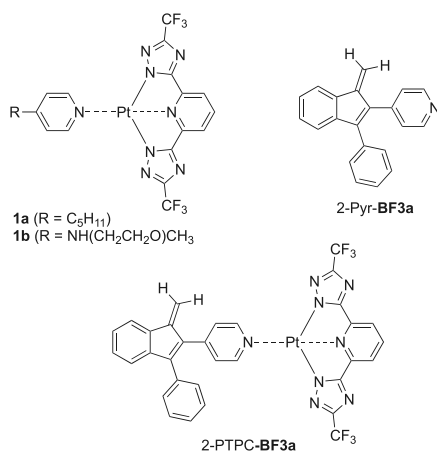
Fig. 1. Structure of compounds **1a,b**, 2-Pyr-**BF3a**, and 2-PTPC-**BF3a**.

Table 1
Experimental conditions used in the photopolymerization experiments of platinum complex 2-PTPC-**BF3a**.

Run	Amount	Irradiated material	Irradiation method	Polymerization (detection)
1	30 mg	Crystalline powder in a 250 mL flask	UV-B lamp, 15 h chamber continuous rotation	Traces (TLC)
2	30 mg	Film[a] in a 250 mL flask	UV-B lamp, 15 h chamber continuous rotation	Traces (TLC)
3	3 mg	Dispersion[b] in CDCl$_3$ in a 5 mm NMR tube	360 nm, 15 h monochromator static	Significant (^{1}H NMR, TLC)
4	5 mg	Dispersion[b] in CDCl$_3$ in a 5 mm NMR tube	360 nm, 15 h monochromator static	Significant (^{1}H NMR, TLC)
5	9 × 5 mg	Dispersion[b] in CDCl$_3$ in a 5 mm NMR tube	360 nm, 15 h monochromator static	Almost complete (TLC) 16 mg after purification

[a] The film samples used in the photopolymerization experiments were prepared by dissolving the indicated amount of benzofulvene derivative 2-PTPC-**BF3a** in the minimum amount of dichloromethane-methanol into the final reactor and by (rapidly) concentrating the resulting solution under reduced pressure while the reactor was kept under continuous rotation.
[b] Dispersion in CDCl$_3$.

scaffolds have shown improved optical properties also suitable for OLED fabrication [24]. Alternatively, some of us have reported the use of formally bis-anionic 2,6-*bis*(1*H*-1,2,4-triazol-5-yl)pyridines as chromophoric ligands for the preparation of neutral Pt(II) complexes **1a,b** with enhanced optical properties both in solution and in the aggregated state, such as high PLQY, and remarkable tendency towards self-assembly that can be finely managed by means of both kinetics and thermodynamic parameters [25].

The discovery that some benzofulvene derivatives are liable to undergo spontaneous polymerization in the apparent absence of catalysts and/or initiator led to development of a large family of new polymers (i. e. polybenzofulvenes) showing peculiar features [26–28]. These include the prompt and quantitative formation by spontaneous thermoreversible polymerization, the tunable solubility both in organic solvents and aqueous media [29–33] joined with interesting optoelectronic features [27,34]. In this regard, the developmental studies in application research led to the discovery of highly emissive polymeric supramolecular assemblies potentially useful in optoelectronic applications such as the development of organic light emitting diodes (OLED) devices [34–40].

Interestingly, we observed that the spontaneous polymerization process involving benzofulvene derivatives appeared to be very sensitive to the presence of bulky substituents in the close proximity of the polymerization center [41]. Very recently, we showed that the presence of a pyridine ring in the position 2 of the 3-phenylbenzofulvene moiety of **BF3a** (Fig. 1, R = 4-pyridyl) depressed the spontaneous solid-state polymerization and the corresponding benzofulvene derivative 2-Pyr-**BF3a** was found to organize into an ordered crystalline solid state apparently incompatible with the spontaneous polymerization [42]. On the other hand, 2-Pyr-**BF3a** was induced to photopolymerize by UV irradiation of the amorphous films [42]. On the bases of these observations, we designed the introduction of a square-planar neutral platinum(II) complex in the position 2 of the 3-phenylbenzofulvene moiety as in compound 2-PTPC-**BF3a** (Fig. 1) in order to evaluate the effects in the aggregation/polymerization behavior of a very bulky substituent in the close proximity of the putative polymerization center. The complex has been selected for its highly tendency to establish intermolecular metal–metal interactions.

The present paper reports on the synthesis, the optoelectronic features, and the photopolymerization behaviour of the newly designed benzofulvene derivative 2-PTPC-**BF3a** with a pyridine in the position 2

of the 3-phenylbenzofulvene moiety behaving as the ancillary ligand and 2,6-bis(3-(trifluoromethyl)-1*H*-1,2,4-triazol-5-yl)pyridine as the tridentate ligand of a neutral platinum(II) complex.

2. Experimental section

2.1. Synthesis

All chemicals used were of reagent grade. Yields refer to purified products and are not optimized. Melting points were determined in open capillaries on a Gallenkamp apparatus and are uncorrected. Merck silica gel 60 (230–400 mesh) was used for column chromatography. Merck TLC plates, silica gel 60 F$_{254}$ were used for TLC. NMR spectra were recorded with a Bruker DRX-400 AVANCE or a Bruker DRX-500 AVANCE spectrometer in the indicated solvents (TMS as internal standard): the values of the chemical shifts are expressed in ppm and the coupling constants (J) in Hz. An Agilent 1100 LC/MSD operating with an electrospray source was used in mass spectrometry experiments.

2.1.1. General procedure for the synthesis of neutral platinum(II) complexes 2-PTPC-BF3a and 2

A mixture of the appropriate pyridine derivative (i. e. 2-Pyr-**BF3a** or **3**) in 2-methoxyethanol-water as the solvent system (3:1 v/v) containing 2,6-bis(3-(trifluoromethyl)-1H-1,2,4-triazol-5-yl)pyridine (**4**), PtCl$_2$(DMSO)$_2$, and diisopropylethylamine (DIPEA) was heated at 80–85 °C for 16 h under an inert atmosphere.

The precipitate was collected by filtration, washed in sequence with 2-methoxyethanol-water (3:1 v/v) and then with petroleum ether-ethyl acetate (1:1 v/v) and dried under reduced pressure. Purification of the crude product by flash chromatography with the suitable eluent gave the expected complex (i. e. 2-PTPC-**BF3** and **2).**

2.1.2. Platinum(II) complex 2-PTPC-BF3a

The title compound was prepared from benzofulvene derivative 2-Pyr-**BF3a** (15 mg, 0.0533 mmol), compound **4** (20 mg, 0.0573 mmol), PtCl$_2$(DMSO)$_2$ (23 mg, 0.0546 mmol), and DIPEA (10 μL) and purified

M. Paolino et al.

by flash chromatography with dichloromethane-methanol (95:5) as the eluent to obtain pure 2-PTPC-**BF3a** (30 mg, yield 68%). ^{1}H NMR (500 MHz, CDCl$_3$): 5.86 (s, 1H), 6.39 (s, 1H), 7.30–7.34 (m, 2H), 7.36–7.44 (m, 8H), 7.77–7.82 (m, 1H), 7.86 (d, J = 7.9, 2H), 8.06 (t, J = 7.9, 1H), 9.50–9.60 (m, 2H). ^{13}C NMR (125 MHz, CDCl$_3$): 114.6, 118.3, 120.3, 121.3, 127.4, 128.1, 128.9, 129.1, 129.2, 131.8, 132.8, 136.4, 141.7, 143.1, 145.5, 146.9, 147.4, 149.1, 152.8, 163.9. MS (MALDI-TOF) m/z: [M+H]$^{+}$ Calcd for C$_{32}$H$_{19}$F$_6$N$_8$Pt 824.1; Found 824.4.

2.1.3. Platinum(II) complex 2

The title compound was prepared from indenone derivative **3** (15 mg, 0.0529 mmol), compound **4** (20 mg, 0.0573 mmol), PtCl$_2$(DMSO)$_2$ (23 mg, 0.0546 mmol), and DIPEA (10 μL) and purified by flash chromatography with dichloromethane-methanol (95:5) as the eluent to obtain pure **6** (34 mg, yield 78%). ^{1}H NMR (400 MHz, CDCl$_3$-CD$_3$OD): 7.20 (d, J = 7.1, 1H), 7.31–7.52 (m, 9H), 7.61 (d, J = 6.9, 1H), 7.86 (d, J = 8.0, 2H), 8.09 (t, J = 7.9, 1H), 9.34 (d, J = 7.0, 2H).

*2.1.4. General procedures for the UV-induced polymerization of 2-PTPC-**BF3a***

The suitable amount (see Table 1) of neutral platinum(II) complex 2-PTPC-**BF3a** was irradiated as described in Table 1 and the progress of the polymerization reaction was monitored by TLC (and by ^{1}H NMR spectroscopy in the cases reported in Table 1). The oligomeric samples were purified by precipitation with *n*-hexane from a solution of the oligomers in dichloromethane-methanol (9:1).

2.2. Wide angle X-ray diffraction (WAXD)

WAXD data were obtained at 20 °C using a Siemens D-500 diffractometer equipped with a Siemens FK 60–10 2000 W tube (Cu K$_\alpha$ radiation, λ = 0.154 nm). The operating voltage and current were 40 kV and 40 mA, respectively.

2.3. Matrix assisted laser desorption/ionization time of flight mass spectrometry (MALDI-TOF MS)

MALDI-TOF mass spectra were recorded in reflectron mode by means of a 4800 Proteomic Analyzer (Applied Biosystems) MALDI-TOF/TOF instrument equipped with a Nd:YAG laser at a wavelength of 355 nm with <500 ps pulse and 200 Hz firing rate. The accelerating voltage was 15 kV. External calibration was performed using an Applied Biosystems calibration mixture consisting of polypeptides with different molar mass values. The irradiance was maintained slightly above the threshold, to obtain a mass resolution of about 7000–9000 fwhm. Mass accuracy was about 50 ppm. The best mass spectra were recorded using *trans*-2-[3-(4-*tert*-butylphenyl)-2-methyl-2-propenylidene]malononitrile (DCTB) as a matrix.

2.4. Photophysical characterization

2.4.1. Instrument details

Absorption spectra were measured on a Varian Cary 100 double-beam UV–VIS spectrophotometer and baseline corrected. Steady-state emission spectra were recorded on a Horiba Jobin-Yvon IBH FL-322 Fluorolog 3 spectrometer equipped with a 450 W xenon arc lamp, double-grating excitation, and emission monochromators (2.1 nm mm^{-1} of dispersion; 1200 grooves mm^{-1}). Emission intensities were recorded with either a PPD 850 single photon counting detector or a Hamamatsu R13456 red sensitive Peltier-cooled PMT detector. Emission and excitation spectra were corrected for source intensity (lamp and grating) and emission spectral response (detector and grating) by standard correction curves. Time-resolved measurements on solid state samples were performed using either time-correlated single-photon counting (TCSPC) or the Multi Channel Scaling (MCS) electronics option on the Fluorolog 3. For TCSPC, NanoLEDs lamps (fwhm < 1.2 ns) with suitable wavelength
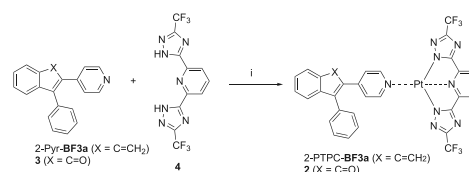
Scheme 1. Synthesis of neutral platinum(II) complexes 2-PTPC-**BF3a** and **2**. Reagents: (i) PtCl$_2$(DMSO)$_2$, DIPEA, CH$_3$OCH$_2$CH$_2$OH, H$_2$O.

and with repetition rates between 10 kHz and 1 MHz were used to excite the sample. For MCS, a pulsed xenon lamp was used instead with μs pulse at the selected excitation wavelength. The excitation sources were mounted directly on the sample chamber at 90° to a double-grating emission monochromator (2.1 nm mm^{-1} of dispersion; 1200 grooves mm^{-1}) and collected by a PPD 850 single-photon-counting detector. The photons collected at the detector are correlated by a time-to-amplitude converter (TAC) to the excitation pulse. Signals were collected using an IBH DataStation Hub photon-counting module and data analysis was performed using the commercially available DAS6 software (Horiba Jobin-Yvon IBH).

2.4.2. Methods

For time resolved measurements, the quality of the fit was assessed by minimizing the reduced χ^2 function and by visual inspection of the weighted residuals. For multi-exponential decays, the intensity, namely I(*t*), has been assumed to decay as the sum of individual single exponential decays (Eq. (1)):

$$I(t) = \sum_{i=1}^{n} \alpha_i e^{-\frac{t}{\tau_i}} \tag{1}$$

where τ_i are the decay times and α_i are the amplitude of the component at $t = 0$. The percentages to the pre-exponential factors, α_i, are listed upon normalization to unity. All the solvents were spectrophotometric grade. Deaerated samples were prepared by the freeze–pumpthaw technique.

Moreover, in SCITEC (CNR) laboratories, UV–vis absorption spectra are obtained with a Perkin Elmer Lambda 900 spectrometer. Photoluminescence (PL) spectra are obtained with a NanoLog composed by a iH320 spectrograph equipped with a Synapse QExtra charge-coupled device by exciting with a monochromated 450 W Xe lamp. The spectra are corrected for the instrument response. PL QY values of solutions were obtained by using quinine sulfate as the reference. PL QY of the powders were measured with a home-made integrating sphere according to the procedure reported elsewhere [43]. Time-resolved TCSPC measurements are obtained with PPD-850 single photon detector module and DeltaTime serie DD-300 DeltaDiode and analysed with the instrument Software DAS6.

2.4.3. Molecular modelling studies

The geometry optimizations for the S$_0$, S$_1$ and T$_1$ 2-PTPC-**BF3a** were performed adopting the cam-b3lyp functional, and using the D95v++(d, p) basis set for N, C, H atoms, The Dresten-Stuttgart pseudopotential and basis set was adopted for Pt. The S$_1$ structure was optimized using the TD-DFT/cam-b3lyp approach, while the T$_1$ optimization was performed using the unrestricted form of cam-b3lyp. Excitations were calculated at the TD-DFT/cam-b3lyp level using the above-mentioned basis set. The 2-PTPC-BF3a dimeric form was optimized with the same functional an Pt pseudopotential as the monomer and by adopting the D95v(d) basis set N, C, H atoms. Calculations were performed with G09 suite of program [44].
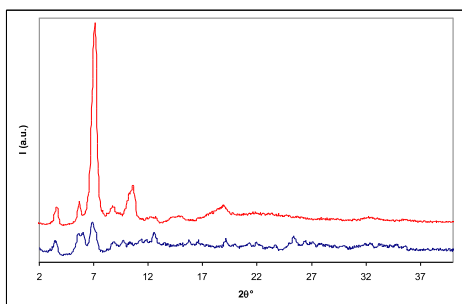
3

Fig. 2. WAXD spectrum obtained with a thin-film of platinum(II) complex 2-PTPC-**BF3a** (red) obtained by the double deposition procedure on a quartz substrate compared with the corresponding spectrum obtained with a powder sample of the same compound (blue). (For interpretation of the references to colour in this figure legend, the reader is referred to the web version of this article.)

3. Results and discussion

3.1. Chemistry

The preparation of the new neutral platinum(II) complex 2-PTPC-**BF3a** was carried out starting from the corresponding benzofulvene derivative 2-Pyr-**BF3a** [42] as depicted in Scheme 1.

The synthetic protocol employed for preparation of the target Pt(II) complexes was reported elsewhere for related derivatives [10]. The pathway employed 2,6-bis(3-(trifluoromethyl)-1*H*-1,2,4-triazol-5-yl) pyridine (**4**) as the tridentate ligand, PtCl$_2$(DMSO)$_2$ as the platinum(II) source, and DIPEA as the base in 2-methoxyethanol-water as the solvent system. This procedure was applied also to indenone intermediate **3** [42] in order to obtain the corresponding complex **2** to be studied for comparative purposes.

The structure of neutral platinum(II) complex 2-PTPC-**BF3a** was characterized by NMR spectroscopy (Figures SI-1 and SI-2), which confirmed that this benzofulvene monomer bearing a bulky substituent near the polymerization center was unable to polymerize spontaneously under this condition. Interestingly, the comparison of the NMR spectra of complex 2-PTPC-**BF3a** with those of benzofulvene derivative 2-Pyr-**BF3a** (Figures SI-1 and SI-2) showed the effect of complexation on the electron distribution on the pyridine ring. In fact, the signals attributed to the pyridine moiety were downfield shifted upon complexation as expected for this class of compounds.

On the other hand, the comparison of the ^{1}H NMR spectrum of complex 2-PTPC-**BF3a** with the one of the corresponding ketone derivative **2** (Figure SI-3) confirmed the consistency of the structures assigned to these neutral platinum complexes.

All attempts to obtain single crystals of the novel neutral platinum(II) complexes 2-PTPC-**BF3a** and **2** suitable for X-ray diffractometric analysis were unfruitful and formation of sharp needles were observed instead. Thus, in order to investigate the potential ability of these neutral Pt(II) complexes to self-assemble into precisely ordered structure, the corresponding powder samples were characterized by WAXD studies (Figure SI-4). The obtained WAXD profiles clearly demonstrated that the powder samples of neutral platinum(II) complexes 2-PTPC-**BF3a** and **2** showed an ordered crystalline structure.

On the basis of the interesting results obtained for the photoinduced polymerization of 2-Pyr-**BF3a** [42], we next evaluated the polymerization features of neutral platinum(II) complex 2-PTPC-**BF3a** by performing a systematic investigation (Table 1) similar to that involving 2-Pyr-**BF3a** [42]. Thus, the propensity of platinum(II) complex 2-PTPC-**BF3a** to assemble into precisely organized architectures was then evaluated also during the building of films showing different thickness. In particular, thin-films of this platinum complex were obtained by a single deposition procedure (drop casting of a 2-PTPC-**BF3a** solution in THF) on a quartz substrate, while a double deposition procedure was used to obtain thicker films showing however similar opacity. The films were then characterized by WAXD studies and compared with the spectrum obtained with 2-PTPC-**BF3a** powder sample (Fig. 2).

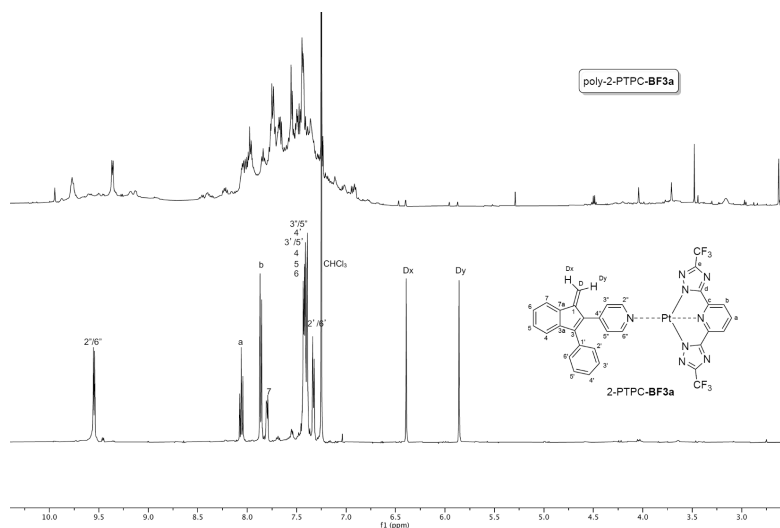The comparison shown in Fig. 2 suggested that the thin-film obtained

Fig. 3. Comparison of ^{1}H NMR spectra of poly-2-PTPC-**BF3a** with that of platinum complex 2-PTPC-**BF3a**.

4
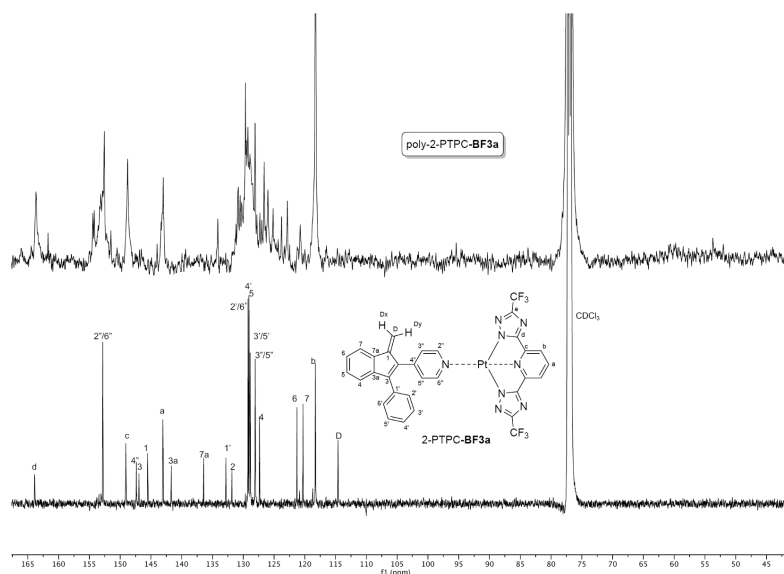
Fig. 4. Comparison of ^{13}C NMR spectra of poly-2-PTPC-**BF3a** (top) with that of platinum complex 2-PTPC-**BF3a** (bottom).

with 2-PTPC-**BF3a** by the double deposition procedure was characterized by a significant order showing peculiar features (i.e. noticeable differences) with respect to that of the corresponding powder sample. On the other hand, the comparison between the spectra obtained with 2-PTPC-**BF3a** films of different thickness showed negligible differences (data not shown). Therefore, platinum complex 2-PTPC-**BF3a** appeared to show a greater tendency to assemble into precisely organized architectures with respect to pyridine derivative 2-Pyr-**BF3a** [42] in agreement with the aggregating role played by the platinum complex, but environmental conditions could play a role in determining the aggregate architectures.

As shown in Table 1 (run 1), we were unable to photopolymerize platinum complex 2-PTPC-**BF3a** in the form of crystalline powder. In fact, the irradiation of the sharp needles of complex 2-PTPC-**BF3a** failed in producing significant polymerization probably because of the tendency of the complex to assemble into precisely organized architectures, which are incompatible with polymerization as already observed with crystalline 2-Pyr-**BF3a** [42].

Quite surprisingly and in disagreement with the results obtained with 2-Pyr-**BF3a** [42], unsatisfactory results were obtained also by irradiating the film obtained by dissolving the indicated amount of 2-PTPC-**BF3a** in the minimum amount of dichloromethane-methanol into

Fig. 5. MALDI-TOF mass spectrum of poly-2-PTPC-**BF3a** sample recorded in reflectron mode using DCTB as the matrix.

5

Table 2
Photophysical features of neutral platinum complexes 2-PTPC-**BF3a** and **2**.

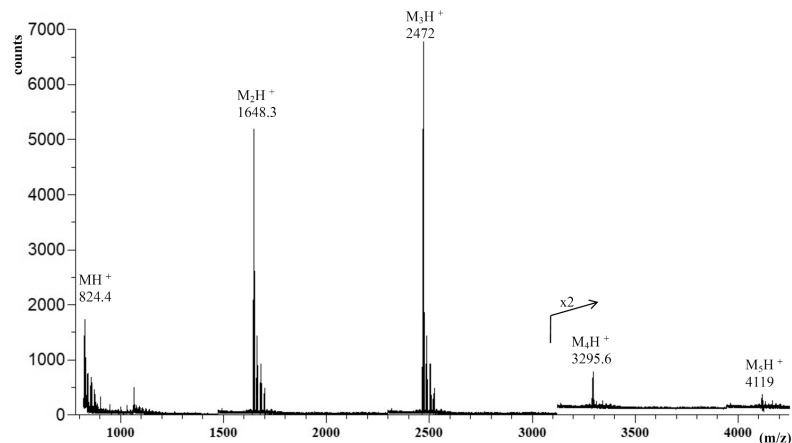| Compound	Solution[a]			Powder		Film pre*/post UV irradiation		
	λ_{ab} (nm)	λ_{em} (nm)	QY(%) (τ_{av}(ns))	λ_{em} (nm)	QY(%) (τ_{av}(µs))	λ_{ab} (nm)	$\lambda\lambda_{em}$ (nm)	QY(%) (τ_{av}(µs))
2	300, 405	439		617	(0.98) [620][a]			
2-PTPC-**BF3a**	350	458	15 (5.7)[458][a]	515	12 (1.19) [520][a]	440*/408	526*/590	<1*/17 (61) [620][a]
Poly-2-PTC-**BF3a**	330, 370	550	0.2	590	1 (35) [590][a]			

[a] Emission wavelength where the lifetime has been recorded is reported in square brackets.

the final reactor and by (rapidly) concentrating the resulting solution while the reactor was kept under continuous rotation (run 2, Table 1). On the other hand, the photopolymerization process appeared to be operative by irradiating the dispersions of complex 2-PTPC-**BF3a** into deuterated chloroform (runs 3 and 4, Table 1). Thus, the experiment was repeated simultaneously on 9 samples of 2-PTPC-**BF3a** dispersion (the complex is only partially soluble) in deuterated chloroform, and the corresponding polymer (poly-PTPC-**BF3a**) was isolated by precipitation with *n*-hexane from a solution in dichloromethane-methanol (9:1) and characterized by NMR spectroscopy, SEC, and MALDI-TOF mass spectrometry (run 5, Table 1).

When ^{1}H NMR spectrum of poly-2-PTPC-**BF3a** was compared with that of the corresponding monomer (Fig. 3), a good correspondence was observed among the sharp peaks of the monomer and the broad ones of the polymer.

However, the contemporary presence of peaks showing different broadness suggested the possible presence of two polymeric components showing rather different molecular weight distribution (MWD) values, or alternatively the presence of oligomers showing marked aggregating features.

Overall, these results confirmed the polymeric nature of poly-2-PTPC-**BF3a** and the tendency of platinum complex 2-PTPC-**BF3a** to photopolymerization in solution.

As expected, ^{13}C NMR spectrum (Fig. 4) was resolved enough to allow a detailed comparison to be made with the corresponding spectrum of platinum complex 2-PTPC-**BF3a** that revealed the close correspondence between the sharp signals of the monomers with the broad ones in the spectrum of the polymer. Moreover, the signal at 114.6 ppm (assigned to the exocyclic methylene carbon D), and the one at 145.5 (assigned to the other vinylidene carbon 1) were up-field shifted at around 54 and 60 ppm in poly-2-PTPC-**BF3a** spectrum similarly as it occurred in poly-Pyr-**BF3a**. This result was suggestive of a vinyl polymerization mechanism (a possible structure for the dimer is shown in Figure SI-5), but owing to the features of ^{13}C NMR spectrum, structural heterogeneities cannot be ruled out.

The polymeric nature of poly-2-PTPC-**BF3a** was confirmed also by MALDI-TOF mass spectrum measurements. In fact, the spectrum reported in Fig. 5 shows a short series of repeating families of peaks showing 823 Da transitions (i. e. the mass of the repeating unit of poly-2-PTPC-**BF3**) spanning from *m/z* ca. 824 up to ca. *m/z* 4119 assigned to the pentamer.

However, the most abundant oligomer in the spectrum appeared to be the trimer showing a molar mass of 2472 Da with just detectable amounts of tetramer and pentamer species. The most intense peak of each family was assigned to the protonated ions of the oligomers terminated with hydrogens at both ends, as already observed in other polybenzofulvene derivatives [45,46].

Probably, the photon absorption produces monomer activation with the formation of a biradical specie in which the first radical is stabilized as indenyl radical [47], whereas the second radical in the exocyclic methylene group could initiate the oligomerization reaction by attacking another monomer molecule.
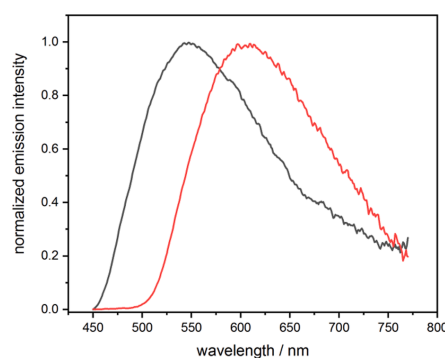
Fig. 6. Emission spectra of compound 2-PTPC-**BF3a** (black trace) and **2** (red trace) in solid state as neat powder upon excitation at λ_{exc} = 420 nm. (For interpretation of the references to colour in this figure legend, the reader is referred to the web version of this article.)

Thus, these results confirmed for 2-PTPC-**BF3a** the lack of tendency towards the spontaneous polymerization in the ordered (crystalline) solid state and the propensity towards the photopolymerization in the appropriate conditions such as those occur in saturated solutions. On the other hand, the apparent ineffective photopolymerization observed in the film was difficult to be explained.

3.2. Photophysical characterization

The photophysical features of the newly-synthesized neutral platinum(II) complex 2-PTPC-**BF3a** were characterized in both solid state and solution and are summarized in Table 2 along with those of indanone derivative **2**.

Upon excitation at λ_{exc} = 350 nm, THF solutions of platinum complex 2-PTPC-**BF3a** display intense luminescence that is characterized by a broad and featureless emission spectrum centred at λ_{em} = 458 with a PLQY of 15% and with an intensity-averaged lifetime τ_{av} = 5.7 ns (see Table 2). On the other hand, upon excitation at λ_{exc} = 420 nm, crystalline powder samples of 2-PTPC-**BF3a** display intense luminescence similarly characterized by a broad and featureless emission spectrum centred at λ_{em} = 515 nm (see Table 2 and Fig. 6). Time-resolved emission analysis show a decay curve that can be fitted with a bi-exponential decay for 2-PTPC-**BF3a** with τ_{av} = 1.19 µs [τ_1 = 1.8 µs (22%) and τ_2 = 0.76 µs (74%)]. For comparison, a mono-exponential kinetics is recorded for **2** being τ = 0.98 µs. Overall, the long-lived photoluminescence of these derivatives in the solid state can be ascribed with confidence to an emitting excited-state with [3]MMLCT character as consequence of the establishment of metallophilic intermolecular $d^8 \cdots d^8$ interactions, in well agreement with findings observed previously on related

6
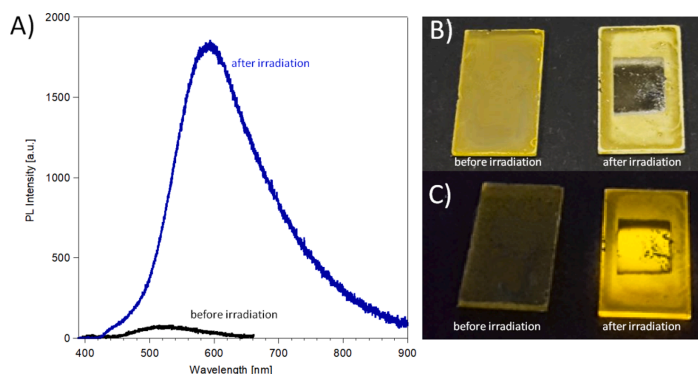
Fig. 7. Left Panel: (A) Emission of a spin-coated film of 2-PTPC-**BF3a** before (black line) and after (blue line) irradiation at 350 nm for 7 min. Right Panels: Picture of a film before (left) and after (right) irradiation in the central area of the film under ambient (B) and UV lamp (C). (For interpretation of the references to colour in this figure legend, the reader is referred to the web version of this article.)

Fig. 8. Left panel: emission of a cast-coated film of 2-PTPC-**BF3a** before (red line) and after (green line) irradiation at 350 nm for 7 min. Right panel: confocal microscope image of a film after partial 405 nm laser irradiation for 30 min. (For interpretation of the references to colour in this figure legend, the reader is referred to the web version of this article.)
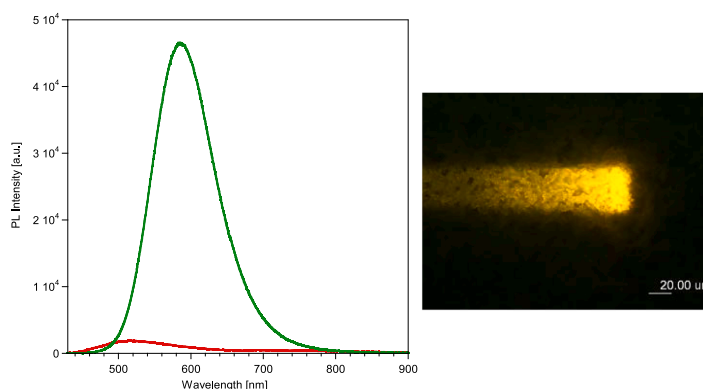
phosphorescent Pt(II) complexes, as reported by some of us[48].

Quite surprisingly, cast or spin-coated films deposited from THF solution of 2-PTPC-**BF3a** display a weak emission that progressively increases upon irradiation at 350 nm for about 7 min. The effect of irradiation is evidenced in Fig. 7 where the picture of a spin-coated film before and after partial irradiation (square in the middle of the film) is shown. The irradiated part of the film becomes transparent under ambient light (Fig. 7, panel B) and strongly emissive under UV light (Fig. 7, panel C).

Similarly, as shown in Fig. 8, the area of a cast film irradiated with the 405 nm laser line of a confocal microscope for 30 min, displays bright emission.

These observations suggest that 2-PTPC-**BF3a** self-assembles in the cast or spin-coated films deposited from THF solution showing an ordered architecture probably different from that of the crystalline powder as supported by both WAXD investigations (see Fig. 2) and the differences in the emission maxima, which appeared slightly red-shifted in the film ($\lambda_{em} = 526$ nm) with respect to the crystalline powder ($\lambda_{em} = 515$ nm). Thus, the UV-irradiation of the film appeared to produce

significant changes both in the transparence of the film and in its absorption and emission features that are suggestive of structure-architecture modifications. A first explanation could be formulated in terms of photopolymerization of 2-PTPC-**BF3a** in the films obtained by drop casting or spin coating from THF solutions. Interestingly, powder samples of poly-2-PTPC-**BF3a** showed a weak emission peaked at 590 nm, which is red-shifted with respect to the one of 2-PTPC-**BF3a** crystalline powders, but well corresponding to the emission of the 2-PTPC-**BF3a** films after UV irradiation (see Fig. 9 and SI-7). The differences in the excitation profiles of poly-2-PTPC-**BF3a** with respect to the 2-PTPC-**BF3a** films after UV irradiation (Fig. 9) however suggest that both monomeric and oligomeric species may contribute to the emission of the UV irradiated film.

In order to obtain information about the composition of the UV-irradiated film, MALDI-TOF mass spectrometry measurements were performed, and the results (Fig. 10) showed the contemporary presence of a significant proportion of the starting platinum complex along with oligomeric species, which could be responsible for the relatively high PLQY value observed.
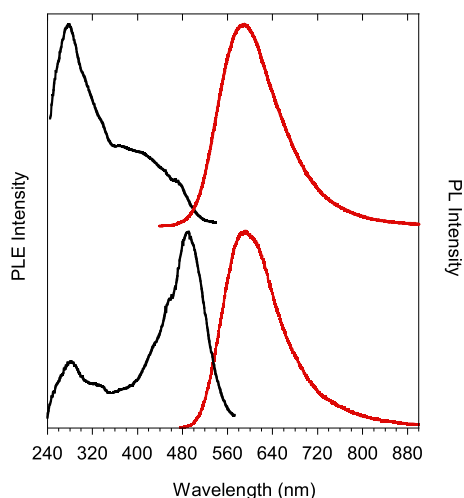
7

19

Fig. 9. PL emission (red line) and PL excitation (PLE, black line) of 2-PTPC-**BF3a** film after UV irradiation (top) and poly-2-PTPC-**BF3a** powders (bottom).

These observations suggest that irradiation of the films deposited from THF provides a polymerization method able to reduce the aggregation-induced quenching observed in the material produced by photo-polymerization in solution for which NMR results highlighted the presence of oligomers showing marked aggregating features.

3.3. Molecular modelling studies

The structure of platinum complex 2-PTPC-**BF3a** was investigated using the DFT. Geometry optimizations were performed for the ground

state S_0 structure (DTT), for the excited S_1 and triplet T_1 structures. The optimized structures are shown in Fig. 11A.

The electronic excitation spectrum is reported in Fig. 11B, where it is also reported the predicted $S_0 \rightarrow S_1$ emission spectrum as well. Also, both excitation and emission calculated in THF are shown.

Interestingly the predicted effect of THF solvation is an enhancement of the excitation dipoles, leading to higher intensities, both in absorption and in emission, while the transition energies show modest changes. The low energy excitation involves both HOMO → LUMO and HOMO → LUMO + 1 transition. The HOMO is essentially localized on the **BF3a** ligand, with a small contribution of Pt. On the other hand, both LUMO and LUMO + 1 are delocalized over the entire complex (See ESI). The S_0 optimized geometry, in line with expectation, features a square-planar arrangement of N atoms bonding to Pt that, in principles might allow for an extended π conjugation. Such a structure is essentially maintained in both S_1 and T_1 optimized structures. Such finding, might indicate that S_1 to T_1 inter-system-crossing cannot be excluded, see also Scheme 2 showing the energy ladders of the S_0, S_1 and T_1 structures.

4. Conclusion

Our work on the spontaneous solid-state polymerization of benzofulvene derivatives has suggested a key role for bulky substituents in the close proximity of the polymerization center in depressing the spontaneous polymerization process. Accordingly, benzofulvene derivative 2-Pyr-**BF3a** bearing a pyridine ring in the position 2 of the 3-phenylbenzofulvene moiety was observed to lack the propensity towards the spontaneous polymerization, and this result was explained with the solid-state organization into ordered columnar aggregates apparently incompatible with the spontaneous polymerization. However, 2-Pyr-**BF3a** was found to photopolymerize by irradiation of amorphous film samples with UV light [42]. Thus, 2-Pyr-**BF3a** was promptly transformed into neutral platinum(II) complex 2-PTPC-**BF3a** bearing, near the putative polymerization center, a very bulky substituent capable of establishing intermolecular metal–metal interactions. Similarly to 2-Pyr-**BF3a,** 2-PTPC-**BF3a** appeared to be unable polymerize spontaneously in the solid-state, but to organize into crystalline powders or films showing noticeable differences in their architectures depending on the
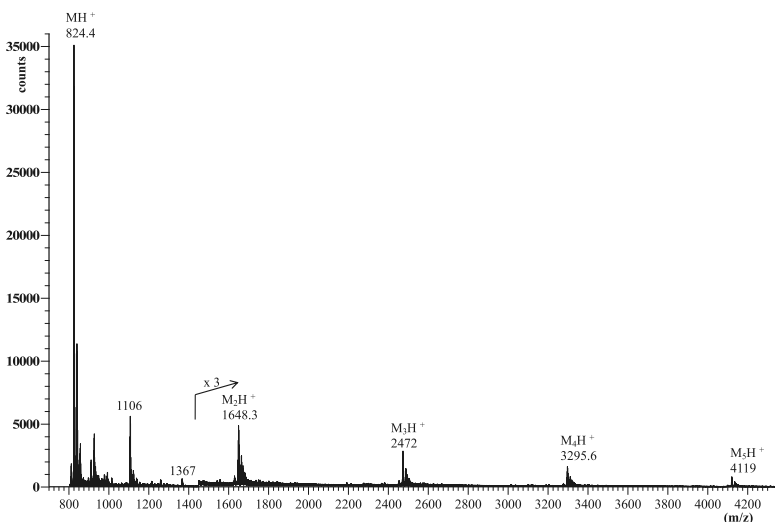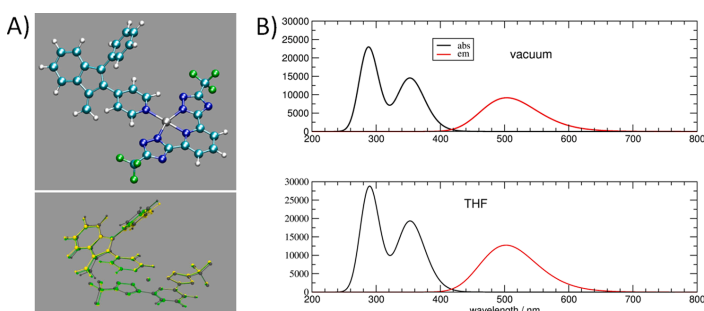

**Fig. 10.** MALDI-TOF spectrum of the UV-irradiated PTPC-**BF3a** film.

8

Fig. 11. (A) 3D graphical representations of 2-PTPC-**BF3a**. Top panel: Ground state S0 optimized structure. Color code: Pt, gray spheres, N, blue spheres, C, cyan spheres, H, white spheres. Bottom panel; overlap of the S_0, S_1 and T_1 structures, color codes; green, ground state (S_0); gray, optimized S_1 structure; yellow, optimized T_1 structure. (B) Simulated absorbance (black line) and emission (red line) spectra of 2-PTPC-**BF3a**. Top panel calculations in vacuum, bottom panel calculations in THF. (For interpretation of the references to colour in this figure legend, the reader is referred to the web version of this article.)
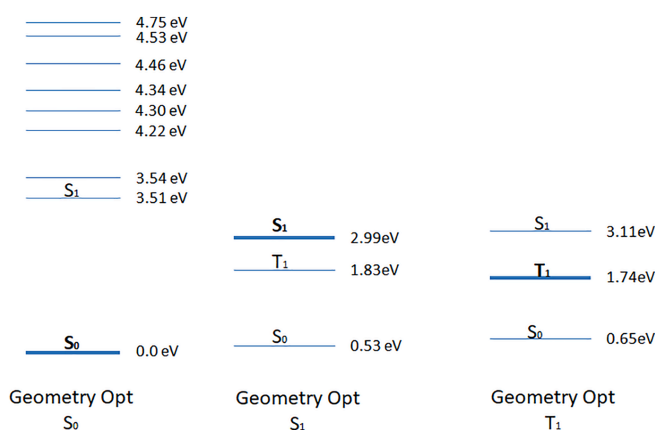
Scheme 2. Energy ladders relative to: (left) ground state S_0 structure, (middle) S_1 optimized structure; (right) optimized T_1 structure. All energies, (in eV) are calculated with respect to the S_0 ground state energy.

environmental conditions in which the aggregation occurred. Similarly to 2-Pyr-**BF3a,** 2-PTPC-**BF3a** appeared to be capable of photopolymerizing by irradiation with UV-light. In particular, the photopolymerization of platinum complex 2-PTPC-**BF3a** appeared to be effective in the conditions of the chloroform dispersions resulting in the formation of poly-2-PTPC-**BF3a**, which was characterized by NMR spectroscopy and MALDI-TOF mass spectrometry. Conversely, the irradiation of 2-PTPC-**BF3a** in the solid-state produced different outcomes, which probably depend on the aggregate architecture. The most intriguing effect was observed in the crystalline films deposited from THF solutions on quartz substrates that showed weak emissions, which progressively increased upon irradiation with the formation of oligomers devoid of the aggregation-induced quenching sites that seemed to affect the emission of poly-2-PTPC-**BF3a**. Finally, molecular modelling studies (i. e. DFT calculations) were performed on platinum complex 2-PTPC-**BF3a** in the aim of rationalizing the experimental photophysical features and were found to be successful in reproducing the experimental absorption and emission spectra.

Author contributions

The manuscript was written through contributions of all authors. All authors have given approval to the final version of the manuscript.

Data availability

The raw/processed data required to reproduce these findings are available from the corresponding author by request.

CRediT authorship contribution statement

Marco Paolino: Conceptualization, Formal analysis, Data curation, Writing - original draft. **Annalisa Reale:** Formal analysis. **Giulia Magrini:** Formal analysis. **Vincenzo Razzano:** Conceptualization, Formal analysis. **Mario Saletti:** Formal analysis. **Germano Giuliani:** Formal analysis, Investigation. **Alessandro Donati:** Formal analysis, Investigation. **Filippo Samperi:** Formal analysis, Data curation, Writing - original draft. **Andrea Scamporrino:** Formal analysis, Investigation. **Maurizio Canetti:** Formal analysis. **Matteo Mauro:** Data Curation, Formal analysis, Writing - original draft. **Francesca Villafiorita-Monteleone:** Formal analysis, Investigation. **Ettore Fois:** Data curation, Formal analysis, Visualization, Writing - original draft. **Chiara Botta:** Data curation, Formal analysis, Writing - original draft. **Andrea Cappelli:** Conceptualization, Data curation, Project administration, Supervisor, Writing - ooriginal draft.

9

Declaration of Competing Interest

The authors declare that they have no known competing financial interests or personal relationships that could have appeared to influence the work reported in this paper.

Appendix A. Supplementary material

Supplementary data to this article can be found online at https://doi.org/10.1016/j.eurpolymj.2021.110597.

References

[1] K. Meerholz, Enlightening solutions, Nature 437 (2005) 327–328, https://doi.org/10.1038/437327a.

[2] J.A.G. Williams, Photochemistry and Photophysics of Coordination Compounds: Platinum, in: V. Balzani, S. Campagna (Eds.), Photochem. Photophysics Coord. Compd. II, Springer, Berlin, Heidelberg, 2007: pp. 205–268. doi:https://doi.org/10.1007/128_2007_134.

[3] V.W.-W. Yam, V.K.-M. Au, S.Y.-L. Leung, Light-Emitting Self-Assembled Materials Based on d8 and d10 Transition Metal Complexes, Chem. Rev. 115 (2015) 7589–7728, https://doi.org/10.1021/acs.chemrev.5b00074.

[4] M.-C. Tang, A.K.-W. Chan, M.-Y. Chan, V.W.-W. Yam, Platinum and Gold Complexes for OLEDs, in: N. Armaroli, H. Bolink (Eds.), Photoluminescent Mater. Electroluminescent Devices, Springer, Cham, 2016: pp. 67–109. doi:https://doi.org/10.1007/978-3-319-59304-3_3.

[5] G. Donati, Photon-driven spin current, Nat. Photon. 10 (2016) 431, https://doi.org/10.1038/nphoton.2016.133.

[6] V. Jankus, A.P. Monkman, Is Poly(vinylcarbazole) a Good Host for Blue Phosphorescent Dopants in PLEDs? Dimer Formation and Their Effects on the Triplet Energy Level of Poly(N-vinylcarbazole) and Poly(N-Ethyl-2-Vinylcarbazole), Adv. Funct. Mater. 21 (2011) 3350–3356, https://doi.org/10.1002/adfm.201100732.

[7] A. Aliprandi, D. Genovese, M. Mauro, L. De Cola, Recent Advances in Phosphorescent Pt(II) Complexes Featuring Metallophilic Interactions: Properties and Applications, Chem. Lett. 44 (2015) 1152–1169, https://doi.org/10.1246/cl.150592.

[8] K.M.-C. Wong, V.W.-W. Yam, Self-Assembly of Luminescent Alkynylplatinum(II) Terpyridyl Complexes: Modulation of Photophysical Properties through Aggregation Behavior, Acc. Chem. Res. 44 (2011) 424–434, https://doi.org/10.1021/ar100130j.

[9] K. Li, G.S. Ming Tong, Q. Wan, G. Cheng, W.-Y. Tong, W.-H. Ang, W.-L. Kwong, C.-M. Che, Highly phosphorescent platinum(ii) emitters: photophysics, materials and biological applications, Chem. Sci. 7 (2016) 1653–1673, https://doi.org/10.1039/C5SC03766B.

[10] M. Mauro, A. Aliprandi, C. Cebrián, D. Wang, C. Kübel, L. De Cola, Self-assembly of a neutral platinum(ii) complex into highly emitting microcrystalline fibers through metallophilic interactions, Chem. Commun. 50 (2014) 7269–7272, https://doi.org/10.1039/C4CC01045K.

[11] C. Po, A.Y.-Y. Tam, K.M.-C. Wong, V.W.-W. Yam, Supramolecular Self-Assembly of Amphiphilic Anionic Platinum(II) Complexes: A Correlation between Spectroscopic and Morphological Properties, J. Am. Chem. Soc. 133 (2011) 12136–12143, https://doi.org/10.1021/ja203920w.

[12] V.C.-H. Wong, C. Po, S.Y.-L. Leung, A.K.-W. Chan, S. Yang, B. Zhu, X. Cui, V.W.-W. Yam, Formation of 1D Infinite Chains Directed by Metal–Metal and/or π–π Stacking Interactions of Water-Soluble Platinum(II) 2,6-Bis(benzimidazol-2′-yl)pyridine Double Complex Salts, J. Am. Chem. Soc. 140 (2018) 657–666, https://doi.org/10.1021/jacs.7b09770.

[13] M.-Y. Yuen, V.A.L. Roy, W. Lu, S.C.F. Kui, G.S.M. Tong, M.-H. So, S.S.-Y. Chui, M. Muccini, J.Q. Ning, S.J. Xu, C.-M. Che, Semiconducting and Electroluminescent Nanowires Self-Assembled from Organoplatinum(II) Complexes, Angew. Chemie Int. Ed. 47 (2008) 9895–9899, https://doi.org/10.1002/anie.200802981.

[14] W. Lu, S.S.-Y. Chui, K.-M. Ng, C.-M. Che, A submicrometer wire-to-wheel metamorphism of hybrid tridentate cyclometalated platinum(II) complexes, Angew. Chem. Int. Ed. Engl. 47 (2008) 4568–4572, https://doi.org/10.1002/anie.200704450.

[15] W. Lu, Y. Chen, V.A.L. Roy, S.S.-Y. Chui, C.-M. Che, Supramolecular Polymers and Chromonic Mesophases Self-Organized from Phosphorescent Cationic Organoplatinum(II) Complexes in Water, Angew. Chemie Int. Ed. 48 (2009) 7621–7625, https://doi.org/10.1002/anie.200903109.

[16] V.N. Kozhevnikov, B. Donnio, B. Heinrich, J.A.G. Williams, D.W. Bruce, Green-blue light-emitting platinum(ii) complexes of cyclometallated 4,6-difluoro-1,3-dipyridylbenzenes showing mesophase organisation, J. Mater. Chem. C 3 (2015) 10177–10187, https://doi.org/10.1039/C5TC02077H.

[17] V.N. Kozhevnikov, B. Donnio, B. Heinrich, D.W. Bruce, Morphology-driven absorption and emission colour changes in liquid-crystalline, cyclometallated platinum(II) complexes, Chem. Commun. 50 (2014) 14191–14193, https://doi.org/10.1039/C4CC06958G.

[18] V.N. Kozhevnikov, B. Donnio, D.W. Bruce, Phosphorescent, Terdentate, Liquid-Crystalline Complexes of Platinum(II): Stimulus-Dependent Emission, Angew. Chemie Int. Ed. 47 (2008) 6286–6289, https://doi.org/10.1002/anie.200802101.

[19] S. Yu-Lut Leung, V. Wing-Wah Yam, Hierarchical helices of helices directed by Pt···Pt and π–π stacking interactions: reciprocal association of multiple helices of dinuclear alkynylplatinum(ii) complex with luminescence enhancement behavior, Chem. Sci. 4 (2013) 4228–4234, https://doi.org/10.1039/C3SC51534F.

[20] A.Y.-Y. Tam, V.W.-W. Yam, Recent advances in metallogels, Chem. Soc. Rev. 42 (2013) 1540–1567, https://doi.org/10.1039/C2CS35354G.

[21] C.A. Strassert, C.-H. Chien, M.D. Galvez Lopez, D. Kourkoulos, D. Hertel, K. Meerholz, L. De Cola, Switching On Luminescence by the Self-Assembly of a Platinum(II) Complex into Gelating Nanofibers and Electroluminescent Films, Angew. Chemie Int. Ed. 50 (2011) 946–950, https://doi.org/10.1002/anie.201003818.

[22] L. Murphy, P. Brulatti, V. Fattori, M. Cocchi, J.A.G. Williams, Blue-shifting the monomer and excimer phosphorescence of tridentate cyclometallated platinum(ii) complexes for optimal white-light OLEDs, Chem. Commun. 48 (2012) 5817–5819, https://doi.org/10.1039/C2CC31330H.

[23] C. Wei, Y. He, X. Shi, Z. Song, Terpyridine-metal complexes: Applications in catalysis and supramolecular chemistry, Coord. Chem. Rev. 385 (2019) 1–19, https://doi.org/10.1016/j.ccr.2019.01.005.

[24] W. Wu, X. Wu, J. Zhao, M. Wu, Synergetic effect of C^N^N/C^N^N coordination and the arylacetylide ligands on the photophysical properties of cyclometaled platinum complexes, J. Mater. Chem. C. 3 (2015) 2291–2301, https://doi.org/10.1039/C4TC02358G.

[25] A. Aliprandi, M. Mauro, L. De Cola, Controlling and imaging biomimetic self-assembly, Nat. Chem. 8 (2016) 10–15, https://doi.org/10.1038/nchem.2383.

[26] A. Cappelli, M. Anzini, S. Vomero, A. Donati, L. Zetta, R. Mendichi, M. Casolaro, P. Lupetti, P. Salvatici, G. Giorgi, New π-stacked benzofulvene polymer showing thermoreversible polymerization: Studies in macromolecular and aggregate structures and polymerization mechanism, J. Polym. Sci. Part A Polym. Chem. 43 (2005) 3289–3304, https://doi.org/10.1002/pola.20783.

[27] A. Cappelli, G. Grisci, M. Paolino, F. Castriconi, G. Giuliani, A. Donati, S. Lamponi, R. Mendichi, A.C. Boccia, F. Samperi, S. Battiato, E. Paccagnini, M. Gentile, M. Licciardi, G. Giammona, S. Vomero, Combining spontaneous polymerization and click reactions for the synthesis of polymer brushes: A "grafting onto" approach, Chem. - A Eur. J. 19 (2013) 9710–9721, https://doi.org/10.1002/chem.201202534.

[28] M. Paolino, G. Grisci, A. Reale, V. Razzano, G. Giuliani, A. Donati, R. Mendichi, D. Piovani, A.C. Boccia, A. Grillo, G. Giorgi, A. Cappelli, Structural manipulation of the conjugated phenyl moiety in 3-phenylbenzofulvene monomers: Effects on spontaneous polymerization, Polymers (Basel) 10 (2018), https://doi.org/10.3390/polym10070752.

[29] A. Cappelli, G. Grisci, M. Paolino, V. Razzano, G. Giuliani, A. Donati, C. Bonechi, R. Mendichi, A.C. Boccia, M. Licciardi, C. Scialabba, G. Giammona, S. Vomero, Polybenzofulvene derivatives bearing dynamic binding sites as potential anticancer drug delivery systems, J. Mater. Chem. B 3 (2015) 361–374, https://doi.org/10.1039/C4TB01268B.

[30] A. Cappelli, M. Paolino, G. Grisci, V. Razzano, G. Giuliani, A. Donati, C. Bonechi, R. Mendichi, S. Battiato, F. Samperi, C. Scialabba, G. Giammona, F. Makovec, M. Licciardi, Hyaluronan-coated polybenzofulvene brushes as biomimetic materials, Polym. Chem. 7 (2016) 6529–6544, https://doi.org/10.1039/c6py01644h.

[31] M. Licciardi, C. Scialabba, G. Giammona, M. Paolino, A. Cappelli, Design and development of hyaluronan-functionalized polybenzofulvene nanoparticles as CD44 receptor mediated drug delivery system, J. Nanopart. Res. (2017) 197, https://doi.org/10.1007/s11051-017-3881-z.

[32] M. Paolino, G. Grisci, F. Castriconi, A. Reale, G. Giuliani, A. Donati, C. Bonechi, G. Giorgi, R. Mendichi, D. Piovani, A.C. Boccia, M. Canetti, F. Samperi, S. Dattilo, C. Scialabba, M. Licciardi, E. Paccagnini, M. Gentile, A. Cappelli, Densely PEGylated polybenzofulvene brushes for potential applications in drug encapsulation, Pharmaceutics 10 (2018) 234, https://doi.org/10.3390/pharmaceutics10040234.

[33] M. Paolino, A. Reale, V. Razzano, G. Giuliani, A. Donati, G. Giorgi, C.A. Boccia, R. Mendichi, D. Piovani, C. Botta, L. Salvini, F. Samperi, C. Savoca, M. Licciardi, E. Paccagnini, M. Gentile, A. Cappelli, Physicochemical Properties of a New PEGylated Polybenzofulvene Brush for Drug Encapsulation, Pharmaceutics 11 (2019), https://doi.org/10.3390/pharmaceutics11090444.

[34] A. Cappelli, F. Villafiorita-Monteleone, G. Grisci, M. Paolino, V. Razzano, G. Fabio, G. Giuliani, A. Donati, R. Mendichi, A.C. Boccia, M. Pasini, C. Botta, Highly emissive supramolecular assemblies based on π-stacked polybenzofulvene hosts and a benzothiadiazole guest, J. Mater. Chem. C 2 (2014) 7897–7905, https://doi.org/10.1039/c4tc01200c.

[35] A. Cappelli, V. Razzano, G. Fabio, M. Paolino, G. Grisci, G. Giuliani, A. Donati, R. Mendichi, W. Mróz, F. Villafiorita-Monteleone, C. Botta, Side chain engineering in π-stacked polybenzofulvene derivatives bearing electron-rich chromophores for OLED applications, RSC Adv. 5 (2015) 101377–101385, https://doi.org/10.1039/c5ra21164f.

[36] F. Villafiorita-Monteleone, A. Cappelli, M. Paolino, M. Colombo, E. Cariati, A. Mura, G. Bongiovanni, C. Botta, Aggregation-Induced Förster Resonance Energy Transfer in Polybenzofulvene/Dye Nanoparticles, J. Phys. Chem. C 119 (2015) 18986–18991, https://doi.org/10.1021/acs.jpcc.5b05589.

[37] W. Mróz, F. Villafiorita-Monteleone, M. Pasini, G. Grisci, M. Paolino, V. Razzano, A. Cappelli, C. Botta, π-stacked polybenzofulvene derivatives as hosts for yellow and red emitting OLEDs, Mater. Lett. 142 (2015) 197–200, https://doi.org/10.1016/j.matlet.2014.12.002.

[38] F. Villafiorita-Monteleone, E. Kozma, M. Pasini, M. Paolino, A. Cappelli, G. Bongiovanni, A. Mura, C. Botta, Polybenzofulvenes-based blends with benzothiadiazole and perylene diimide derivatives emitting from yellow to the

10

deep-red by resonant energy transfer processes, Appl. Phys. Lett. 110 (2017), 183301, https://doi.org/10.1063/1.4983022.

[39] F. Villafiorita-Monteleone, E. Kozma, U. Giovanella, M. Catellani, M. Paolino, V. Collico, M. Colombo, A. Cappelli, C. Botta, Red and deep-red emissive polymeric nanoparticles based on polybenzofulvene and perylenediimide derivatives, Dye. Pigment. 149 (2018) 331–335, https://doi.org/10.1016/j.dyepig.2017.10.010.

[40] M. Paolino, A. Reale, V. Razzano, G. Giorgi, G. Giuliani, F. Villafiorita-Monteleone, C. Botta, C. Coppola, A. Sinicropi, A. Cappelli, Design, synthesis, structure, and photophysical features of highly emissive cinnamic derivatives, New J. Chem. 44 (2020) 13644–13653, https://doi.org/10.1039/D0NJ02429E.

[41] A. Cappelli, S. Galeazzi, G. Giuliani, M. Anzini, A. Donati, L. Zetta, R. Mendichi, M. Aggravi, G. Giorgi, E. Paccagnini, S. Vomero, Structural manipulation of benzofulvene derivatives showing spontaneous thermoreversible polymerization. Role of the substituents in the modulation of polymer properties, Macromolecules 40 (2007) 3005–3014, https://doi.org/10.1021/ma0629236.

[42] M. Paolino, A. Reale, G. Magrini, V. Razzano, G. Giuliani, A. Donati, G. Giorgi, F. Samperi, M. Canetti, M. Mauro, F. Villafiorita-Monteleone, E. Fois, C. Botta, A. Cappelli, UV-light-induced polymerization in the amorphous solid-state of a spontaneously non-polymerizing 3-phenylbenzofulvene monomer, Eur. Polym. J. 137 (2020), 109923, https://doi.org/10.1016/j.eurpolymj.2020.109923.

[43] J. Moreau, U. Giovanella, J.-P. Bombenger, W. Porzio, V. Vohra, L. Spadacini, G. Di Silvestro, L. Barba, G. Arrighetti, S. Destri, M. Pasini, M. Saba, F. Quochi, A. Mura, G. Bongiovanni, M. Fiorini, M. Uslenghi, C. Botta, Highly Emissive Nanostructured Thin Films of Organic Host-Guests for Energy Conversion, ChemPhysChem. 10 (2009) 647–653, https://doi.org/10.1002/cphc.200800682.

[44] M.J. Frisch, G.W. Trucks, H.B. Schlegel, G.E. Scuseria, M.A. Robb, J.R. Cheeseman, G. Scalmani, V. Barone, G.A. Petersson, H. Nakatsuji, X. Li, M. Caricato, A. V. Marenich, J. Bloino, B.G. Janesko, R. Gomperts, B. Mennucci, H.P. Hratchian, J. V.

Ortiz, A.F. Izmaylov, J.L. Sonnenberg, D. Williams-Young, F. Ding, F. Lipparini, F. Egidi, J. Goings, B. Peng, A. Petrone, T. Henderson, D. Ranasinghe, V.G. Zakrzewski, J. Gao, N. Rega, G. Zheng, W. Liang, M. Hada, M. Ehara, K. Toyota, R. Fukuda, J. Hasegawa, M. Ishida, T. Nakajima, Y. Honda, O. Kitao, H. Nakai, T. Vreven, K. Throssell, J.E. Montgomery, {Jr.}, J. A. Peralta, F. Ogliaro, M.J. Bearpark, J.J. Heyd, E.N. Brothers, K.N. Kudin, V.N. Staroverov, T.A. Keith, R. Kobayashi, J. Normand, K. Raghavachari, A.P. Rendell, J.C. Burant, S.S. Iyengar, J. Tomasi, M. Cossi, J.M. Millam, M. Klene, C. Adamo, R. Cammi, J.W. Ochterski, R.L. Martin, K. Morokuma, O. Farkas, J.B. Foresman, D.J. Fox, Gaussian 09, (2009).

[45] A. Cappelli, M. Paolino, P. Anzini, G. Giuliani, S. Valenti, M. Aggravi, A. Donati, R. Mendichi, L. Zetta, A.C. Boccia, F. Bertini, F. Samperi, S. Battlato, E. Paccagnini, S. Vomero, Structure-property relationships in densely grafted π-stacked polymers, J. Polym. Sci. Part A Polym. Chem. 48 (2010) 2446–2461, https://doi.org/10.1002/pola.24016.

[46] A. Cappelli, V. Razzano, M. Paolino, G. Grisci, G. Giuliani, A. Donati, R. Mendichi, F. Samperi, S. Battiato, A.C. Boccia, A. Mura, G. Bongiovanni, W. Mróz, C. Botta, Bithiophene-based polybenzofulvene derivatives with high stacking and hole mobility, Polym. Chem. 6 (2015) 7377–7388, https://doi.org/10.1039/C5PY00904A.

[47] M.J. Bearpark, F. Bernardi, M. Olivucci, M.A. Robb, B.R. Smith, Can Fulvene S1 Decay Be Controlled? A CASSCF Study with MMVB Dynamics, J. Am. Chem. Soc. 118 (1996) 5254–5260, https://doi.org/10.1021/ja9542799.

[48] D. Genovese, A. Aliprandi, E.A. Prasetyanto, M. Mauro, M. Hirtz, H. Fuchs, Y. Fujita, H. Uji-I, S. Lebedkin, M. Kappes, L. De Cola, Mechano- and Photochromism from Bulk to Nanoscale: Data Storage on Individual Self-Assembled Ribbons, Adv. Funct. Mater. 26 (2016) 5271–5278, https://doi.org/10.1002/adfm.201601269.

11

2.7. Research article: "Spontaneous polymerization of benzofulvene derivatives bearing complexed or un-complexed pyridine rings".

Authors: Marco Paolino, **Mario Saletti**, Annalisa Reale, Vincenzo Razzano, Germano Giuliani, Alessandro Donati, Gianluca Giorgi, Andrea Atrei, Matteo Mauro, Andrea Scamporrino, Filippo Samperi, Ettore Fois, Gloria Tabacchi, Chiara Botta, Andrea Cappelli.

Contribution: The Ph.D. candidate's contribution to this work refers to the synthesis, preliminary characterization of compounds, formal analysis, and the writing of the experimental section of the original draft.

In this research article, two novel 3-phenylbenzofulvene derivatives bearing complexed and un-complexed pyridine rings (6-PTPC-**BF3k** and 6-Pyr-**BF3k**) have been designed and synthesized. In particular, bulky platinum complex substituents able of generating metallophilic interactions have been introduced in position 6 of the 3-phenylbenzofulvene scaffold to evaluate their effects on spontaneous solid-state polymerization. It has been found that both monomers spontaneously polymerize upon solvent removal under reduced pressure in the absence of catalysts or initiators. Curiously, the benzofulvene monomer bearing complexed pyridine rings (6-PTPC-**BF3k**) showed a more elaborate polymerization behavior than the corresponding un-complexed one (6-Pyr-**BF3k**). Indeed, experimental evidence suggested that the spontaneous polymerization of 6-PTPC-**BF3k**, which bears the platinum complex, appeared to be in competition with its crystallization, probably because of the presence of the bulky and rigid platinum complex. The obtained polymer (*poly*-6-

PTPC-**BF3k**) appeared to reveal the features of a copolymer rather than those expected for the corresponding homopolymer.

Spontaneous polymerization of benzofulvene derivatives bearing complexed or un-complexed pyridine rings

Marco Paolino [a], Mario Saletti [a], Annalisa Reale [a], Vincenzo Razzano [a], Germano Giuliani [a], Alessandro Donati [a], Claudia Bonechi [a], Gianluca Giorgi [a], Andrea Atrei [a], Matteo Mauro [b], Andrea Scamporrino [c], Filippo Samperi [c], Ettore Fois [d], Gloria Tabacchi [d], Chiara Botta [e], Andrea Cappelli [a, *]

[a] *Dipartimento di Biotecnologie, Chimica e Farmacia (Dipartimento di Eccellenza 2018-2022), Università degli Studi di Siena, Via Aldo Moro 2, 53100 Siena, Italy*
[b] *Université de Strasbourg, CNRS, Institut de Physique et Chimie des Matériaux de Strasbourg (IPCMS), UMR 7504, 23 Rue du Loess, 67000 Strasbourg, France*
[c] *Istituto per i Polimeri, Compositi e Biomateriali (IPCB) U.O.S. di Catania, CNR, Via Gaifami 18, 95126 Catania, Italy*
[d] *Dipartimento di Scienza e Alta Tecnologia, Università degli Studi dell'Insubria, Via Valleggio 11, 22100 Como, Italy*
[e] *Istituto di Scienze e Tecnologie Chimiche "G. Natta" – SCITEC (CNR), Via A. Corti 12, 20133 Milano, Italy*

ABSTRACT

Benzofulvene derivatives bearing complexed and un-complexed pyridine rings are designed and synthesized to assess the effects on the spontaneous solid-state polymerization of the presence in position 6 of the 3-phenylbenzofulvene moiety of bulky substituents capable of establishing metallophilic interactions. Both the benzofulvene monomers are found to polymerize spontaneously upon solvent removal under reduced pressure in the apparent absence of catalysts or initiators. The resulting polybenzofulvene derivatives are characterized by NMR spectroscopy, MALDI-TOF mass spectrometry, and in photophysical studies.

1. Introduction

Topochemical polymerization and, in a special way, the preparation of large-size polymer single crystals is recently a topic of great interest [1–5].

This polymerization technique is based on monomeric species capable to yield ordered structures in solid-state and/or in solution by means of intermolecular non-covalent interactions (hydrogen bonding, π-π stacking, CH-π, and hydrophobic interactions, among other) [6–9]. To date, many monomers involved in additive-free topochemical polymerization via heating, pressure or light-irradiation have been found [10,11]. Among these, particular attention was paid to diacetylenes [12–14], alkenes [15,16], dinitrosobenzene [17], quinodimethanes [18,19], and azido-alkyne terminated molecules [20]. On the other hand, in our laboratories, 3-phenyl benzofulvene compounds (i. e. **BF3** derivatives in Fig. 1) were studied as interesting examples of monomers capable of polymerizing spontaneously in high concentrated solution and in solid-state without the addition of catalysts and/or initiators [21–24]. After an extensive structure-property study we recognized as driving force for the polymerization of the monomers an initial process

of affinity recognition in solution mediated by π-π-stacking interactions [23,25–27]. The corresponding polybenzofulvene derivatives have shown very intriguing features such as the very fast and practically quantitative formation [21,24,27–29], the thermoreversibility of the polymerization process [21,23,27,30–32], the tunable solubility in both organic and aqueous solvents [31–39], and interesting optoelectronic properties [25,40–47]. Polybenzofulvene macromolecules are thought to be formed by stacked arrays of π-electron systems conjugated through-space alongside a single (π-stacked) polymer chain [23–25,31,40,41,44].

However, the presence of bulky substituents (i. e. *t*-butyl, dimethylaminocarbonyl, 4-pyridyl) appeared to inhibit the spontaneous polymerization process involving benzofulvene derivatives when they are located in the close proximity of the polymerization center [23,48,49]. On the other hand, the process appeared to be compatible with steric bulk when bulky substituents were located far from the polymerization center as in the case of 6-DMFL-**BF3k** [40]. Interestingly, *poly*-6-DMFL-**BF3k** was used in the building of highly emissive polymeric supramolecular assemblies useful in optoelectronic applications [40,42,45,46]. Thus, a pyridine ring was introduced in position 6 of the 3-

---

Chapter 2. Investigation of aggregation/polymerization behavior of innovative benzofulvene-based derivatives

phenylbenzofulvene moiety as in compound 6-Pyr-**BF3k** (Fig. 1) and exploited in the formation of the neutral tridentate platinum complex 6-PTPC-**BF3k**, where the 6-Pyr-**BF3k** moiety is employed as ancillary ligand.

These benzofulvene monomers were assessed from the point of view of their susceptibility to the spontaneous polymerization and the corresponding polybenzofulvene derivatives were characterized by NMR spectroscopy, MALDI-TOF mass spectrometry, and in photophysical studies. Our interest was focused on the effects of the presence in position 6 of the 3-phenylbenzofulvene moiety of bulky substituents capable of establish metallophilic interactions on the polymer features.

2. Experimental section

2.1. Synthesis

All chemicals used were of reagent grade. Yields refer to purified products and are not optimized. Melting points were determined in open capillaries on a Gallenkamp apparatus and are uncorrected. Merck silica gel 60 (230–400 mesh) was used for column chromatography. Merck TLC plates, silica gel 60 F_{254} were used for TLC. NMR spectra were recorded with a Bruker DRX-400 AVANCE or a Bruker DRX-500 AVANCE spectrometer in the indicated solvents (TMS as internal standard): the values of the chemical shifts are expressed in ppm and the coupling constants (*J*) in Hz. An Agilent 1100 LC/MSD operating with an electrospray source was used in mass spectrometry experiments.
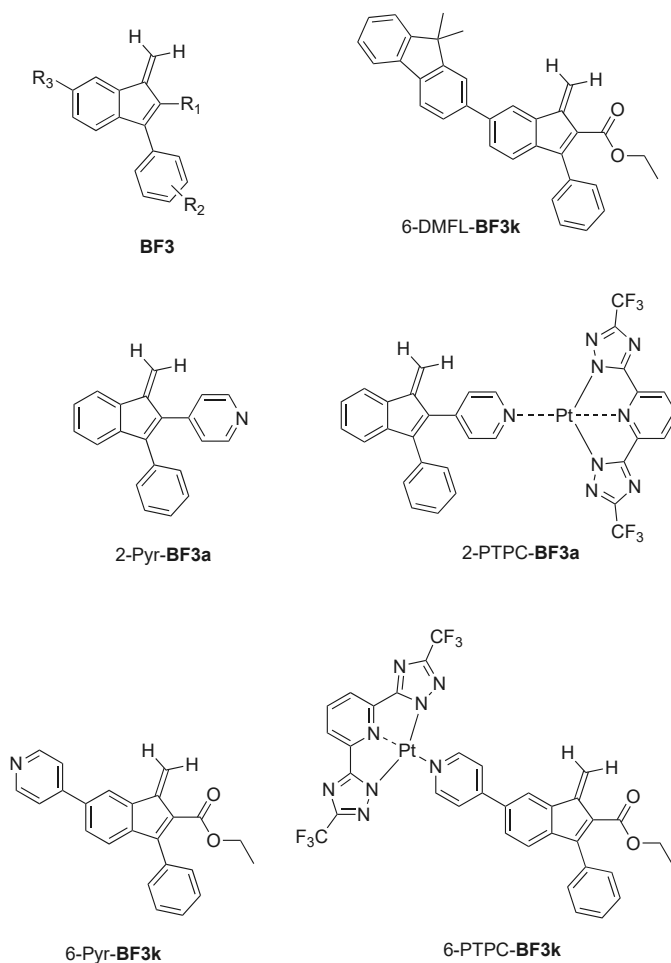

Fig. 1. Structure of 6-PTPC-**BF3k**, a benzofulvene derivative bearing a bulky platinum complex in position 6 of its 3-phenylindene nucleus, and those of some related compounds.
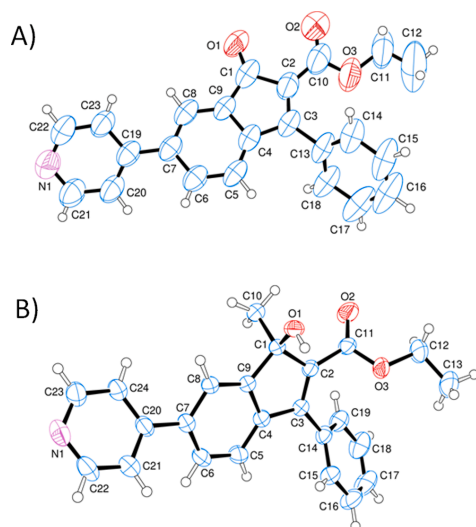
2

Fig. 2. Structure of indenone derivative **2** (A) and indenol derivative **3** (B) as determined by crystallography. Ellipsoids enclose 50% probability.

2.1.1. Ethyl 1-oxo-3-phenyl-6-(pyridin-4-yl)-1H-indene-2-carboxylate (2)

A degassed mixture of 4-pyridineboronic acid (73 mg, 0.594 mmol) in 9.0 mL of 1,4-dioxan-ethanol (8:1), 2,6-di-*tert*-butyl-4-methylphenol (BHT, 64 mg, 0.29 mmol) and K_3PO_4 (376 mg, 1.77 mmol) was stirred at room temperature for 10 min. Subsequently, $Pd(PPh_3)_2Cl_2$ (82 mg, 0.117 mmol), triphenylphosphine (15 mg, 0.057 mmol), and triflate **1** (250 mg, 0.586 mmol) were added in sequence and the resulting mixture was refluxed for 8 h. The reaction mixture was concentrated under reduced pressure, and the residue was partitioned between dichloromethane and water. The organic layer was dried over sodium sulfate and concentrated under reduced pressure. Purification of the residue by flash chromatography with petroleum ether-ethyl acetate (6:4) as the eluent gave indenone derivative **2** as a yellow solid (156 mg, yield 75%). Recrystallization of **2** from ethyl acetate by slow evaporation afforded yellow crystals suitable for X-ray diffraction studies melting at 170–171 °C. ^{1}H NMR (400 MHz, $CDCl_3$): 1.17 (t, $J = 7.1$, 3H), 4.22 (q, $J = 7.1$, 2H), 7.33 (d, $J = 7.7$, 1H), 7.47–7.60 (m, 7H), 7.70 (dd, $J = 7.7$, 1.6, 1H), 7.89 (d, $J = 1.2$, 1H), 8.72 (br s, 2H). MS (ESI) m/z: $[M+Na]^+$ Calcd for $C_{23}H_{17}NNaO_3$ 378.1; Found 378.0.

2.1.2. Ethyl 1-hydroxy-1-methyl-3-phenyl-6-(pyridin-4-yl)-1H-indene-2-carboxylate (3)

To a solution of compound **2** (0.46 g, 1.29 mmol) in dichloromethane (20 mL), a 2 M solution of $Al(CH_3)_3$ (2.58 mL, 5.16 mmol) in toluene was added, and the reaction mixture was stirred at room temperature for 30 min. Subsequently, the $Al(CH_3)_3$ excess was decomposed with a 1 N solution of NaOH and the solid was filtered off. The organic phase was dried over sodium sulfate and concentrated under reduced pressure. The resulting residue was purified by flash chromatography with petroleum ether-ethyl acetate (1:1) as the eluent to obtain indenol derivative **3** as a pale-yellow solid (0.386 g, yield 81%). An analytical sample was obtained by recrystallization from ethyl acetate by slow evaporation (mp 178–179 °C). ^{1}H NMR (400 MHz, $CDCl_3$): 1.07 (t, $J = 7.1$, 3H), 1.82 (s, 3H), 3.75 (br s, 1H), 4.05–4.27 (m, 2H), 7.27 (d, $J = 7.9$, 1H), 7.37–7.49 (m, 5H), 7.55–7.62 (m, 3H), 7.85 (d, $J = 1.2$, 1H), 8.67 (d, $J = 5.4$, 2H). MS (ESI) m/z: $[M+H]^+$ Calcd for $C_{24}H_{22}NO_3$ 372.2; Found 372.0.

2.1.3. Ethyl 1-methylene-3-phenyl-6-(pyridin-4-yl)-1H-indene-2-carboxylate (6-Pyr-BF3k)

A mixture of indenol derivative **3** (0.38 g, 1.02 mmol) in $CDCl_3$ (25 mL) containing *p*-toluenesulfonic acid monohydrate (0.625 g, 3.29 mmol) was heated to reflux for 1 h. The reaction mixture was then washed with a saturated solution of $NaHCO_3$ and dried over sodium sulfate to obtain a solution of benzofulvene monomer 6-Pyr-**BF3k**. ^{1}H NMR (500 MHz, $CDCl_3$): 1.07 (t, $J = 7.1$, 3H), 4.15 (q, $J = 7.1$, 2H), 6.49 (s, 1H), 6.68 (s, 1H), 7.35 (d, $J = 7.9$, 1H), 7.39–7.51 (m, 5H), 7.53–7.60 (m, 3H), 7.96 (s, 1H), 8.67 (d, $J = 5.4$, 2H); see also Fig. 3. ^{13}C NMR (125 MHz, $CDCl_3$): 13.8, 60.4, 118.0, 118.6, 121.7, 122.8, 126.4, 127.2, 128.1, 128.5, 128.6, 134.1, 137.7, 138.0, 142.1, 143.5, 148.3, 150.3, 152.2, 164.8; see also Fig. 4. MS (ESI) m/z: $[M+H]^+$ Calcd for $C_{24}H_{20}NO_2$ 354.1; Found 354.1.

2.1.4. Poly[ethyl 1-methylene-3-phenyl-6-(pyridin-4-yl)-1H-indene-2-carboxylate] (poly-6-Pyr-BF3k)

The solution of benzofulvene monomer 6-Pyr-**BF3k** in $CDCl_3$ was concentrated under reduced pressure. The resulting residue was dissolved into chloroform and again evaporated (this process of dissolution/evaporation was repeated three times). The last residue was purified by precipitation with *n*-hexane from a solution of the polymer in chloroform-ethanol (1:1) and dried under reduced pressure to obtain *poly*-6-Pyr-**BF3k** as a pale-yellow solid (0.25 g, yield 69% in monomeric unit). ^{1}H NMR (500 MHz, $CDCl_3$): see Fig. 3. ^{13}C NMR (125 MHz, $CDCl_3$): see Fig. 4.

2.1.5. Platinum(II) complex 5

A mixture of indenol derivative **3** (40 mg, 0.108 mmol) in 4.0 mL of 2-methoxyethanol-water (3:1) as the solvent system containing **4** (40 mg, 0.115 mmol), $PtCl_2(DMSO)_2$ (46 mg, 0.109 mmol), and diisopropylethylamine (20 µL) was heated at 80–85 °C for 16 h under an inert atmosphere. The precipitate was collected by filtration, washed in sequence with 2-methoxyethanol-water (3:1) and then with petroleum ether-ethyl acetate (1:1) and dried under reduced pressure to obtain pure **5** (80 mg, yield 81%) as a yellow solid melting 244–247 °C (dec.). ^{1}H NMR (400 MHz, $CDCl_3$-CD_3OD): 1.10 (t, $J = 7.1$, 3H), 1.89 (s, 3H), 4.12–4.22 (m, 2H), 7.35 (d, $J = 7.9$, 1H), 7.39–7.45 (m, 2H), 7.47–7.56 (m, 3H), 7.74 (dd, $J = 8.0$, 1.8, 1H), 7.79 (d, $J = 7.9$, 2H), 7.85 (d, $J = 7.0$, 2H), 7.98 (d, $J = 1.7$, 1H), 8.10 (t, $J = 8.0$, 1H), 9.54 (d, $J = 6.3$, 2H). MS (ESI) m/z: $[M+H]^+$ Calcd for $C_{35}H_{25}F_6N_8O_3Pt$ 914.7; Found 914.8.

2.1.6. Platinum(II) complex 6-PTPC-BF3k

A mixture of platinum complex **5** (50 mg, 0.0547 mmol) in 15 mL of $CDCl_3$-TFA (5:1) containing *p*-toluenesulfonic acid monohydrate (40 mg, 0.044 mmol) was heated to reflux for 1 h. The reaction mixture was then washed with water and dried over sodium sulfate to obtain a solution of benzofulvene monomer 6-PTPC-**BF3k**. ^{1}H NMR (400 MHz, $CDCl_3$): 1.09 (t, $J = 7.1$, 3H), 4.18 (q, $J = 7.2$, 2H), 6.51 (s, 1H), 6.72 (s, 1H), 7.38–7.54 (m, 6H), 7.69 (dd, $J = 8.0$, 1.7, 1H), 7.81 (d, $J = 7.9$, 2H), 7.86 (d, $J = 6.8$, 2H), 8.02 (t, $J = 7.9$, 1H), 8.08 (d, $J = 1.7$, 1H), 9.67 (d, $J = 6.9$, 2H); see also Fig. 7. MS (ESI) m/z: $[M+H]^+$ Calcd for $C_{35}H_{23}F_6N_8O_2Pt$ 896.7; Found 896.8.

2.1.7. Poly-6-PTPC-BF3k

2.1.7.1. Procedure SE.
The solution of monomer 6-PTPC-**BF3k** in $CDCl_3$ was allowed to concentrate at room temperature by spontaneous evaporation of the solvent to obtain *poly*-6-PTPC-**BF3k**-SE. ^{1}H NMR (400 MHz, $CDCl_3$): see Fig. 8.

2.1.7.2. Procedure FE.
The solution of monomer 6-PTPC-**BF3k** in $CDCl_3$ was concentrated under reduced pressure and the residue was purified by washing with ethyl acetate to afford *poly*-6-PTPC-**BF3k**-FE as a yellow solid (41 mg, yield 84% in monomeric unit).
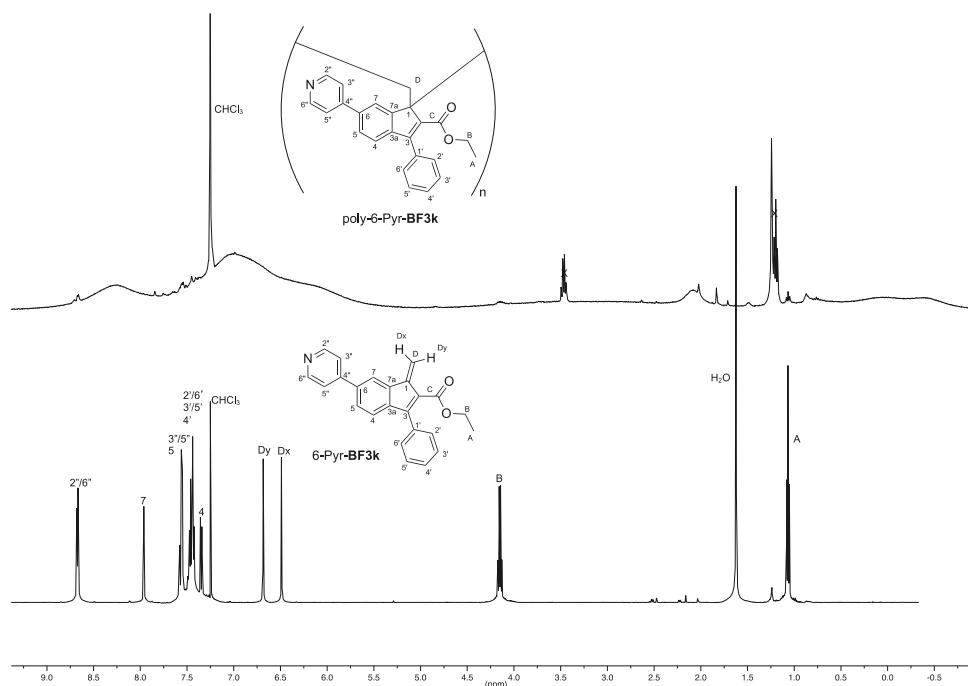
Fig. 3. Comparison of ^{1}H NMR spectrum (CDCl₃, 400 MHz) of *poly*-6-Pyr-**BF3k** with that of corresponding benzofulvene derivative 6-Pyr-**BF3k** (CDCl₃, 500 MHz).

2.2. X-Ray crystallography

Single crystals of compounds **2** and **3** were submitted to X-ray data collection on an Oxford-Diffraction Xcalibur Sapphire 3 diffractometer with a graphite monochromated Mo-Kα radiation (λ = 0.71073 Å) at 293 K. The structures were solved by direct methods implemented in SHELXS-97 program [50]. The refinements were carried out by full-matrix anisotropic least-squares on F² for all reflections for non-H atoms by means of the SHELXL-97 program [51]. Crystallographic data (excluding structure factors) for the structures in this paper have been deposited with the Cambridge Crystallographic Data Centre as supplementary publications no. CCDC 2117334 (**2**) and CCDC 2117335 (**3**). Copies of the data can be obtained, free of charge, on application to CCDC, 12 Union Road, Cambridge CB2 1EZ, UK; (fax: + 44 (0) 1223 336 033; or e-mail: deposit@ccdc.cam.ac.uk).

2.3. Matrix assisted laser desorption/ionization time of flight mass spectrometry (MALDI-TOF MS)

MALDI-TOF mass spectra were recorded in reflectron mode by means of a 4800 Proteomic Analyzer (Applied Biosystems) MALDI-TOF/TOF instrument equipped with a Nd:YAG laser at a wavelength of 355 nm with < 500 ps pulse and 200 Hz firing rate. The accelerating voltage was 15 kV. External calibration was performed using an Applied Biosystems calibration mixture consisting of polypeptides with different molar mass values. The irradiance was maintained slightly above the threshold, to obtain a mass resolution of about 5000–7000 fwhm. Mass accuracy was about 75 ppm. The best mass spectra were recorded using *trans*-2-[3-(4-*tert*-butylphenyl)-2-methyl-2-propenylidene]malononitrile (DCTB) or alpha-cyano-4-hydroxycinnamic acid (α-cyano) as a matrix. Working in

linear mode low mass resolved mass spectra (about 800–1000 fwhm) were also obtained from *m/z* 1000 up to *m/z* 15,000.

2.4. Size exclusion chromatography (SEC)

The SEC measurements of the polymer samples were carried out by a Waters 515 apparatus (Milan, Italy) equipped with four Ultrastyragel HR columns (ID = 7.8 mm, L = 300 mm, 5 μm of particle size) in the order HR-4, HR-3, HR-2 and HR-1 connected in series and a Waters R401 detector, using CHCl₃ as mobile phase (1 mL/min of flow rate). The SEC traces were processed using a Clarity-GPC software (Data Apex, Prague, Czech Republic) provided by DataApex and applying the calibration curve built using PS narrow standards. Average weight molar mass (Mw), average number molar mass (Mn) and the molar mass distribution (D = Mw/Mn) were calculated.

2.5. Wide angle X-ray diffraction studies

For the Wide-Angle X-ray Diffraction (WAXD) measurements a Philips X'Pert PRO PW 3040/60 diffractometer working in the Bragg-Brentano geometry, equipped with a X'CeleratorPW3015 detector was used. Diffractograms were collected with non monochromatized Cu Kα radiation, in the 3–60° 2θ range and with a step of 0.017°.

2.6. Modeling

Modeling studies were performed on the isolated 6-PTPC-**BF3k**, 1-TPC-6-PTPC-**BF3k**, and on the three-coordinated Pt complex. The calculations were performed adopting the ωb97xd [52] approximation to Density Functional Theory. We adopted the D95v(d) basis set for all light
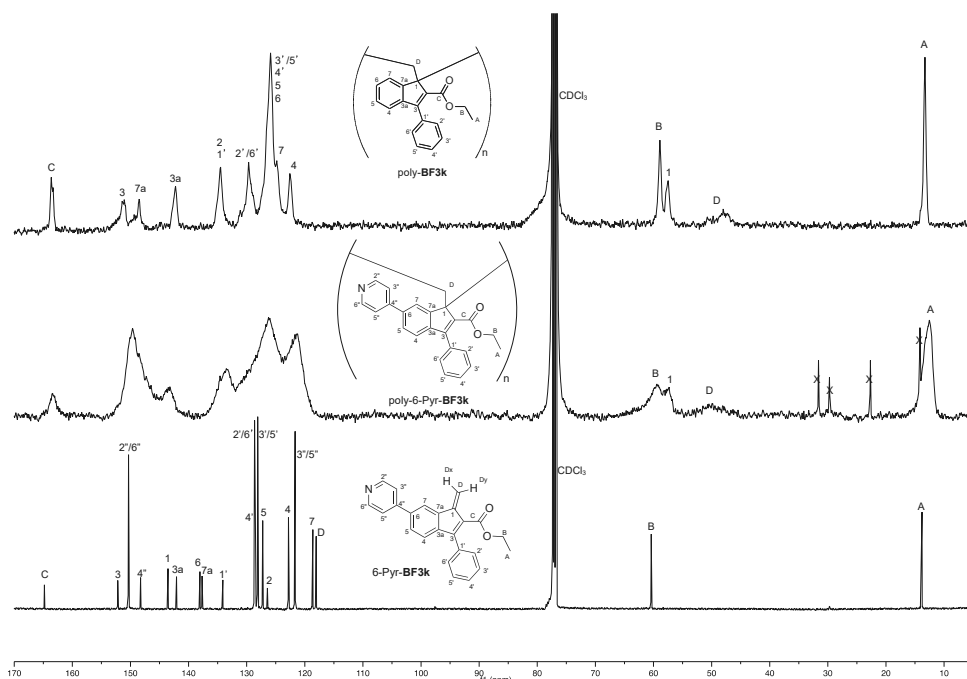
Fig. 4. Comparison of ^{13}C NMR spectrum (CDCl$_3$, 125 MHz) of *poly*-6-Pyr-**BF3k** with that of corresponding benzofulvene monomer 6-Pyr-**BF3k** and with that of closely related polybenzofulvene derivative *poly*-**BF3k**.
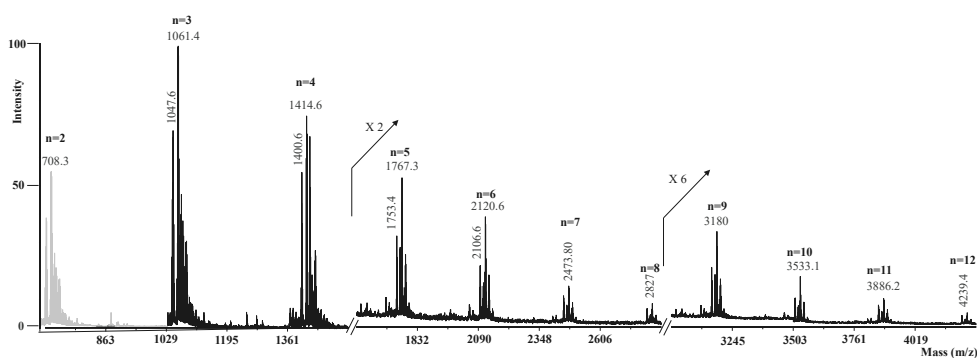
Fig. 5. MALDI-TOF mass spectrum of *poly*-6-Pyr-**BF3k** recorded in reflection mode using α-cyano as matrix.

atoms [53], while we adopted the Stuttgard-Cologne pseudopotential and corresponding basis set for Pt [54]. Such a combination of DFT approximation and basis set was already successfully used for the studies of diverse divalent metal complexes [55,56]. Geometry optimization were carried out without imposing symmetry constraints in vacuum. Harmonic analysis was performed on the optimized structures adopting the same level of theory as for the geometry optimizations. The g09 suite of programs was used for all the calculations [57].

2.7. Photophysical characterization

Photoluminescence (PL) and PL excitation spectra (PLE) are obtained with a NanoLog composed by a iH320 spectrograph equipped with a Synapse QExtra charge-coupled device by exciting with a mono-chromated 450 W Xe lamp. Phosphorescence (Ph) spectra are obtained with PPD-850 single photon detector module with Time-Gated Separation by exciting with a pulsed Xe lamp. The spectra are corrected for the instrument response. PL QY were measured with a home-made

5
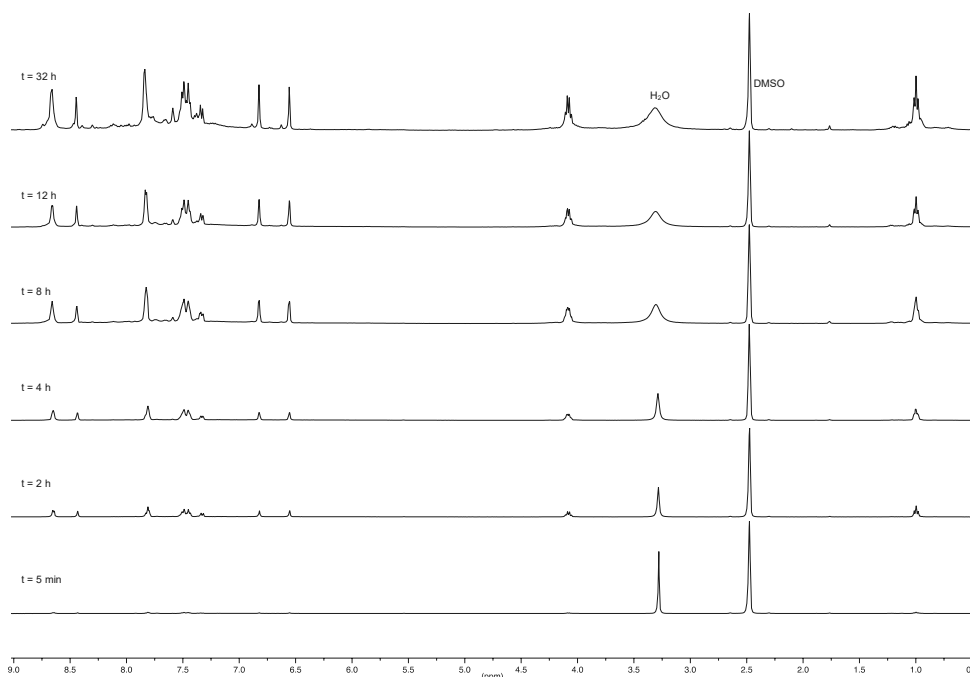
Fig. 6. Thermo-induced depolymerization of *poly*-6-Pyr-**BF3k** followed by ^{1}H NMR spectroscopy. A mixture of 5.0 mg of the polymer in 0.75 mL of DMSO-d_6 was heated at 150 °C and ^{1}H NMR spectra (400 MHz) were recorded at regular time intervals. The solvent (DMSO) peak was used as the concentration reference.

integrating sphere according to the procedure reported elsewhere [58]. Time-resolved TCSPC measurements are obtained with PPD-850 single photon detector module and DeltaTime serie DD-405L DeltaDiode Laser and analysed with the instrument Software DAS6.

3. Results and discussion

3.1. Synthesis and characterization

The preparation of benzofulvene derivative 6-Pyr-**BF3k** is summarized in Scheme 1.

Suzuki-Miyaura cross-coupling between triflate **1** [40] and the commercially available 4-pyridineboronic acid (Aldrich) provided the access to indenone derivative **2** through the insertion of the 4-pyridyl moiety in position 6 of the 3-phenyl-1-indenone nucleus. The structure of this synthetic intermediate was confirmed by crystallography (Fig. 2A).

Indenone derivative **2** was used as starting material in the already described methylation procedure [21,25,26] to obtain indenol derivative **3** (the structure obtained by crystallography is shown in Fig. 2B), which was dehydrated with *p*-toluensulfonic acid (PTSA) in chloroform to give benzofulvene monomer 6-Pyr-**BF3k**.

As expected, benzofulvene derivative 6-Pyr-**BF3k** showed the tendency towards the spontaneous polymerization typically shown by many structurally-related benzofulvene derivatives. Thus, the evaporation of the solvent (*i.e.* either CHCl₃ or CDCl₃) at reduced pressure into a rotary evaporation apparatus from a monomer solution gave *poly*-6-Pyr-**BF3k**, which was purified by precipitation with *n*-hexane from a solution in CHCl₃-ethanol. The polymeric nature of *poly*-6-Pyr-**BF3k** was

confirmed by its ^{1}H NMR spectrum (Fig. 3), which showed very broad signals in the aromatic region that were up-field shifted with respect to those appearing in the spectrum of monomer 6-Pyr-**BF3k**.

Furthermore, the aliphatic region of *poly*-6-Pyr-**BF3k** spectrum contains two broad signals (at around 0 and −0.4 ppm), which were assigned to the methyl of the ester group. The remarkable shielding effect could be explained in terms of magnetic anisotropy and proximity in the 3D space of the aromatic rings with the methyl group, and the presence of two signals suggested the existence of conformational or configurational (*i.e.* syndiotactic and isotactic) isomers in the polymer backbone.

The macromolecular structure of *poly*-6-Pyr-**BF3k** was also supported by ^{13}C NMR spectroscopic analysis. Interestingly, the ^{13}C NMR spectrum (Fig. 4) of the polybenzofulvene derivative showed a resolution sufficient to allow a signal-to-signal comparison to be made with the spectrum of corresponding monomer 6-Pyr-**BF3k**.

In fact, the sharp signals in the spectrum of the monomer found an almost perfect correspondence with the broad peaks present in the polymer spectrum with two important exceptions: the signal attributed to the exocyclic methylene carbon (C-D, at 118.0 ppm) and the one assigned to the other vinylidene carbon (C-1, at 143.5). These two signals were up-field shifted (at about 50 and 57 ppm, respectively) in *poly*-6-Pyr-**BF3k** spectrum owing to the change in hybridization produced by the polymerization in agreement with the results obtained with related polybenzofulvene derivatives (*i.e. poly*-**BF3k** as shown in Fig. 4) [23,30]. In particular, the perfect correspondence between the ^{13}C NMR spectra of the polybenzofulvene derivatives shown in Fig. 4 (especially in the peaks attributed to C-1 and C-D) supported the consistency of the vinyl (*i.e.* 1,2) polymerization mechanism in *poly*-6-Pyr-**BF3k** as already
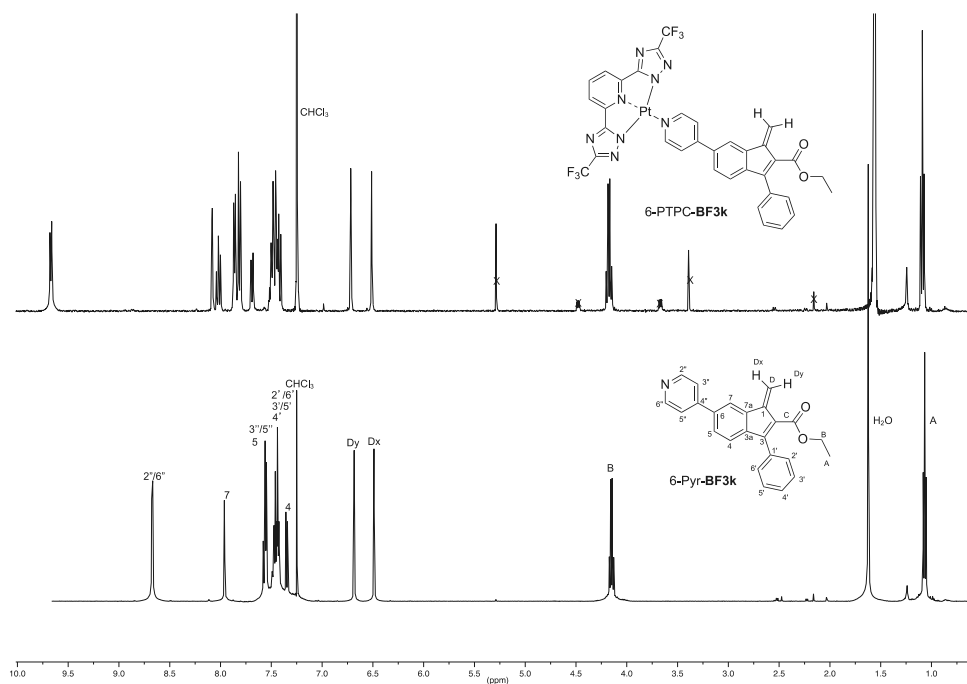
6

31

Fig. 7. Comparison of ^{1}H NMR spectrum (CDCl$_3$, 400 MHz) of neutral platinum(II) complex 6-PTPC-**BF3k** with that of corresponding benzofulvene derivative 6-Pyr-**BF3k** (CDCl$_3$, 500 MHz).

observed in *poly*-**BF3k** [30,31]. Thus, the vinyl structure of the newly synthesized polymer appeared to be marginally affected by the presence of the pyridine ring in position 6 of the 3-phenylindene nucleus. Probably, some subtle differences in the shape of the peaks attributed to C-D (see Fig. 4) could reflect differences in the conformational or configurational isomerism of the two closely related polybenzofulvene derivatives.

The polymeric nature of *poly*-6-Pyr-**BF3k** was further supported by the results of MALDI-TOF mass spectrometry characterization. The spectrum shown in Fig. 5, indeed showed a series of repeating peak families from *m/z* 680 up to about *m/z* 4300 showing 353.1 ± 0.1 Da intervals corresponding to the mass of the repeating unit of *poly*-6-Pyr-**BF3k** (*i.e.* 353.1 Da). The most intense peaks corresponded to the molecular ions of the expected oligomers terminated with hydrogens at both ends from the dimer up to the dodecamer. The presence of these terminal groups supported the formation of macrobiradical species during the polymerization process that underwent termination by hydrogen radical abstraction, as previously suggested for similar polybenzofulvene derivatives. [27].

Finally, SEC analysis (Fig. S1) confirmed the polymeric nature of *poly*-6-Pyr-**BF3k** and gave the molar mass distribution value Mw = 46,500 g/mol; Mn = 14,500 g/mol; D = 3.2.

Unexpectedly, *poly*-6-Pyr-**BF3k**, in spite of its good solubility in chloroform, showed a low solubility in DMSO at room temperature, but its solubility increased by increasing the temperature. As the thermo-reversibility of the polymerization process is one of the most intriguing features shown by polybenzofulvene derivative, thermo-induced depolymerization studies were performed in order to compare the behavior of the newly synthesized polymer with those of other members of the

family. For instance, the depolymerization of *poly*-**BF3k** was found to be almost complete after 6 h heating at 150 °C and the heating for prolonged times led to the appearance of peaks attributed to products deriving from monomer decomposition [24].

Thus, the dispersion of *poly*-6-Pyr-**BF3k** (5.0 mg) in deuterated DMSO (0.75 mL) was heated at 150 °C and ^{1}H NMR spectra were recorded at regular time intervals. The comparison of the stacked spectra (Fig. 6) clearly showed the appearance of sharp signals and their progressive increase in intensity as consequences of the exposure to high temperature, which appeared to produce an unzipping depolymerization process similar to the one shown by polycyanoacrylates [24].

These sharp signals could be attributed to benzofulvene monomer 6-Pyr-**BF3k**, but the appearance of a second set of small sharp signals after 32 h heating raised the question of possible isomerization/decomposition matters after heating for prolonged times.

Subsequently, indenol intermediated **3** was used as the starting material in the synthesis of neutral platinum(II) complex 6-PTPC-**BF3k** as shown in Scheme 2.

In particular, indenol intermediated **3** was transformed into the corresponding neutral platinum(II) complex **5** by employing a similar procedure previously described by Mauro, De Cola *et al.* [59] This method employed 2,6-*bis*(3-(trifluoromethyl)-1*H*-1,2,4-triazol-5-yl)pyridine (**4**) as the tridentate ligand, PtCl$_2$(DMSO)$_2$ as the platinum(II) source, and diisopropylethylamine (DIPEA) as the base in 2-methoxyethanol-water as the solvent system. Complexed carbinol intermediate **5** was dehydrated with PTSA in a mixture of trifluoroacetic acid and CDCl$_3$ to obtain complexed benzofulvene monomer 6-PTPC-**BF3k**. The structure of this neutral platinum(II) complex was characterized by ^{1}H NMR spectroscopy (Fig. 7).
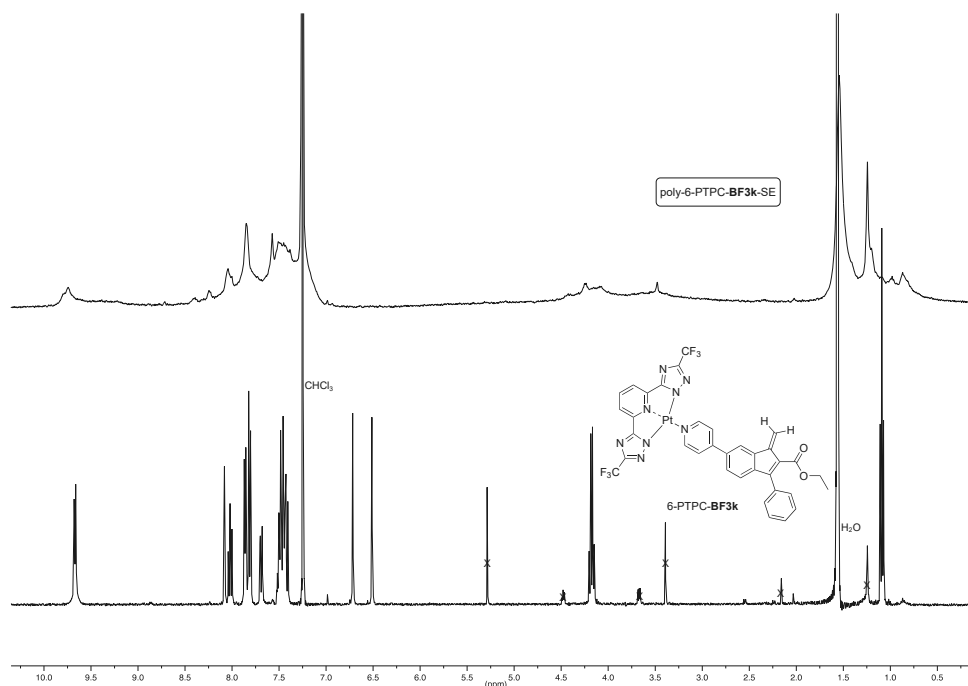
7

Fig. 8. Comparison of ¹H NMR spectrum (CDCl₃, 400 MHz) of *poly*-6-PTPC-**BF3k**-SE with that of corresponding benzofulvene derivative 6-PTPC-**BF3k** (CDCl₃, 400 MHz).

The comparison of the NMR spectrum of complex 6-PTPC-**BF3k** with that of benzofulvene derivative 6-Pyr-**BF3k** (Fig. 7) confirmed the effects of complexation on the signals assigned to the pyridine moiety that were down-field shifted in the spectra of the complex with respect to the same signals in the spectra of the un-complexed benzofulvene derivative 6-Pyr-**BF3k**, as already observed in similar platinum complexes [48,49].

The solution used in ¹H NMR studies was allowed to concentrate by slow evaporation (SE) of the solvent at room temperature and led to the formation of a polymeric material (*poly*-6-PTPC-**BF3k**-SE). The ¹H NMR spectrum of this material (Fig. 8) revealed the presence of soluble oligomers.

This result supported the propensity of bulky benzofulvene monomer 6-PTPC-**BF3k** to the spontaneous polymerization, but the presence in the polymerization mixture of quenching agents such as atmospheric water and oxygen appeared to prevent the formation of high molecular weight polymers. The MALDI-TOF mass spectrometry characterization of *poly*-6-PTPC-**BF3k**-SE confirmed the polymeric nature of the material. In fact, the MALDI-TOF spectrum shown in Fig. 9 showed a series of peaks from *m/z* 800 up to ca. *m/z* 4500 showing 895.7 ± 0.1 Da transitions, corresponding to the mass of the repeating unit of *poly*-6-PTPC-**BF3k** (*i.e.* 895.7 Da). The most intense peaks correspond to the molecular ions of the expected totally complexed oligomers terminated with hydrogens at both ends (*i.e.* peaks at *m/z* 1793.4, 2689.1, 3584.8 and 4480.5). However, besides to these expected peaks, the mass spectrum shows also those belonging to the partially complexed oligomers (*i.e.* mass peaks at *m/z* 1604.3, 2146.7, 2500, 3042.4, 3395.7, 3584.8, 3938.1, 4291.4). The mass spectrum presents also mass peaks at *m/z* 1061.4 and 1415.2 due to the totally uncomplex oligomers corresponding to the *poly*-6-Pyr-**BF3k** trimers and tetramers, respectively, which were formed by

polymerization of the un-complexed 6-Pyr-**BF3k** monomer. The mass spectrum of *poly*-6-PTPC-**BF3k**-SE sample is dominate by the peak at *m/z* 895.7, which correspond to the molecular ions of the 6-PTPC-**BF3k** monomer. From the comparison with NMR data (Fig. 8), the identification of the 6-PTPC-**BF3k** monomer suggests that a depolymerization process may occur during the sample preparation for MALDI analysis of *poly*-6-PTPC-**BF3k**-SE sample, suggesting low stability of this polybenzofulvene derivative.

Thus, the polymerization procedure was then performed under reduced pressure (fast evaporation, FE) on a larger scale (*i.e.* 50 mg of the monomer) and in three independent experiments to assess the reproducibility of the polymerization process. The results of these experiments confirmed that this benzofulvene monomer bearing a very bulky substituent in position 6 of the 3-phenylindene nucleus was capable of polymerizing spontaneously by solvent removal under reduced pressure. However, the corresponding polymer (*i.e. poly*-6-PTPC-**BF3k**-FE) was demonstrated to be of difficult characterization owing to its low solubility both in chloroform and in DMSO. An explanation for this dramatic change in the solubility from the soluble monomer to the insoluble polymers and from un-complexed *poly*-6-Pyr-**BF3k** (soluble in chloroform) to *poly*-6-PTPC-**BF3k**-FE was tentatively conceived in the possible metallophilic interactions, which could be assumed to favour the formation of a stereoregular *poly*-6-PTPC-**BF3k**-FE. To evaluate this assumption, the corresponding powder samples were characterized by wide angle X-ray diffraction (WAXD) studies (Fig. 10).

The WAXD diffractogram of *poly*-6-Pyr-**BF3k**, being characterized by two broad peaks (centered at around 6 and 22°) was very similar to those of other polybenzofulvene derivatives [26]. Also the

Chapter 2. Investigation of aggregation/polymerization behavior of innovative benzofulvene-based derivatives
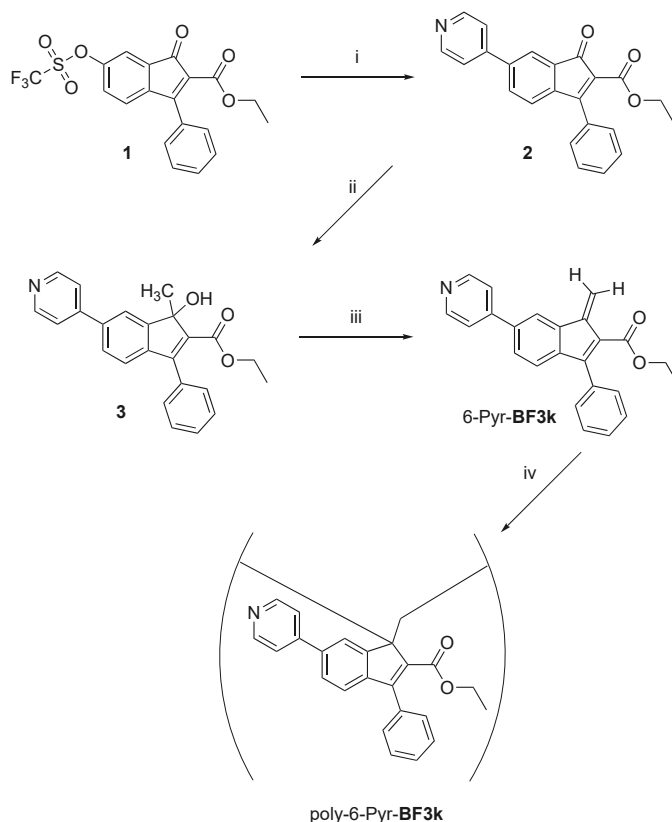
Scheme 1. Preparation and spontaneous polymerization of benzofulvene derivative 6-Pyr-**BF3k**. **Reagents**: (i) 4-pyridineboronic acid, Pd(PPh₃)₂Cl₂, PPh₃, K₃PO₄, 2,6-di-*tert*-butyl-4-methylphenol, 1,4-dioxan, EtOH; (ii) Al(CH₃)₃, CH₂Cl₂; (iii) PTSA, CDCl₃; (iv) solvent evaporation at reduced pressure.

diffractograms obtained with two samples of *poly*-6-PTPC-**BF3k**-FE are characterized by two broad peaks, but the complexation of the pyridine nitrogen produced a peak shift towards higher 2θ values supporting the formation of structures with a smaller periodicity than in the polymer *poly*-6-Pyr-**BF3k**. A particular case was represented by the third sample of *poly*-6-PTPC-**BF3k**-FE that showed a WAXD diffractogram (green line in Fig. 10) composed by a complex array of both broad and sharp peaks, besides those due to sodium sulfate. The presence of a further set of sharp peaks suggested the existence of an ordered organization in the solid state of the third sample.

The MALDI-TOF mass spectrometry characterization of *poly*-6-PTPC-**BF3k**-FE (batch 1) confirmed the presence of complexed oligomers in the material. In fact, the MALDI-TOF spectrum shown in Fig. 11 showed the mass peaks at *m/z* 1793.4, 2689, 3585 and 4480.8 corresponding to the totally complexed oligomers (dimers, trimers, tetramers, and pentamers) terminated with hydrogens at both ends. As already observed in the mass spectrum of the *poly*-6-PTPC-**BF3k**-SE (Fig. 9), the mass spectrum of *poly*-6-PTPC-**BF3k**-FE (batch 1) shows the presence of mass peaks belonging to either partially (*m/z* 1251, 1604.3, 2146.8, 2500, 3042.4, 3396, 3938.1, 4291.7 and 4839) at and totally (*m/z* 1061.4 and 1416.4) un-complexed oligomers. The presence of the intense peak at *m/z* 895.4 due to the 6-PTPC-**BF3k** monomer confirms that during the

MALDI-TOF MS sample preparation a reversible depolymerization process may occur.

In agreement with the WAXD spectra obtained with powder samples of *poly*-6-PTPC-**BF3k**-FE, MALDI-TOF mass spectrometry characterization of *poly*-6-PTPC-**BF3k**-FE (batch 2) produced results very similar to those obtained with *poly*-6-PTPC-**BF3k**-FE (batch 1), whereas the mass spectrum obtained with *poly*-6-PTPC-**BF3k**-FE (batch 3) was characterized by the almost exclusive presence of monomer 6-PTPC-**BF3k**. These results were confirmed by the SEC analyses; the chromatogram obtained with *poly*-6-PTPC-**BF3k**-FE (batch 2) is reported in Fig. S2 and the one obtained with *poly*-6-PTPC-**BF3k**-FE (batch 3) is reported in Fig. S3. Both chromatograms showed the presence of relatively high molar mass polymer chains that eluted between 23 and 30 mL, and oligomer chains that eluted from 30 to 40 mL. However, while the chromatogram obtained with batch 2 was characterized by the presence of a significant polymer component, in the one obtained with batch 3, the polymer component was less significant from the quantitative point of view. From these curves the following molar mass distributions of high molar mass components of both polymers were calculated. *Poly*-6-PTPC-**BF3k**-FE (batch 2): Mw = 38,200 g/mol; Mn = 11,200 g/mol; D = 3.4. *Poly*-6-PTPC-**BF3k**-FE (batch 3): Mw = 32,800 g/mol; Mn = 8600 g/mol; D = 3.8.

9
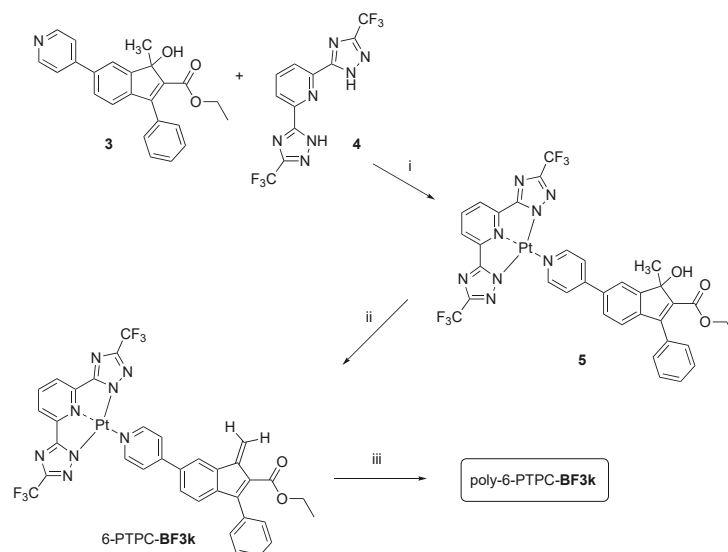
Scheme 2. Preparation and spontaneous polymerization of neutral platinum(II) complex 6-PTPC-**BF3k**. **Reagents**: (i) PtCl$_2$(DMSO)$_2$, DIPEA, CH$_3$OCH$_2$CH$_2$OH, H$_2$O; (ii) PTSA, CF$_3$COOH, CDCl$_3$; (iii) solvent evaporation.
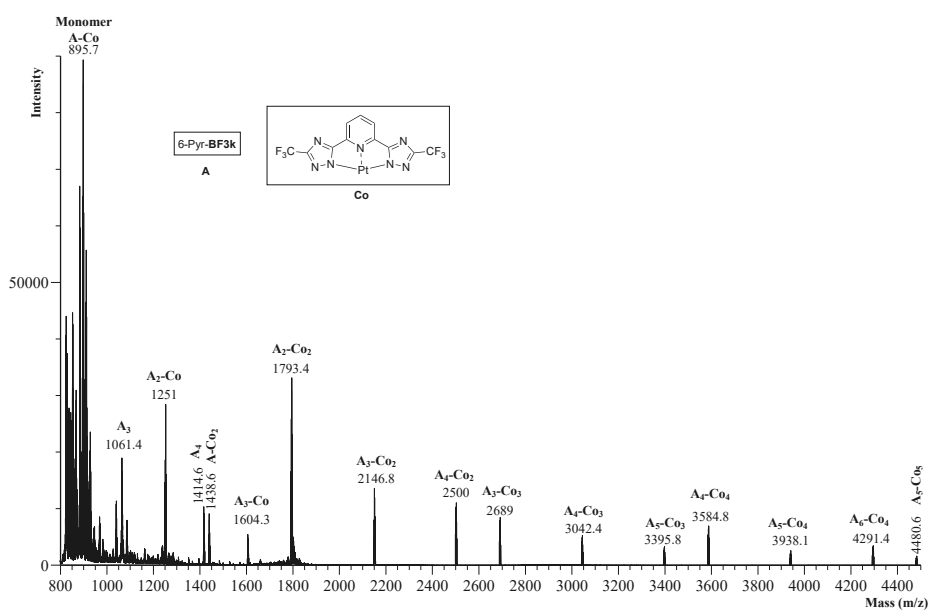
Fig. 9. MALDI-TOF mass spectrum of *poly*-6-PTPC-**BF3k**-SE recorded in reflection mode using malononitrile as matrix.

10
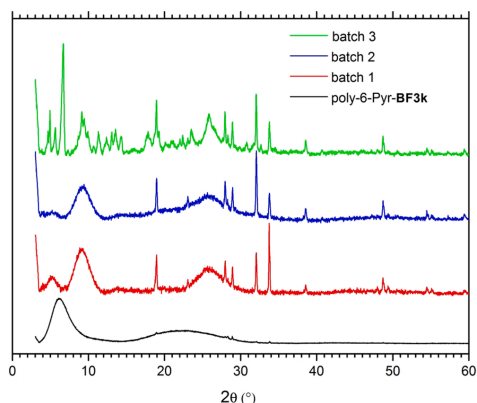
Fig. 10. WAXD spectra obtained with powder samples of *poly*-6-PTPC-**BF3k**-FE (three different preparations: batch 1, red line; batch 2, blue line; batch 3, green line) and *poly*-6-Pyr-**BF3k** (black line). The sharp peaks (well visible in the spectra of batch 1 and batch 2) are related to the traces of sodium sulfate used in the drying of the monomer solutions after the dehydration reaction. (For interpretation of the references to color in this figure legend, the reader is referred to the web version of this article.)

Curiously, the MALDI-TOF mass spectrum of the *poly*-6-PTPC-**BF3k**-FE sample shows an intense peak at *m/z* 1438.3 (see inset in Fig. 11). We assigned this peak to supramolecular species containing one 6-Pyr-**BF3k** unit and two platinum(II) complex systems (*i.e.* 1-TPC-6-PTPC-**BF3k**, Fig. 12A). The formation of this adduct could be due to the transfer of the platinum(II) complex system from the pyridine lone pair to the benzofulvene π-electron system during the spontaneous thermoreversible polymerization process leading to the production of the *poly*-6-PTPC-**BF3k** polybenzofulvene derivative.

In order to gain microscopic details on the structure of the complex 1-TPC-6-PTPC-**BF3k** (see above), we performed a series of calculations using a Density Functional Theory approach. The optimized 1-TPC-6-PTPC-**BF3k** structure is reported in Fig. 12B.

The modeling was performed by positioning a Pt(II) three-coordinated with a doubly deprotonated moiety (compound **4** in Scheme 2) on top of the 6-PTPC-**BF3k** structure. The Pt atom of the three coordinated complex was initially positioned at about 4 Å from both the C=CH$_2$ and the C=O double bonds of 6-PTPC-**BF3k**. However, the final optimized structure (Fig. 12B) clearly indicates that the three-coordinated Pt moiety is linked to the C=CH$_2$ double bond, thus preferring the π-interaction with the ethylene double bond with respect to coordination to the C=O group. It should be stressed that, by performing a vibrational analysis, the optimized 1-TPC-6-PTPC-**BF3k** structure is a stable complex because all calculated harmonic frequencies resulted positive. In passing, we notice that also the frequencies of the optimized 6-PTPC-**BF3k** and of the optimized three-coordinated Pt moieties were positive, thus indicating that both structures are true minima as well. A deeper analysis of the 1-TPC-6-PTPC-**BF3k** optimized structure reveals that, in this complex, the coordination of Pt with the C=CH$_2$ double bond is nearly symmetric, as the bonding distance
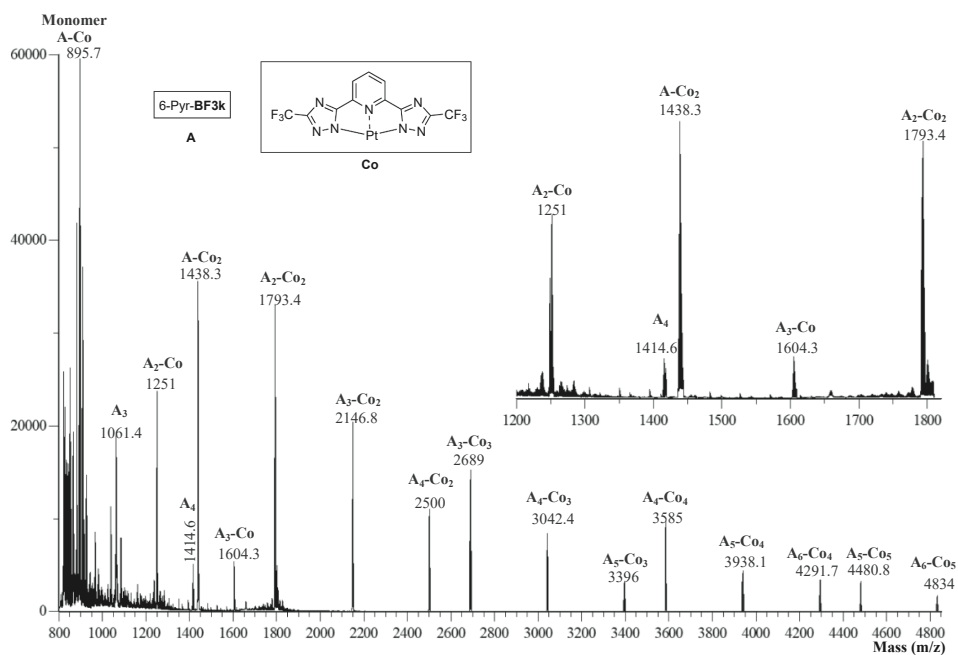
Fig. 11. MALDI-TOF mass spectrum of *poly*-6-PTPC-**BF3k**-FE (batch 1) recorded in reflectron mode using malononitrile as matrix.

11

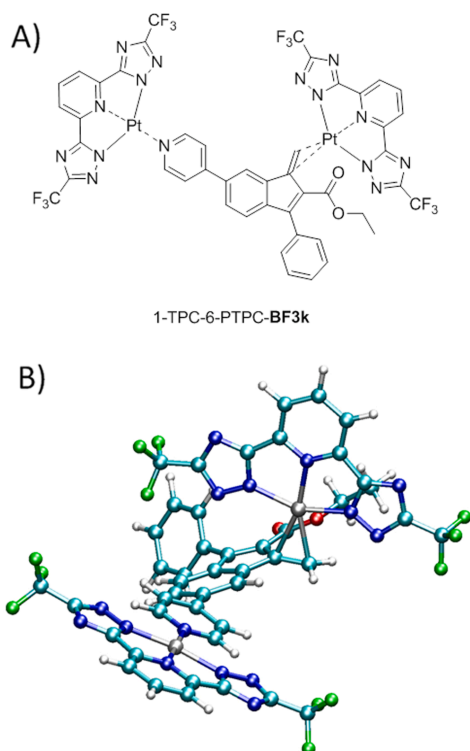**Fig. 12.** Hypothesized structure for complex 1-TPC-6-PTPC-**BF3k** (A) and Graphical representation of the optimized structure of 1-TPC-6-PTPC-**BF3k** (B), color code; H, white; C, cyan; N, blue; O, red; F, green; Pt, gray. (For interpretation of the references to color in this figure legend, the reader is referred to the web version of this article.)

between the Pt atom and the CH₂ carbon is 2.304 Å, while it is 2.306 Å with the other C of the C=CH₂ group. Interestingly, the binding energy for the formation of 1-TPC-6-PTPC-**BF3k** from 6-PTPC-**BF3k** and the three coordinated Pt complex amounts to 56.9 kcal/mol (including zero-point energies), thus suggesting a high stability of such a di-platinum complex.

3.2. Photophysical features

The photophysical properties of powder samples of *poly*-6-PTPC-**BF3k**-FE and platinum(II) complex **5**, are reported in Table 1 and Figs. 13 and 14 together with those of polybenzofulvene derivative *poly*-6-Pyr-**BF3k**.

Table 1
Photophysical features powder samples of *poly*-6-PTPC-**BF3k**-FE, platinum(II) complex **5**, and *poly*-6-Pyr-**BF3k**. (* time gated spectra; $\tau_{av} = \sum \frac{A_i \tau_i^2}{A_i \tau_i}$).

compound	PLE (nm)	PL (nm)	QY (%)	Lifetime τ_{av}
poly-6-Pyr-**BF3k**	370	485	13	8.5 ns
complex **5**	508	591, 590*	1	48 μs
poly-6-PTPC-**BF3k**-FE	366	435		560 ps
	490	590, 620*	<0.1	85 μs

Polybenzofulvene derivative *poly*-6-Pyr-**BF3k** displays an intense fluorescent blue emission centered at 485 nm, characterized by an averaged lifetime of 8.5 ns (Fig. 13A and Fig. S4). On the other hand, platinum complex **5** shows a yellow emission peaked at 590 nm (Fig. 13B) arising from an excited state with triplet metal-metal-to-ligand charge transfer (³MMLCT) in agreement with related complexes [ref. 59]. The phosphorescence nature is confirmed by time-resolved analysis (*i.e.* average lifetime of 48 μs, Fig. S5, Fig. S6), in agreement with related compounds [49]. *Poly*-6-PTPC-**BF3k**-FE displays similar properties even though with reduced emission efficiency and longer lifetimes with respect to complex **5** (see Fig. 14, Fig. S5 and Fig. S6). A detailed analysis reveals that *poly*-6-PTPC-**BF3k** emission is wavelength dependent, displaying, upon excitation at short wavelengths, a weak short-lived (average lifetime of 560 ps, Fig. 14, bottom, and Fig. S7) blue fluorescence, whose excitation profile well corresponds to that of *poly*-6-Pyr-**BF3k**. These results suggest that the analyzed powders contain small amounts of un-complexed sequences, in agreement with the MALDI-TOF MS data (see above). Owing to the high structural homogeneity of starting monomer 6-PTPC-**BF3k** (as suggested by the ¹H NMR spectrum show in Figs. 7 and 8) the result suggested that decomplexation occurred during the spontaneous polymerization process involving monomer 6-PTPC-**BF3k**.

4. Conclusion

In conclusion, two benzofulvene derivatives bearing complexed (*i.e.* 6-PTPC-**BF3k**) and un-complexed (*i.e.* 6-Pyr-**BF3k**) pyridine rings in position 6 of the 3-phenylbenzofulvene scaffold were designed and synthesized to evaluate the effects on the spontaneous solid-state polymerization of the presence of bulky substituents capable of establishing metallophilic interactions. First, the benzofulvene monomer 6-Pyr-**BF3k** bearing a free pyridine ring was easily prepared and found to polymerize spontaneously by removing the solvent at reduced pressure in the apparent absence of catalysts or initiators. The resulting polybenzofulvene derivative was characterized by NMR spectroscopy, MALDI-TOF mass spectrometry, and in photophysical studies. The results of MALDI-TOF mass spectrometry characterization supported the polymeric nature of *poly*-6-Pyr-**BF3k**, and NMR studies suggested the consistency of the vinyl (*i.e.* 1,2) thermoreversible polymerization mechanism as already observed in several structurally related polybenzofulvene derivatives. Photophysical characterization studies showed that polybenzofulvene derivative *poly*-6-Pyr-**BF3k** displayed a significant fluorescent blue emission centered at 485 nm and characterized by a quantum yield value of 13% and an averaged lifetime of 8.5 ns. On the other hand, benzofulvene monomer 6-PTPC-**BF3k** showed a more complex polymerization behaviour. In fact, experimental evidence suggested that the spontaneous polymerization of this platinum complex appeared to be in competition with its crystallization probably because of the presence of bulky and rigid platinum complex. In fact, in the formed polymeric material some monomeric unities relieve their bulkiness by transferring the platinum complex moiety to benzofulvene monomer 6-PTPC-**BF3k** molecules, which are near in the space where the polymerization occurred. Thus, *poly*-6-PTPC-**BF3k** appeared to show the features of a copolymer rather than those expected for the corresponding homopolymer, as suggested by MALDI-TOF mass spectrometry and photophysical characterization results.

Data availability

The raw/processed data required to reproduce these findings are available from the corresponding author by request.

CRediT authorship contribution statement

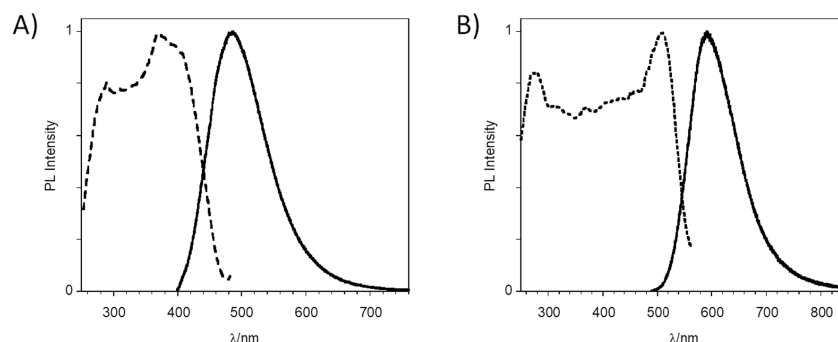**Marco Paolino:** Conceptualization, Methodology, Investigation,

Fig. 13. PL (solid line) and PLE (dashed line) spectra of (A) *poly*-6-Pyr-**BF3k** (λ_{ex} = 390 nm, λ_{em} = 490 nm) and of (B) platinum(II) complex **5** (λ_{ex} = 460 nm, λ_{e_m} = 590 nm).
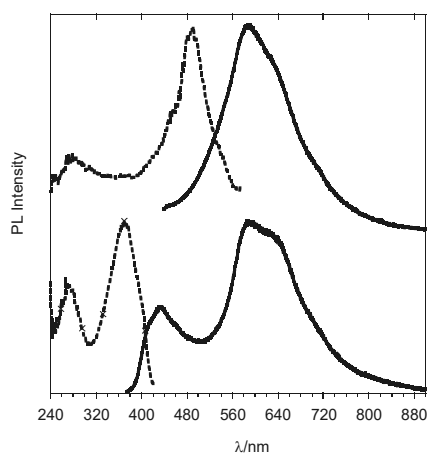

Fig. 14. PL (solid line) and PLE (dashed line) spectra of *poly*-6-PTPC-**BF3k**-FE. Top: λ_{ex} = 410 nm, λ_{e_m} = 590 nm. Bottom: λ_{ex} = 340 nm, λ_{e_m} = 440 nm.

Writing – original draft. **Mario Saletti:** Methodology, Formal analysis, Investigation, Writing – original draft. **Annalisa Reale:** Validation, Investigation. **Vincenzo Razzano:** Validation, Investigation. **Germano Giuliani:** Validation, Formal analysis, Investigation. **Alessandro Donati:** Investigation. **Claudia Bonechi:** Investigation, Data curation. **Gianluca Giorgi:** Investigation, Data curation. **Andrea Atrei:** Formal analysis, Investigation. **Matteo Mauro:** Validation, Investigation. **Andrea Scamporrino:** Formal analysis, Investigation. **Filippo Samperi:** Methodology, Investigation, Data curation, Writing – original draft. **Ettore Fois:** Methodology, Investigation, Data curation, Writing – original draft. **Gloria Tabacchi:** Formal analysis, Investigation. **Chiara Botta:** Methodology, Investigation, Data curation, Writing – original draft. **Andrea Cappelli:** .

Declaration of Competing Interest

The authors declare that they have no known competing financial interests or personal relationships that could have appeared to influence the work reported in this paper.

Appendix A. Supplementary material

Additional photophysical characterization. The following file is available free of charge. Supplementary data to this article can be found online at https://doi.org/10.1016/j.eurpolymj.2022.111137.

References

[1] M. Hasegawa, Photopolymerization of diolefin crystals, Chem. Rev. 83 (1983) 507–518, https://doi.org/10.1021/cr00057a001.
[2] K. Biradha, R. Santra, Crystal engineering of topochemical solid state reactions, Chem. Soc. Rev. 42 (2013) 950–967, https://doi.org/10.1039/C2CS35343A.
[3] M. Hasegawa, Photodimerization and Photopolymerization of Diolefin Crystals, in: D.B.T.-A. in P.O.C. Bethell (Ed.), Academic Press, 1995, pp. 117–171. doi: https://doi.org/10.1016/S0065-3160(08)60034-9.
[4] L. Dou, Y. Zheng, X. Shen, G. Wu, K. Fields, W.-C. Hsu, H. Zhou, Y. Yang, F. Wudl, Single-Crystal Linear Polymers Through Visible Light–Triggered Topochemical Quantitative Polymerization, Science (80-.) 343 (6168) (2014) 272–277, https://doi.org/10.1126/science.1245875.
[5] R. Mohanrao, K. Hema, K.M. Sureshan, Topochemical synthesis of different polymorphs of polymers as a paradigm for tuning properties of polymers, Nat. Commun. 11 (2020) 865, https://doi.org/10.1038/s41467-020-14733-y.
[6] A. Matsumoto, T. Tanaka, T. Tsubouchi, K. Tashiro, S. Saragai, S. Nakamoto, Crystal Engineering for Topochemical Polymerization of Muconic Esters Using Halogen−Halogen and CH/π Interactions as Weak Intermolecular Interactions, J. Am. Chem. Soc. 124 (2002) 8891–8902, https://doi.org/10.1021/ja0205333.
[7] J.-M. Heo, Y. Kim, S. Han, J.F. Joung, S. Lee, S. Han, J. Noh, J. Kim, S. Park, H. Lee, Y.M. Choi, Y.-S. Jung, J.-M. Kim, Chromogenic Tubular Polydiacetylenes from Topochemical Polymerization of Self-Assembled Macrocyclic Diacetylenes, Macromolecules 50 (2017) 900–913, https://doi.org/10.1021/acs.macromol.6b02493.
[8] J. Fan, X. Xu, W. Yu, Z. Wei, D. Zhang, Hydrogen-bond-driven supramolecular self-assembly of diacetylene derivatives for topochemical polymerization in solution, Polym. Chem. 11 (2020) 1947–1953, https://doi.org/10.1039/C9PY01745C.
[9] E. Jahnke, I. Lieberwirth, N. Severin, J.P. Rabe, H. Frauenrath, Topochemical Polymerization in Supramolecular Polymers of Oligopeptide-Functionalized Diacetylenes, Angew. Chemie Int. Ed. 45 (2006) 5383–5386, https://doi.org/10.1002/anie.200600610.
[10] K. Hema, A. Ravi, C. Raju, J.R. Pathan, R. Rai, K.M. Sureshan, Topochemical polymerizations for the solid-state synthesis of organic polymers, Chem. Soc. Rev. 50 (2021) 4062–4099, https://doi.org/10.1039/D0CS00840K.
[11] R. Khazeber, K.M. Sureshan, Topochemical Ene-Azide Cycloaddition Reaction, Angew. Chemie Int. Ed. 60 (2021) 24875–24881, https://doi.org/10.1002/anie.202109344.
[12] K. Bae, J.-M. Heo, M.I. Khazi, J.F. Joung, S. Park, Y. Kim, J.-M. Kim, Macrocyclic Diacetylene-Terthiophene Cocrystal: Molecular Self-Assembly, Topochemical Polymerization, and Energy Transfer, Cryst. Growth Des. 20 (2020) 434–441, https://doi.org/10.1021/acs.cgd.9b01351.

13

[13] L. Zhu, H. Tran, F.L. Beyer, S.D. Walck, X. Li, H. Ågren, K.L. Killops, L.M. Campos, Engineering Topochemical Polymerizations Using Block Copolymer Templates, J. Am. Chem. Soc. 136 (2014) 13381–13387, https://doi.org/10.1021/ja507318u.

[14] E. Jahnke, J. Weiss, S. Neuhaus, T.N. Hoheisel, H. Frauenrath, Synthesis of Diacetylene-Containing Peptide Building Blocks and Amphiphiles, Their Self-Assembly and Topochemical Polymerization in Organic Solvents, Chem. – Eur. J. 15 (2009) 388–404, https://doi.org/10.1002/chem.200801668.

[15] T. Hoang, J.W. Lauher, F.W. Fowler, The Topochemical 1,6-Polymerization of a Triene, J. Am. Chem. Soc. 124 (2002) 10656–10657, https://doi.org/10.1021/ja027444a.

[16] A. Matsumoto, K. Sada, K. Tashiro, M. Miyata, T. Tsubouchi, T. Tanaka, T. Odani, S. Nagahama, T. Tanaka, K. Inoue, S. Saragai, S. Nakamoto, Reaction Principles and Crystal Structure Design for the Topochemical Polymerization of 1,3-Dienes, Angew. Chemie Int. Ed. 41 (2002) 2502–2505, https://doi.org/10.1002/1521-3773(20020715)41:14<2502::AID-ANIE2502>3.0.CO;2-9.

[17] G. Gallo, A. Mihanović, I. Rončević, R. Dinnebier, H. Vančik, Crystal structure and ON-OFF polymerization mechanism of poly(1,4-phenyleneazine-N, N-dioxide), a possible wide bandgap semiconductor, Polymer (Guildf). 214 (2021), 123235, https://doi.org/10.1016/j.polymer.2020.123235.

[18] S. Nomura, T. Itoh, H. Nakasho, T. Uno, M. Kubo, K. Sada, K. Inoue, M. Miyata, Crystal Structures and Topochemical Polymerizations of 7,7,8,8-Tetrakis (alkoxycarbonyl)quinodimethanes, J. Am. Chem. Soc. 126 (2004) 2035–2041, https://doi.org/10.1021/ja0386086.

[19] C.L. Anderson, H. Li, C.G. Jones, S.J. Teat, N.S. Settineri, E.A. Dailing, J. Liang, H. Mao, C. Yang, L.M. Klivansky, X. Li, J.A. Reimer, H.M. Nelson, Y. Liu, Solution-processable and functionalizable ultra-high molecular weight polymers via topochemical synthesis, Nat. Commun. 12 (2021) 6818, https://doi.org/10.1038/s41467-021-27090-1.

[20] J.R. Pathan, K.M. Sureshan, Solvent-Free and Catalyst-Free Synthesis of Cross-Linkable Polyfumaramides via Topochemical Azide-Alkyne Cycloaddition Polymerization, ACS Sustain. Chem. Eng. 9 (2021) 9871–9878, https://doi.org/10.1021/acssuschemeng.1c02796.

[21] A. Cappelli, G.P. Mohr, M. Anzini, S. Vomero, A. Donati, M. Casolaro, R. Mendichi, G. Giorgi, F. Makovec, Synthesis and Characterization of a New Benzofulvene Polymer Showing a Thermoreversible Polymerization Behavior, J. Org. Chem. 68 (2003) 9473–9476, https://doi.org/10.1021/jo035104h.

[22] A. Cappelli, M. Anzini, S. Vomero, A. Donati, L. Zetta, R. Mendichi, M. Casolaro, P. Lupetti, P. Salvatici, G. Giorgi, New π-stacked benzofulvene polymer showing thermoreversible polymerization: Studies in macromolecular and aggregate structures and polymerization mechanism, J. Polym. Sci. Part A Polym. Chem. 43 (2005) 3289–3304, https://doi.org/10.1002/pola.20783.

[23] A. Cappelli, S. Galeazzi, G. Giuliani, M. Anzini, A. Donati, L. Zetta, R. Mendichi, M. Aggravi, G. Giorgi, E. Paccagnini, S. Vomero, Structural manipulation of benzofulvene derivatives showing spontaneous thermoreversible polymerization. Role of the substituents in the modulation of polymer properties, Macromolecules 40 (2007) 3005–3014, https://doi.org/10.1021/ma0629236.

[24] A. Cappelli, M. Paolino, G. Grisci, G. Giuliani, A. Donati, A.C. Boccia, F. Samperi, R. Mendichi, S. Vomero, Reversible polymerization techniques leading to π-stacked polymers., in: T. Nakano (Ed.), π-Stacked Polym. Mol., Ed., Sprin, Springer Japan, Japan: Osaka, 2014, pp. 51–149. doi: 10.1007/978-4-431-54129-5_2.

[25] A. Cappelli, M. Paolino, G. Grisci, G. Giuliani, A. Donati, R. Mendichi, A.C. Boccia, C. Botta, W. Mróz, F. Samperi, A. Scamporrino, G. Giorgi, S. Vomero, Synthesis and characterization of charge-transporting π-stacked polybenzofulvene derivatives, J. Mater. Chem. 22 (2012) 9611, https://doi.org/10.1039/c2jm16790e.

[26] M. Paolino, G. Grisci, A. Reale, V. Razzano, G. Giuliani, A. Donati, R. Mendichi, D. Piovani, A. Boccia, A. Grillo, G. Giorgi, A. Cappelli, Structural Manipulation of the Conjugated Phenyl Moiety in 3-Phenylbenzofulvene Monomers: Effects on Spontaneous Polymerization, Polymers (Basel) 10 (2018) 752, https://doi.org/10.3390/polym10070752.

[27] A. Cappelli, G. Grisci, M. Paolino, F. Castriconi, G. Giuliani, A. Donati, S. Lamponi, R. Mendichi, A.C. Boccia, F. Samperi, S. Battiato, E. Paccagnini, M. Gentile, M. Licciardi, G. Giammona, S. Vomero, Combining spontaneous polymerization and click reactions for the synthesis of polymer brushes: A "grafting onto" approach, Chem. - A Eur. J. 19 (2013) 9710–9721, https://doi.org/10.1002/chem.201202534.

[28] M. Paolino, G. Grisci, G. Giuliani, I. Zanardi, M. Andreassi, V. Travagli, M. Licciardi, C. Scialabba, G. Giammona, A. Cappelli, S. Vomero, π-Stacked polymers in drug delivery applications, J. Drug Deliv. Sci. Technol. 32 (2016) 142–166, https://doi.org/10.1016/j.jddst.2015.04.001.

[29] M. Paolino, A. Reale, V. Razzano, G. Giuliani, A. Donati, G. Giorgi, C.A. Boccia, R. Mendichi, D. Piovani, C. Botta, L. Salvini, F. Samperi, C. Savoca, M. Licciardi, E. Paccagnini, M. Gentile, A. Cappelli, Physicochemical Properties of a New PEGylated Polybenzofulvene Brush for Drug Encapsulation, Pharm. 11 (2019), https://doi.org/10.3390/pharmaceutics11090444.

[30] A. Cappelli, S. Galeazzi, G. Giuliani, M. Anzini, M. Aggravi, A. Donati, L. Zetta, A. C. Boccia, R. Mendichi, G. Giorgi, E. Paccagnini, S. Vomero, Anionic polymerization of a benzofulvene monomer leading to a thermoreversible π-stacked polymer. Studies in macromolecular and aggregate structure, Macromolecules 41 (2008) 2324–2334, https://doi.org/10.1021/ma702319h.

[31] A. Cappelli, M. Paolino, P. Anzini, G. Giuliani, S. Valenti, M. Aggravi, A. Donati, R. Mendichi, L. Zetta, A.C. Boccia, F. Bertini, F. Samperi, S. Battlato, E. Paccagnini, S. Vomero, Structure-property relationships in densely grafted π-stacked polymers, J. Polym. Sci. Part A Polym. Chem. 48 (2010) 2446–2461, https://doi.org/10.1002/pola.24016.

[32] A. Cappelli, M. Paolino, G. Grisci, G. Giuliani, A. Donati, R. Mendichi, A.C. Boccia, F. Samperi, S. Battiato, E. Paccagnini, E. Giacomello, V. Sorrentino, M. Licciardi, G. Giammona, S. Vomero, A click chemistry-based "' grafting through "' approach to the synthesis of a biorelevant polymer brush, Polym. Chem. 2 (11) (2011) 2518.

[33] A. Cappelli, S. Galeazzi, G. Giuliani, M. Anzini, M. Grassi, R. Lapasin, G. Grassi, R. Farra, B. Dapas, M. Aggravi, A. Donati, L. Zetta, A.C. Boccia, F. Bertini, F. Samperi, S. Vomero, Synthesis and spontaneous polymerization of oligo (ethylene glycol)-conjugated benzofulvene macromonomers. A polymer brush forming a physical hydrogel, Macromolecules 42 (2009) 2368–2378, https://doi.org/10.1021/ma802429g.

[34] M. Licciardi, M. Grassi, M. Di Stefano, L. Feruglio, G. Giuliani, S. Valenti, A. Cappelli, G. Giammona, PEG-benzofulvene copolymer hydrogels for antibody delivery, Int. J. Pharm. 390 (2010) 183–190, https://doi.org/10.1016/j.ijpharm.2010.02.002.

[35] M. Licciardi, G. Amato, A. Cappelli, M. Paolino, G. Giuliani, B. Belmonte, C. Guarnotta, G. Pitarresi, G. Giammona, Evaluation of thermoresponsive properties and biocompatibility of polybenzofulvene aggregates for leuprolide delivery, Int. J. Pharm. 438 (1-2) (2012) 279–286.

[36] A. Cappelli, G. Grisci, M. Paolino, V. Razzano, G. Giuliani, A. Donati, C. Bonechi, R. Mendichi, A.C. Boccia, M. Licciardi, C. Scialabba, G. Giammona, S. Vomero, Polybenzofulvene derivatives bearing dynamic binding sites as potential anticancer drug delivery systems, J. Mater. Chem. B. 3 (2015) 361–374, https://doi.org/10.1039/c4tb01268b.

[37] A. Cappelli, M. Paolino, G. Grisci, V. Razzano, G. Giuliani, A. Donati, C. Bonechi, R. Mendichi, S. Battiato, F. Samperi, C. Scialabba, G. Giammona, F. Makovec, M. Licciardi, Hyaluronan-coated polybenzofulvene brushes as biomimetic materials, Polym. Chem. 7 (2016) 6529–6544, https://doi.org/10.1039/C6PY01644H.

[38] M. Licciardi, C. Scialabba, G. Giammona, M. Paolino, V. Razzano, G. Grisci, G. Giuliani, F. Makovec, A. Cappelli, Design and development of hyaluronan-functionalized polybenzofulvene nanoparticles as CD44 receptor mediated drug delivery system, J. Nanopart. Res. 19 (6) (2017), https://doi.org/10.1007/s11051-017-3881-z.

[39] M. Paolino, G. Grisci, F. Castriconi, A. Reale, G. Giuliani, A. Donati, C. Bonechi, G. Giorgi, R. Mendichi, D. Piovani, A. Boccia, M. Canetti, F. Samperi, S. Dattilo, C. Scialabba, M. Licciardi, E. Paccagnini, M. Gentile, A. Cappelli, Densely PEGylated polybenzofulvene brushes for potential applications in drug encapsulation, Pharmaceutics 10 (2018), https://doi.org/10.3390/pharmaceutics10040234.

[40] A. Cappelli, F. Villafiorita-Monteleone, G. Grisci, M. Paolino, V. Razzano, G. Fabio, G. Giuliani, A. Donati, R. Mendichi, A.C. Boccia, M. Pasini, C. Botta, Highly emissive supramolecular assemblies based on π-stacked polybenzofulvene hosts and a benzothiadiazole guest, J. Mater. Chem. C. 2 (37) (2014) 7897–7905.

[41] A. Cappelli, V. Razzano, M. Paolino, G. Grisci, G. Giuliani, A. Donati, R. Mendichi, F. Samperi, S. Battiato, A.C. Boccia, A. Mura, G. Bongiovanni, W. Mróz, C. Botta, Bithiophene-based polybenzofulvene derivatives with high stacking and hole mobility, Polym. Chem. 6 (2015) 7377–7388, https://doi.org/10.1039/C5PY00904A.

[42] W. Mróz, F. Villafiorita-Monteleone, M. Pasini, G. Grisci, M. Paolino, V. Razzano, A. Cappelli, C. Botta, π-stacked polybenzofulvene derivatives as hosts for yellow and red emitting OLEDs, Mater. Lett. 142 (2015) 197–200, https://doi.org/10.1016/j.matlet.2014.12.002.

[43] A. Cappelli, V. Razzano, G. Fabio, M. Paolino, G. Grisci, G. Giuliani, A. Donati, R. Mendichi, W. Mróz, F. Villafiorita-Monteleone, C. Botta, Side chain engineering in π-stacked polybenzofulvene derivatives bearing electron-rich chromophores for OLED applications, RSC Adv. 5 (2015) 101377–101385, https://doi.org/10.1039/c5ra21164f.

[44] F. Fabrizi de Biani, A. Reale, V. Razzano, M. Paolino, G. Giuliani, A. Donati, G. Giorgi, W. Mróz, D. Piovani, C. Botta, A. Cappelli, Electrochemical and optoelectronic properties of terthiophene- and bithiophene-based polybenzofulvene derivatives, RSC Adv. (2018) 10836–10847, https://doi.org/10.1039/C6RA08981J.

[45] F. Villafiorita-Monteleone, E. Kozma, U. Giovanella, M. Catellani, M. Paolino, V. Collico, M. Colombo, A. Cappelli, C. Botta, Red and deep-red emissive polymeric nanoparticles based on polybenzofulvene and perylenediimide derivatives, Dye. Pigment. 149 (2018) 331–335, https://doi.org/10.1016/j.dyepig.2017.10.010.

[46] F. Villafiorita-Monteleone, E. Kozma, M. Pasini, M. Paolino, A. Cappelli, G. Bongiovanni, A. Mura, C. Botta, Polybenzofulvenes-based blends with benzothiadiazole and perylene diimide derivatives emitting from yellow to the deep-red by resonant energy transfer processes, Appl. Phys. Lett. 110 (2017) 183301. doi: 10.1063/1.4983022.

[47] M. Paolino, A. Reale, V. Razzano, G. Giorgi, G. Giuliani, F. Villafiorita-Monteleone, C. Botta, C. Coppola, A. Sinicropi, A. Cappelli, Design, synthesis, structure, and photophysical features of highly emissive cinnamic derivatives, New J. Chem. 44 (2020) 13644–13653, https://doi.org/10.1039/D0NJ02429E.

[48] M. Paolino, A. Reale, G. Magrini, V. Razzano, G. Giuliani, A. Donati, G. Giorgi, F. Samperi, M. Canetti, M. Mauro, F. Villafiorita-Monteleone, E. Fois, C. Botta, A. Cappelli, UV-light-induced polymerization in the amorphous solid-state of a spontaneously non-polymerizing 3-phenylbenzofulvene monomer, Eur. Polym. J. 137 (2020), 109923, https://doi.org/10.1016/j.eurpolymj.2020.109923.

[49] M. Paolino, A. Reale, G. Magrini, V. Razzano, M. Saletti, G. Giuliani, A. Donati, F. Samperi, A. Scamporrino, M. Canetti, M. Mauro, F. Villafiorita-Monteleone, E. Fois, C. Botta, A. Cappelli, Synthesis and UV-light induced oligomerization of a benzofulvene-based neutral platinum(II) complex, Eur. Polym. J. 156 (2021), 110597, https://doi.org/10.1016/j.eurpolymj.2021.110597.

[50] G.M. Sheldrick, A short history of SHELX, Acta Crystallogr. Sect. A. 64 (2008) 112–122, https://doi.org/10.1107/S0108767307043930.

14

39

[51] G.M. Sheldrick, Crystal structure refinement with SHELXL, Acta Crystallogr. Sect. C. 71 (2015) 3–8, https://doi.org/10.1107/S2053229614024218.

[52] J.-D. Chai, M. Head-Gordon, Long-range corrected hybrid density functionals with damped atom–atom dispersion corrections, Phys. Chem. Chem. Phys. 10 (2008) 6615–6620, https://doi.org/10.1039/B810189B.

[53] T.H. Dunning, P.J. Hay, Gaussian Basis Sets for Molecular Calculations, in: H.F. Schaefer (Ed.), Methods Electron. Struct. Theory. Mod. Theor. Chem., Springer, Boston, MA, 1977. doi: https://doi.org/10.1007/978-1-4757-0887-5_1.

[54] D. Andrae, U. Häußermann, M. Dolg, H. Stoll, H. Preuß, Energy-adjusted ab initio pseudopotentials for the second and third row transition elements, Theor. Chim. Acta. 77 (1990) 123–141, https://doi.org/10.1007/BF01114537.

[55] M. Klotzsche, D. Barreca, L. Bigiani, R. Seraglia, A. Gasparotto, L. Vanin, C. Jandl, A. Pöthig, M. Roverso, S. Bogialli, G. Tabacchi, E. Fois, E. Callone, S. Dirè, C. Maccato, Facile preparation of a cobalt diamine diketonate adduct as a potential vapor phase precursor for Co₃O₄ films, Dalton Trans. 50 (2021) 10374–10385, https://doi.org/10.1039/D1DT01650D.

[56] D. Barreca, E. Fois, A. Gasparotto, C. Maccato, M. Oriani, G. Tabacchi, The Early Steps of Molecule-to-Material Conversion in Chemical Vapor Deposition (CVD): A Case Study, Molecules 26 (7) (2021) 1988, https://doi.org/10.3390/molecules26071988.

[57] M.J. Frisch, G.W. Trucks, H.B. Schlegel, G.E. Scuseria, M.A. Robb, J.R. Cheeseman, G. Scalmani, V. Barone, G.A. Petersson, H. Nakatsuji, X. Li, M. Caricato, A. Marenich, J. Bloino, B.G. Janesko, R. Gomperts, B. Mennucci, H.P. Hratchian, J. V. Ortiz, A.F. Izmaylov, J.L. Sonnenberg, D. Williams-Young, F. Ding, F. Lipparini, F. Egidi, J. Goings, B. Peng, A. Petrone, T. Henderson, D. Ranasinghe, V.G. Zakrzewski, J. Gao, N. Rega, G. Zheng, W. Liang, M. Hada, M. Ehara, K. Toyota, R. Fukuda, J. Hasegawa, M. Ishida, T. Nakajima, Y. Honda, O. Kitao, H. Nakai, T. Vreven, K. Throssell, J.A.J. Montgomery, J.E. Peralta, F. Ogliaro, M. Bearpark, J.J. Heyd, E. Brothers, K.N. Kudin, V.N. Staroverov, T. Keith, R. Kobayashi, J. Normand, K. Raghavachari, A. Rendell, J.C. Burant, S.S. Iyengar, J. Tomasi, M. Cossi, J.M. Millam, M. Klene, C. Adamo, R. Cammi, J.W. Ochterski, R.L. Martin, K. Morokuma, O. Farkas, J.B. Foresman, D.J. Fox, Gaussian, (2016).

[58] J. Moreau, U. Giovanella, J.-P. Bombenger, W. Porzio, V. Vohra, L. Spadacini, G. Di Silvestro, L. Barba, G. Arrighetti, S. Destri, M. Pasini, M. Saba, F. Quochi, A. Mura, G. Bongiovanni, M. Fiorini, M. Uslenghi, C. Botta, Highly Emissive Nanostructured Thin Films of Organic Host-Guests for Energy Conversion, ChemPhysChem 10 (2009) 647–653, https://doi.org/10.1002/cphc.200800682.

[59] M. Mauro, A. Aliprandi, C. Cebrián, D. Wang, C. Kübel, L. De Cola, Self-assembly of a neutral platinum(ii) complex into highly emitting microcrystalline fibers through metallophilic interactions, Chem. Commun. 50 (2014) 7269–7272, https://doi.org/10.1039/C4CC01045K.

15

Chapter 3

Chemical-structural manipulation of the benzofulvene scaffold for the design and synthesis of novel light-responsive biomimetic molecular switch

3.1.1. Light-Driven Molecular Switches (LDMSs).

Light-Driven Molecular Switches (LDMSs) are organic molecules capable of interconverting between at least two different isomeric forms characterized by distinct absorption spectra as a result of a light stimulus,[1] which may be considered a very clean, non-contaminating "reagent" that can be delivered with high spatiotemporal precision. Concerning their chemical structure, LDMSs represent overcrowded olefins capable of rotation around the exocyclic double bond. In this way, light energy drives the rotation of a portion of the molecule, called *rotor*, with respect to a fixed portion named *stator* via a *cis* to *trans* and/or *trans* to *cis* isomerization of the exocyclic double bond (Figure 3.1). [2]
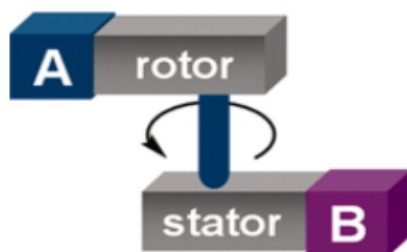
Figure 3.1. Schematic representation of the structure of the LDMS.

To improve the physicochemical properties of LDMSs, researchers aim to control the rotational speed, modulate the absorption wavelength, increase the quantum yield of isomerization,[3] increase stability with increased numbers of photocycles,[4] or unidirectional movement[5] and expand the solubility in different organic and aqueous solvents (e. g. by means of PEGylation strategies).

3.1.2. Real-life application of LDMSs.

Regarding the real-life applications of LDMSs, these molecules recently became important tools in complex biological systems. A large number of living processes are regulated by natural LDMSs embedded in complex natural light-sensitive proteins such as Rhodopsins, Photoactive Yellow Protein (PYP), and Green Fluorescent Protein (GFP). These biological systems inspired the design of novel efficient prototype photoswitches largely employed as molecular elements in several pharmaceutical and technological fields. In this way, Olivucci and coworkers have synthesized and characterized a first, fully synthetic Rhodopsin mimic combining an unnatural *N*-protonated indanylidene

pyrroline Schiff bases (NHIP) photoswitch, capable to mimic the photochemical behavior of the protonated Schiff base of retinal (rPSB), with a bile acid binding protein (BABP), an intracellular lipid binding protein. The resulting BABP-NHIP construct could provide the basis for the development of novel light-triggered delivery systems.[6] A further interesting application of photoswitches regards the innovative field of photopharmacology. Paolino and collaborators have designed and synthesized novel multitarget drugs with light-modulated biological activity. These resulting photoswitches are able to inhibit acetylcholinesterase (AChE) and monoamine oxidase B (MAO-B), with remarkable selectivity over butyrylcholinesterase (BChE) and MAO-A.[7] Concerning the azobenzene-based photoswitches, they have been largely used in the photocontrol of protein structure and function. These photoswitches, containing two electrophiles, react with pairs of nucleophilic residues on peptides and proteins, most of which are cysteine residues. The subsequent structure-based studies and molecular modeling methods have helped to identify the proper sites for the mutation to cysteine for cross-linking.[8] Moreover, the azobenzene-based photoswitches play a *key role* in specific nanosystems called *nanoflasks*. Starting from the *trans* isomer in a hydrophobic environment, after irradiation with UV light, the formation of the polar *cis* isomer occurs, making the *nanoflasks* systems capable of incorporating water, fluorescent dyes, and other polar molecules. Nowadays, these tools are potentially useful for improving the yields of hydrolysis reactions or Diels-Alder cycloadditions in a totally light-dependent way.[9] In addition, photoswitches have been widely used in the fascinating field of drug delivery. In this way, Pianowski and coworkers have discovered a drug-releasing system based on photochromic low molecular weight supramolecular hydrogels, that are triggered with visible light. They have demonstrated that the green-light induced release of structurally unmodified antibiotic, anticancer, and anti-inflammatory drugs under physiological conditions.[10]

3.2. A natural and intriguing light-sensitive protein: Green Fluorescent Protein (GFP).

The Green Fluorescent Protein (GFP) is a natural light-sensitive first protein isolated from the jellyfish *Aequorea Victoria*. GFP is made up of 238 amino acids and its molecular mass is 26.9 kDa. Its intriguing peculiarity is bioluminescence, being able to emit an

intense green light after irradiation at specific wavelengths in the visible and UV regions of the UV-vis spectrum. In the last years, thanks to its distinctive bioluminescence, the GFP has changed from a nearly unknown protein to a commonly used tool in molecular biology, medicine, and cell biology. In this context, GFP is widely used as a biological marker.[11] The chromophore responsible for bioluminescence is the 4-(*p*-hydroxybenzylidene)-1,2-dimethylimidazolidin-5-one (*p*-HBDI), contained in the *β*-barrel cavity, typical of the three-dimensional structure of the GFP (Figure 3.2). [12]
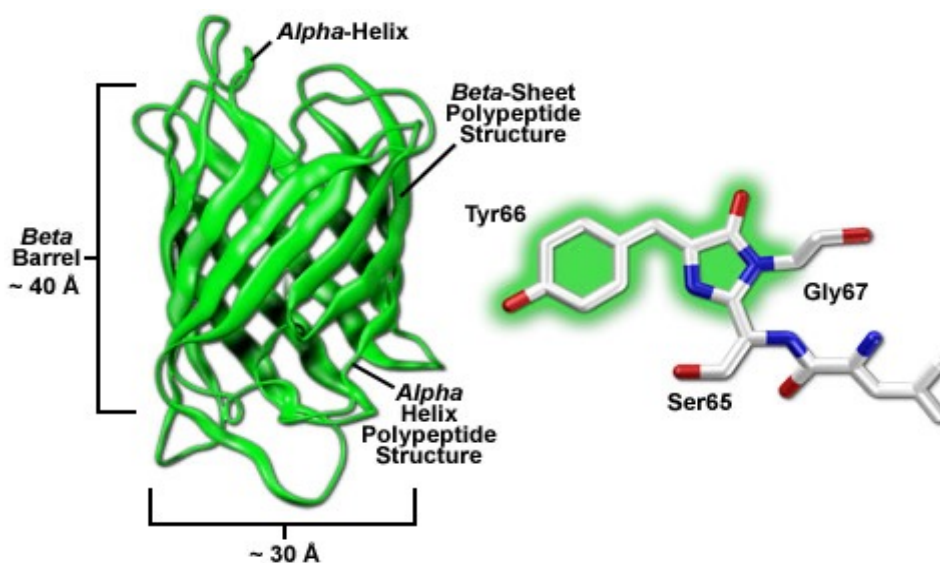
Figure 3.2. Green Fluorescent Protein and its fluorophore *p*-HBDI.

The *p*-HBDI fluorophore emits a green light after being excited at 400-500 nm wavelengths radiation. Interestingly, this bioluminescence mechanism only occurs inside the *β*-barrel cavity of the GFP, because it is capable of impeding the double bond rotation of *p*-HBDI.[13] It has been revealed that, when the fluorophore in solution is free in its conformational motion, a significant loss of fluorescence occurs due to the rapid dissipation of the energy absorbed by the rotation of the double bonds.[14] Protein folding is also essential for both chromophore formation and fluorescence. From these observations, a primary function of the polypeptide fold is to tightly restrain the chromophore. Thus, this feature limits the use of the *p*-HBDI as an isolated fluorescent marker, but it has still widely inspired the design of novel efficient LDMSs that featured sub-picosecond *E/Z* photoisomerization under UV light exposure.[15,16]

3.3. PEG and the versatile PEGylation process.

Poly(ethylene glycol), also known as PEG, is a biocompatible linear amphiphilic polyether with terminal hydroxyl groups, devoid of immunogenicity and toxicity (Figure 3.3).
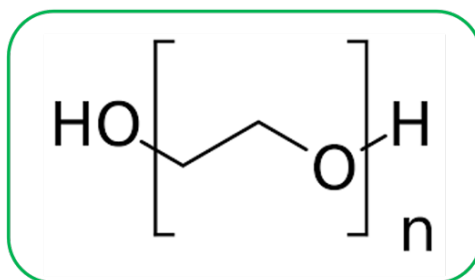
Figure 3.3. Chemical structure of linear amphiphilic PEG.

Among the PEG derivatives, the most widely used is monomethoxy polyethylene glycol, a linear structure compound, available in different molecular weights. PEG is soluble both in organic and aqueous solvents thanks to the hydrogen bonds formation of three water molecules per unit of ethylene oxide. Moreover, the terminal hydroxyl groups of the solubilizing PEG chain can be chemically manipulated to introduce several functionalities which can be used to conjugate the resulting PEG to the designed molecules. The suitable functional group is chosen based on the type of the available reactive group on the molecule that will be coupled to the PEG. As a result of its versatility, PEGylation is the most widely used procedure in medicinal and pharmaceutical-applicative chemistry to expand the solubility of several organic compounds in different aqueous solvents.

In this context, the covalent PEGylation process is exploited for the chemical modification of therapeutic peptides and liposomes to improve their pharmacokinetic properties, increase both their solubility and half-life, reducing at the same time renal clearance.[17,18] Nanoparticles (NPs) and peptides, exploited for pharmaceutical applications, must be properly PEGylated (Figure 3.4) to avoid their elimination by the immune system. In particular, PEG coatings reduce the adsorption of opsonins in vivo.
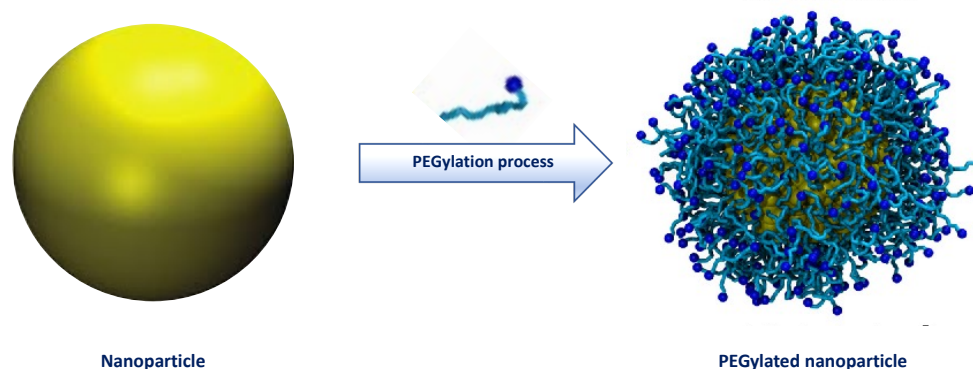
Figure 3.4. PEGylated nanoparticle (NP) for pharmaceutical applications.

The formation of an opsonin crown would immediately alert the mononuclear phagocyte system (MPS), preventing accumulation in target cells and tissues, and promoting the rapid elimination of the NP-opsonin complex from the bloodstream. The growth of a protein crown hinders the interaction of NPs with the cell membrane, reducing their absorption.[19] Furthermore, the PEGylation process represents one of the most used conjugation techniques to modulate the physico-chemical toxicological properties of dendrimers, such as poly(amidoamine) (PAMAM) and poly(propylene imine) (PPI) dendrimers. It has been shown that the monofunctional PEG chains reduce cytotoxicity and increase the size and cellular absorption,[20] while homo-bifunctional PEG chains have been used for the construction of dendrimer-based hydrogels.[21]

3.4. References.

1. Feringa, B. L.; Koumura, N.; van Delden, R. A.; ter Wiel, M. K. J. *Appl. Phys. A* **2002**, *75*, 301-308.

2. Bauer, J.; Hou, L.; Kistemaker, J. C. M.; Feringa, B. L. *J. Org. Chem.* **2014**, *79*, 4446-4455.

3. Filatov, M.; Paolino, M.; Min, S. K.; Choi, C. H. *Chem. Commun.* **2019**, *55*, 5247-5250.

4. Kornman, C. T.; Li, L.; Weldeab, A. O.; Ghiviriga, I.; Abboud, K. A.; Castellano, R. K. *Chem. Sci.* **2020**, *11*, 10190-10197.

5. Filatov, M.; Paolino, M.; Min, S. K.; Kim, K. S. *J. Phys. Chem. Lett.* **2018**, *9*, 4995-5001.

6. Pagano, K.; Paolino, M.; Fusi, S.; Zanirato, V.; Trapella, C.; Giuliani, G.; Cappelli, A.; Zanzoni, S.; Molinari, H.; Ragona, L.; Olivucci, M. *J. Phys. Chem. Lett.* **2019**, *10*, 2235-2243.

7. Paolino, M.; Rullo, M.; Maramai, S.; de Candia, M.; Pisani, L.; Catto, M.; Mugnaini, C.; Brizzi, A.; Cappelli, A.; Olivucci, M.; Corelli, F.; Altomare, D. C. *RSC Med. Chem.* **2022**, *13*, 873-883.

8. Zhu, M.; Zhou, H. *Org Biomol Chem.* **2018**, *16* (44), 8434-8445.

9. Zhao, H.; Sen, S.; Udayabhaskararao, T.; Sawczyk, M.; Kučanda, K.; Manna, D.; Kundu, P. K.; Lee, J. -W.; Kràl, P.; Klajn, R. *Nat Nanotechnol.* **2016**, *11* (1), 82-88.

10. Karcher, J.; Pianowski, Z. L. *Chem. Eur J.* **2018**, *24* (45), 11605-11610.

11. Zimmer, M. *Chem Rev.* **2002**, *102* (3), 759-782.

12. Chalfie, M. *Photochem Photobiol.* **1995**, *62* (4), 651-656.

13. Craggs, T. D. *Chem Soc Rev.* **2009**, *38* (10), 2865.

14. Stavrov, S. S.; Solntsev, K. M.; Tolbert, L. M.; Huppert, D. *J Am Chem Soc.* **2006**, *128* (5), 1540-1546.

15. Paolino, M.; Gueye, M.; Pieri, E.; Manathunga, M.; Fusi, S.; Cappelli, A.; Latterini, L.; Pannacci, D.; Filatov, M.; Léonard, J.; Olivucci, M. *J. Am. Chem. Soc.* **2016**, *138*, 9807-9825.

16. Paolino, M.; Giovannini, T.; Manathunga, M.; Latterini, L.; Zampini, G.; Pierron, R.; Léonard, J.; Fusi, S.; Giorgi, G.; Giuliani, G.; Cappelli, A.; Cappelli, C.; Olivucci, M. *J. Phys. Chem. Lett*. **2021**, *12*, 3875-3884.

17. Hargreaves, A. E.; Hargreaves, T. *RSC* **2003**, 32.

18. Veronese, F. M.; Pasut, G. *Drug Discov. Today* **2005**, *10*, 1451-1458.

19. Suk, J. S.; Xu, Q.; Kim, N.; Hanes, J.; Ensign L. M. *Adv. Drug Deliv. Rev.* **2016**, *99*, 28-51.

20. Somani, S.; Laskar, P.; Altwaijry, N.; Kewcharoenvong, P.; Irving, C.; Robb, G.; Pickard, B. S.; Dufès, C. *Sci. Rep*. **2018**, *8*, 9410.

21. Wang, J.; He, H.; Cooper, R.C.; Gui, Q.; Yang, H. *Mol. Pharm*. **2019**, *16*, 1874.

3.5. Research article: "Design, Synthesis and Characterization of a Visible-Light- Sensitive Molecular Switch and Its PEGylation Towards a Self-Assembling Molecule".

Authors: Marco Paolino, **Mario Saletti**, Annalisa Reale, Mariano Licciardi, Paola Varvarà, Arnaud Marquette, Jérémie Léonard, Claudia Bonechi, Alessandro Donati, Gianluca Giorgi, Germano Giuliani, Benedetta Carlotti, Fausto Ortica, Loredana Latterini, Mariangela Gentile, Eugenio Paccagnini, Massimo Olivucci, Andrea Cappelli.

Contribution: The Ph.D. candidate's contribution to this work refers to the synthesis, preliminary NMR analysis of compounds, and the writing of the experimental section.

The current work reports on the design, synthesis, and characterization of a novel molecular photoswitch inspired by both the molecular features of GFP chromophore (*p*-HBDI) and the supramolecular features (e. g. self-assembling by π-stacking interactions) of the 3-phenylbenzofulvene scaffold. Therefore, the benzofulvene structure of compound 6-MO-**BF3k** has been used to host the rotating head of HBDI-like photoswitches to obtain the novel photoswitch prototype in which two aromatic rings are conjugated with the amide carbonyl employing a diene moiety, able to extend the electronic conjugation. The subsequent coupling of the chromophore within complex systems of synthetic or biological nature could be made possible by replacing the methoxy group with an ethyl azide group available for Copper(I)-Catalyzed Azide Alkyne 1,3-dipolar Cycloaddition (CuAAC) reactions. Finally, methyl-end-capped nona(ethylene glycol) (NEG) side chain, an amphiphilic solubilizing group, has been

conjugated to explore the practicability of the *click* reaction and increase the solubility of the chromophore in water. The introduction of the solubilizing NEG side chain has led to the formation of an amphiphilic visible LDMS capable of self-assembling in nanometric micelles in water solutions and operated by visible light.

www.chemeurj.org

Design, Synthesis and Characterization of a Visible-Light-Sensitive Molecular Switch and Its PEGylation Towards a Self-Assembling Molecule

Marco Paolino,*[a] Mario Saletti,[a] Annalisa Reale,[a] Mariano Licciardi,[b] Paola Varvarà,[b] Arnaud Marquette,[c] Jérémie Léonard,[c] Claudia Bonechi,[a] Alessandro Donati,[a] Gianluca Giorgi,[a] Germano Giuliani,[a] Benedetta Carlotti,[d] Fausto Ortica,[d] Loredana Latterini,[d] Mariangela Gentile,[e] Eugenio Paccagnini,[e] Massimo Olivucci,[a, f] and Andrea Cappelli*[a]

Abstract: HBDI-like chromophores represent a novel set of biomimetic switches mimicking the fluorophore of the green fluorescent protein that are currently studied with the hope to expand the molecular switch/motor toolbox. However, until now members capable of absorbing visible light in their neutral (i.e. non-anionic) form have not been reported. In this contribution we report the preparation of an HBDI-like chromophore based on a 3-phenylbenzofulvene scaffold capable of absorbing blue light and photoisomerizing on the picosecond timescale. More specifically, we show that double-bond photoisomerization occurs in both the *E*-to-*Z* and *Z*-to-*E* directions and that these can be controlled by irradiating with blue and UV light, respectively. Finally, as a preliminary applicative result, we report the incorporation of the chromophore in an amphiphilic molecule and demonstrate the formation of a visible-light-sensitive nanoaggregated state in water.

[a] *Dr. M. Paolino, Dr. M. Saletti, Dr. A. Reale, Dr. C. Bonechi, Prof. A. Donati, Prof. G. Giorgi, Dr. G. Giuliani, Prof. M. Olivucci, Prof. A. Cappelli*
Dipartimento di Biotecnologie, Chimica e Farmacia (Dipartimento di Eccellenza 2018–2022)
Università degli Studi di Siena
Via A. Moro 2, 53100 Siena (Italy)
E-mail: paolino3@unisi.it
andrea.cappelli@unisi.it

[b] *Prof. M. Licciardi, Dr. P. Varvarà*
Dipartimento di Scienze e Tecnologie Biologiche, Chimiche e Farmaceutiche (STEBICEF), Università degli Studi di Palermo
Via Archirafi 32, 90123 Palermo (Italy)

[c] *Dr. A. Marquette, Dr. J. Léonard*
Institut de Physique et Chimie des Matériaux de Strasbourg
Université de Strasbourg
CNRS UMR, 7504 Strasbourg (France)

[d] *Prof. B. Carlotti, Prof. F. Ortica, Prof. L. Latterini*
Dipartimento di Chimica, Biologia e Biotecnologie
Università di Perugia
Via Elce di Sotto, 8, 06123 Perugia (Italy)

[e] *Dr. M. Gentile, Dr. E. Paccagnini*
Dipartimento di Scienze della Vita
Università degli Studi di Siena
Via A. Moro, 53100 Siena (Italy)

[f] *Prof. M. Olivucci*
Chemistry Department
Bowling Green State University
43403 Bowling Green, OH (USA) ok

Introduction

Light-driven molecular switches (LDMSs) are molecules capable of interconverting between at least two different isomeric forms characterized by distinct absorption spectra as a result of a light stimulus.[1] Nature, more perfectly than humans, uses LDMSs to regulate numerous biological processes.[2] Natural light-sensitive proteins, such as Rhodopsins and Photoactive Yellow Protein (PYP), provided a template for the design of increasingly efficient synthetic LDMS as molecular elements for nanodevices and nanomedicines.[3–6] In the last decade, many classes of molecules (i.e. azobenzenes,[7,8] spiropyrans,[9,10] stilbenes,[11] diarylethenes,[12] indigoids,[13] etc.) have been designed for the conversion of light in mechanical motion of isolated molecules[14,15] but also in 2D ordered supramolecular structures.[16,17] Among these, overcrowded olefins capable of rotation around the C=C double bond showed interesting properties and promising applications.[18,19] In these structures, light energy fuels the rotation of a portion of the molecule (rotor) with respect to a reference fixed portion (stator) via a *cis to trans* and/or *trans to cis* isomerization of an exocyclic double bond.[20] Numerous studies aim to control the rotational speed,[21] modulate the absorption wavelength,[22,23] increase the quantum yield of isomerization,[24,25] increase stability (showing increased numbers of photocycles)[26,27] or unidirectional movement (evolution from photoswitches to light-driven molecular rotors),[28,29] and to expand the solubility in different organic and aqueous solvents in these systems.[30–32]

51

Over the past decade, part of our work has been focused on the design, synthesis, and computational characterization of new LDMS. In particular, we have successfully tried to mimic the reactivity of the retinal chromophore embedded in the Rhodopsin cavity. To this scope, we have prepared analogues positively charged N-alkylated or N-protonated indanylidene pyrroline Schiff bases (NAIPs and NHIPs respectively), which perform ultra-fast double bond photoisomerization.[33–37] The same biomimetic approach was then used to design a negatively charged LDMS.[38,39] In this last design effort, we were inspired by the structure of the Green Fluorescent Protein (GFP) fluorophore 5-(4-hydroxybenzylidene)-1*H*-imidazol-2(5*H*)-one (*p*-HBDI), to transform an efficient emitter into an LDMS that featured a sub-picosecond *E/Z* photoisomerization (**HBDI-LPs**, see Figure 1A) under UV light exposure.[38,39]

In parallel, some of us have developed the concept of "affinity polymerization" based on the molecular recognition between 3-phenylbenzofulvene derivatives (i.e. 6-MO-**BF3k**[40] reported in Figure 1C) mediated by intermolecular π-stacking interactions.[41–44] In these systems, spontaneous polymerization occurs in the apparent absence of catalysts or initiators and involves the exocyclic double bond of these *trans*-diene monomers. However, the introduction of a methyl group on the exocyclic methylene (i.e. **BF3p**) prevents spontaneous polymerization while allowing the formation of columnar aggregates in the solid-state.[45] Interestingly, the through-space conjugated monomeric units of these polybenzofulvene derivatives showed emissive properties and the ability to transfer the absorbed energy to small molecule guests by fluorescence resonance energy transfer (FRET) mechanism.[44,46–51]

In the present paper, we report a novel HBDI-like homologue photoswitch capable of functioning in both the *E*-to-*Z* and *Z*-to-*E* directions via visible and UV light, respectively. More specifically, **1** features an extended conjugation due to a 3-phenylindene-2-carboxylate scaffold, the structure at the basis of the polybenzofulvene monomeric unit (Figure 1C).[52–65] We also show that the obtained LDMS **1** can be easily functionalized with a clickable azide group (compound **2**) for the insertion of the photoswitch in more complex synthetic and/or biological structures via azide-alkyne click reactions. In fact, we report that methyl-end-capped nona(ethylene glycol) (NEG) side chain, an amphiphilic solubilizing group,[66] can be successfully conjugated with **2** in a preliminary effort to obtain an amphiphilic LDMS capable of self-assembling in nanometric micelles in water solution and operated by visible light (Figure 1D).

Results and Discussion

Design and Synthesis

Recently, our research team reported on the synthesis and characterization of molecular photoswitches inspired by the chromophore of GFP.[38,39] These photoswitches (**HDBI-LPs** in Figure 1, panel A) share with the natural GFP and PYP[67] chromophores, the cinnamic structure characterized by an
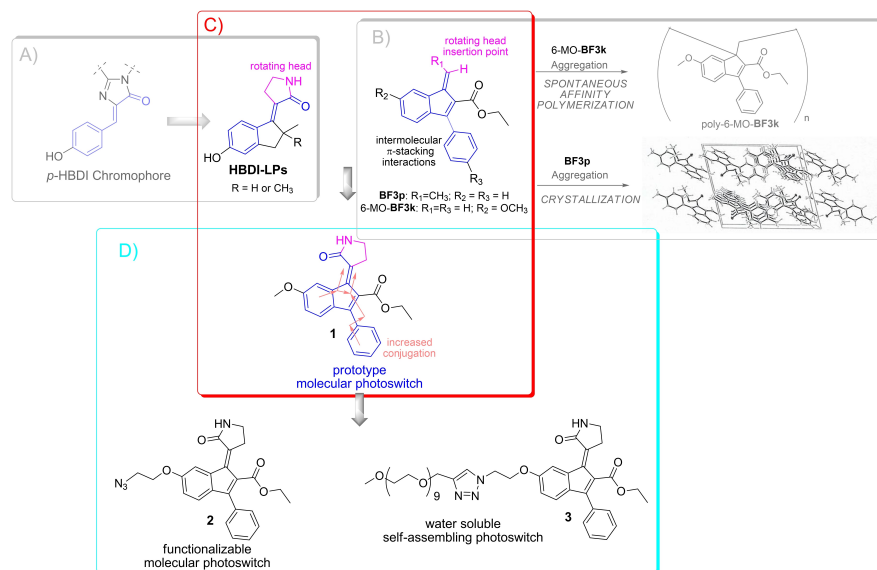
Figure 1. Design of the new LDMS **1** from GFP fluorophore through HBDI-like photoswitch and its rational conversion in the functionalizable LDMS **2** and pegylated water-soluble self-assembling LDMS **3**.

aromatic ring connected by means of an exocyclic double bond to a carbonyl group. As introduced above, the cinnamic structure is also present in another chemical scaffold widely studied in our laboratories, namely ethyl 1-methylene-3-phenyl-1*H*-indene-2-carboxylate, which we will call benzofulvene scaffold hereafter.[68] In this structure, the double bond of the cinnamic scaffold is harnessed in the 5-term ring without the possibility of isomerization. However, as in **HDBI-LP**, also in the benzofulvene scaffold there is an exocyclic double bond, which, in the dependence of the appropriate functionalization, can lead to the formation of distinct configurational isomers. Therefore, the benzofulvene structure of compound 6-MO-**BF3k**[40] (Figure 1, panel B) was used to insert the rotating head of **HDBI-LP** to obtain the newly designed photoswitch prototype **1**, in which two aromatic rings are conjugated with the amide carbonyl by means of a diene moiety, which extends the electronic conjugation with respect to that of the previous **HDBI-LP**.

Among the benzofulvene structures studied in our laboratories, the **BF3k** scaffold bearing a methoxy group in position 6 of the indene nucleus (i.e. 6-MO-**BF3k**) was selected due to its tolerance to synthetic structural manipulation. The presence of the oxygen atom in position 6 was then exploited to introduce a clickable azide group without altering the chromophore structure as in compound **2** (Figure 1, panel C). A first example of compound **2** functionalization is represented by amphiphilic compound **3** (Figure 1, panel C), obtained by conjugation with a chain of methyl-end-capped nona(ethylene glycol) (NEG). The synthetic efforts and the characterization of the compounds are accurately described in the Supporting Information and reported in Schemes S1–S3.

Particular attention has been paid to the crystallographic structure of compound **1**, which allows us to unequivocally assign the *E* configuration to the preponderant diastereomer,

and gives the opportunity to observe relevant intermolecular H-bond interactions in the crystalline packing occurring between the pyrrolidinone heads (Figure 2).

Photophysical and photochemical features of the novel chromophore

The initial photophysical and photochemical characterization focused on the *E/Z* diastereoisomers of **1**. The absorption spectrum of *E*-**1** in methanol (Figure 3) is composed of a main band centered at 282 nm, a shoulder at 340–360 nm and a weaker band centered at 435 nm and spanning up to about 550 nm. Similar absorption spectra were obtained both in chloroform and dichloromethane. However, in these aprotic solvents, despite an apparently rapid dissolution of the crystals, a few minutes are required to get *E*-**1** molecularly dissolved (Figure S1). The difference in the dissolution speed may be due to the presence of solute-solute (intermolecular) hydrogen bonds (as suggested by the crystallographic studies, see Figure 2), which could be rapidly broken in methanol. Similar optical features were observed in the UV-vis spectra of *Z*-**1**. However, both components of the UV-vis spectra of *Z*-**1** are blue-shifted and with a lower absorbance with respect to the spectra of *E*-**1**. This blue-shift effect is particularly evident in the visible region, in which the *Z*-**1** absorption maximum is 30–35 nm shifted with respect to *E*-**1** (Figure 3, inset).

For comparison, the visible component in the absorption spectra of model compound **1** is absent in those of the original **HBDI-LPs** consistently with the increased conjugation. Moreover, as expected, the UV-visible absorption features of clickable compound *E*-**2** are similar to those of **1** supporting the basic design assumptions (Figure S3).
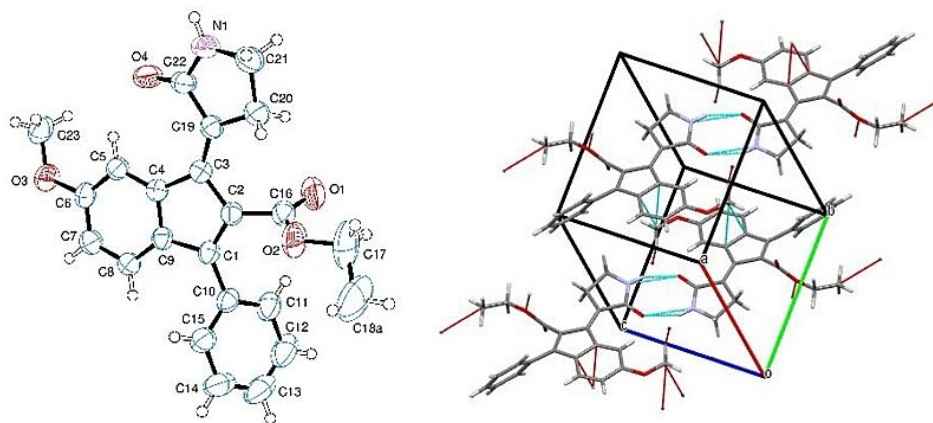

Figure 2. Left panel: Structure of the major isomer of compound 1 obtained by crystallographic studies. Ellipsoids enclose 50% probability. Right panel: H-bond interaction involving the pyrrolidinone moiety and short contacts in the crystal of model compound **1**.
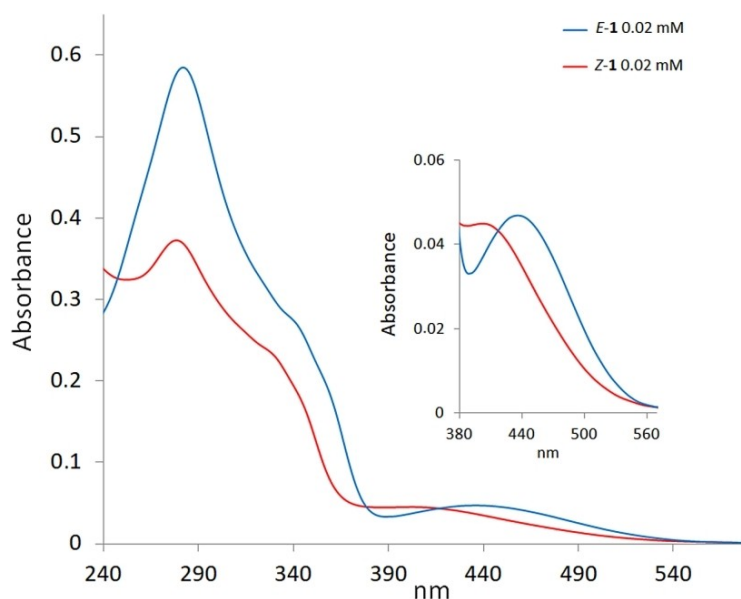
Figure 3. Comparison of the UV-vis spectra of *E*-**1** (blue lines) and *Z*-**1** (red lines) registered at 0.02 mM in methanol.

Based on the UV-vis absorption spectra, the photoisomerization of **1** was evaluated by irradiating its $CDCl_3$ solution into a Pyrex NMR tube at room temperature with three different wavelengths each corresponding to one of the described bands. The results are shown in Figure 4.

The *E/Z* ratio of the photostationary states (PSS) of **1** was determined using ^1H NMR spectroscopy by computing the area ratio of the well distinguishable *E* ad *Z* signals. The *Z* isomer proportion of the PSS composition increased from 33% to 43% and 49% when increasing the excitation wavelength from 320 nm, to 380 nm and 440 nm, respectively. This behaviour the PSS allows to modulate the *E/Z* composition in solution through the UV and visible light. The solutions at the PSSs were stored at room temperature in the dark for a few days without displaying a significant change in *E/Z* composition suggesting the presence of a considerable interconversion thermal barrier between the two isomers. Moreover, high thermal stability (without any isomerization or decomposition) was confirmed for *E*-isomer by means of ^1H NMR spectroscopy after heating at 50 °C in deuterated methanol or at 100 °C in DMSO-d_6 for 24 h.

To gain insight into the photoreaction dynamics of **1**, we performed transient absorption (TA) spectroscopy (see Experimental Section/Methods) on two solutions of *E*-**1** dissolved in dichloromethane at a concentration of 1.9 mM, in two experiments using a pump pulse tuned at $\lambda_{pu} = 450$ nm or $\lambda_{pu} = 290$ nm. For the latter experiment, the probing detection window was specifically extended down to 320 nm (see

Experimental Section/Methods) in order to monitor the recovery of the ground state bleach (GSB). Both datasets are displayed in Figure 5A and 5B, and reveal a very similar, picosecond-lived induced absorption ($\Delta A > 0$ coded in green to red) with local maxima around 375 nm, 510 nm and 640 nm. This spectrally very broad induced absorption is assigned to the S_1 excited state absorption (ESA) since it is observed when exciting at $\lambda_{pu} = 450$ nm (Figure 5B), i.e. in the weak, low-energy absorption band of *E*-**1**. With $\lambda_{pu} = 290$ nm, we excite *E*-**1** in its stronger UV absorption band and populate a higher-lying S_X electronic state (X > 1), which is characterized by an ESA band centred around 530 nm and observed only around time zero in Figure 5A and 6C. This initial S_X ESA disappears within the instrument response function to give rise to the S_1 ESA, indicating ultrafast internal conversion from the initial S_X state to S_1 on a time scale faster than the experimental time resolution (~60 to 80 fs). The initial GSB signal ($\Delta A < 0$) observed at $\lambda < 350$ nm in Figure 5A and 6A decays on the same sub-80 fs time scale, which we interpret as due to the formation of the S_1 ESA which would extend also in the UV to $\lambda = 310$ nm or shorter wavelengths and thus spectrally overlap and partially cancel the GSB signature. Following this initial internal conversion from S_X to S_1, the kinetics of the S_1 ESA decay is almost identical in both datasets as illustrated for a selection of probe wavelengths in Figure 6.

The quantitative analysis of both datasets is performed independently by global analysis (see Experimental Section/
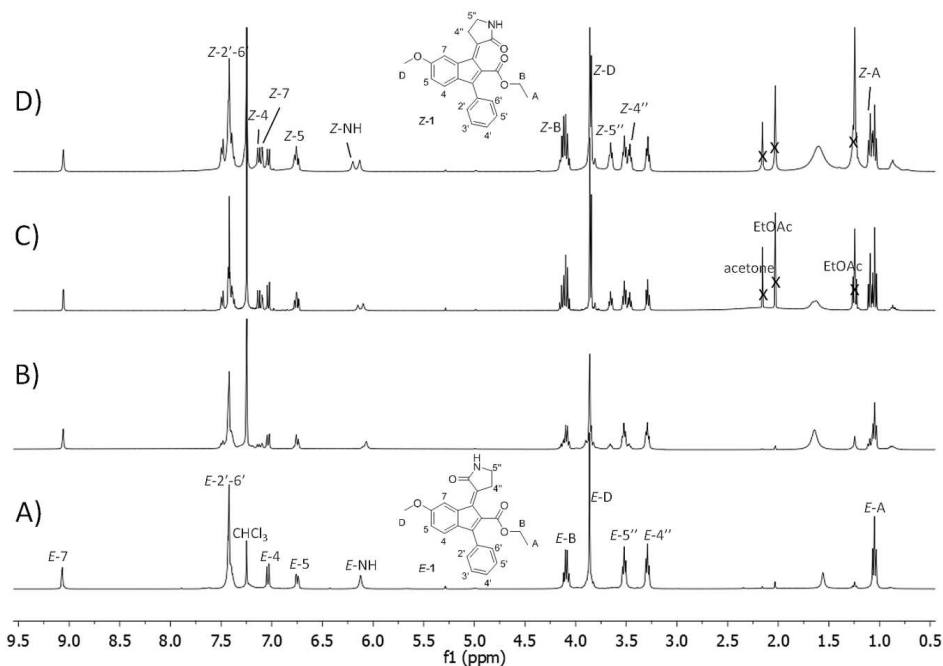
Figure 4. Comparison of the ^{1}H NMR spectra (400 MHz, CDCl$_3$) of prototype molecular photoswitch *E*-**1** (A) with the mixture of the *E* and *Z* isomers at the PSSs reached after irradiation at 320 nm (B), 380 nm (C), and 440 nm (D).
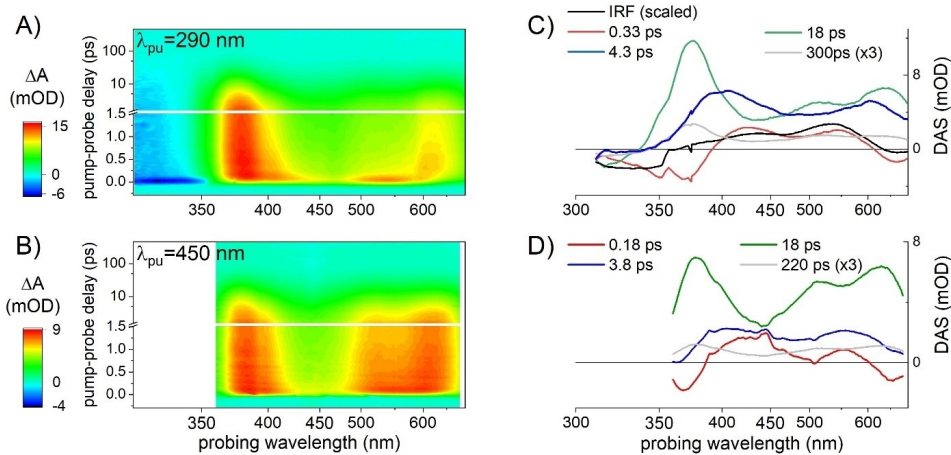
Figure 5. Transient absorption data (ΔA, coded in flase-color scale) as a function pump-probe delay (ps) and probing wavelength (nm), recorded on a dichloromethane solution of *E*-**1** upon excitation at (A) λ$_{pu}$ = 290 nm and (B) λ$_{pu}$ = 450 nm, and the corresponding decay associated spectra (DAS) resulting from their global analysis (C) and (D), respectively.
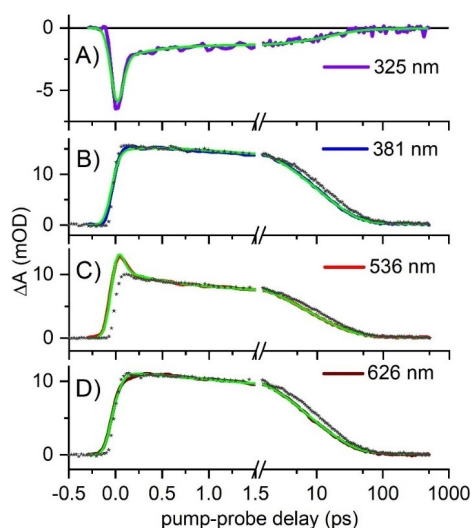
Figure 6. Selection of kinetic traces recorded for a dichloromethane solution of *E*-**1** upon excitation at $\lambda_{pu} = 290$ nm (solid lines) and their global fit (in green), for a selection of probing wavelengths. In panels B to D, the kinetic traces recorded at the same probing wavelengths for $\lambda_{pu} = 450$ nm (grey stars) are overlapped (after normalization), showing that the only differences are (i) in the 5 to 10 ps range where the decay appears slightly slower when $\lambda_{pu} = 450$ nm, and (ii) in panel C, where the overshoot around time zero for $\lambda_{pu} = 290$ nm is the very short-lived signature of the S_X ESA observed before internal conversion to S_1.

Methods). The results are illustrated by the decay-associated spectra (DAS) displayed in Figure 5C and 5D for $\lambda_{pu} = 290$ nm and $\lambda_{pu} = 450$ nm, respectively. Besides the spectroscopic signature characterizing the ultrafast, non-resolved decay of the S_X signature (black line "IRF" in panel C), the decay-associated spectra (DAS) are nearly identical in both experiments. In particular an early spectral relaxation is observed in S_1 within 0.33 and 0.17 ps for $\lambda_{pu} = 290$ nm and $\lambda_{pu} = 450$ nm, respectively, corresponding to the blue shift of the 375 nm band and red shift of the 640 nm band of the broad S_1 ESA (red DAS in Figures 5C and 5D). Then the S_1 ESA decays on two dominating time scales of 3.8 to 4.3 ps and 18 ps (blue and green DAS in Figures 5C and 5D, respectively, and a minor time scale of 200–300 ps (grey DAS, scaled x3 in Figures 5C and 5D). The shapes of these DAS hardly depend on the pump wavelength, and the 18 ps and 200–300 ps DAS have almost identical shapes. We note that the 18 ps DAS becomes negative at wavelengths $\lambda < 340$ nm which clearly reveals the GSB recovery – i.e. S_1 to S_0 decay – on this time scale. The 4 ps DAS is nearly vanishing in the same spectral region where we already noticed that GSB and S_1 ESA signatures overlap and partially cancel out. Hence, we argue that the very weak amplitude of the 4 ps DAS for $\lambda < 340$ nm is the result of the concomitant GSB recovery (negative decay amplitude) and ESA decay (positive decay

amplitude). Altogether, we propose that the 4 ps and 18 ps DAS characterize the bi- (multi-) exponential decay of two (or a distribution of) S_1 subpopulations.

In addition, we note that the relative amplitude of the 4 ps (green) DAS relative to the 18 ps (blue) DAS is larger for $\lambda_{pu} = 290$ nm as compared to $\lambda_{pu} = 450$ nm. In the former case, we expect that the higher photon energy results in a globally hotter S_1 population produced upon ultrafast internal conversion from S_X. Hence, we propose that the 4 ps decay component characterizes a vibrationally hotter subpopulation while the 18 ps lifetime would correspond to cooler molecules. Finally, the 220 to 300 ps decay time scale would correspond to a minor, vibrationally relaxed S_1 population which would decay to S_0 by overcoming an S_1 energy barrier trapping this subpopulation over few hundred ps.

To summarize, the reaction kinetics revealed by the S_1 spectral relaxation and triexponential decay kinetics observed upon excitation at both wavelengths is compatible with a slowing down of the S_1 population decay – suggesting that the S_1-to-S_0 decay region of the conformational space becomes less and less accessible – while the vibrational relaxation proceeds in S_1. Finally, at the longest time delays (500 ps) achieved in this experiment, a very weak signal persists which still displays a spectral signature very similar to the 18 ps and 200 to 300 ps DAS representative of the S_1 ESA. In particular, no *Z-E* difference spectrum clearly emerges suggesting that the *E*-to-*Z* photo-isomerization quantum yield (QY) is small. This observation is confirmed by the independent determination of the photo-isomerization quantum yield, revealing that QY < 0.1 % (see Experimental Section/Methods).

As compared to the related **HBDI-LP** compounds,[38,39] the modified electronic structure of *E*-**1** (increased π electron conjugation) results in (i) a significant reduction of the S_0-S_1 energy gap and oscillator strength, evidenced by the weak absorption band around 435 nm as compared to $\lambda_{max} = 320$ nm for **HBDI-LP**, (ii) a significantly longer excited state lifetime reaching and exceeding the 10 ps time scale (vs. sub-ps to ps for **HBDI-LPs** in its anionic[38,39] or neutral (unpublished) forms), indicating a larger energy gap or barrier between the S_1 minimum and the conical intersection, and (iii) a strongly reduced photoisomerization quantum yield respect to the anionic **HBDI-LPs** (QY = 17–19 %).[38,39]

Photophysical features of the chromophore in the amphiphilic compound

Owing to its amphiphilic character, the photophysical features of **3** were investigated both in water and methanol. The methanol solutions of *E*-**3** showed absorption spectra (Figure 7) very similar to that of *E*-**1** (Figure 3), suggesting the presence of isolated chromophores, rather than an aggregate, in solution in the tested concentration range (0.1 mM–0.01 mM). On the other hand, the absorption spectra of PEGylated compound *E*-**3** in water (Figure 7) are affected by the concentration in the range 0.1–0.01 mM suggesting the possibility of aggregate formation. At the highest concentration tested, the UV-vis spectrum shows
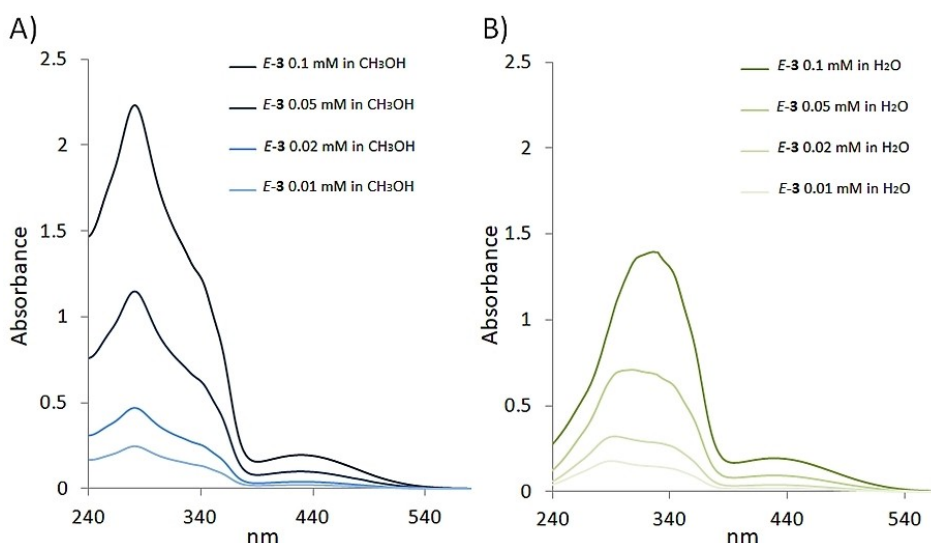
Figure 7. Comparison of the UV-vis absorption spectra of the compound *E*-3 in methanol (A), and water (B) at concentrations ranging from 0.1 to 0.01 mM. The methanolic solution of compound *E*-3 follows the Lambert-Beer law, however the spectra at different concentrations in this solvent are shown for a direct comparison with those recorded in water.

an intense band centered at about 325 nm and a weaker and wider one centered at 430 (spanned up to about 550 nm). A progressive blue-shift of the main band in the UV range was observed with the decrease of the concentration.

To further investigate the aggregation behaviour, the ^{1}H NMR spectra of compound *E*-3 were performed in D_2O and CD_3OD (Figure 8). The spectrum of the water solution showed much broader signals than in methanol-d_4 and deuterated chloroform suggesting the aggregation propensity of *E*-3 in water environment.

Thus, the aggregation features of *E*-3 in water was investigated by means of different approaches such as pyrene fluorescence analysis, dynamic light scattering (DLS), and transmission electron microscopy (TEM and CryoTEM) techniques.[69] Fluorescence analysis with pyrene as the probe allowed us to determine a critical aggregation concentration (CAC) value of 0.07 mg/ml as reported in Figure 9A suggesting high aggregation liability for *E*-3 in water. The transparent solutions of water-soluble derivative in bidistilled water were analyzed by dynamic light scattering (DLS). DLS analysis confirmed the propensity of *E*-3 to generate several heterogeneous populations nanoaggregates in water at the concentrations above its CAC (see Figure 8B). The most stable population showed small mean diameters (from 3 to 10 nm) and were assumed to be composed by small aggregates. On the other hand, the other components showed greater dimensions (around 30 and 200 nm) and were obviously constituted by a large number of molecules.

The cryoTEM investigations performed on a 10 mg/mL water solution (i.e. at a concentration well above its CAC) confirmed the presence of heterogeneous populations of spherical particles with a large preponderance of small particles showing dimensions in the range 10–80 nm (Figure 10). Similar results were obtained by TEM investigations performed by negative staining with uranyl acetate on the same sample as used in cryoTEM studies confirming the presence of heterogeneous populations of spherical particles with a large preponderance of small and very small particles (Figure 9).

E to *Z* photoisomerization via ambient light irradiation

Owing to the presence of a significant absorption band in the visible region, we placed our attention on the interaction of compound **3** with the visible light by comparing its behavior in water and methanol solutions. When water and methanol solutions of pure compound *E*-3 were analyzed by ^{1}H NMR spectroscopy after some weeks of storage at ambient conditions (i.e. room temperature and indoor light irradiation), interesting differences were observed involving the photoisomerization process in the two samples. In particular, the ^{1}H NMR spectrum obtained with the sample dissolved in deuterated water showed the presence of almost equivalent amounts of the two isomers (Figure 11), whereas in the spectrum obtained with methanol solution we observed, along with the signals attributed to *E*-3 a set of small signals
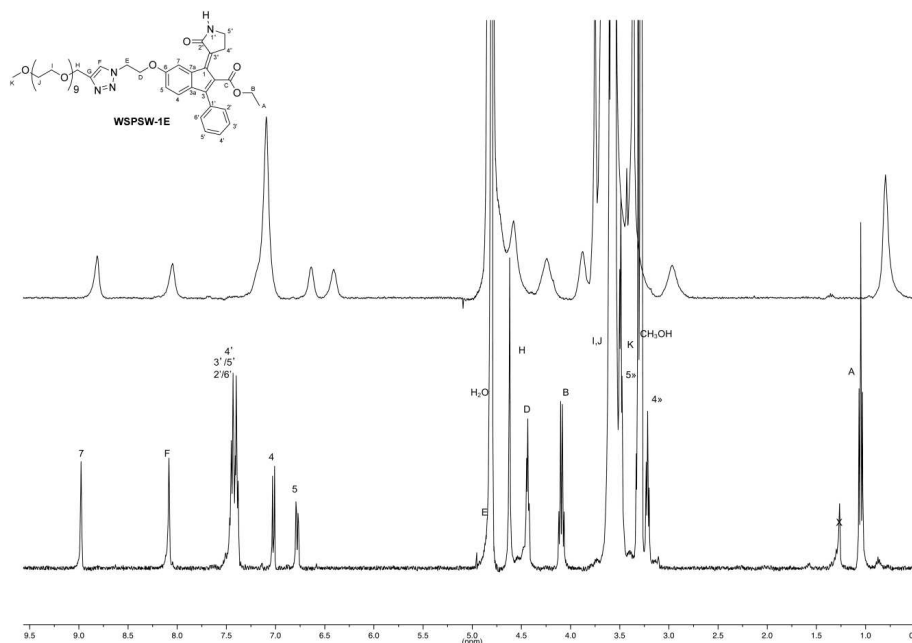
Figure 8. Comparison of ^{1}H NMR spectrum (400 MHz) of *E*-**3** in deuterated water (top trace), CD$_3$OD (bottom trace).
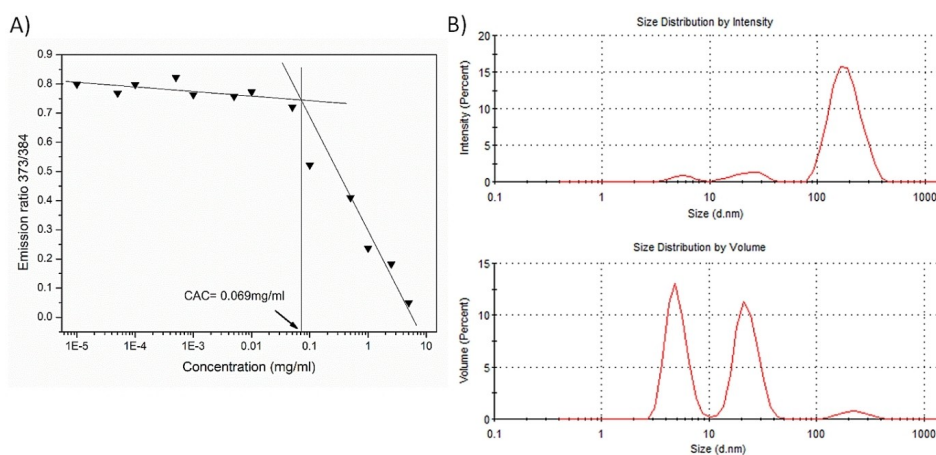
Figure 9. A) I$_{373}$/I$_{384}$ intensity ratio obtained from pyrene emission spectra in the presence of pure *E*-**3** as a function of the logarithm of its concentration in water. B) DLS size distribution histograms (by intensity and volume) of *E*-**3** dispersions in bidistilled water at concentration values of 0.1 mg/mL.

attributed to slight decomposition. For comparison, a similar monitoring was also performed on *E*-**1** in methanol and no photoisomerization was observed for prolonged exposure to room light.
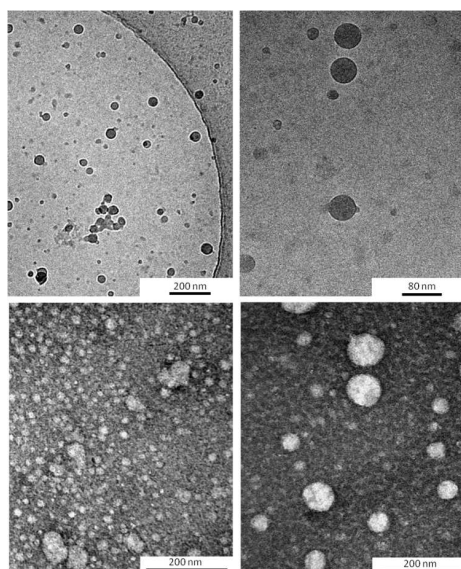
Figure 10. CryoTEM image (up panels) and TEM image (bottom panels) obtained with a water solution of **3** at a concentration of 10 mg/mL, i.e. well above its CAC.

Thus, a kinetic study was performed to further evaluate the effect of indoor light irradiation on the *E*-**3** solution in deuterated water. Specifically, two samples were prepared in two 5 mm NMR tubes and kept in the lab conditions, but one was kept carefully protected from the indoor light by using an aluminum film around the NMR tube. The results of these experiments supported the key role of the indoor visible light in triggering the photoisomerization process, which was not operative in the absence of light and led to an almost complete inversion of the configuration at the exocyclic carbon-carbon double bond after 17 weeks.

These observations confirmed that the compound *E*-**3** was susceptible of isomerizing in the ambient conditions and the isomerization process could be affected by environment features such as solvent[70,71] or, more interesting, the aggregation state[72,73] which can influence the energy barrier of the double bond interconversion.

Conclusion

In summary, we have designed a new generation of our LDMS, in which the structure of the original compound **HBDI-LP** has been manipulated. In particular, the chromophore conjugation was extended in the aim of shifting the absorption spectrum in the visible range, and a clickable azide group was introduced without altering the chromophore structure. The resulting

compounds **1**–**3** showed the expected photophysical features with an absorption tail spanning up to 550 nm in the visible range. Photoisomerization studies performed on **1** showed that the *Z* isomer composition of the PSS increases with the increase of the illumination wavelength, allowing the *E/Z* composition to be modulated in solution through alternative UV or blue light irradiation. TAS analysis revealed that the S_1 ESA decay is multiexponential with dominating time constants of 4 ps and 18 ps. We propose that the S_1 decay slows down while the S_1 population cools down, indicating the presence of an excited state energy barrier (or extended flat region) trapping the vibrationally relaxed S_1 subpopulation. This excited state dynamics is very different from that of the **HBDI-LP**, where the S_1 population decays on a the ps to sub-ps time scale, that is. before complete vibrational relaxation and cooling.[38]

Interestingly, compound **3** appeared to photoisomerize when exposed to the indoor visible light of our lab in a process affected by the solvent, being more pronounced in water than in methanol. This difference should be related to the solvent and aggregation features since **3** appeared to be molecularly dissolved in methanol, but strongly aggregated in water. In these aggregates, the amphiphilic oligo(ethylene glycol) chains-tails are probably located in the aggregate edge and exposed to the water environment, while the relatively hydrophobic chromophores would be preferentially located inside the core of the micelle. In this organization, the intermolecular H-bond interactions seen in the solid – state of compound **1** could be conserved and can lead to the formation oheterogeneousus supramolecular species governed by H-bonds in a hydrophobic shell stabilized by the well-know intermolecular π-stacked interactions derived from the 3-phenylbenzofulvene nucleus. These interactions established among the chromophores apparently affected the photoisomerization mechanism and efficiency. The nanostructured aggregates (i.e. spherical nano-particles) in water can represent an intermediate aggregation form of the chromophore that looks towards the well ordinate crystalline solid state and represents an interesting opportunity to characterize in depth the differences in photophysical and photochemical features between isolated molecules and aggre-gate species. The actual mechanism at the basis of this outstanding effect is at the present under computational and experimental investigations.

Experimental Section

X-ray crystallography: Single crystal of *E*-**1** was submitted to X-ray data collection on an Oxford-Diffraction Xcalibur Sapphire 3 diffractometer with a graphite monochromated Mo–Kα radiation ($\lambda = 0.71073$ Å) at 293 K. The structure was solved by direct methods implemented in SHELXS-97 program.[74] The refinement was carried out by full-matrix anisotropic least squares on F2 for all reflections for non-H atoms by means of the SHELXL program.[75]

Deposition Number 2071148 (for *E*-1) contain the supplementary crystallographic data for this paper. These data are provided free of charge by the joint Cambridge Crystallographic Data Centre and Fachinformationszentrum Karlsruhe Access Structures service.

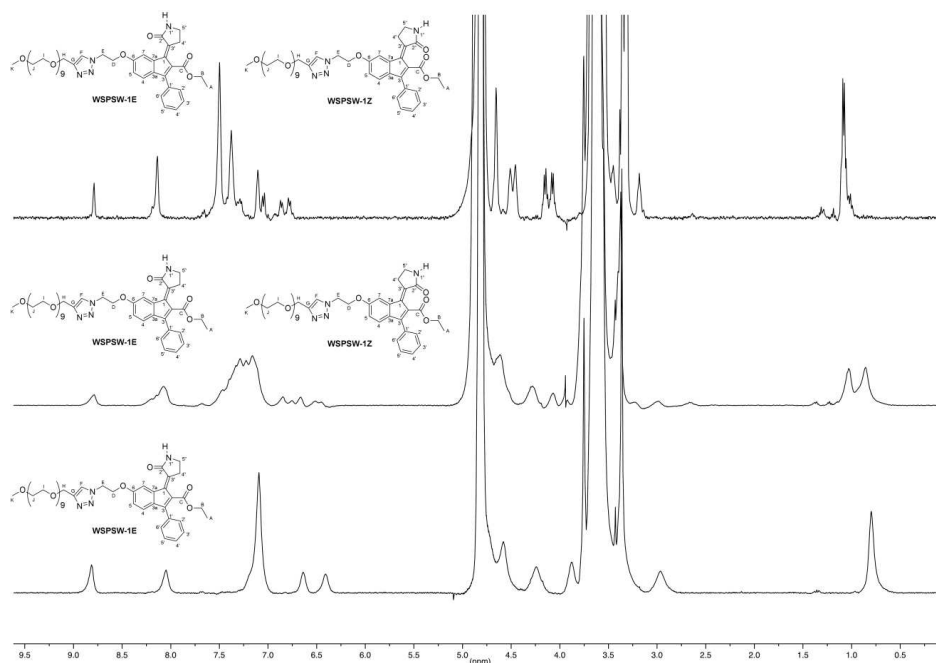**Figure 11.** Isomerization of compound *E*-3 in deuterated water at ambient conditions. Comparison of ¹H NMR spectrum (400 MHz) of *E*-3 in deuterated water (bottom trace) with that of the same solution obtained after four months storage at ambient conditions (middle trace). The top trace represents the spectrum obtained by addition of methanol to the water solution in order to break the aggregates; methanol was added immediately before of recording the spectrum.

Transient absorption (TA) spectroscopy: TA experiments were performed with an experimental set-up already described elsewhere[38,76,77] In short, an amplified Ti:Sa laser system (Amplitude) delivering 40 fs, 800 nm pulses at 5 kHz is used to pump a commercial optical parametric amplifier (TOPAS, Light conversion) followed by a frequency mixing stage in order to produce tunable pump pulses centered at $\lambda_{pu} = 290$ nm or $\lambda_{pu} = 450$ nm, with ~60 to 80 fs duration. A few µJ of the fundamental 800-nm pulse is used to generate a white light supercontinuum in CaF$_2$, used as a probe pulse in the 310–700 nm range. The pump-induced change of the sample absorbance ΔA is monitored by detecting the transmission of the probe pulse through the sample with a spectrograph offering a ~300-nm broad detection window. The data displayed in Figure 5 are the result of one experiment with $\lambda_{pu} = 450$ nm with the probing detection range tuned to $\lambda_{pr} = 360$–690 nm, and two experiments with $\lambda_{pu} = 290$ nm with probing detection windows of $\lambda_{pr} = 360$–690 nm and $\lambda_{pr} = 300$–400 nm (through UG11 color filter). Both datasets obtained with $\lambda_{pu} = 290$ nm are appended in one single dataset illustrated in Figure 5A. For each TA experiment performed on *E*-1 in solution, the same experiment is performed immediately after in the same conditions on the pure solvent in order to record and subtract solvent signal. In addition, the data displayed in Figure 5 panels A and B are also further processed to correct for the probe light dispersion (so-called chirp) which results in a wavelength-dependent time origin in the raw data (not shown).[78] Both datasets are analyzed independently via global analysis[79] consisting of singular value decomposition (data reduc-

tion) and global fit of the 3 dominating singular kinetic traces using a multiexponential decaying function convolved with a gaussian instrument response function (IRF), see for example ref [38, 77] for details about data analysis procedures. The result of the fit is displayed by plotting the decay-associated spectra (DAS) which reveal the spectral dependence of the amplitude associated to each decay time of the multiexponential function. Positive (resp. negative) DAS means decaying (resp. rising) TA signal at the corresponding wavelengths.

Quantum yield measurements: The *trans→cis* photoisomerization quantum yield ($\varphi_{trans \to cis}$) of compound **1** was evaluated by collecting the absorption spectra while irradiating the *trans* isomer in methanol (concentration 5×10^{-5} M) at 320 nm. Negligible modifications were observed in the spectra (suggesting that the change in absorbance is lower than 0.02) during the 2 h (7200 s) of irradiation. In particular, the transformation was followed at 282 nm, where the difference in the molar absorption coefficients of the *trans* and *cis* isomers is the largest ($\Delta \varepsilon \approx 11000$ M^{-1}cm^{-1}). The xenon lamp emitted intensity at 320 nm was measured by potassium ferrioxalate actinometry and found to be 2.2×10^{14} photons s^{-1}, corresponding to 3.65×10^{-10} Einstein s^{-1}. An estimate of the photoisomerization quantum yield ($\varphi_{trans \to cis} < 7 \times 10^{-4}$) was obtained according to the following equation:

$$\phi = \frac{mol\ photoproduct}{mol\ photons}$$

$$< \frac{\frac{0.02}{11000\ M^{-1}cm^{-1} \times 1\ cm} \times 10^{-3}L}{3.65 \times 10^{-10}\ Einstein\ s^{-1} \times 7200\ s} = 6.9 \times 10^{-4}$$

Determination of CAC values by fluorescence analysis: A stock solution of pyrene (6.0×10^{-5} M in acetone) was prepared and then aliquots of 5 µL were placed into vials and evaporated to remove acetone in an orbital shaker at 37 °C. Subsequently, 0.5 mL of compound **3** solution in bidistilled water, at concentrations ranging from 1×10^{-5} to 10 mg/mL were added to the pyrene residue; the final concentration of pyrene was 6.0×10^{-7} M in each sample. The solutions were kept at 37 °C for 24 h under continuous stirring to equilibrate pyrene with micelles. Pyrene emission spectra were recorded at 37 °C using an excitation wavelength of 333 nm. The CAC of the compound was calculated by plotting the I_{373}/I_{384} (I_1/I_3) ratio, obtained from the emission spectra recorded at 37 °C, versus the logarithm of the compound concentration.

DLS measurements: DLS measurements were performed at 25 °C using a Malvern Zetasizer NanoZS instrument, fitted with a 532 nm laser at a fixed scattering angle of 173° with dispersions of **3** in bidistilled water.

Transmission electron microscopy (TEM) experiments: A drop of 3.5 µL of **3** solution in water was dropped onto a 300 mesh formvar-coated copper grid. After 2 min, the excess of sample was blotted by filter paper and the grids were stained with 1% of aqueous uranyl acetate solution. Samples were observed in a FEI Tecnai G2 Spirit transmission electron microscopy at an acceleration voltage of 100 kV.

Cryo-transmission electron microscopy (CryoTEM) experiments: Vitrified specimens were prepared by adding 2.5 µL of compound 3 solution (10 mg/mL) to freshly plasma cleaned QUANTIFOIL®R 2/1 300-mesh copper grids. A Vitrobot Mark IV (FEI) with 100% humidity at 20 °C, a blot time of 3 s, the blot force set to −3, and a wait time of 2 s, was used to plunge freeze the grids in liquid ethane. The images were collected on CM 200 FEG (Philips) operating at 200 kV, equipped with a TVIPS F224HD CCD camera using TVIPS EM-Menu software for image acquisition.

Acknowledgements

Conflict of Interest

The authors declare no conflict of interest.

Data Availability Statement

The data that support the findings of this study are available from the corresponding author upon reasonable request.

[1] B. L. Feringa, N. Koumura, R. A. Van Delden, M. K. J. Ter Wiel, *Appl. Phys. A* **2002**, *75*, 301–308.
[2] M. Baroncini, S. Silvi, A. Credi, *Chem. Rev.* **2020**, *120*, 200–268.
[3] K. Inoue, S. Ito, Y. Kato, Y. Nomura, M. Shibata, T. Uchihashi, S. P. Tsunoda, H. Kandori, *Nat. Commun.* **2016**, *7*, 13415.
[4] N. AzimiHashemi, K. Erbguth, A. Vogt, T. Riemensperger, E. Rauch, D. Woodmansee, J. Nagpal, M. Brauner, M. Sheves, A. Fiala, L. Kattner, D. Trauner, P. Hegemann, A. Gottschalk, J. F. Liewald, *Nat. Commun.* **2014**, *5*, 5810.
[5] K. Pagano, M. Paolino, S. Fusi, V. Zanirato, C. Trapella, G. Giuliani, A. Cappelli, S. Zanzoni, H. Molinari, L. Ragona, M. Olivucci, *J. Phys. Chem. Lett.* **2019**, *10*, 2235–2243.
[6] M. Ui, Y. Miyauchi, M. Inoue, M. Murakami, Y. Araki, T. Wada, K. Kinbara, *ChemPhotoChem* **2019**, *3*, 356–360.
[7] S. L. Oscurato, M. Salvatore, P. Maddalena, A. Ambrosio, *Nat. Photonics* **2018**, *7*, 1387–1422.
[8] X. Liang, H. Nishioka, N. Takenaka, H. Asanuma, *ChemBioChem* **2008**, *9*, 702–705.
[9] C. Li, A. Iscen, L. C. Palmer, G. C. Schatz, S. I. Stupp, *J. Am. Chem. Soc.* **2020**, *142*, 8447–8453.
[10] W. Francis, A. Dunne, C. Delaney, L. Florea, D. Diamond, *Sens. Actuators B* **2017**, *250*, 608–616.
[11] R. E. Dawson, S. F. Lincoln, C. J. Easton, *Chem. Commun.* **2008**, *34*, 3980–3982.
[12] Z. Li, C. He, Z. Lu, P. Li, Y.-P. Zhu, *Dyes Pigm.* **2020**, *182*, 108623.
[13] C. Petermayer, H. Dube, *Acc. Chem. Res.* **2018**, *51*, 1153–1163.
[14] J. M. Abendroth, O. S. Bushuyev, P. S. Weiss, C. J. Barrett, *ACS Nano* **2015**, *9*, 7746–7768.
[15] V. García-López, F. Chen, L. G. Nilewski, G. Duret, A. Aliyan, A. B. Kolomeisky, J. T. Robinson, G. Wang, R. Pal, J. M. Tour, *Nature* **2017**, *548*, 567–572.
[16] P. She, Y. Qin, X. Wang, Q. Zhang, *Adv. Mater.* **2021**, *34*, 2101175.
[17] F. Yu, W. Liu, B. Li, D. Tian, J.-L. Zuo, Q. Zhang, *Angew. Chem. Int. Ed.* **2019**, *58*, 16101–16104; *Angew. Chem. Int. Ed.* **2019**, *131*, 16247–16250.
[18] D. Roke, S. J. Wezenberg, B. L. Feringa, *Proc. Nat. Acad. Sci.* **2018**, *115*, 9423–9431.
[19] W. R. Browne, B. L. Feringa, *Nat. Nanotechnol.* **2006**, *1*, 25–35.
[20] J. Bauer, L. Hou, J. C. M. Kistemaker, B. L. Feringa, *J. Org. Chem.* **2014**, *79*, 4446–4455.
[21] J. Vicario, A. Meetsma, B. L. Feringa, *Chem. Commun.* **2005**, *47*, 5910–5912.
[22] D. Roke, M. Sen, W. Danowski, S. J. Wezenberg, B. L. Feringa, *J. Am. Chem. Soc.* **2019**, *141*, 7622–7627.
[23] J. Sun, Y. Wu, Z. Liu, D. Cao, Y. Wang, C. Cheng, D. Chen, M. R. Wasielewski, J. F. Stoddart, *J. Phys. Chem. A* **2015**, *119*, 6317–6325.
[24] M. Filatov, M. Paolino, S. K. Min, C. H. Choi, *Chem. Commun.* **2019**, *55*, 5247–5250.
[25] J. Conyard, A. Cnossen, W. R. Browne, B. L. Feringa, S. R. Meech, *J. Am. Chem. Soc.* **2014**, *136*, 9692–9700.
[26] C. T. Kornman, L. Li, A. O. Weldeab, I. Ghiviriga, K. A. Abboud, R. K. Castellano, *Chem. Sci.* **2020**, *11*, 10190–10197.
[27] W. A. Velema, M. J. Hansen, M. M. Lerch, A. J. M. Driessen, W. Szymanski, B. L. Feringa, *Bioconjugate Chem.* **2015**, *26*, 2592–2597.
[28] G. Marchand, J. Eng, I. Schapiro, A. Valentini, L. M. Frutos, E. Pieri, M. Olivucci, J. Léonard, E. Gindensperger, *J. Phys. Chem. Lett.* **2015**, *6*, 599–604.
[29] M. Filatov, M. Paolino, S. K. Min, K. S. Kim, *J. Phys. Chem. Lett.* **2018**, *9*, 4995–5001.
[30] S. Grunder, P. L. McGrier, A. C. Whalley, M. M. Boyle, C. Stern, J. F. Stoddart, *J. Am. Chem. Soc.* **2013**, *135*, 17691–17694.

61

[31] C. Özçoban, T. Halbritter, S. Steinwand, L.-M. Herzig, J. Kohl-Landgraf, N. Askari, F. Groher, B. Fürtig, C. Richter, H. Schwalbe, B. Suess, J. Wachtveitl, A. Heckel, *Org. Lett.* **2015**, *17*, 1517–1520.

[32] S. Ludwanowski, M. Ari, K. Parison, S. Kalthoum, P. Straub, N. Pompe, S. Weber, M. Walter, A. Walther, *Chem. A Eur. J.* **2020**, *26*, 13203–13212.

[33] R. Rossi Paccani, D. Donati, S. Fusi, L. Latterini, G. Farina, V. Zanirato, M. Olivucci, *J. Org. Chem.* **2012**, *77*, 1738–1748.

[34] J. Léonard, I. Schapiro, J. Briand, S. Fusi, R. R. Paccani, M. Olivucci, S. Haacke, *Chem. A Eur. J.* **2012**, *18*, 15296–15304.

[35] M. Gueye, M. Paolino, E. Gindensperger, S. Haacke, M. Olivucci, J. Léonard, *Faraday Discuss.* **2020**, *221*, 299–321.

[36] M. Gueye, M. Manathunga, D. Agathangelou, Y. Orozco, M. Paolino, S. Fusi, S. Haacke, M. Olivucci, J. Léonard, *Nat. Commun.* **2018**, *9*, 313.

[37] I. Schapiro, M. Gueye, M. Paolino, S. Fusi, G. Marchand, S. Haacke, M. E. Martin, M. Huntress, V. P. Vysotskiy, V. Veryazov, J. Léonard, M. Olivucci, *Photochem. Photobiol. Sci.* **2019**, *18*, 2259–2269.

[38] M. Paolino, M. Gueye, E. Pieri, M. Manathunga, S. Fusi, A. Cappelli, L. Latterini, D. Pannacci, M. Filatov, J. Léonard, M. Olivucci, *J. Am. Chem. Soc.* **2016**, *138*, 9807–9825.

[39] M. Paolino, T. Giovannini, M. Manathunga, L. Latterini, G. Zampini, R. Pierron, J. Léonard, S. Fusi, G. Giorgi, G. Giuliani, A. Cappelli, C. Cappelli, M. Olivucci, *J. Phys. Chem. Lett.* **2021**, *12*, 3875–3884.

[40] A. Cappelli, M. Paolino, P. Anzini, G. Giuliani, S. Valenti, M. Aggravi, A. Donati, R. Mendichi, L. Zetta, A. C. Boccia, F. Bertini, F. Samperi, S. Battiato, E. Paccagnini, S. Vomero, *J. Polym. Sci. Part A* **2010**, *48*, 2446–2461.

[41] A. Cappelli, G. Grisci, M. Paolino, F. Castriconi, G. Giuliani, A. Donati, S. Lamponi, R. Mendichi, A. C. Boccia, F. Samperi, S. Battiato, E. Paccagnini, M. Gentile, M. Licciardi, G. Giammona, S. Vomero, *Chem. A Eur. J.* **2013**, *19*, 9710–9721.

[42] A. Cappelli, M. Paolino, G. Grisci, G. Giuliani, A. Donati, A. C. Boccia, F. Samperi, R. Mendichi, S. Vomero, in *π-Stacked Polym. Mol.* (Ed.: T. Nakano), Springer Japan, Japan: Osaka, **2014**, pp. 51–149.

[43] M. Paolino, G. Grisci, A. Reale, V. Razzano, G. Giuliani, A. Donati, R. Mendichi, D. Piovani, A. C. Boccia, A. Grillo, G. Giorgi, A. Cappelli, *Polymers (Basel)*. **2018**, *10*, 752.

[44] A. Cappelli, M. Paolino, G. Grisci, G. Giuliani, A. Donati, R. Mendichi, A. C. Boccia, C. Botta, W. Mróz, F. Samperi, A. Scamporrino, G. Giorgi, S. Vomero, *J. Mater. Chem.* **2012**, *22*, 9611.

[45] A. Cappelli, S. Galeazzi, G. Giuliani, M. Anzini, A. Donati, L. Zetta, R. Mendichi, M. Aggravi, G. Giorgi, E. Paccagnini, S. Vomero, *Macromolecules* **2007**, *40*, 3005–3014.

[46] F. Villafiorita-Monteleone, A. Cappelli, M. Paolino, M. Colombo, E. Cariati, A. Mura, G. Bongiovanni, C. Botta, *J. Phys. Chem. C* **2015**, *119*, 18986–18991.

[47] F. Villafiorita-Monteleone, E. Kozma, M. Pasini, M. Paolino, A. Cappelli, G. Bongiovanni, A. Mura, C. Botta, *Appl. Phys. Lett.* **2017**, *110*, 183301.

[48] A. Cappelli, F. Villafiorita-Monteleone, G. Grisci, M. Paolino, V. Razzano, G. Fabio, G. Giuliani, A. Donati, R. Mendichi, A. C. Boccia, M. Pasini, C. Botta, *J. Mater. Chem. C* **2014**, *2*, 7897–7905.

[49] W. Mróz, F. Villafiorita-Monteleone, M. Pasini, G. Grisci, M. Paolino, V. Razzano, A. Cappelli, C. Botta, *Mater. Lett.* **2015**, *142*, 197–200.

[50] F. Villafiorita-Monteleone, E. Kozma, U. Giovanella, M. Catellani, M. Paolino, V. Collico, M. Colombo, A. Cappelli, C. Botta, *Dyes Pigm.* **2018**, *149*, 331–335.

[51] A. Cappelli, V. Razzano, G. Fabio, M. Paolino, G. Grisci, G. Giuliani, A. Donati, R. Mendichi, W. Mróz, F. Villafiorita-Monteleone, C. Botta, *RSC Adv.* **2015**, *5*, 101377–101385.

[52] A. Cappelli, G. Grisci, M. Paolino, V. Razzano, G. Giuliani, A. Donati, C. Bonechi, R. Mendichi, A. C. Boccia, M. Licciardi, C. Scialabba, G. Giammona, S. Vomero, *J. Mater. Chem. B* **2015**, *3*, 361–374.

[53] A. Cappelli, M. Paolino, G. Grisci, V. Razzano, G. Giuliani, A. Donati, C. Bonechi, R. Mendichi, S. Battiato, F. Samperi, C. Scialabba, G. Giammona, F. Makovec, M. Licciardi, *Polym. Chem.* **2016**, *7*, 6529–6544.

[54] A. Cappelli, M. Paolino, G. Grisci, G. Giuliani, A. Donati, R. Mendichi, A. C. Boccia, F. Samperi, S. Battiato, E. Paccagnini, E. Giacomello, V. Sorrentino, M. Licciardi, G. Giammona, S. Vomero, *Polym. Chem.* **2011**, *2*, 2518–2527.

[55] M. Licciardi, G. Amato, A. Cappelli, M. Paolino, G. Giuliani, B. Belmonte, C. Guarnotta, G. Pitarresi, G. Giammona, *Int. J. Pharm.* **2012**, *438*, 279–286.

[56] A. Cappelli, V. Razzano, M. Paolino, G. Grisci, G. Giuliani, A. Donati, R. Mendichi, F. Samperi, S. Battiato, A. C. Boccia, A. Mura, G. Bongiovanni, W. Mróz, C. Botta, *Polym. Chem.* **2015**, *6*, 7377–7388.

[57] M. Paolino, G. Grisci, G. Giuliani, I. Zanardi, M. Andreassi, V. Travagli, M. Licciardi, C. Scialabba, G. Giammona, A. Cappelli, S. Vomero, *J. Drug Delivery Sci. Technol.* **2016**, *32*, 142–166.

[58] M. Licciardi, C. Scialabba, G. Giammona, M. Paolino, V. Razzano, G. Grisci, G. Giuliani, F. Makovec, A. Cappelli, *J. Nanopart. Res.* **2017**, *19*, 197.

[59] M. Paolino, G. Grisci, F. Castriconi, A. Reale, G. Giuliani, A. Donati, C. Bonechi, G. Giorgi, R. Mendichi, D. Piovani, A. C. Boccia, M. Canetti, F. Samperi, S. Dattilo, C. Scialabba, M. Licciardi, E. Paccagnini, M. Gentile, A. Cappelli, *Pharmaceutica* **2018**, *10*, 234.

[60] F. Fabrizi de Biani, A. Reale, V. Razzano, M. Paolino, G. Giuliani, A. Donati, G. Giorgi, W. Mróz, D. Piovani, C. Botta, A. Cappelli, *RSC Adv.* **2018**, *8*, 10836–10847.

[61] A. Cappelli, S. Galeazzi, G. Giuliani, M. Anzini, M. Grassi, R. Lapasin, G. Grassi, R. Farra, B. Dapas, M. Aggravi, A. Donati, L. Zetta, A. C. Boccia, F. Bertini, F. Samperi, S. Vomero, *Macromolecules* **2009**, *42*, 2368–2378.

[62] M. Paolino, A. Reale, V. Razzano, G. Giuliani, A. Donati, G. Giorgi, C. A. Boccia, R. Mendichi, D. Piovani, C. Botta, L. Salvini, F. Samperi, C. Savoca, M. Licciardi, E. Paccagnini, M. Gentile, A. Cappelli, *Pharmaceutica* **2019**, *11*, 444.

[63] M. Paolino, A. Reale, G. Magrini, V. Razzano, G. Giuliani, A. Donati, G. Giorgi, F. Samperi, M. Canetti, M. Mauro, F. Villafiorita-Monteleone, E. Fois, C. Botta, A. Cappelli, *Eur. Polym. J.* **2020**, *137*, 109923.

[64] M. Paolino, A. Reale, G. Magrini, V. Razzano, M. Saletti, G. Giuliani, A. Donati, F. Samperi, A. Scamporrino, M. Canetti, M. Mauro, F. Villafiorita-Monteleone, E. Fois, C. Botta, A. Cappelli, *Eur. Polym. J.* **2021**, *156*, 110597.

[65] M. Paolino, M. Saletti, A. Reale, V. Razzano, G. Giuliani, A. Donati, C. Bonechi, G. Giorgi, A. Atrei, M. Mauro, A. Scamporrino, F. Samperi, E. Fois, G. Tabacchi, C. Botta, A. Cappelli, *Eur. Polym. J.* **2022**, *169*, 111137.

[66] R. Shen, X. Shen, Z. Zhang, Y. Li, S. Liu, H. Liu, *J. Am. Chem. Soc.* **2010**, *132*, 8627–8634.

[67] G. Tassone, M. Paolino, C. Pozzi, A. Reale, L. Salvini, G. Giorgi, M. Orlandini, F. Galvagni, S. Mangani, X. Yang, B. Carlotti, F. Ortica, L. Latterini, M. Olivucci, A. Cappelli, *ChemBioChem* **2022**, *23*, e202100449.

[68] M. Paolino, A. Reale, V. Razzano, G. Giorgi, G. Giuliani, F. Villafiorita-Monteleone, C. Botta, C. Coppola, A. Sinicropi, A. Cappelli, *New J. Chem.* **2020**, *44*, 13644–13653.

[69] M. Paolino, A. Reale, V. Razzano, G. Giuliani, A. Donati, C. Bonechi, G. Caselli, M. Visintin, F. Makovec, C. Scialabba, M. Licciardi, E. Paccagnini, M. Gentile, L. Salvini, F. Tavanti, M. C. Menziani, A. Cappelli, *New J. Chem.* **2019**, *43*, 6834–6837.

[70] F. Serra, E. M. Terentjev, *Macromolecules* **2008**, *41*, 981–986.

[71] J. C. Corchado, M. L. Sánchez, I. Fdez Galván, M. E. Martín, A. Muñoz-Losa, R. Barata-Morgado, M. A. Aguilar, *J. Phys. Chem. B* **2014**, *118*, 12518–12530.

[72] H. Qian, Y.-Y. Wang, D.-S. Guo, I. Aprahamian, *J. Am. Chem. Soc.* **2017**, *139*, 1037–1040.

[73] Z. Chu, Y. Han, T. Bian, S. De, P. Král, R. Klajn, *J. Am. Chem. Soc.* **2019**, *141*, 1949–1960.

[74] G. M. Sheldrick, *Acta Crystallogr. Sect. A* **2008**, *64*, 112–122.

[75] G. M. Sheldrick, *Acta Crystallogr. Sect. C* **2015**, *71*, 3–8.

[76] J. Briand, O. Braem, J. Rehault, J. Leonard, A. Cannizzo, M. Chergui, V. Zanirato, M. Olivucci, J. Helbing, S. Haacke, *Phys. Chem. Chem. Phys.* **2010**, *12*, 3178–3187.

[77] A. I. Skilitsi, D. Agathangelou, I. Shulov, J. Conyard, S. Haacke, Y. Mély, A. Klymchenko, J. Léonard, *Phys. Chem. Chem. Phys.* **2018**, *20*, 7885–7895.

[78] S. Kovalenko, A. Dobryakov, J. Ruthmann, N. Ernsting, *Phys. Rev. A* **1999**, *59*, 2369–2384.

[79] I. H. M. Van Stokkum, D. S. Larsen, R. Van Grondelle, *Biochim. Biophys. Acta Bioenerg.* **2004**, *1657*, 82–104.

Chapter 4

Hyaluronan-based Graft Copolymers for the development of biocompatible materials useful in the pharmaceutical field

4.1. Hyaluronic Acid (HA): an overview.

Since the early *1880s*, when the scientist Portes observed that mucin from the vitreous body differs from other mucoids in cornea and cartilage and named it *"hyalomucine"*, the nonsulfated glycosaminoglycan hyaluronic acid (HA), also called hyaluronan or hyaluronate, has been widely studied. During the second half of the *20th Century*, the progressive understanding of HA's biological functions determined an increasing interest in its production and development in the biomedical field. Nowadays, HA represents a *key* molecule to formulate drug delivery systems and it is still being studied to clarify its biosynthetic pathways, optimize its biotechnological production, and synthesize derivatives with enhanced properties.[1] Chemically, HA is characterized by a non-branched polysaccharide chain, obtained by the condensation of disaccharide units. Each unit is made up of an uronic sugar, *glucuronic acid*, and an amino sugar such as *N-acetylglucosamine*, alternatively linked by β_{1-4} and β_{1-3} glycosidic bonds and intramolecular hydrogen bonds, which stabilize the conformations. At physiological pH, the chemical structure of HA presents ionized carboxyl groups. For this reason, it shows high polarity and, consequently, high solubility in water, so it can absorb large amounts of water, reaching a high degree of hydration. Furthermore, HA constitutes the extracellular matrix (ECM), and it is implicated in the early stages of cell adhesion by interacting with CD44 receptors (Figure 4.1), which is a multifunctional transmembrane glycoprotein diffused in almost all human cell types.
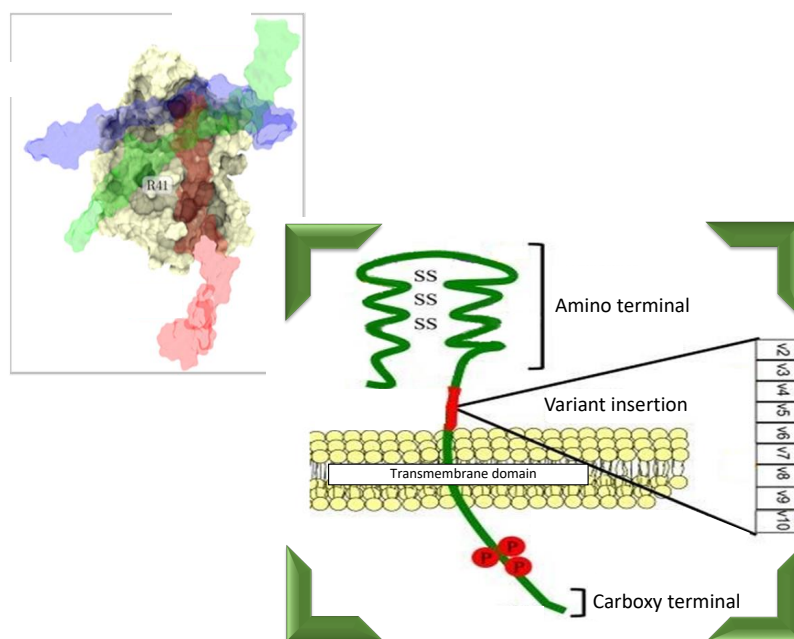

Figure 4.1. Schematic representation of the transmembrane receptor CD44.[2]

Thanks to its physicochemical (e. g. intrinsic viscosity and chain stiffness) and biological properties (e. g. interactions with proteins and receptors using specific complementary binding domains), HA plays a wide range of important roles in the human body such as joint lubrication, maintenance of tissue hydration, cell adhesion, migration and differentiation, morphogenesis, and tissue repair.[3] The biological functions of HA are closely affected by its molecular weight and size. In particular, high molecular weight hyaluronan polymers (Mw > 500 kDa) are used as space-filling, antiangiogenic, and immunosuppressive; medium molar mass hyaluronan chains (ranging from 20 to 200 kDa) are involved in ovulation, embryogenesis, and wound repair; oligosaccharides composed of 15–50 repeating disaccharide units (6 - 20 kDa) are inflammatory, immuno-stimulatory, and angiogenic while small oligomers (ranging from 400 to 4000 Da) are anti-apoptotic and inducers of heat shock proteins.[4]

Due to its biocompatibility and remarkable viscoelasticity, HA and its derivatives represent interesting biomaterials for biomedical applications. In dermatology and surgery, HA (or rather its water-soluble sodium salt) is the main component of facial fillers, used to shrink wrinkles and prevent skin aging. The progressive loss of hydration and elasticity of the skin with aging is due to the decrease in the availability of HA in adult tissues, so anti-aging HA is widely applied in cosmetics to restore the physiological microenvironment typical of youthful skin. In ophthalmic care, HA is the active pharmaceutical ingredient (API) of artificial eye drops and it finds application during ophthalmic interventions on the vitreous body. HA is also extensively used as a lubricant to preserve the synovial fluid of the joints and is applied against inflammation and ulcerative lesions of the mouth, particularly post-surgical chemotherapy incision, immediately reducing pain and promoting wound healing. Moreover, viscosupplementation of HA represents an approach to treat osteoarticular diseases and slow down the progression of this pathology.[1]

To improve and customize its properties and applications, the native structure of HA can undergo chemical manipulations such as conjugation and cross-linking to obtain new biocompatible and biodegradable materials for drug delivery and tissue engineering. These chemical modifications involve esterification, amidation, or etherification of the carboxyl group of glucuronic acid, primary and secondary hydroxyl groups, and the N-acetyl group (after deamidation). The addition and condensation of cross-linking agents have led to HA-based materials capable of supplying hydrogels. Cross-linking technique

is particularly exploited to improve HA's rheological and swelling properties and reduce its degradation rate. However, toxic chemicals used in the synthetic pathways may preclude the biomedical applications of HA hydrogels. Therefore, developing environmentally safe strategies compatible with industrial processes appears pivotal.[5]
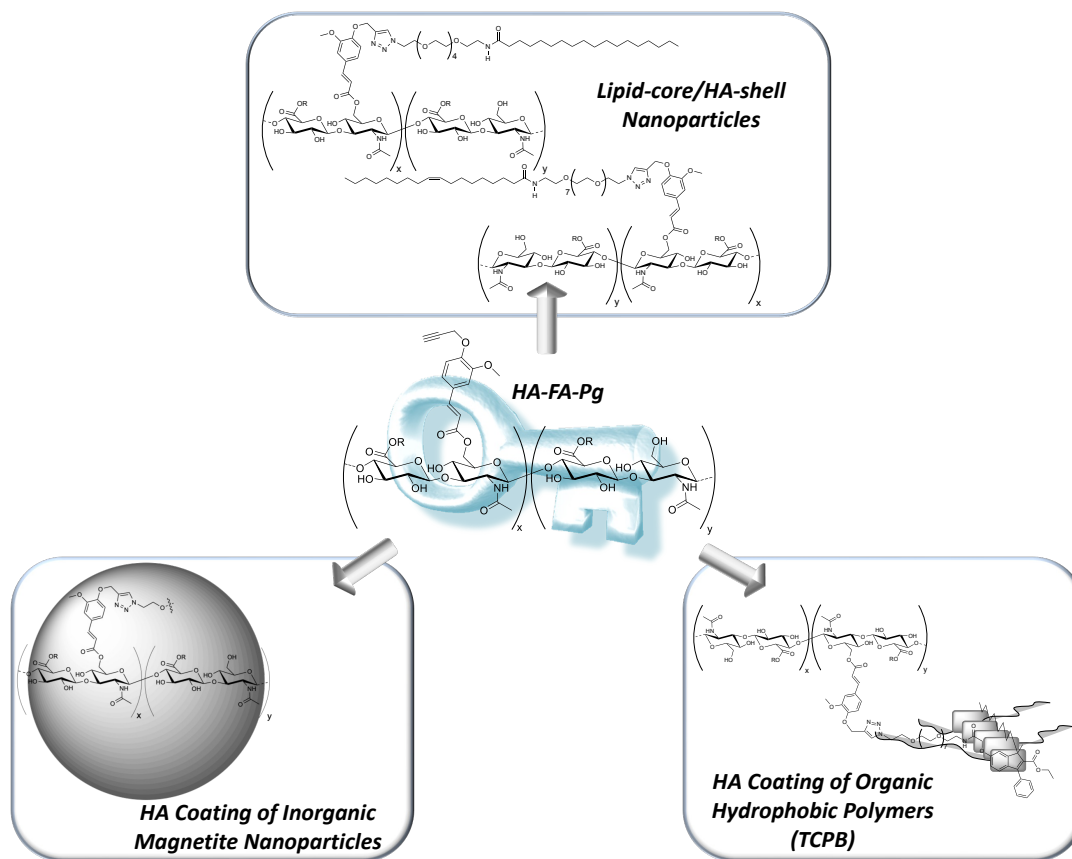
4.2. Hyaluronan-based Graft Copolymers.

The research group of Prof. Cappelli has developed a synthetic procedure to transform HA into an **HA-FA** copolymer, combining the outstanding properties of two natural compounds, hyaluronic acid and ferulic acid (FA).[6,7] The latter is a cinnamic acid derivative (i. e. 4-hydroxy-3-methoxycinnamic acid) with a powerful antioxidant activity since it is a free radical scavenger and an inhibitor of enzymes that catalyze free radical generation. It is allocated in the plant cell wall and its residues are incorporated employing an ester bond to the primary alcoholic function of arabinose side chains in the cell wall arabinoxylan polysaccharides, where it is implicated in cross-linking polysaccharides and proteins during cell wall synthesis.[8] It also possesses a large variety of physiological functions ranging from anti-inflammatory activity to antidiabetic effect.

To obtain **HA-FA** graft copolymers of interest, the grafting procedure was optimized using a derivative of the ferulic acid functionalized with a propargyl group to introduce "*clickable*" propargyl groups into the hyaluronic acid chain, which is suitable for the subsequent *click-chemistry* reaction, a Copper(I)-Catalyzed Alkyne-Azide 1,3-dipolar Cycloaddition (CuAAC). This synthetic procedure was first exploited using low molar mass value HA (i. e. Mw = 8.7 kDa) to give grafted copolymers **HA-FA-Pg** with a variable grafting degree, ranging from 10% to 35%. These copolymers have been characterized and used as materials for the development of technological platforms to cover different surfaces and obtain a biocompatible and biomimetic hyaluronic coating (BBHC). This strategy was employed in the covalent coating of polybenzofulvene cylindrical brush surface, using **HA-FA-Pg** graft copolymers, obtaining the tri-component polymer brush (TCPB). These compounds have shown interesting properties as Doxorubicin transport systems to tumor cells due to their active targeting generated by the interaction of the hyaluronic acid coating with the overexpressed CD44 receptors in cancer cells.[9,10] Subsequently, this approach was gradually transformed into a technology platform, which was applied to coating the surfaces of different nanostructures ranging from small unilamellar vesicles (SUV)[11] to magnetic nanoparticles (NP). In this last case,

the core of TCPB has also been replaced with inorganic NP based on magnetite (Fe_3O_4)[12] to realize a peculiar system able to respond to the magnetic field and potentially useful in therapeutic and diagnostic applications (Figure 4.2).

Figure 4.2. Coating technology based on hyaluronan graft copolymers bearing propargylated ferulate fluorophores (**HA-FA-Pg**).

4.3.1. Novel polymeric nanomaterials: dendrimers.

The expression dendrimer is derived from the Greek term "*dendron*" which means "tree", inspired by their typical structure with several branching units. Dendrimers are three-dimensional globular macromolecular entities characterized by a nanometric size range (1-100 nm), a highly branched architecture, a great degree of symmetry, and monodispersity. Thanks to these relevant features, dendrimers are presented as ideal "*hosts*" for small molecules ("*guests*") in the development of original polymeric nanomaterials for drug delivery. Since the 1970s, dendrimers have aroused a great interest in organic chemistry. These molecules were first discovered by Fritz Vogtle in 1978,

followed by Donald Tomalia and coworkers who studied and developed poly(amidoamine) (PAMAM) dendrimers. Later, Newkome carefully investigated "*arborol dendrimers*", followed by poly(propylene imine) dendrimers, also called PPI, and polyether dendrimers (Figure 4.3).[13]
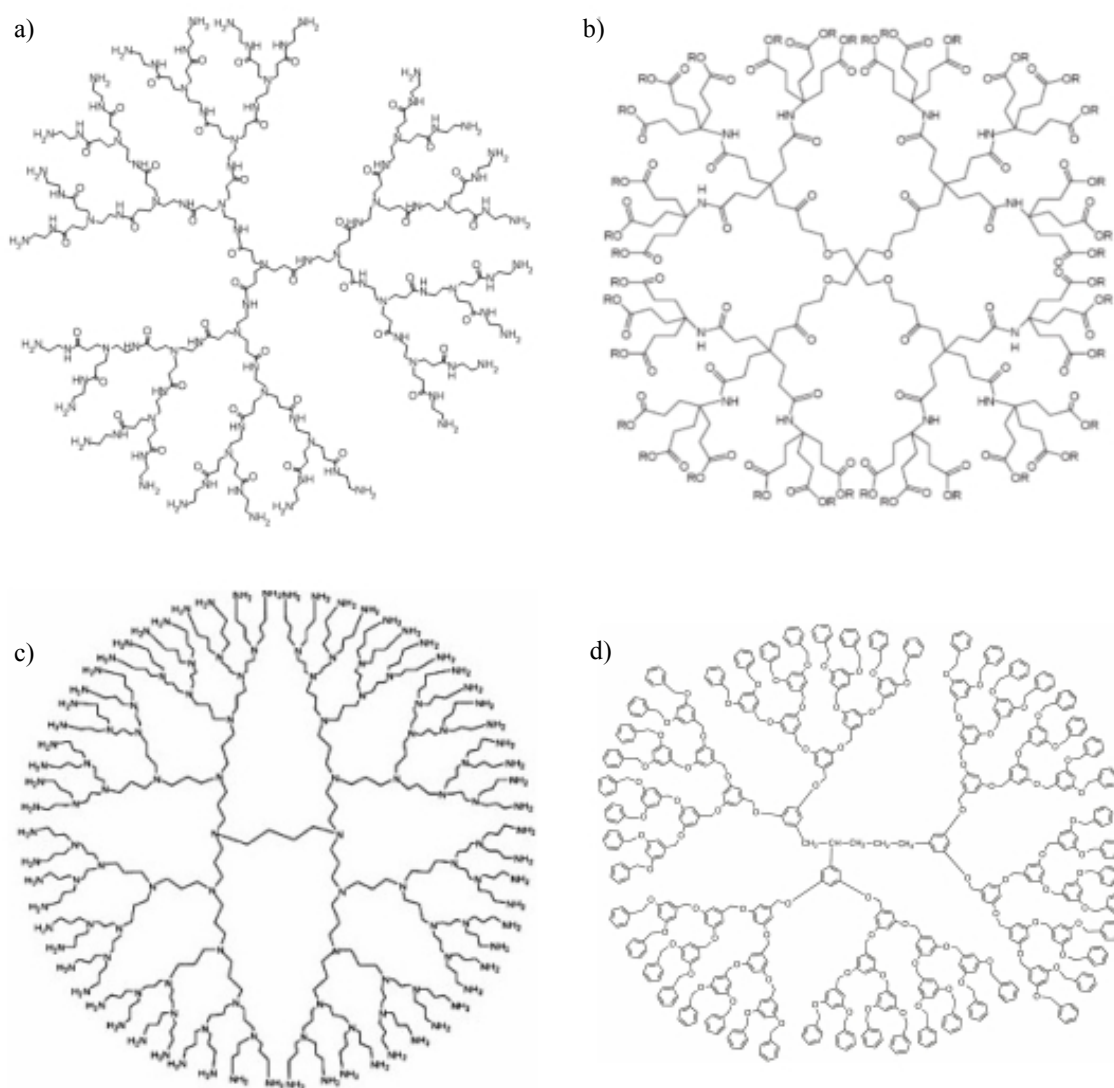
Figure 4.3. (a) poly(amidoamine) dendrimer (PAMAM); (b) Newkome's dendrimer; (c) poly(propylene imine) dendrimer (PPI); (d) polyether dendrimer.

Concerning their chemical structure, dendrimers are characterized by three *key portions*: the "*core*" or initiator center, a central area that contains the secondary branches starting from the core, and an external surface where the functionalizable terminal groups are located (Figure 4.4).
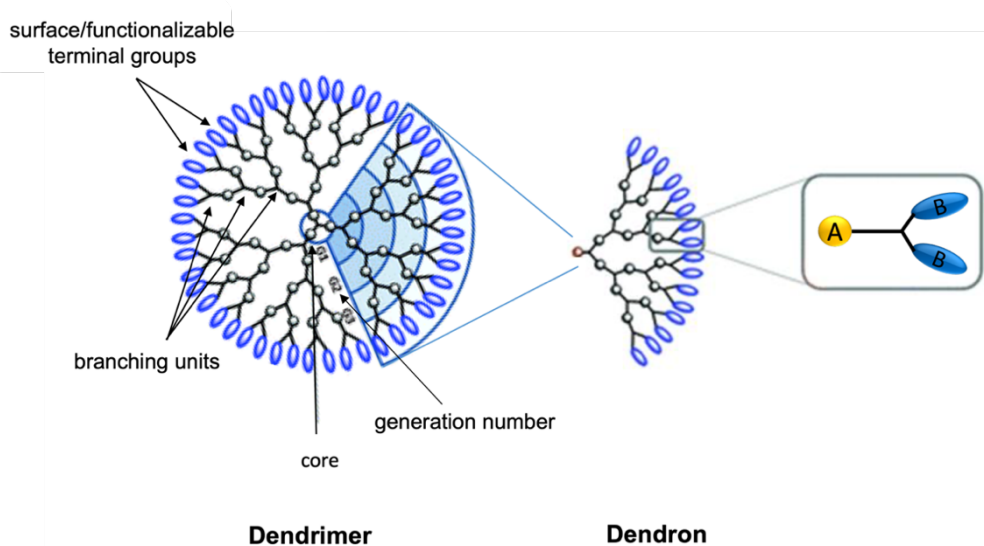
Figure 4.4. Structural schematic representation of a generic dendrimer.[14]

The core is crucial in characterizing the final structure because it affects the shape, size, and multiplicity of the dendrimer. The intermediate zone is characterized by symmetrical branching, which gives peculiar physicochemical properties and influences the presence of free internal volume capable of host molecules.[15] The number of focal points (branch points) that can be observed from the core to the periphery of dendrimers represents the generation number. With increasing generations, dendrimers tend to linearly increase in diameter and adopt a globular shape.

4.3.2. Physicochemical properties and synthetic strategies.

Dendrimers are similar in size to several biological structures, for example, 5.0 G PAMAM dendrimers are approximately the same size and shape as Hemoglobin (Hb) (5.5 nm diameter).[16] Due to their molecular architecture, dendrimers exhibit better physical and chemical properties than traditional linear polymers. In solution, linear chains exhibit remarkable flexibility, while dendrimers organize themselves to form a sphere, which greatly impacts their rheological properties. In addition, the dendrimer solutions show a significantly lower viscosity than linear polymer solutions. When the molecular weight of dendrimers increases, their intrinsic viscosity passes through a maximum and then begins to decrease, unlike linear polymers (e. g. Polystyrene) in which the intrinsic viscosity increases with increasing molecular weight (Figure 4.5). This is due

to the reduction of space between the branches with rising generation results of growth globular-type and non-linear-type.[17]
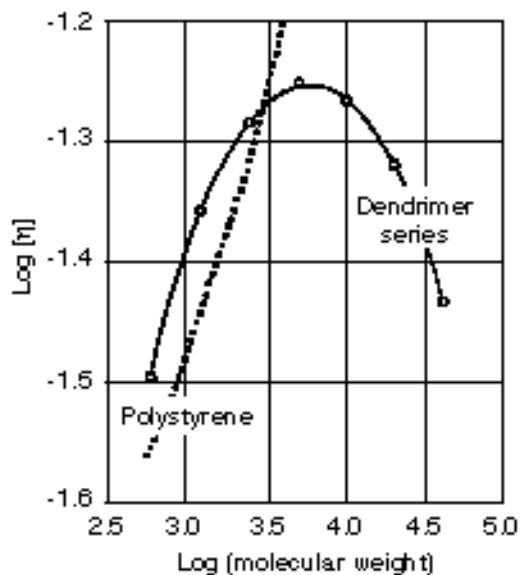
Figure 4.5. Comparison between the intrinsic viscosity of a linear polymer (e. g. Polystyrene) and dendrimer series.[17]

Additionally, in linear polymers the polymerization degree is random, and the synthetic process gives heterogeneous macromolecules. On the contrary, the dimension and molecular weight of dendrimers can be easily controlled during synthesis. Furthermore, the synthesis of dendrimers offers the opportunity to generate desired macromolecular structures by using traditional organic reagents, such as ethylenediamine and alkyl acrylates, in an iterative sequence of reactions in which each repetition step results in a new generation. The synthetic pathway can proceed from the core to the periphery (the divergent method, Figure 4.6A)[18] or from the periphery to the core (the convergent method, Figure 4.6B).[19]
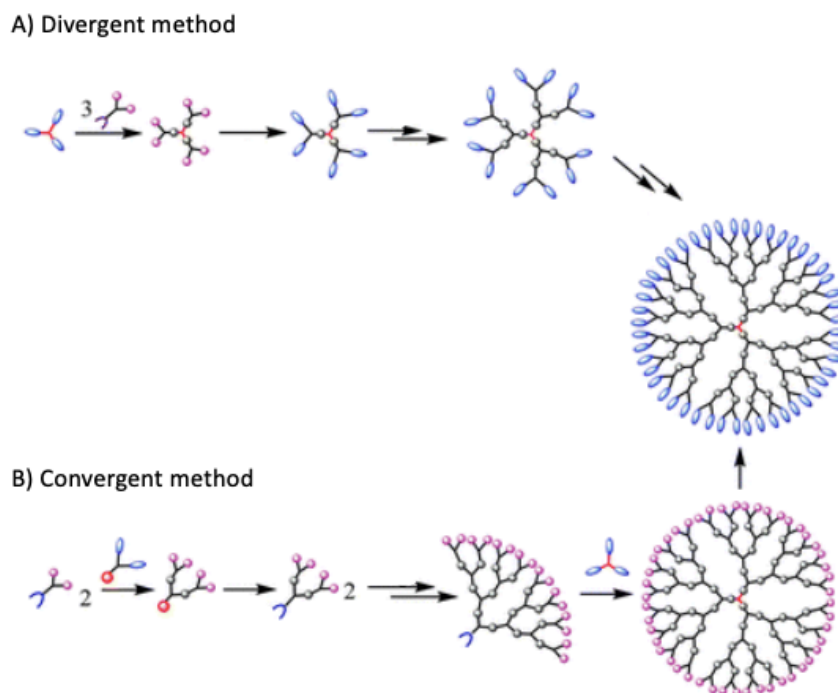
Figure 4.6. Schematic representation of A) divergent and B) convergent synthesis.

The divergent method approach, introduced by Tomalia, involves assembling monomer units in a radial pattern, according to defined rules. However, this method has some drawbacks such as the exponential increase in the number of reaction points during the synthesis of the dendrimer and the consequent increase in the molecular weight, making generational growth difficult. Furthermore, with increasing generations, the surface of the dendrimer tends to congest, leading to a change in the stoichiometry and kinetics of the reactions. This strategy is suitable for synthesizing symmetrical dendrimers such as PAMAM and PPI dendrimers.

The second synthetic strategy, discovered by Hawker and Fréchet, proceeds according to the convergent method. In this case, the dendrimer is not built from the core, but from the periphery through the synthesis of dendrons that will constitute the final dendrimer. At the end of the process, the dendrons react with the central molecule (or atom) with an equimolar ratio to points of attack. The great advantage of the convergent method is the possibility to purify the dendrons after each synthetic step. Furthermore, several functional groups can be incorporated at the dendrimer's periphery, branches, or core, making this synthetic methodology suitable for "*tailor-made*" dendrimers with desired properties. The convergent strategy is also a helpful method for the synthesis of asymmetric dendrimers, where heterogeneous dendrons are assembled to create

dendrimers with different morphology in the final step of coupling. Nevertheless, this type of procedure is generally limited to the production of lower-generation dendrimers because of the steric hindrance when attaching the dendrons to the nucleus.[20]

4.3.3. Poly(propylene imine) (PPI) dendrimers.

Among dendrimers, PPI dendrimers represent a particular type of symmetrical dendrimers discovered by Vogtle. They are sometimes mentioned as "DAB dendrimers", where DAB refers to the core structure which is based on a 1,4-diaminobutane scaffold (Figure 4.7).
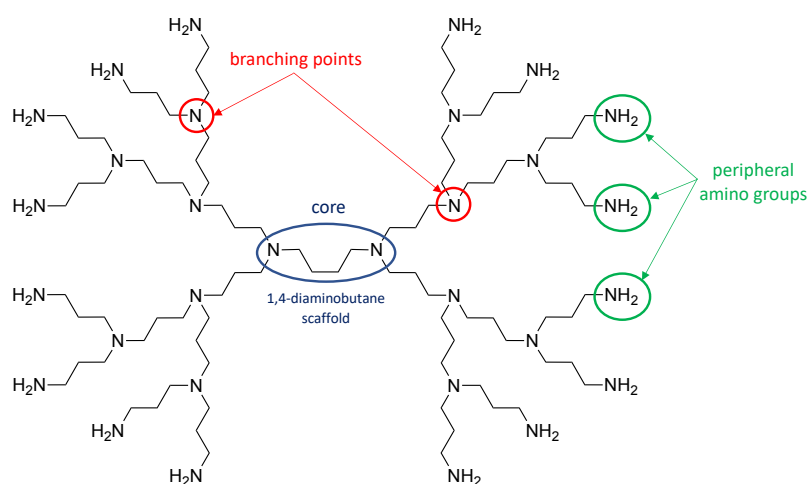
Figure 4.7. Architectural components of typical PPI dendrimers.

PPI dendrimers are synthesized starting from the 1,4-diaminobutane compound which undergoes a double Michael addition with acrylonitrile in the presence of small quantities of acetic acid as a catalyst. Then, the CN groups are reduced to primary amines by catalytic hydrogenation with Raney Cobalt, as shown in Figure 4.8. These reaction sequences are repeated an adequate number of times, following an appropriate stoichiometric ratio, and can be obtained up to the fifth generation.
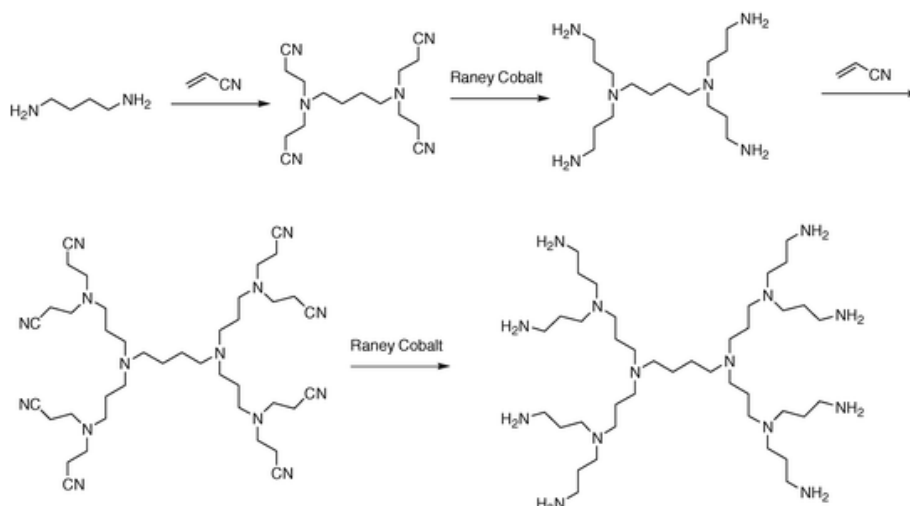
Figure 4.8. The synthetic procedure of PPI dendrimers.

Once the desired generation is reached, the amino end groups can be modified with several functional groups to exploit the PPI dendrimers as drug delivery systems in the pharmaceutical field. However, as mentioned above, PPI dendrimers show intrinsic toxicity attributed to the interaction of their external surface, featuring positive charges formed with the protonation of the terminal amino groups, with the negatively charged biological membranes. Therefore, cell membranes are damaged causing hemolytic toxicity and cytotoxicity. To overcome this problem, the coating by glycosylation or PEGylation technique leads to the formation of an outer shell that improves biocompatibility and allows PPI dendrimers to be used as a system for delivering drugs and diagnostic agents.[21]

4.3.4. Poly(propylene imine) (PPI) dendrimers as nanocarriers for drug delivery.

In recent years, the design of polymeric materials with potential applications as drug delivery systems (DDSs) has considerably increased. In this context, PPI dendrimers appear to be promising scaffolds owing to their peculiarities. Thanks to the simultaneous presence of hydrophobic internal areas and hydrophilic external surfaces, these hyperbranched molecules show a micellar nature that offers the opportunity to improve the bioavailability of guest molecules, increasing their half-life.[13] However, due to the presence of positively charged primary amino groups on their surface, PPI dendrimers show toxicity issues, which could be attenuated by coating with sugar molecules. In fact,

the glycosylation of PPI dendrimers led to the formation of a glyco-shell, which reduced the toxicity and allowed glycodendrimers to be used in the development of drug carriers. Additionally, toxicity problems can be solved by masking their positive surface charge with hydrophilic molecules such as poly(ethylene glycol) (PEG) to improve biocompatibility and increase solubility.[22] Therefore, in addition to their suitable pharmacokinetic parameters, PPI dendrimers represent the ideal candidates for the development of innovative drug delivery systems (DDSs), especially in chemotherapy. In this way, the drug can be hosted into the dendrimer free internal volume, or it can be weakly bound to the surface of the PPI dendrimer, which bears functional groups capable of increasing the solubility in biological fluids or targeting molecules. Once the PPI dendrimer reaches its target, the link with the drug is enzymatically or photochemically broken and the active pharmaceutical ingredient (API) can perform its therapeutic action.[23,24] Another recent application of dendrimers as polymeric nanocarriers regards their multivalent conjugation with choline, which showed potent inhibitory activity toward Streptococcus pneumoniae (Pneumococcus). The cell wall of Pneumococcus is particularly rich in teichoic acid, and phosphocholine acts as an anchor site for choline-binding proteins (CBP) involved in processes of virulence, such as the release of bacterial toxins and in adherence to the guest. Since CBP has a common structure in all serotypes, it is a very attractive target for the treatment of diseases caused by Pneumococcus. Choline and choline analogs competitively inhibit the binding of CBP to the cell wall, preventing the cell separation of S. pneumoniae. However, too high concentrations are required for the use as antimicrobial agents *in vivo*. This problem can be solved by linking the terminal amino groups of PPI dendrimers to choline molecules, as shown in Figure 4.9. In this regard, choline-functionalized PPI dendrimers as potential antimicrobial agents capable of establishing multivalent interactions between choline and binding sites with high affinity and specificity, able to reduce the *in vivo* concentrations of the antimicrobial agents have been designed and synthesized.[25]
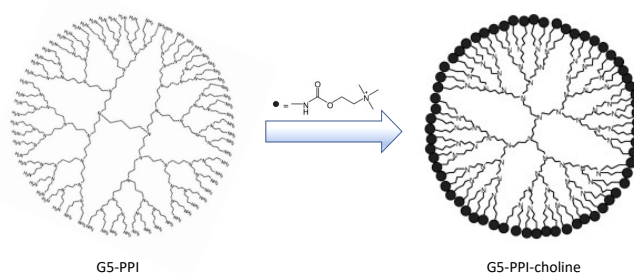
Figure 4.9. Chemical structures of the choline-functionalized PPI dendrimers.

4.4. References.

1. Fallacara, A.; Baldini, E.; Manfredini, S.; Vertuani, S. *Polymers* **2018**, *10* (7), 701.

2. Suniti, M.; Hascall, V. C.; Markwald, R. R.; Ghatak, S. *Front. Immunol.* **2015**, *6*.

3. Donati, A.; Magnani, A.; Bonechi, C.; Barbucci, R.; Rossi, C. *Biopolymers*, **2001**, *59*, 434-445.

4. *International Journal of Carbohydrate Chemistry* Volume 2013.

5. Burdick, J. A.; Prestwich, G. D. *Adv. Healthc.* **2011**, *23* (12), 41-56.

6. Cappelli, A.; Grisci, G.; Paolino, M.; Giuliani, G.; Donati, A.; Mendichi, R.; Artusi, R.; Demiranda, M.; Zanardi, A. Giorgi, G.; Vomero, S. *J. Mater. Chem. B* **2014**, *2*, 4489-4499.

7. Valacchi, G.; Grisci, G.; Sticozzi, C.; Lim, Y.; Paolino, M.; Giuliani, G.; Mendichi, R.; Belmonte, G.; Artusi, R.; Zanardi, A.; Garofalo, P.; Giorgi, G.; Cappelli, A.; Rovati, L. *J. Mater. Chem. B* **2015**, *3*, 7037-7045.

8. de O. Buanafina, M. M. *Mol. Plant.* **2009**, *5*, 861-872.

9. Cappelli, A.; Paolino, M.; Grisci, G.; Razzano, V.; Giuliani, G.; Donati,A.; Bonechi, C.; Mendichi, R.; Battiato, S.; Samperi, F.; Scialabba, C.; Giammona, G.; Makovec, F.; Licciardi, M. *Polym. Chem.* **2016**, *7*, 6529-6544.

10. Licciardi, M.; Scialabba, C.; Giammona, C.; Paolino, M.; Razzano, V.; Grisci, G.; Macovek, F.; Giuliani, G.; Cappelli, A. *J Nanopart Res.* **2017**, *19*, 197.

11. Cappelli, A.; Paolino, M.; Reale, A.; Razzano, V.; Grisci, G.; Giuliani, G.; Donati, A.; Bonechi, C.; Lamponi, S.; Mendichi, R.; Battiato, S.; Samperi, F.; Makovec, F.; Licciardi, M.; Depau, L.; Botta, C. *RSC Adv.* **2018**, *8*, 5864-5881.

12. *Materials Science and Engineering: C* Volume 107, **2020**, 110271.

13. Abbasi, E.; Fekri Aval, S.; Akbarzadeh, A.; Milani, M.; Tayefi Nasrabadi, H.; Woo Joo, S.; Hanifehpour, Y.; Nejati-Koshki, K.; Pashaei-Asl, R. *Nanoscale Res. Lett.* **2014**, *9*, 247-256.

14. Štimac, A.; Šekutor, M.; Majerski, K.; Frkanec, L.; Frkanec, R. *Molecules*, **2017**, *22*, 1-14.

15. Helms, B.; Meijer, E. W. *Science* **2006**, *313*, 929-930.

16. Boas, U.; Heegaard, P. M. H. *Chem. Soc. Rev.* **2004**, *33*, 43-63.

17. Wooley, K. L.; Hawker, C. J.; Fréchet, J. M. J. *Pure Appl. Chem.* **1994**, 1627-1645.

18. Bosman, A.W.; Janssen, H. M.; Meijer E. W.; *Chem. Rev.* **1999**, *99*, 1665-1688.

19. Grayson, S. M.; Fréchet, J. M. J. *Chem. Rev.* **2001**, *101*, 3819-3867.

20. Svenson, S.; Tomalia, D. A. *Adv. Drug Deliv. Rev.* **2005**, *57*, 2106-2129.

21. Kaur, D.; Jain, K.; Mehra, N. K.; Kesharwani, P.; Jain, N. K. *J. Nanoparticle Res.* **2016**, *18*, 1-14.

22. Tripathy, S.; Das, M. K. *J. Appl. Pharm. Sci.* **2013**, *3*, 142-149.

23. Bhadra, D.; Bhadra, S.; Jain, S.; Jain, N. K. *Int. J. Pharm.* **2003**, *257*, 111-124.

24. Koijma, C.; Kono, K.; Maruyama, K.; Takagishi, T. *Bioconjug. Chem.* **2000**, *11*, 910-917.

25. Hernàndez-Rocamora, V. M.; Maestro, B.; de Waal, B.; Morales, M.; Garcìa, P.; Meijer, E. W.; Merkx, M.; Sanz, J. M. *Chem. Int.* **2009**, *48*, 948-951.

4.5. Research article: "Hyaluronan-coated poly(propylene imine) dendrimers as biomimetic nanocarriers of doxorubicin".

Authors: Marco Paolino, Paola Varvarà, **Mario Saletti**, Annalisa Reale, Mariangela Gentile, Eugenio Paccagnini, Germano Giuliani, Hartmut Komber, Mariano Licciardi, Andrea Cappelli.

Contribution: The Ph.D. candidate's contribution to this work refers to the synthesis and the preliminary characterization of compounds, as well as the investigation and the data curation.

In this work, the coating technology based on **HA-FA-Pg** (constituted by low molecular weight HA and FA) has been applied to low-generation (1-3) poly(propylene imine) (PPI) dendrimers. In particular, the propargyl groups of **HA-FA-Pg** have been exploited in the coupling with the terminal amino groups in the periphery of low-generation PPI dendrimers through an azido-terminated biocompatible spacer composed of six ethylene glycol monomeric units. The resulting **HA-FA-HEG-PPID** derivatives showed remarkable aggregation features and pronounced loading capability of the antineoplastic agent Doxorubicin. Interestingly, the interactions of these materials with the drug were so strong that decreased the aggregation, compacted the dimensions, and hindered the drug release in the physiological condition. The stable nanostructured loaded delivery systems were found both to be internalized into cells expressing the HA receptor CD44 and to demonstrate high cytotoxicity comparable to that shown by equivalent amounts of free Doxorubicin used as positive controls. In this way, **HA-FA-HEG-PPID** dendrimeric

materials have been proposed as biocompatible drug carriers with promising features in transporting Doxorubicin to tumor cells.

RESEARCH ARTICLE

Journal of Applied Polymer Science WILEY

Hyaluronan-coated poly(propylene imine) dendrimers as biomimetic nanocarriers of doxorubicin

Marco Paolino[1] | **Paola Varvarà**[2] | **Mario Saletti**[1] | **Annalisa Reale**[1] | **Mariangela Gentile**[3] | **Eugenio Paccagnini**[3] | **Germano Giuliani**[1] | **Hartmut Komber**[4] | **Mariano Licciardi**[2] | **Andrea Cappelli**[1]

[1]Dipartimento di Biotecnologie, Chimica e Farmacia (Dipartimento di Eccellenza 2018–2022), Università degli Studi di Siena, Siena, Italy

[2]Dipartimento di Scienze e Tecnologie Biologiche, Chimiche e Farmaceutiche (STEBICEF), Università degli Studi di Palermo, Palermo, Italy

[3]Dipartimento di Scienze della Vita, Università degli Studi di Siena, Siena, Italy

[4]Center Macromolecular Structure Analysis, Leibniz Institute for Polymer Research, Dresden, Germany

Correspondence

Marco Paolino, Dipartimento di Biotecnologie, Chimica e Farmacia (Dipartimento di Eccellenza 2018–2022), Università degli Studi di Siena, Via A. Moro 2, Siena 53100, Italy.
Email: paolino3@unisi.it

Funding information
Italian MUR

Abstract

A coating technology based on low molecular weight hyaluronic acid (HA) and ferulic acid (FA) was applied to the coating of low generation poly(propylene imine) dendrimers through a biocompatible hexa(ethylene glycol) spacer. The ensuing HA-FA-HEG-PPID dendrimeric materials showed interesting loading capability (between 7.65% and 9.08%) regarding anticancer agent doxorubicin, and their interactions with the drug appeared to hamper the drug release in the physiological environment. Thus, the stable nanostructured loaded delivery systems were able to internalize into cells expressing the HA receptor CD44 and to demonstrate high cytotoxicity comparable to that shown by equivalent amounts of free doxorubicin. Thus, HA-FA-HEG-PPID dendrimeric materials were proposed as biocompatible drug carriers capable of transporting anticancer doxorubicin to tumor cells.

KEYWORDS

CuAAC, hyaluronic acid, nanocarriers, poly(propylene imine) dendrimer

1 | INTRODUCTION

Dendrimers are macromolecular entities that have focused a great deal of attention because of peculiar features such as the high symmetry, the highly branched architecture, the monodispersity, multivalence property, and so forth.[1–3] The request of new dendrimeric structures is continuously increasing given their large application in biomedical field, but also as materials for catalytic processes and composite materials.[4,5] Among these, poly(propylene imine) (PPI) and poly(amidoamine) (PAMAM) dendrimers represent two outstanding constructs that have been extensively investigated from the point of view of their potential

applications as drug and gene carriers.[3,6–13] These dendrimers are characterized by terminal amino groups generating a positively charged surface, which represents the portion most exposed to the external environment. Thus, their functionalization significantly modulates the physico-chemical properties of these dendrimers.[14] Moreover, unmodified poly-amine terminated dendrimers show toxicity issues, which could be attenuated by the surface derivatization.[15,16] To this purpose, the terminal amino groups have been derivatized with different molecules and polymers generating ordered and highly surface-functionalized 3D structures. Poly(ethylene glycol) (PEG) conjugation represents one of the most widely used techniques to modulate the physico-chemical and
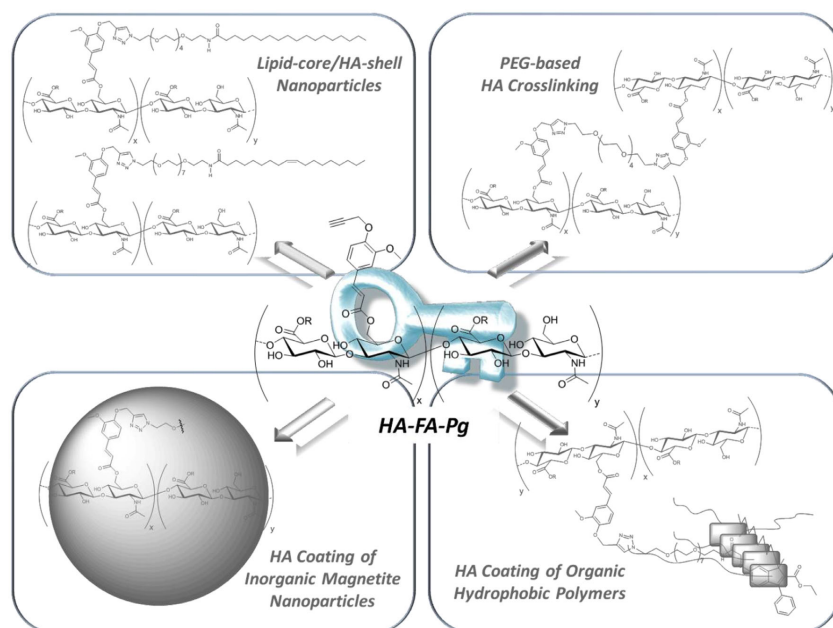
Chapter 4. Hyaluronan-based Graft Copolymers for the development of biocompatible materials useful in the pharmaceutical field

FIGURE 1 Structures of HA-FA-Pg derivatives involved in previously reported applications as coatings, shells, and crosslinkers. [Color figure can be viewed at wileyonlinelibrary.com]

toxicological properties of PAMAM and PPI dendrimers. The presence of monofunctional PEG chains reduces cytotoxicity and enhance size, zeta potential and cellular absorption,[17,18] while homo-bifunctional PEG chains have been used for the construction of dendrimer-based hydrogels.[19,20] Conjugation on the dendrimeric surface with targeting agents (such as folic acid or methotrexate to target tumor cells[21,22] or choline to develop multivalent antibacterial systems)[23,24] represents an interesting strategy for biomedical applications. Moreover, particular interest was given to the surface glycosylation,[25–27] which drastically reduces the toxicity of these polyamines and creates a cluster of H-bonds available for interactions with small drug molecules, proteins and receptors.[28–36]

Hyaluronic acid (HA)[37] is a natural polysaccharide, which may exist (i.e., on the surface of cells) in a large number of different conformations such as elongated chains, condensed rod-shaped structures, helices, relaxed helices, and pearl necklace structures.[38–40] Furthermore, HA macromolecules are able to interact each other to form fibrils, webs, and other supramolecular structures.[39] HA is generally recognized to play an important role in the early processes of cellular adhesion interacting with

the CD44 receptor, a widely-distributed transmembrane glycoprotein over-expressed in primary tumor cells and cancer-initiating cells.[41–44] Therefore, HA-based coating strategies have been developed in order to confer biocompatibility to different materials and realize tumor targeted drug delivery systems.[45–49]

Recently, our research group reported a versatile synthetic strategy for the derivatization of HA with ferulic acid (4-hydroxy-3-methoxycinnamic acid, FA) to obtain the HA-FA grafted copolymer.[50,51] FA is a natural compound largely distributed in the plant cellular wall,[52] where it is covalently bounded through an ester linkage to primary alcohol groups of arabinose pendant units of arabinoxylans. FA has shown many health benefits: it owns antioxidant, anti-inflammatory, antidiabetic, anticarcinogenic, antibacterial, anti-aging, and neuroprotective activities.[52] Moreover, FA is an interesting biocompatible fluorophore whose emissive properties strongly depend on solvent polarity, pH, and aggregation state making this molecule a versatile fluorescent bioprobe.[53,54]

Since, we are involved in the development of a HA-based technology platform, which aims to use this biomaterial in the coating of nanoparticles. The "key" of

80

FIGURE 2 Covalent coating strategy used to cover PPI nanoparticles by stiff oligomers of hyaluronic acid resulting in biomimetic HA-FA-HEG-PPID materials. [Color figure can be viewed at wileyonlinelibrary.com]
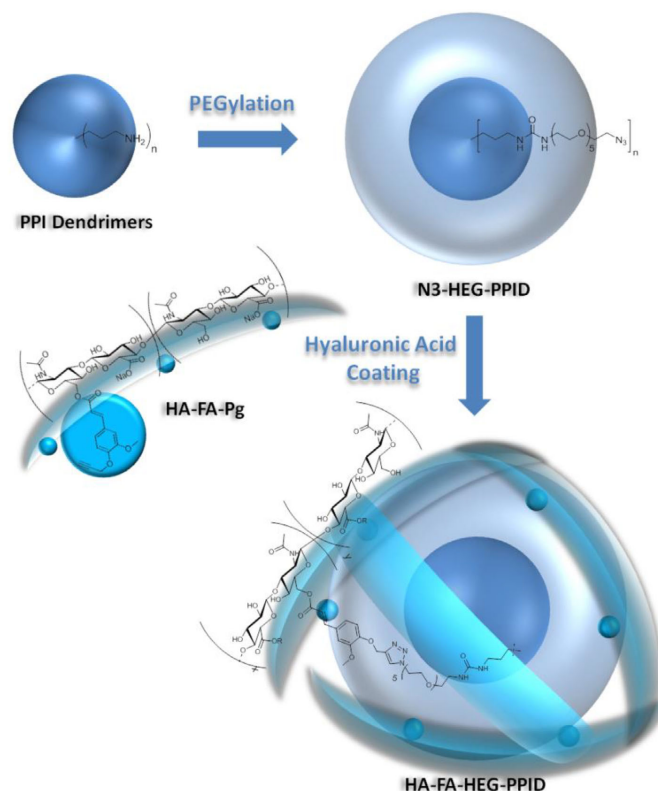
this strategy is the functionalization of low molecular weight HA with aggregation-induced emission (AIE) fluorogenic FA residues bearing a propargyl group gave HA-FA-Pg derivatives (Figure 1) that could be employed in Cu(I)-catalyzed azide-alkyne 1,3-dipolar cycloaddition (CuAAC, a click chemistry reaction)[55] conjugation.[56] This approach was employed in the covalent HA-based coating of our synthetic organic polymers (polybenzofulvene brushes),[56,57] magnetic nanoparticles,[58] lipid-core/HA-shell nanoparticles,[59] and small unilamellar vesicles (SUV) with the formation of biomimetic perivesicular coats,[53] and in the covalent crosslinking of HA-FA-Pg by azido terminated PEG chains.[60]

On the bases of the encouraging obtained results, we were interested in evaluating the effects of the covalent coating of HA (showing a largely adaptable linear geometry) around the spheroidal geometry of PPI dendrimers on the architecture and aggregation features of hybrid materials HA-FA-HEG-PPID (Figure 2).

Thus, in the present paper we describe the results obtained in the CuAAC coupling of HA-FA-Pg graft copolymer with the PPI dendrimers of first, second, and third generation (i.e., PPID-1, PPID-2, and PPID-3) bearing azide groups at the end of a hexa(ethylene glycol) spacer directly linked to each terminal amine group (i.e., N_3-HEG-PPID-1, N_3-HEG-PPID-2, and N_3-HEG-PPID-3). Moreover, we report on the results of the characterization of the materials (i.e., HA-FA-HEG-PPID-1, HA-FA-HEG-PPID-2, and HA-FA-HEG-PPID-3) and on their possible applications in the biomedical field.

2 | RESULTS AND DISCUSSION

2.1 | Synthesis and structural characterization

The synthesis started with the activation of hexa(ethylene glycol) derivative 1[59] bearing an azide group at one end and an amino group at the other extremity by reaction
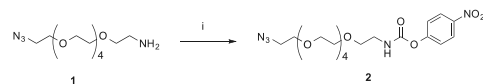
Reagents: (i) bis(4-nitrophenyl) carbonate, CH₂Cl₂.

SCHEME 1 Preparation of reactive intermediate 2. Reagents: (i) bis(4-nitrophenyl) carbonate, CH₂Cl₂

Reagents: (i) TEA, THF.

SCHEME 2 Preparation of N₃-HEG-PPID dendrimeric derivatives. Reagents: (i) TEA, THF

with bis(4-nitrophenyl) carbonate to obtain reactive intermediate 2 (yield 80%) as depicted in Scheme 1.

The PPI dendrimers of the appropriate generation (Scheme 2) were then reacted with the suitable excess of intermediate 2 to afford t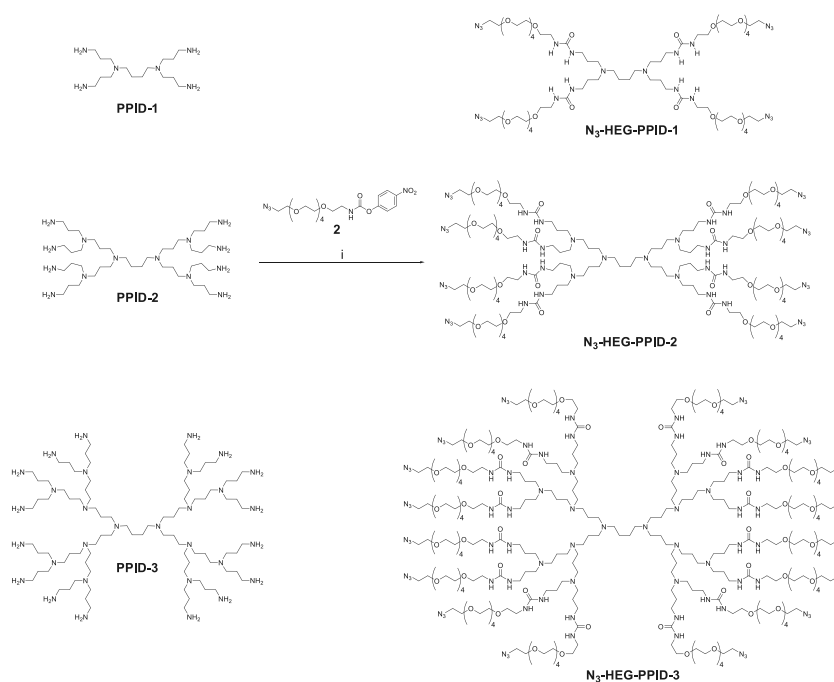he exhaustive functionalization of the primary amine groups and obtain the monodispersed N₃-HEG-PPID-1, N₃-HEG-PPID-2, or N₃-HEG-PPID-3 dendrimers which were characterized by NMR spectroscopy (see below) and ESI MS (Figures S1–S3). N₃-HEG-PPID dendrimers were used in the CuAAC coupling with HA-FA-Pg graft copolymer bearing 4–5 clickable fluorogenic FA residues each macromolecule to

obtain HA-FA-HEG-PPID-1, HA-FA-HEG-PPID-2, or HA-FA-HEG-PPID-3 materials, respectively (Scheme 3).

HA-FA-Pg graft copolymer bearing 4-5 clickable fluorogenic FA residues each macromolecule was selected among the HA-FA-Pg derivatives showing different grafting degrees[56] because of the compatibility of the clickable propargyl groups with the azide ones in N₃-HEG-PPID-1 (4 azide groups), N₃-HEG-PPID-2 (8 azide groups), or N₃-HEG-PPID-2 (16 azide groups). This compatibility was assumed to minimize the crosslinking among a great number of HA macromolecules. Moreover, the choice of using low generation

82
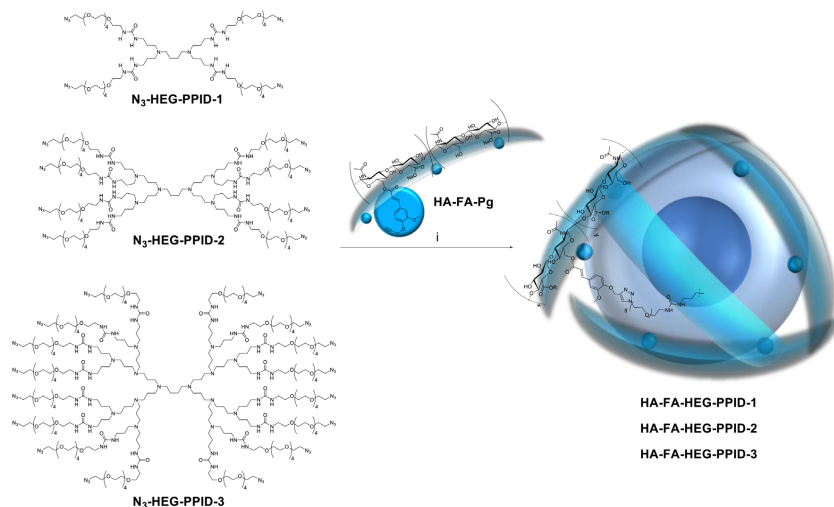
Reagents: (i) CuSO4, sodium ascorbate, H2O, *tert*-butanol.

SCHEME 3   Preparation of HA-FA-HEG-PPID materials. Reagents: (i) CuSO4, sodium ascorbate, H2O, tert-butanol [Color figure can be viewed at wileyonlinelibrary.com]

FIGURE 3   Comparison of the ^{1}H NMR spectrum of HA-FA-HEG-PPID-1 material (c) with those of the starting materials HA-FA-Pg (b; B′ and D′ are the signals of the CH2 and CH proton, resp., of the Pg group)[59] and N3-HEG-PPID-1 (a; E′ and F′ are signals of the methylene groups next to –N3). "Et" indicates the signals of ethyl groups of the HA monomeric units with R = C2H5.[53] Solvent: D2O
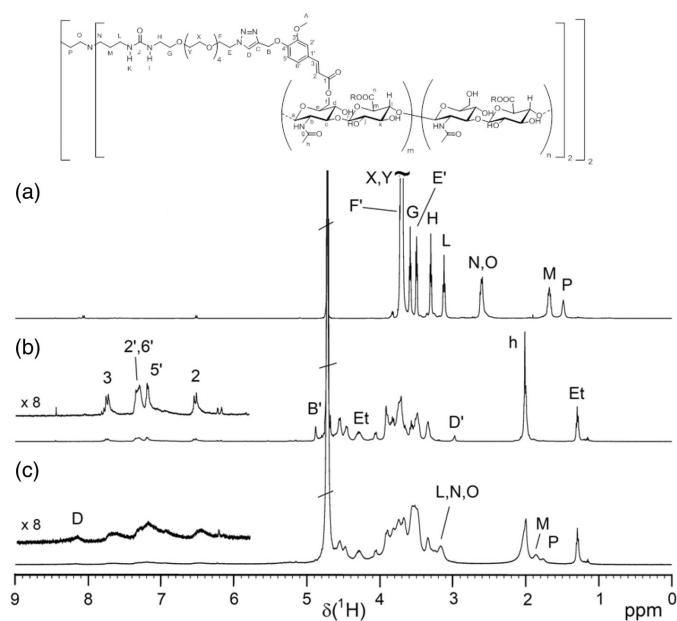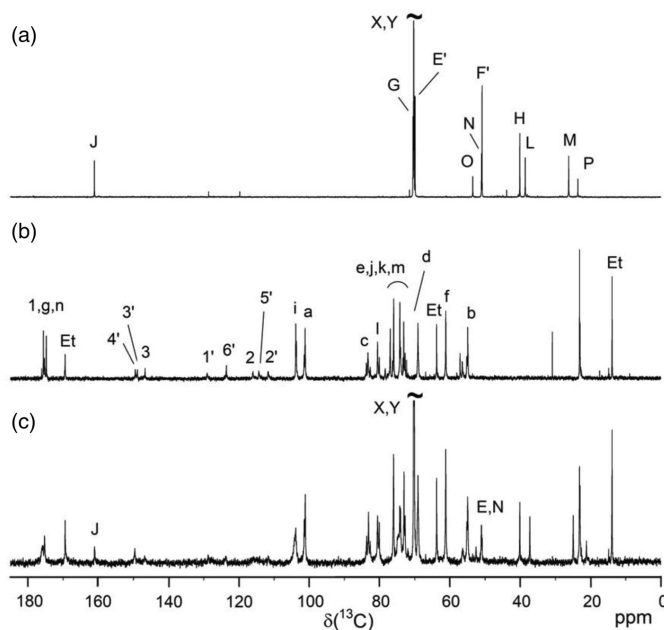
FIGURE 4 Comparison of the ^{13}C NMR spectrum of HA-FA-HEG-PPID-1 material (c) with those of the starting materials HA-FA-Pg (b; B′ and D′ are the signals of the CH$_2$ and CH carbons, resp., of the Pg group)[59] and N$_3$-HEG-PPID-1 (a; E′ and F′ are signals of the methylene carbons next to –N$_3$). "Et" indicates the signals of ethyl groups of the HA monomeric units with R = C$_2$H$_5$.[53] Solvent: D$_2$O

dendrimers should simplify the characterization of the resulting materials.

HA-FA-HEG-PPID-1, HA-FA-HEG-PPID-2, and HA-FA-HEG-PPID-3 materials were purified by dialysis and subsequent precipitation with acetone to obtain off-white solids (yields 65%–86%).

The structure of HA-FA-HEG-PPID-1, HA-FA-HEG-PPID-2, and HA-FA-HEG-PPID-3 materials was studied by ^{1}H and ^{13}C NMR spectroscopy in D$_2$O as the solvent.

Due to their complex structures, the ^{1}H NMR spectra of HA-FA-HEG-PPID materials (Figures 3c and S4) are composed by a set of broad and overlapped signals belonging to the different substructures, namely HEG-PPI dendrimer core, FA-triazole moiety, and hyaluronan shell. On the other hand, the corresponding ^{13}C NMR spectra (Figures 4c and S5) show a higher resolution and allowed a closer look on the chemical structures.

Thus, the study started with the ^{1}H and ^{13}C signal assignment of the N$_3$-HEG-PPID derivatives that form the core substructures. The task was smoothly accomplished by combining 1D and 2D NMR methods, by virtue the simplicity of the spectra owing to the high symmetry of the dendrimer molecules (Figures 3a, 4a, S7, and S8). ^{1}H and ^{13}C signal assignments for the precursor HA-FA-Pg (Figure 3b and 4b) were reported by us in a previous study.[59] Based on the signal assignments of both precursors, most ^{1}H and ^{13}C NMR signals of the HA-FA-HEG-PPID materials could be assigned (Figures 3c and 4c).

Unfortunately, the NMR signals of the structural unit containing the newly formed triazole ring and the ferulic acid ester are particularly broadened and sometimes not observable. This is not surprising,[59] as this substructure represents the most hydrophobic part of the structure and poor solvation in D$_2$O results in the pronounced line broadening. Nevertheless, the almost quantitative efficiency of the CuAAC coupling reaction to produce HA-FA-HEG-PPID materials was demonstrated by the disappearance of the signals of propargyl protons B′ (4.88 ppm) and D′ (2.98 ppm), which are not overlapped by other signals of HA-FA-HEG-PPID. Complementary, a broad but well detectable signal appears at about 8.25 ppm representing the triazole proton of the newly formed connecting group between the HEG-PPID core and HA-FA shell. The ^{13}C NMR spectra are consistent with this conclusion, although the sensitivity is lower than that of the ^{1}H NMR spectra.

2.2 │ Doxorubicin entrapment and biological characterization

As mentioned above, the coupling of HA-FA-Pg graft copolymer with the PPI dendrimers increases the chances to obtain nanostructures with a reduced toxicity, allowing their application in the biomedical field. For this reason, the capability of HA-FA-HEG-PPID dendrimers to act as

84

TABLE 1 Dimensional properties, surface charge, and drug content. Z-average, PDI, zeta potential, and drug loading % of empty and doxorubicin loaded dendrimeric materials.

Sample	Z-average (nm)	PDI	Zeta potential (mV)	Drug loading % p/p
HA-FA-HEG-PPID-1	290	0.47	-21.8 ± 6.61	-
HA-FA-HEG-PPID-2	553	0.12	-21.1 ± 3.50	-
HA-FA-HEG-PPID-3	257	0.28	-26.9 ± 4.08	-
HA-FA-HEG-PPID-1/Dox	174	0.31	-9.92 ± 5.71	7.65 ± 0.19
HA-FA-HEG-PPID-2/Dox	159	0.48	-15.00 ± 3.83	9.08 ± 0.10
HA-FA-HEG-PPID-3/Dox	147	0.41	-13.8 ± 4.54	7.93 ± 0.04

drug delivery systems was assessed by selecting doxorubicin as a model drug to produce loaded nanostructures for potential use in cancer treatment. This drug was approved as anticancer in the United States in 197 and suffers from solubility problems and important side effects. Therefore, the search for new polymeric carriers capable of increasing the solubility, favoring the site-specific release, and reducing the side effects is of fundamental importance. In this direction, our research group has obtained interesting results in the doxorubicin delivery using aromatic polymeric materials characterized by the presence of propyleneimine pincers[61] or hyaluronic acid filaments[57] in the outer shell. HA-FA-HEG-PPID dendrimers combine the structural properties of our previous materials into a new three-dimensional structure potentially capable of interacting and transporting anticancer drugs such as doxorubicin. To this aim, the dimensional and surface properties of the empty HA-FA-HEG-PPID dendrimeric materials were first analyzed, displaying average hydrodynamic diameters ranging from about 257–553 nm and negative (and comparable) Zeta potentials of $-21 \div -27$ mV (Table 1). Surprisingly, the data did not follow the expected trend. In particular, similar dimensions were observed for HA-FA-HEG-PPID-1 and HA-FA-HEG-PPID-3, whereas significantly greater diameters were recorded for HA-FA-HEG-PPID-2 in disagreement with the generation, the dimension, and the number of terminal groups of the dendrimer portion. Interestingly, the importance of aggregation phenomena of relatively small objects was rapidly appearing when number plots (see Figures S11 and S12) were taken into consideration. The strong aggregation features can be easily explained based on the complementary nature of the conjugated macromolecules: HA bearing negative surface charges and PPI dendrimers with internal protonated tertiary amines.

The size and shape of the empty HA-FA-HEG-PPID were also investigated by transmission electron microscopy (TEM) analysis (Figure 5). The samples, solubilized in water at a concentration of 1 mg ml^{-1} and left to equilibrate for 24 h, showed the presence of spherical aggregates with dimensions in line with those observed in the DLS analysis. Curiously, the TEM pictures let us to perceive different compactness of the materials, which grows with the increase in the dendrimer generation. In particular, the nanoparticles obtained with HA-FA-HEG-PPID-1 showed low density and very spherical shape, while those obtained with HA-FA-HEG-PPID-3 showed a high density with a jagged spherical shape in which the aggregation of smaller nanoparticles is perceived.

The entrapment of doxorubicin was performed by simply incubating the dispersed dendrimeric materials with a concentrated solution of the drug, allowing the formation of physical bonds, including electrostatic interactions between the positively charged doxorubicin amino group and the anionic HA moieties. As shown in Table 1, the entire set of dendrimers demonstrated the capability to load relatively high amounts of the drug, reaching doxorubicin weight percentages between 7.65% and 9.08%. As expected, the surface charge became less negative, with lower Zeta potentials with respect to concerning the empty dendrimers. From the dimensional point of view, a significant decrease in the average hydrodynamic diameters was observed after doxorubicin loading, measuring values less than 200 nm in the intensity plots (see Figure S12 and Table 1) and around 20 nm in the number plots (see Figure S12). These results suggest that doxorubicin interactions with the HA moieties of the dendrimeric materials, intercalating between the electrostatic interactions responsible for particle aggregation, produced a disaggregating effect, compacting the nanostructures, as well as reducing the Zeta potential.

In order to evaluate the drug release profile of the doxorubicin loaded dendrimeric materials, release studies simulating a two compartments model at pH 7.4 were performed. The whole set of the dendrimeric materials was tested, among these HA-FA-HEG-PPID-1/Dox, HA-FA-HEG-PPID-2/Dox kept the drug seized, while HA-FA-HEG-PPID-2/Dox released just a detectable amount of doxorubicin (Figure 6) reaching a plateau after releasing approximately 20% of the encapsulated drug and touching the highest value of 28% in 24 h. Given these results, we
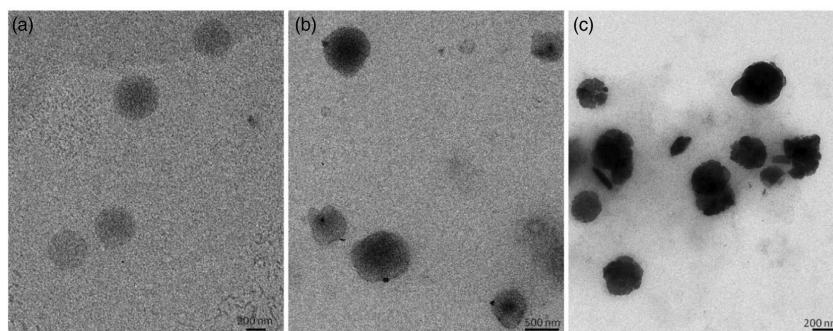
FIGURE 5 Structure of macromolecular aggregates in water found by TEM analysis of (a) HA-FA-HEG-PPID-1 (scale bar 200 nm), (b) HA-FA-HEG-PPID-2 (scale bar 500 nm), (c) HA-FA-HEG-PPID-3 (scale bar 200 nm)
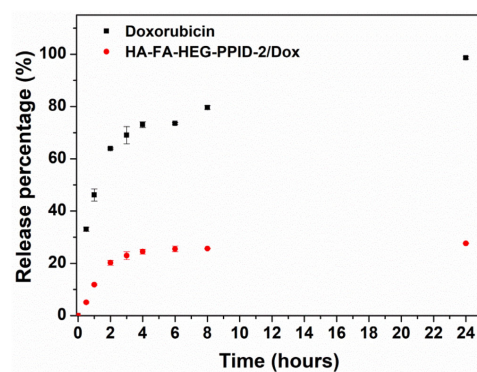
FIGURE 6 Release studies. Cumulative percentage of doxorubicin released from HA-FA-HEG-PPID-2/Dox (red circles) compared with the dissolution profile of free doxorubicin hydrochloride (black squares) in PBS pH 7.4. [Color figure can be viewed at wileyonlinelibrary.com]

FIGURE 7 Cytotoxicity assay. Cell viability of HCT116 cell line after 24 h incubation with different concentrations of empty HA-FA-HEG-PPID-1 (black squares), HA-FA-HEG-PPID-2 (green circles) and HA-FA-HEG-PPID-3 (blue triangles). [Color figure can be viewed at wileyonlinelibrary.com]

assumed that HA-FA-HEG-PPID-1/Dox, HA-FA-HEG-PPID-2/Dox, and HA-FA-HEG-PPID-3/Dox appeared to strongly interact with doxorubicin jeopardizing the liberation of the drug at physiological pH (i.e., 7.4).

Materials' biocompatibility is a crucial feature pursuing to address biomedical applications. In this context, PPI-based glycodendrimers are considered fascinating issues in drug delivery due to their tunable properties and good biocompatibility.[35] Therefore, to assess the cytocompatibility of the designed hyaluronan-dendrimers, the viability of human colon cancer cell line HCT116 (previously reported as over-expressing cells of the CD44 receptor)[57] was measured after 24 h incubation with increasing concentrations of HA-FA-HEG-PPID

materials. Not surprisingly, all the analyzed glycodendrimers resulted cytocompatible regardless the tested concentration, recording cell viability values that never fell under 80% (Figure 7). The findings of the current study suggest that HA conjugation endows the proposed dendrimers with high cytocompatibility.

The in vitro cytotoxic effect of doxorubicin loaded HA-FA-HEG-PPID systems was then evaluated on the same cell line (HCT 116) using an equivalent amount of free doxorubicin as a positive control. As depicted in Figure 8, HA-FA-HEG-PPID/Dox series of dendrimers appeared considerably cytotoxic towards HCT116 after 24 h of incubation (Figure 8a), exhibiting more

FIGURE 8 Cytotoxicity tests on doxorubicin loaded nanostructures. Cell viability of HCT116 cell line after 24 h (a) or 48 h (b) incubation with different concentrations HA-FA-HEG-PPID-1/Dox (black squares), HA-FA-HEG-PPID-2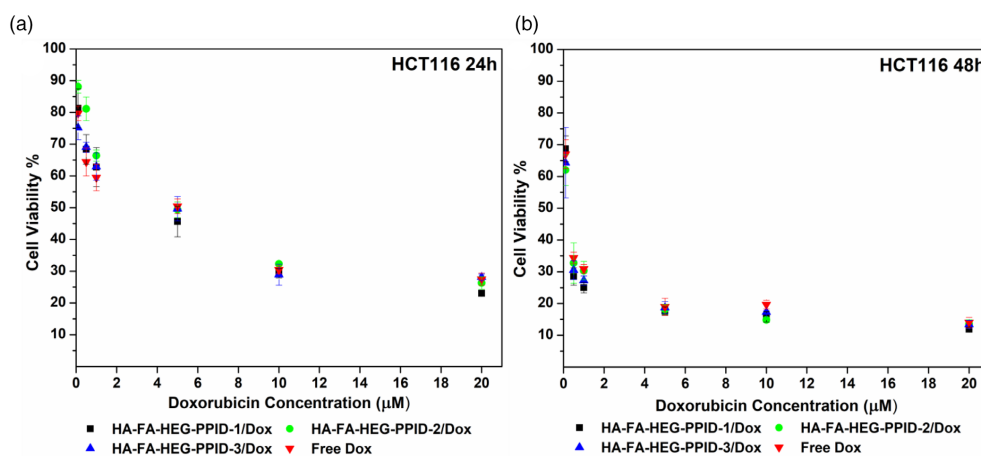/Dox (green circles) and HA-FA-HEG-PPID-3/Dox (blue triangles), compared to free doxorubicin (red inverted triangles). [Color figure can be viewed at wileyonlinelibrary.com]

pronounced antitumor efficacy in case of prolonged exposure (48 h, Figure 8b). All the samples tested showed antineoplastic activity, recording a minimum cell viability of about 12% after 48 h, with Dox IC_{50} after 48 h 10-fold higher (0.25 μM) with respect to IC_{50} measured at 24 h (5 μM). Given the previous data from release studies, the in vitro antitumor effect of HA-FA-HEG-PPID-1/Dox and HA-FA-HEG-PPID-3/Dox was not obvious, as it was not recorded any doxorubicin release from the drug delivery systems. Nevertheless, it is interesting to note that there are no significant differences between HA-FA-HEG-PPID/Dox series of dendrimers in terms of cytotoxic effect on the HCT116 cell line, suggesting that the entire set of samples is able to exert a strong antineoplastic effect.

Aiming to further investigate on the results of cytotoxicity assays, doxorubicin cell uptake from the loaded dendrimers on HCT116 cell line was evaluated. This study was performed through fluorescence microscopy incubating HA-FA-HEG-PPID/Dox dendrimers at a concentration corresponding to the calculated IC_{50} (24 h – 5 μM of doxorubicin) for 2 h (Figure S13), 8 h (Figure 9) or 24 h (Figure S14). Fluorescence micrographs acquired after 8 h (Figure 9) showed no visible differences among the systems tested, revealing a massive internalization of doxorubicin (intense red fluorescence), mostly localized in the cell nucleus. These findings are in line with cytotoxicity studies, suggesting that the antitumor effect of HA-FA-HEG-PPID/Dox may occur after internalization of the whole loaded nanometric

structure, that might be able to release its cargo directly in the intracellular environment. Nevertheless, it is also possible the concurrence of different uptake mechanisms, including the diffusion/transportation of the active molecule after drug liberation in the cell nearby, although further experimental investigations are needed to investigate this aspect.

3 | CONCLUSIONS

In conclusion, in the present work, our coating technology based on two natural compounds from biorenewable resources, namely low molecular weight HA and FA was applied to the coating of low generation poly(propylene imine) dendrimers (from G1 to G3 generation). In particular, the propargyl groups (4-5 clickable residues each macromolecule) of HA-FA-Pg derivatives were exploited in the coupling with the terminal amino groups in the periphery of low generation PPI dendrimers through an azido terminated biocompatible spacer composed of six ethylene glycol monomeric units. The resulting HA-FA-HEG-PPID derivatives showed remarkable aggregation features and pronounced loading capability regarding to anticancer agent doxorubicin (between 7.65% and 9.08%). Interestingly, the interactions of these dendrimeric materials with the drug were so strong that decreased the aggregation, compacted the dimensions, and hindered the drug release in the physiological environment. Again more interestingly, the stable nanostructured loaded systems were found both to be
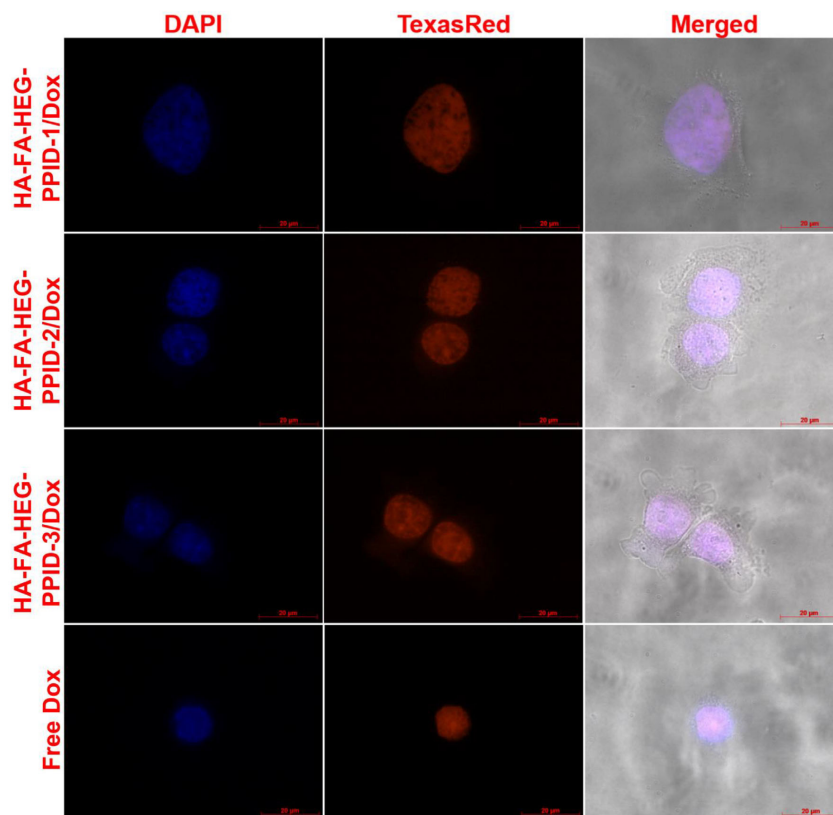
FIGURE 9 Doxorubicin uptake of HA-FA-HEG-PPID-1/Dox, HA-FA-HEG-PPID-2/Dox, HA-FA-HEG-PPID-3/Dox, and free doxorubicin after 8 h incubation with HCT116 cell line. Magnification: 100×; scale bar: 20 μm [Color figure can be viewed at wileyonlinelibrary.com]

internalized into cells expressing the HA receptor CD44 and to demonstrate high cytotoxicity comparable to that shown by equivalent amounts of free doxorubicin used as positive controls. Thus, HA-FA-HEG-PPID dendrimeric materials represent biocompatible drug carriers, which show very promising features in transporting anticancer doxorubicin to tumor cells.

4 | EXPERIMENTAL SECTION

4.1 | Synthesis and characterization

All reagents and solvents were purchased from Sigma-Aldrich and were used as received. Merck TLC aluminum sheets, silica gel 60 F_{254} were used for TLC. NMR spectra were recorded with either a Bruker DRX-400 AVANCE or a Bruker AVANCE III 500 spectrometer operating at 400.13 and 500.13 MHz for ^1H and at 100.61 and 125.75 MHz for ^{13}C respectively, in the indicated solvents. The chemical shifts are referenced to the solvent signal for $CDCl_3$ (δ [^1H] = 7.26 ppm) and CD_3OD (δ[^1H] = 3.31 ppm), or to the signal of a acetone trace for solutions in D_2O (δ[^1H] = 2.22 ppm, δ (^{13}C) CH_3 = 30.89 ppm). An Agilent 1100 LC/MSD running with an electrospray source was used in mass spectrometry measurements. Spectra/Por dialysis tubing, Sartorius cellulose acetate syringe filters and Whatman regenerated cellulose syringe filters were employed during this study. Milli-Q water (resistivity 18.2 MΩ cm at 25°C) was used for the whole set of experiments.

4.2 | 4-Nitrophenyl (17-azido-3,6,9,12,15-pentaoxaheptadecyl) carbamate (2)

A mixture of 17-azido-3,6,9,12,15-pentaoxaheptadecan-1-amine (1)[59] (0.54 g, 1.76 mmol) in dry CH_2Cl_2 (20 ml) containing bis(4-nitrophenyl) carbonate (0.80 g, 2.63 mmol) was stirred at room temperature for 6 h and then concentrated under reduced pressure. Purification of the residue by flash chromatography with ethyl acetate gave 2 as a colorless oil (0.66 g, yield 80%). ^{1}H NMR (400 MHz, $CDCl_3$, δ): 3.36 (t, J = 5.0 Hz, 2H), 3.47 (q, J = 5.1 Hz, 2H), 3.61–3.77 (m, 20H), 6.05 (br t, 1H), 7.31 (d, J = 9.2 Hz, 2H), 8.23 ppm (d, J = 9.1 Hz, 2H). MS (ESI) m/z: $[M + H]^+$ Calcd. for $C_{19}H_{30}N_5O_9^+$ 472.20; Found 472.4.

4.3 | General procedure for the synthesis of dendrimer derivatives N₃-HEG-PPID

A mixture of the appropriate PPI dendrimer (1 equivalent in terminal amino groups) in dry THF and TEA containing 4-nitrophenyl (17-azido-3,6,9,12,15-pentaoxaheptadecyl)carbamate (2, 1.5 equivalents) was refluxed overnight and then concentrated under reduced pressure. Purification of the residue by washing with diethyl ether gave the expected dendrimer derivatives N₃-HEG-PPID as a pale yellow oil.
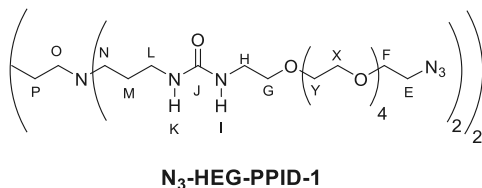
N₃-HEG-PPID-1

4.4 | Dendrimer derivative N₃-HEG-PPID-1

The title compound (80 mg, yield 69%) has been prepared starting from PPID-1 (Aldrich, 22 mg, 0.070 mmol) using 20 ml of dry THF and 5.0 ml of TEA. ^{1}H NMR (400 MHz, CD_3OD, δ): 1.48 (m, 4H; P), 1.65 (m, 8H; M), 2.51 (12H; O, N), 3.15 (t, J = 6.7 Hz,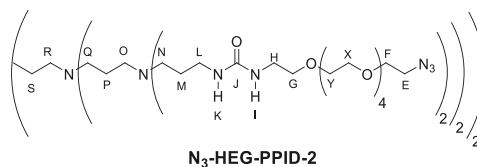 8H; L), 3.30 (m, 8H, overlapped with CD_2HOD; H), 3.38 (t, J = 4.6 Hz, 8H; E), 3.52 (t, J = 5.2 Hz, 8H; G), 3.59–3.77 ppm (72H; F, X, Y). ^{1}H NMR (500 MHz, D_2O, δ): 1.48 (m, 4H; P), 1.67 (m, 8H; M), 2.55–2.65 (12H; O, N), 3.12 (t, J = 6.6 Hz, 8H; L), 3.30 (t, J = 5.3 Hz, 8H; H), 3.49 (t, J = 5.0 Hz, 8H; E), 3.58 (t, J = 5.3 Hz, 8H; G), 3.65–3.75 ppm (72H; F, X, Y). ^{13}C NMR (125 MHz,

D_2O, δ): 23.5 (P), 26.2 (M), 38.5 (L), 40.2 (H), 50.8 (E), 51.0 (N), 53.5 (O), 69.9 (F), 70.1–70.3 (X, Y), 70.5 (G), 161.1 ppm (J). MS (ESI) m/z: $[M + 2H]^{2+}$ Calcd for $C_{68}H_{138}N_{22}O_{24}^{2+}$ 823.51; Found 823.5 (Figure S1).

N₃-HEG-PPID-2

4.5 | Dendrimer derivative N₃-HEG-PPID-2

The title compound (130 mg, yield 86%) has been prepared starting from PPID-2 (34 mg, 0.044 mmol) dissolved in 20 ml of dry THF and 5.0 ml of TEA. ^{1}H NMR (400 MHz, CD_3OD, δ): 1.48 (m, 4H; S), 1.64 (m, 24H; P, M), 2.48 (m, 36H; R, Q, O, N), 3.16 (t, J = 6.7 Hz, 16H; L), 3.31 (m, 16H, overlapped with CD_2HOD; H), 3.38 (t, J = 4.6 Hz, 16H; E), 3.53 (t, J = 5.3 Hz, 16H; G), 3.58–3.75 ppm (m, 144H; F, X, Y). ^{1}H NMR (500 MHz, D_2O, δ): 1.47 (br, 4H; S), 1.60–1.70 (24H; P, M), 2.45–2.60 (36H; R, Q, O, N), 3.11 (t, J = 6.7 Hz, 16H; L), 3.30 (t, J = 5.4 Hz, 16H; H), 3.50 (t, J = 4.9 Hz, 16H; E), 3.58 (t, J = 5.4 Hz, 16H; G), 3.65–3.75 (144H; F, X, Y). ^{13}C NMR (125 MHz, D_2O, δ): 22.4 (P), 24.1 (S), 26.6 (M), 38.9 (L), 40.1 (H), 50.9 (E), 51.1 (N), 51.8 and 51.9 (Q, O), 53.7 (R), 69.9 (F), 70.1–70.3 (X, Y), 70.5 (G), 161.0 ppm (J). MS (ESI) m/z: $[M + 4H]^{4+}$ Calcd. for $C_{144}H_{292}N_{46}O_{48}^{4+}$ 858.79; Found 858.8 (Figure S2).

N₃-HEG-PPID-3
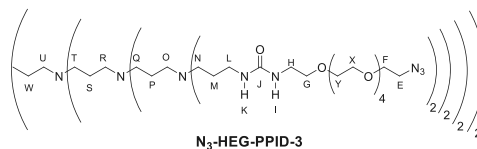
4.6 | Dendrimer derivative N₃-HEG-PPID-3

The title compound (95 mg, yield 65%) has been prepared starting from PPID-3 (35 mg, 0.0208 mmol) dissolved in 20 ml of dry THF and 5.0 ml of TEA. ^{1}H NMR (400 MHz, CD_3OD, δ): 1.48 (m, 4H; W), 1.65 (m, 56H; M, P, S), 2.50 (m, 84H; N, O, Q, R, T), 3.16 (t, J = 6.5 Hz, 32H; L), 3.31 (m, 32H, overlapped with

CD_2HOD; H), 3.38 (t, $J = 4.6$ Hz, 32H; E), 3.53 (t, $J = 5.3$ Hz, 32H; G), 3.60–3.71 ppm (m, 288H; F, X, Y). ^{1}H NMR (500 MHz, D_2O, δ): 1.46 (br, 4H; W), 1.60–1.70 (56H; M, P, S), 2.40–2.60 (84H; N, O, Q, R, T), 3.11 (t, $J = 6.7$ Hz, 32H; L), 3.30 (t, $J = 5.4$ Hz, 32H; H), 3.49 (t, $J = 4.9$ Hz, 32H; E), 3.58 (t, $J = 5.4$ Hz, 32H; G), 3.65–3.80 ppm (288H; F, X, Y). ^{13}C NMR (125 MHz, D_2O, δ): 22.6 (P, S), 24.2 (W), 26.6 (M), 38.9 (L), 40.1 (H), 50.9 (E), 51.1 (N), 51.8–52.1 (O, Q, R, T), 54.0 (U), 69.9 (F), 70.2–70.3 (X, Y), 70.5 (G), 160.9 ppm (J). MS (ESI) *m/z*: $[M + 6H]^{6+}$ Calcd for $C_{296}H_{598}N_{94}O_{96}^{6+}$ 1168.25; Found 1168.3 (Figure S3).

4.7 | Synthesis of HA-FA-HEG-PPID materials

Under an inert atmosphere, a 10 ml flask was charged with *tert*-butanol (2.0 ml), water (2.0 ml), and a solution of $CuSO_4$ pentahydrate (24 mg, 0.096 mmol) in 0.50 ml of water. A 1 M solution of sodium ascorbate in water (0.50 ml) was then added and 1.0 ml of the resulting mixture was used as the catalyst. A mixture of the appropriate N_3-HEG-PPID (from generation one to three) and low molecular weight HA-FA-Pg[56] graft copolymer bearing 4-5 clickable fluorogenic FA residues each macromolecule in *tert*-butanol (25 ml) and water (25 ml) was treated with the catalyst solution (1.0 ml) and the reaction mixture was stirred overnight at room temperature. The reaction mixture was then concentrated under reduced pressure to a 5 ml volume, and the resulting mixture was purified by dialysis (molecular weight cut off, MWCO, 1000 Da) against distilled water. The expected HA-FA-HEG-PPID material was obtained by precipitation with acetone and was dried under reduced pressure. The ^{1}H and ^{13}C NMR spectra of all HA-FA-HEG-PPID materials are depicted in Figure 3 and S4 and in Figure 4 and S5, respectively. As expected, the spectra are very similar and therefore the data are reported exemplarily for HA-FA-HEG-PPID-1.

4.8 | HA-FA-HEG-PPID-1

This material was prepared from N_3-HEG-PPID-1 derivative (40 mg, 0.024 mmol) and HA-FA-Pg graft copolymer (200 mg) and was obtained as an off-white solid (209 mg).

^{1}H NMR (500 MHz, D_2O, δ): 1.30 (CH_3 of R = Et), 1.77 (P), 1.86 (M), 2.02 (h), 3.17 (L,N,O), 3.2–4.7 (A, HA and HEG signals, CH_2 of R = Et), 6.54 (v br; 2), 7.1–7.4 (2′, 5′, 6′), 7.74 (v br; 3), 8.25 ppm (v br; D). ^{13}C NMR (125 MHz, D_2O, δ): 13.9 (CH_3 of R = Et), 21.2 (P), 23.2 (h), 25.0 (M), 37.3 (L), 40.1 (H), 51.1 (E,N), 52.6 (O), 55.0 (b), 56.4 (A), 61.2 (f), 63.8 (CH_2 of R = Et), 69.1 (d), 69.4 (F), 70.3 (G,X,Y), 72–77 (e,j,m,k), 80–81 (l), 82.5–84.5 (c), 101.3 (a), 104 (i), 110–130 (broad signals; 2,1′,2′,5′,6′,D), 145–150 (broad signals; 3,3′4′), 161.0 (J), 169.4 (C=O of R = Et), 175–177 ppm (n,g).

4.9 | HA-FA-HEG-PPID-2

This material was prepared from N_3-HEG-PPID-2 derivative (40 mg, 0.012 mmol) and HA-FA-Pg graft copolymer (200 mg) and was obtained as an off-white solid (172 mg).

4.10 | HA-FA-HEG-PPID-3
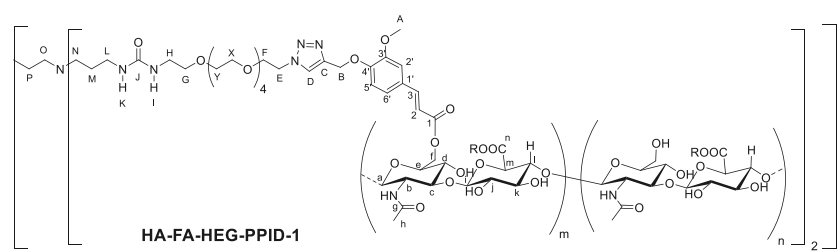
This material was prepared from N_3-HEG-PPID-3 derivative (42 mg, 0.0060 mmol) and HA-FA-Pg graft copolymer (200 mg) and was obtained as an off-white solid (204 mg).

4.11 | Preparation of doxorubicin loaded HA-FA-HEG-PPID-1, HA-FA-HEG-PPID-2, and HA-FA-HEG-PPID-3 materials

Doxorubicin loaded systems were formulated by dispersing 30 mg of HA-FA-HEG-PPID-1, HA-FA-HEG-

HA-FA-HEG-PPID-1

PPID-2, or HA-FA-HEG-PPID-3 dendrimer derivatives in ultrapure water to obtain the final concentration of 2 mg ml^{-1}, aiding the process by performing 3 cycles of stirring/sonication (15 min/15 min) followed by 1 h of magnetic stirring at 40 °C. A solution of doxorubicin hydrochloride in ultrapure water (3 mg in 1 ml) was added dropwise to the previously dispersed samples. The mixtures were placed in Benchtop 808C Incubator Orbital Shaker (Thermo Scientific, model 420) for 2 h at 37°C, 100 rpm, and then lyophilized to obtain HA-FA-HEG-PPID-1/Dox, HA-FA-HEG-PPID-2/Dox, and HA-FA-HEG-PPID-3/Dox systems.

4.12 | Determination of doxorubicin payload and release studies

The doxorubicin content of loaded systems was measured by UV–vis spectroscopy by means of Shimadzu VIS–NIR 2400 spectrophotometer. Exactly weighted samples of HA-FA-HEG-PPID-1/Dox, HA-FA-HEG-PPID-2/Dox, and HA-FA-HEG-PPID-3/Dox were dispersed in DMSO and the drug was extracted by performing 3 cycles of stirring/sonication (30 min/15 min). The samples were thus filtered through syringe filter (cut-off 0.2 μm), analyzed by UV–vis spectroscopy by evaluating the absorbance value at the wavelength of 480 nm, and data were expressed as weight percentage of doxorubicin hydrochloride with respect to the total weight of the loaded systems. Drug loading percentages were calculated via comparison with a calibration curve of doxorubicin hydrochloride solutions in DMSO (wavelength: 480 nm; linearity range 0.001–0.1 mg ml^{-1}; R^2: 0.999).

The drug release from HA-FA-HEG-PPID-1/Dox, HA-FA-HEG-PPID-2/Dox, and HA-FA-HEG-PPID-3/Dox was studied using a two-compartments model. Exactly weighted samples (or an equivalent amount of free doxorubicin hydrochloride) were dispersed in ultrapure water, placed in a dialysis tube (MWCO 2 kDa) and incubated at 37°C, 100 rpm with PBS pH 7.4 as the external medium. At fixed time intervals (0.5, 1, 2, 3, 4, 6, 8, and 24 h), 1 ml of the outer medium was withdrawn, replaced with fresh PBS, and freeze-dried. The lyophilized samples were then dispersed in DMSO to allow the dissolution of doxorubicin, centrifuged, and filtered (cut-off 0.2 μm) before UV–vis spectroscopy analysis. Drug release percentages were calculated comparing the results with a calibration curve of doxorubicin hydrochloride solutions in DMSO (wavelength: 480 nm; linearity range 0.001–0.1 mg ml^{-1}; R^2: 0.999). All values are the average of three experiments ±SD.

4.13 | Dynamic light scattering measurements and zeta potential evaluation

Hydrodynamic diameters, polydispersity indexes (PDI), and Zeta potentials were measured through Malvern Zetasizer NanoZS instrument, equipped with a 632.8 nm laser with the fixed angle of 173°. The samples were dispersed in ultrapure water (1 mg ml^{-1}) and analyzed after syringe filtration (cut-off 5 μm) at 25°C. The mean hydrodynamic diameter and the polydispersity index (PDI) were obtained by evaluating the cumulants of the correlation function. The Zeta potential (mV) was calculated from electrophoretic mobility using the Smoluchowsky relationship and assuming $K_a \gg 1$ (where K and $_a$ are the Debye–Hückel parameter and the particle radius, respectively).

4.14 | Transmission electron microscopy

Solutions of HA-FA-HEG-PPID materials in water (1 mg ml^{-1}) were dropped onto a 300 mesh formvar-coated copper grid. The sample excess was then blotted by filter paper. Samples were observed in a FEI Tecnai G2 Spirit transmission electron microscope at an acceleration voltage of 100 kV equipped with TVIPS TemCam-F216 2048x2048 CMOS camera.

4.15 | In vitro studies

HCT116 human colon cancer cells were purchased from Istituto Zooprofilattico Sperimentale della Lombardia e dell'Emilia Romagna "B. Ubertini" (Italy) and cultured in Dulbecco's Modified Eagle Medium (DMEM) enriched with 10% vol/vol of fetal bovine serum (FBS), streptomycin (100 mg ml^{-1}), penicillin G (100 units ml^{-1}), amphotericin B (2.5 μg ml^{-1}), L-glutamine (2 mM), purchased from Euroclone and incubated al 37 °C in a humidified environment with 5% of CO$_2$. Cell viability was assessed through MTS [3-(4,5-dimethylthiazol-2-yl)-5-(3-carboxymethoxyphenyl)-2-(4-sulphophenyl)-2H-tetrazolium] reagent Cell Titer 96 Aqueous One Solution Cell Proliferation assay (Promega) and used according to the manufacturer's instructions. DAPI (diamidino-2-phenylindole) staining was purchased from Thermo Scientific.

4.16 | Cytocompatibility and cytotoxicity tests

The cytocompatibility of the proposed materials was assessed on human colon cancer cell line (HCT116)

through MTS colorimetric assay. HCT116 cells were cultured in supplemented DMEM and seeded at the density of 2×10^4 cells per well on 96-well plate. Cells were allowed to adhere for 24 h in humidified environment with 5% CO_2 at 37°C and then incubated with fresh dispersions of HA-FA-HEG-PPID-1, HA-FA-HEG-PPID-2, or HA-FA-HEG-PPID-3 in DMEM at the concentrations of 150, 75, 37.5, 7.5, 3.75, and 0.75 μg ml^{-1}. Cytotoxicity tests of the loaded dendrimers were performed on HCT 116 cell line as well, using the same protocol described above. In this case, the doxorubicin containing systems HA-FA-HEG-PPID-1, HA-FA-HEG-PPID-2, HA-FA-HEG-PPID-3, or free doxorubicin hydrochloride were incubated with HCT 116 seeded in 96-well plates, at the equivalent drug concentrations of 0.1, 0.5, 1, 5, 10, 20 μM. In both experiments, after 24 h (empty and loaded systems) or 48 h (loaded systems) of incubation at 37°C, each well content was replaced with 20 μl of MTS solution diluted using 100 μl of DMEM and the plate was incubated for further 2 h at 37°C. All experiments were carried out in triplicate and obtained results were expressed as mean ± *SD*. Potential statistical differences were analyzed by Student's *T*-test. *P*-value <0.05 was defined as the level of statistical significance. Cell viability was calculated by reading the absorbance of the samples at the wavelength of 492 nm through microplate reader (Eppendorf PlateReader AF2200). Cell viability was expressed as a percentage of viability compared to untreated cells used as negative control.

4.17 | Uptake studies

To investigate the doxorubicin cell uptake after incubation with loaded dendrimeric materials, HCT 116 cell line was seeded at the density of 4×10^4 cells per well into eight well cover glass bottom plates and cultured for 24 h as reported above. The study was performed incubating cells for 2, 8, and 24 h in the presence of fresh dispersions of HA-FA-HEG-PPID-1/Dox, HA-FA-HEG-PPID-2/Dox, HA-FA-HEG-PPID-3/Dox or free doxorubicin dispersed in DMEM at the equivalent concentration of doxorubicin of 5 μM. Cells were fixed with 4% formaldehyde and the nuclei stained with 4′,6-diamidino-2-phenylindole (DAPI). Images were acquired using a fluorescence microscope equipped with an Axio Cam MRm (Zeiss).

AUTHOR CONTRIBUTIONS
Paola Varvarà: Data curation (equal); formal analysis (equal); investigation (equal). **Mario Saletti:** Data curation (equal); formal analysis (equal); investigation (equal). **Annalisa Reale:** Formal analysis (equal); methodology (equal). **Mariangela Gentile:** Formal analysis (equal); investigation (supporting). **Eugenio Paccagnini:** Formal analysis (equal); investigation (supporting). **Germano Giuliani:** Formal analysis (equal); investigation (equal). **Hartmut Komber:** Data curation (equal); formal analysis (lead); investigation (lead); methodology (equal); validation (supporting); writing – original draft (equal). **Mariano Licciardi:** Data curation (equal); formal analysis (lead); investigation (equal); methodology (equal); writing – original draft (equal). **Andrea Cappelli:** Conceptualization (equal); data curation (equal); project administration (equal); supervision (lead); writing – original draft (lead).

DATA AVAILABILITY STATEMENT
The data that support the findings of this study are available from the corresponding author upon reasonable request.

ORCID
Marco Paolino https://orcid.org/0000-0003-1387-7875
Paola Varvarà https://orcid.org/0000-0003-0814-5805
Mario Saletti https://orcid.org/0000-0002-8414-3134
Mariangela Gentile https://orcid.org/0000-0002-4928-4652
Eugenio Paccagnini https://orcid.org/0000-0002-9784-2057
Germano Giuliani https://orcid.org/0000-0001-8111-3776
Hartmut Komber https://orcid.org/0000-0001-6176-6737
Mariano Licciardi https://orcid.org/0000-0003-4539-9337
Andrea Cappelli https://orcid.org/0000-0003-4140-3028

REFERENCES
[1] A. W. Bosman, H. M. Janssen, E. W. Meijer, *Chem. Rev.* **1999**, *99*, 1665.
[2] U. Boas, P. M. H. Heegaard, *Chem. Soc. Rev.* **2004**, *33*, 43.
[3] S. Galeazzi, T. M. Hermans, M. Paolino, M. Anzini, L. Mennuni, A. Giordani, G. Caselli, F. Makovec, E. W. Meijer, S. Vomero, A. Cappelli, *Biomacromolecules* **2010**, *11*, 182.
[4] P. Kesharwani, K. Jain, N. K. Jain, *Prog. Polym. Sci.* **2014**, *39*, 268.
[5] D. Astruc, F. Chardac, *Chem. Rev.* **2001**, *101*, 2991.
[6] M. Paolino, L. Mennuni, G. Giuliani, M. Anzini, M. Lanza, G. Caselli, C. Galimberti, M. C. Menziani, A. Donati, A. Cappelli, *Chem. Commun.* **2014**, *50*, 8582.
[7] S. Svenson, D. A. Tomalia, *Adv. Drug Delivery Rev.* **2005**, *57*, 2106.
[8] D. Kaur, K. Jain, N. K. Mehra, P. Kesharwani, N. K. Jain, *J. Nanopart. Res.* **2016**, *18*, 146.

[9] R. S. Ambekar, M. Choudhary, B. Kandasubramanian, *Eur. Polym. J.* **2020**, *126*, 109546.

[10] M. Paolino, H. Komber, L. Mennuni, G. Caselli, D. Appelhans, B. Voit, A. Cappelli, *Biomacromolecules* **2014**, *15*, 3985.

[11] F. Castriconi, M. Paolino, A. Donati, G. Giuliani, M. Anzini, L. Mennuni, C. Sabatini, M. Lanza, G. Caselli, F. Makovec, M. Sbraccia, P. Molinari, T. Costa, A. Cappelli, *Med. Chem. Commun.* **2017**, *8*, 647.

[12] P. Kesharwani, S. Banerjee, U. Gupta, M. C. I. Mohd Amin, S. Padhye, F. H. Sarkar, A. K. Iyer, *Mater. Today* **2015**, *18*, 565.

[13] P. Kesharwani, A. K. Iyer, *Drug Discovery Today* **2015**, *20*, 536.

[14] M. Zhang, R. Guo, M. Kéri, I. Bányai, Y. Zheng, M. Cao, X. Cao, X. Shi, *J. Phys. Chem. B* **2014**, *118*, 1696.

[15] N. A. Stasko, C. B. Johnson, M. H. Schoenfisch, T. A. Johnson, E. L. Holmuhamedov, *Biomacromolecules* **2007**, *8*, 3853.

[16] F. Najafi, M. Salami-Kalajahi, H. Roghani-Mamaqani, A. Kahaie-Khosrowshahi, *J. Biomed. Mater. Res. Part A* **2020**, *108*, 485.

[17] S. Somani, P. Laskar, N. Altwaijry, P. Kewcharoenvong, C. Irving, G. Robb, B. S. Pickard, C. Dufès, *Sci. Rep.* **2018**, *8*, 9410.

[18] D. Luong, P. Kesharwani, R. Deshmukh, M. C. I. Mohd Amin, U. Gupta, K. Greish, A. K. Iyer, *Acta Biomater.* **2016**, *43*, 14.

[19] L. Xu, R. C. Cooper, J. Wang, W. A. Yeudall, H. Yang, *ACS Biomater. Sci. Eng.* **2017**, *3*, 1641.

[20] J. Wang, H. He, R. C. Cooper, Q. Gui, H. Yang, *Mol. Pharm.* **2019**, *16*, 1874.

[21] Y. Wang, X. Cao, R. Guo, M. Shen, M. Zhang, M. Zhu, X. Shi, *Polym. Chem.* **2011**, *2*, 1754.

[22] M. Golshan, M. Salami-Kalajahi, H. Roghani-Mamaqani, M. Mohammadi, *Appl. Organomet. Chem.* **2017**, *31*, e3789.

[23] V. M. Hernández-Rocamora, B. Maestro, B. de Waal, M. Morales, P. García, E. W. Meijer, M. Merkx, J. M. Sanz, *Angew. Chemie Int. Ed.* **2009**, *48*, 948.

[24] S. Ribes, J. Riegelmann, S. Redlich, B. Maestro, B. de Waal, E. W. Meijer, J. M. Sanz, R. Nau, *Chemotherapy* **2013**, *59*, 138.

[25] M. Paolino, F. Ennen, S. Lamponi, M. Cernescu, B. Voit, A. Cappelli, D. Appelhans, H. Komber, *Macromolecules* **2013**, *46*, 3215.

[26] M. Paolino, F. Ennen, H. Komber, M. Cernescu, A. Cappelli, B. Brutschy, B. Voit, D. Appelhans, *Polym. Chem.* **2012**, *3*, 3239.

[27] B. Klajnert, D. Appelhans, H. Komber, N. Morgner, S. Schwarz, S. Richter, B. Brutschy, M. Ionov, A. K. Tonkikh, M. Bryszewska, *Chem. A Eur. J.* **2008**, *14*, 7030.

[28] T. Dutta, H. B. Agashe, M. Garg, P. Balasubramanium, M. Kabra, N. K. Jain, *J. Drug Targeting* **2007**, *15*, 89.

[29] J. Keerti, V. A. Kumar, M. P. Ranjan, J. N. Kumar, *Antimicrob. Agents Chemother.* **2021**, *59*, 2479.

[30] P. Kesharwani, R. K. Tekade, V. Gajbhiye, K. Jain, N. K. Jain, *Nanomed. Nanotechnol. Biol. Med.* **2011**, *7*, 295.

[31] J. L. Jiménez, M. Pion, F. J. de la Mata, R. Gomez, E. Muñoz, M. Leal, M. a. a. Muñoz-Fernandez, *New J. Chem.* **2012**, *36*, 299.

[32] D. Bhadra, A. K. Yadav, S. Bhadra, N. K. Jain, *Int. J. Pharm.* **2005**, *295*, 221.

[33] O. Klementieva, E. Aso, D. Filippini, N. Benseny-Cases, M. Carmona, S. Juvés, D. Appelhans, J. Cladera, I. Ferrer, *Biomacromolecules* **2013**, *14*, 3570.

[34] A. Janaszewska, K. Mączyńska, G. Matuszko, D. Appelhans, B. Voit, B. Klajnert, M. Bryszewska, *New J. Chem.* **2012**, *36*, 428.

[35] D. Appelhans, B. Klajnert-Maculewicz, A. Janaszewska, J. Lazniewska, B. Voit, *Chem. Soc. Rev.* **2015**, *44*, 3968.

[36] R. Gupta, N. K. Mehra, N. K. Jain, *Eur. J. Pharm. Biopharm.* **2014**, *86*, 449.

[37] S. Vasvani, P. Kulkarni, D. Rawtani, *Int. J. Biol. Macromol.* **2020**, *151*, 1012.

[38] P. Taweechat, R. B. Pandey, P. Sompornpisut, *Carbohydr. Res.* **2020**, *493*, 108026.

[39] M. A. Selyanin, P. Y. Boykov, V. N. Khabarov, F. Polyak, *Hyaluronic Acid: Preparation, Properties, Application in Biology and Medicine (Eds: M.A. Selyanin, P.Y. Boykov, V.N. Khabarov and F. Polyak), John Wiley & Sons,* Hoboken, New Jersey **2015**, Ch. 4, p. 97. https://doi.org/10.1002/9781118695920.ch4

[40] I. Hargittai, M. Hargittai, *Struct. Chem.* **2008**, *19*, 697.

[41] E. Zimmerman, B. Geiger, L. Addadi, *Biophys. J.* **2002**, *82*, 1848.

[42] J. Lam, N. F. Truong, T. Segura, *Acta Biomater.* **2014**, *10*, 1571.

[43] A. Spadea, J. M. Rios de la Rosa, A. Tirella, M. B. Ashford, K. J. Williams, I. J. Stratford, N. Tirelli, M. Mehibel, *Mol. Pharmaceutics* **2019**, *16*, 2481.

[44] D. S. Bhattacharya, D. Svechkarev, J. J. Souchek, T. K. Hill, M. A. Taylor, A. Natarajan, A. M. Mohs, *J. Mater. Chem. B* **2017**, *5*, 8183.

[45] O. Gotov, G. Battogtokh, Y. T. Ko, *Mol. Pharmaceutics* **2018**, *15*, 4668.

[46] S. Luan, Y. Zhu, X. Wu, Y. Wang, F. Liang, S. Song, *ACS Biomater. Sci. Eng.* **2017**, *3*, 2410.

[47] J. Yoo, N. S. Rejinold, D. Lee, I. Noh, W.-G. Koh, S. Jon, Y.-C. Kim, *ACS Biomater. Sci. Eng.* **2020**, *6*, 494.

[48] I. S. Bayer, *Molecules* **2020**, *25*, 25.

[49] H. Knopf-Marques, M. Pravda, L. Wolfova, V. Velebny, P. Schaaf, N. E. Vrana, P. Lavalle, *Adv. Healthcare Mater.* **2016**, *5*, 2841.

[50] A. Cappelli, G. Grisci, M. Paolino, G. Giuliani, A. Donati, R. Mendichi, R. Artusi, M. Demiranda, A. Zanardi, G. Giorgi, S. Vomero, *J. Mater. Chem. B* **2014**, *2*, 4489.

[51] G. Valacchi, G. Grisci, C. Sticozzi, Y. Lim, M. Paolino, G. Giuliani, R. Mendichi, G. Belmonte, R. Artusi, A. Zanardi, P. Garofalo, G. Giorgi, A. Cappelli, L. Rovati, *J. Mater. Chem. B* **2015**, *3*, 7037.

[52] M. M. Buanafina, *Mol. Plant* **2009**, *2*, 861.

[53] A. Cappelli, M. Paolino, A. Reale, V. Razzano, G. Grisci, G. Giuliani, A. Donati, C. Bonechi, S. Lamponi, R. Mendichi, S. Battiato, F. Samperi, F. Makovec, M. Licciardi, L. Depau, C. Botta, *RSC Adv.* **2018**, *8*, 5864.

[54] J. Qian, B. Z. Tang, *Chem* **2017**, *3*, 56.

[55] M. Meldal, C. W. Tomøe, *Chem. Rev.* **2008**, *108*, 2952.

[56] A. Cappelli, M. Paolino, G. Grisci, V. Razzano, G. Giuliani, A. Donati, C. Bonechi, R. Mendichi, S. Battiato, F. Samperi, C. Scialabba, G. Giammona, F. Makovec, M. Licciardi, *Polym. Chem.* **2016**, *7*, 6529.

[57] M. Licciardi, C. Scialabba, G. Giammona, M. Paolino, A. Cappelli, *J. Nanopart. Res.* **2017**, *19*, 197.

[58] A. Atrei, C. Innocenti, S. Lamponi, S. Paesano, G. Leone, A. Reale, M. Paolino, A. Cappelli, *Mater. Sci. Eng. C* **2020**, *107*, 110271.

93

[59] M. Paolino, M. Licciardi, C. Savoca, G. Giammona, L. M. de Mohac, A. Reale, G. Giuliani, H. Komber, A. Donati, C. Savoca, G. Giammona, L. Modica de Mohac, A. Reale, G. Giuliani, H. Komber, A. Donati, G. Leone, A. Magnani, M. Anzini, A. Cappelli, *Pharmaceutics* **2019**, *11*, 675.

[60] M. Saletti, M. Paolino, L. Ballerini, G. Giuliani, G. Leone, S. Lamponi, M. Andreassi, C. Bonechi, A. Donati, D. Piovani, A. G. Schieroni, A. Magnani, A. Cappelli, *Pharmaceutics* **2022**, *14*, 14.

[61] A. Cappelli, G. Grisci, M. Paolino, V. Razzano, G. Giuliani, A. Donati, C. Bonechi, R. Mendichi, A. C. Boccia, M. Licciardi, C. Scialabba, G. Giammona, S. Vomero, *J. Mater. Chem. B* **2015**, *3*, 361.

SUPPORTING INFORMATION

Additional supporting information can be found online in the Supporting Information section at the end of this article.

4.6. Research article: "Click-Chemistry Cross-Linking of Hyaluronan Graft Copolymers".

Authors: **Mario Saletti**, Marco Paolino, Lavinia Ballerini, Germano Giuliani, Gemma Leone, Stefania Lamponi, Marco Andreassi, Claudia Bonechi, Alessandro Donati, Daniele Piovani, Aberto Giacometti Schieroni, Agnese Magnani, Andrea Cappelli.

Contribution: The Ph.D. candidate's contribution to this work refers to the synthesis and the preliminary characterization of compounds, as well as the revised of the published version of the manuscript.

In this research paper, an easy and sustainable cross-linking procedure by *click-chemistry* of HA has been developed to expand the chemistry of **HA-FA-Pg** macromolecules. In particular, the "*clickable*" propargyl groups of hyaluronane-based **HA-FA-Pg** graft copolymers showing low (i. e. Mw = 8.7 kDa) and medium molecular weight (i. e. Mw = 270 kDa) values have been exploited in a cross-linking procedure by *click-chemistry* by using a hexa(ethylene glycol) spacer. The obtained cross-linked HA derivatives **HA-FA-HEG-CL** have been characterized by NMR spectroscopy and from the point of view of their rheological and cytocompatibility features. Particularly, the interaction of resulting **HA-FA-HEG-CL** materials with water led to the formation of hydrogels which show a wide range of gelation features thanks to the possibility to tune the cross-linking degree. Consequently, different rheological behaviors have been observed, and the tunable rheological behavior of **HA-FA-HEG-CL** materials led to their applicability in different biomedical fields.

Article

Click-Chemistry Cross-Linking of Hyaluronan Graft Copolymers

Mario Saletti [1], Marco Paolino [1,*], Lavinia Ballerini [1], Germano Giuliani [1], Gemma Leone [1], Stefania Lamponi [1], Marco Andreassi [1], Claudia Bonechi [1], Alessandro Donati [1], Daniele Piovani [2], Alberto Giacometti Schieroni [2], Agnese Magnani [1] and Andrea Cappelli [1,*]

[1] Dipartimento di Biotecnologie, Chimica e Farmacia (Dipartimento di Eccellenza 2018–2022), Università degli Studi di Siena, Via Aldo Moro 2, 53100 Siena, Italy; mario.saletti@student.unisi.it (M.S.); lavinia.ballerini@student.unisi.it (L.B.); giuliani5@unisi.it (G.G.); gemma.leone@unisi.it (G.L.); stefania.lamponi@unisi.it (S.L.); marco.andreassi@unisi.it (M.A.); claudia.bonechi@unisi.it (C.B.); alessandro.donati@unisi.it (A.D.); agnese.magnani@unisi.it (A.M.)

[2] Istituto di Scienze e Tecnologie Chimiche "G. Natta"-SCITEC (CNR), Via A. Corti 12, 20133 Milano, Italy; piovani@ismac.cnr.it (D.P.); alberto.giacometti@scitec.cnr.it (A.G.S.)

* Correspondence: paolino3@unisi.it (M.P.); andrea.cappelli@unisi.it (A.C.); Tel.: +39-0577-234320 (A.C.)

Abstract: An easy and viable crosslinking procedure by click-chemistry (click-crosslinking) of hyaluronic acid (**HA**) was developed. In particular, the clickable propargyl groups of hyaluronane-based **HA-FA-Pg** graft copolymers showing low and medium molecular weight values were exploited in crosslinking by click-chemistry by using a hexa(ethylene glycol) spacer. The resulting **HA-FA-HEG-CL** materials showed an apparent lack of in vitro cytotoxic effects, tuneable water affinity, and rheological properties according to the crosslinking degree that suggests their applicability in different biomedical fields.

Keywords: hyaluronic acid; ferulic acid; click-chemistry; crosslinking; hydrogel

1. Introduction

Hyaluronic acid (**HA**, hyaluronan) is a glycosaminoglycan derivative playing a wide range of important roles in the human body [1]. Among them, **HA** is one of the extra-cellular matrix (ECM) components, whose main physiological functions range from the maintenance of cell osmotic balance and tissues structural support to lubrication, wear, and the damping of excessive loads on the joints [2]. One of the most intriguing **HA** functions is the constitution of a pericellular coat, which was suggested to affect the early stages of cell adhesion by interacting with the CD44 receptor [3]. The resulting activation of **HA**-CD44 signaling pathways controls different cell biological functions such as angiogenesis, cell migration, proliferation, aggregation, and adhesion to ECM components [2]. Furthermore, thanks to its ability to absorb large amounts of water, **HA** regulates tissues hydratation and represents a lubricant supplementation for the treatment of osteoarticular and eye diseases [4]. **HA** (cross-linked and non-cross-linked) derivatives have been largely used in the formation of biocompatible hydrogels for pharmaceutical and medical applications [5–7].

Ferulic acid (**FA**) is a cinnamic acid derivative (i.e., 4-hydroxy-3-methoxycinnamic acid), which is basically allocated in the plant cellular wall [8]. **FA** residues are inserted by means of an ester bond to primary alcohol of arabinose side chains in the cell wall arabinoxylan polysaccharides, where it is then involved in cross-linking polysaccharides and proteins during cell wall synthesis [8–13].

In our laboratories, the **HA** macromolecules were grafted with **FA** residues to obtain **HA-FA** graft copolymers [14,15], and subsequently the chemistry was used in the development of a tri-component polymer brush based on a polybenzofulvene derivative bearing nona(ethylene glycol) side chains [16,17]. In particular, this polybenzofulvene cylindrical brush was prepared by means of a convergent approach employing a copper(I)-catalyzed azide-alkyne 1,3-dipolar cycloaddition (CuAAC) of the suitable hyaluronan derivative

---

HA-FA-Pg (Figure 1) bearing propargyl groups bound to an **HA** backbone through **FA** fluorophores [16,18].
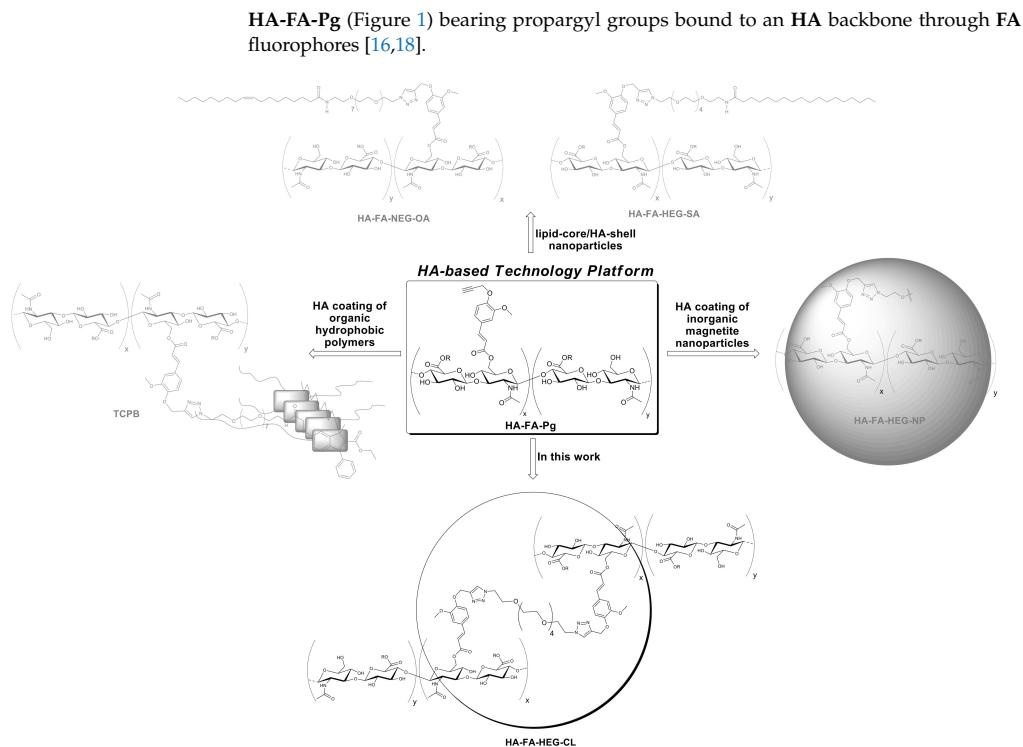
Figure 1. Development and applications of the **HA**-based technology platform employing **HA-FA-Pg** graft copolymers.

The procedure of coating a polybenzofulvene cylindrical brush surface with **HA** by means of **HA-FA-Pg** graft copolymers was gradually transformed into a technology platform which was applied to the coating of the surfaces of different nanostructures such as liposomes [19], self-assembling micelles [20], and magnetic nanoparticles [21].

With the aim of further extending the application of **HA-FA-Pg** graft copolymers to the development of new materials based on two natural compounds from biorenewable resources, we developed a cross-linking procedure in which the propargyl groups of **HA-FA-Pg** derivatives showing different molar mass and grafting degree values were exploited in the CuAAC coupling with a hexa(ethylene glycol) derivative terminated with azide groups at both ends (compound **1**, azido-**HEG**-azido) to obtain cross-linked **HA** derivatives (i.e., **HA-FA-HEG-CL**) (Figure 2).

First, the grafting procedure based on imidazolide derivative **2** was applied to **HA** showing a medium molar mass value (i.e., Mw = 270 KDa) to expand the **HA-FA-Pg** armamentarium in our laboratories. The resulting **HA(270)-FA-Pg** derivatives showing different grafting degree values (i.e., 10, 20, and 40%) were characterized and then used in the CuAAC coupling with compound **1** (azido-**HEG**-azido) to obtain cross-linked **HA** derivatives (i.e., **HA-FA-HEG-CL**) showing different cross-linking densities. The same cross-linking procedure was also applied to the previously published **HA-FA-Pg** graft copolymer showing a low molar mass value (i.e., Mw = 8.7 KDa) and a grafting degree of 20% (i.e., **HA-FA-Pg-3F**) to obtain cross-linked **HA** derivative **HA(8.7)-FA-HEG-CL-20**. The cross-linked **HA** derivatives were characterized from the point of view of their

rheological and cytocompatibility features and proposed as biocompatible material with high potentiality in biomedical applications.
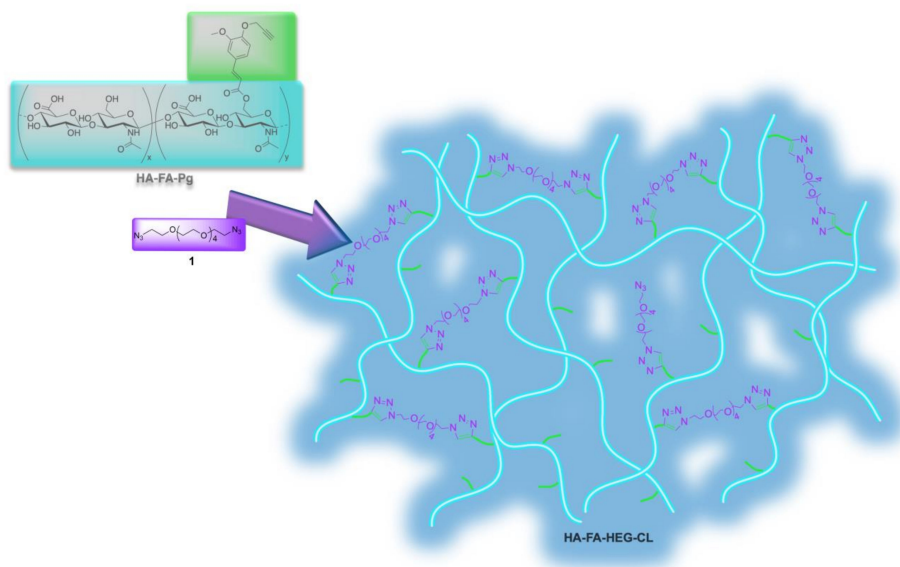
Figure 2. Click-chemistry cross-linking of **HA-FA-Pg** graft copolymers.

2. Experimental Section

2.1. Synthesis and Characterization

All reagents and solvents were purchased from Sigma–Aldrich and were used as received, with the exceptions noted. Merck TLC aluminum sheets, silica gel 60 F_{254} were used for TLC. NMR spectra were recorded with either a Bruker AMX-600 AVANCE or a Varian Mercury 300 spectrometer in the indicated solvents. The chemical shifts are referenced to the solvent signal (CDCl$_3$: δ (^{1}H) = 7.25 ppm, δ (^{13}C) = 77.0 ppm; CD$_3$OD: δ (^{1}H) = 3.34 ppm, δ (^{13}C) = 49.86 ppm) or to the signal of a trace acetone for solutions in D$_2$O (δ (^{1}H) = 2.22 ppm, δ (^{13}C) CH$_3$ = 30.9 ppm). Chemical shifts (δ) are reported in ppm and the H-H coupling constants (*J*) are reported in Hz. An Agilent 1100 LC/MSD running with an electrospray source was used in mass spectrometry measurements. The intermediate α,ω-diazido-hexa(ethylene glycol) **1** was synthesized as previously reported in [20].

2.1.1. Grafting Procedure for the Preparation of **HA(270)-FA-Pg** Copolymers

A mixture of medium molar mass **HA** (sodium hyaluronate from Biophil Italia SpA, Mw = 270 KDa, 1.0 g, 2.49 mmol in monomeric units) in formamide (10 mL) was heated at 50 °C into a two-necked round-bottomed 50 mL flask until the complete dissolution was obtained. To the resulting solution cooled to room temperature, triethylamine (TEA, 0.37 mL, 2.66 mmol) and **2** [16] (see the amounts in Table 1) were added in rapid sequence. The reaction mixture was homogenized by mechanical stirring and stirred overnight at room temperature. A 5% NaCl solution (5.0 mL) was then added, and the resulting mixture was stirred at room temperature for an additional 15 min. The graft copolymer was isolated by treatment of the mixture with acetone (40 mL) and purified by washing four times with the same solvent. The white solid was dried under reduced pressure to afford the expected **HA(270)-FA-Pg** graft copolymer. ^{1}H NMR (600 MHz, D$_2$O) (Figure 3).

2.1.2. Click-Chemistry Cross-Linking of **HA-FA-Pg** Graft Copolymers

Under an inert atmosphere, a 10 mL flask was charged with *tert*-butanol (2.0 mL), water (2.0 mL), and a solution of CuSO$_4$ pentahydrate (12.5 mg, 0.050 mmol) in 0.50 mL of water. A 1M solution of sodium ascorbate in water (0.50 mL) was then added and, subsequently, 1.0 mL of the resulting mixture was used as the catalyst. A mixture of **1** (see the amounts below) and the appropriate **HA-FA-Pg** graft copolymer (250 mg) in *tert*-butanol (25 mL) and water (25 mL) was treated with the catalyst solution (1.0 mL); the reaction mixture was stirred overnight at room temperature and then concentrated under reduced pressure. Purification of the gel residue by washing with acetone resulted in the corresponding **HA-FA-HEG-CL** material, which was dried under reduced pressure.

2.1.3. **HA(270)-FA-HEG-CL-10** Material

This cross-linked **HA** derivative was prepared by the above general procedure from **HA(270)-FA-Pg-10** (250 mg) and divalent hexa(ethylene glycol) derivative **1** (10 mg, 0.030 mmol) to obtain **HA(270)-FA-HEG-CL-10** material (246 mg) as a white solid. ^{1}H NMR (600 MHz, D$_2$O) (Figures 4 and 5A).

2.1.4. **HA(270)-FA-HEG-CL-20** Material

This cross-linked **HA** derivative was prepared using the above general procedure from **HA(270)-FA-Pg-20** (250 mg) and the divalent hexa(ethylene glycol) derivative **1** (23 mg, 0.069 mmol) to obtain **HA(270)-FA-HEG-CL-20** material (256 mg) as an off-white solid. ^{1}H NMR (600 MHz, D$_2$O) (Figure S1).

2.1.5. **HA(270)-FA-HEG-CL-40** Material

This cross-linked **HA** derivative was prepared using the above general procedure from **HA(270)-FA-Pg-40** (250 mg) and the divalent hexa(ethylene glycol) derivative **1** (41 mg, 0.123 mmol) to obtain **HA(270)-FA-HEG-CL-40** material (280 mg) as a pale yellow solid. ^{1}H NMR (600 MHz, D$_2$O) (Figure S1).

2.1.6. **HA(8.7)-FA-HEG-CL-20** Material

This cross-linked **HA** derivative was prepared using the above general procedure from **HA-FA-Pg-3F** (250 mg) and the divalent hexa(ethylene glycol) derivative **1** (20 mg, 0.060 mmol) to obtain **HA(8.7)-FA-HEG-CL-20** material (268 mg) as a brown solid. ^{1}H NMR (600 MHz, D$_2$O) (Figure S1).

2.1.7. Diethyl 3,3′-(((((3,6,9,12,15-Pentaoxaheptadecane-1,17-Diyl)Bis(1*H*-1,2,3-Triazole-1,4-Diyl))Bis(Methylene))Bis(Oxy))Bis(3-Methoxy-4,1-Phenylene))(2*E*,2′*E*)-Diacrylate (**6**)

To a solution of divalent hexa(ethylene glycol) derivative **1** (0.58 g, 1.75 mmol) in dry THF (25 mL) compound **5** (0.92 g, 3.54 mmol), DIPEA (1.52 mL, 8.75 mmol), and CuBr (0.13 g, 0.87 mmol) were added. The reaction mixture was stirred overnight at room temperature under a nitrogen atmosphere and then concentrated under reduced pressure. The resulting residue was partitioned between CH$_2$Cl$_2$ and a saturated NH$_4$Cl solution. The organic layer was dried over sodium sulfate and evaporated under reduced pressure. Purification of the residue by flash chromatography with ethyl acetate resulted in **6** (1.2 g, yield 80%) as an orange oil. ^{1}H NMR (300 MHz, CD$_3$OD): 1.29 (t, *J* = 7.1, 6H), 3.48 (s, 16H), 3.79 (s, 6H), 3.80–3.84 (m, 4H), 4.19 (q, *J* = 7.1 Hz, 4H), 4.49–4.55 (m, 4H), 5.16 (s, 4H), 6.37 (d, *J* = 16.0, 2H), 7.03–7.11 (m, 4H), 7.17 (d, *J* = 1.6, 2H), 7.57 (d, *J* = 15.9, 2H), 8.08 (s, 2H). MS (ESI): *m/z* 875.4 (M + Na$^+$).

2.1.8. Ethyl (*E*)-3-(4-((1-(17-Azido-3,6,9,12,15-Pentaoxaheptadecyl)-1*H*-1,2,3-Triazol-4-Yl)Methoxy)-3-Methoxyphenyl)Acrylate (**7**)

To a solution of divalent hexa(ethylene glycol) derivative **1** (0.64 g, 1.92 mmol) in dry THF (20 mL) compound **5** (0.50 g, 1.92 mmol), DIPEA (1.7 mL, 9.60 mmol), and CuBr (0.14 g, 0.96 mmol) were added. The resulting mixture was stirred overnight at room temperature

under a nitrogen atmosphere and then concentrated under reduced pressure. The resulting residue was partitioned between CH_2Cl_2 and a saturated NH_4Cl solution. The organic layer was dried over sodium sulfate and evaporated under reduced pressure. Purification of the residue by flash chromatography with ethyl acetate resulted in **7** (0.13 g, yield 11%) as a yellow oil. ^1H NMR (300 MHz, CD_3OD): 1.34 (t, *J* = 7.1, 3H), 3.31–3.35 (m, 2H), 3.53–3.60 (m, 16H), 3.60–3.64 (m, 2H), 3.84 (s, 3H), 3.85–3.89 (m, 2H), 4.22 (q, *J* = 7.1, 2H), 4.56–4.60 (m, 2H), 5.22 (s, 2H), 6.41 (d, *J* = 15.9, 1H), 7.08–7.16 (m, 2H), 7.22 (d, *J* = 1.7, 1H), 7.61 (d, *J* = 16.0, 1H), 8.13 (s, 1H). MS (ESI): *m/z* 615.3 (M + Na$^+$).

2.1.9. (2*E*,2'*E*)-3,3'-(((((3,6,9,12,15-Pentaoxaheptadecane-1,17-Diyl)Bis(1*H*-1,2,3-Triazole-1,4-Diyl))Bis(Methylene))Bis(Oxy))Bis(3-Methoxy-4,1-Phenylene))Diacrylic Acid (**3**)

To a solution of compound **6** (0.89 g, 1.04 mmol) in ethanol (16 mL), a 2 N solution of NaOH (10 mL) was added, and the resulting reaction mixture was heated under reflux for 2 h. Then, the reaction mixture was cooled to 0 °C and 3 N HCl was added dropwise until pH 2, and the crude was extracted with CH_2Cl_2. The organic layer was dried over sodium sulfate and evaporated under reduced pressure to give us compound **3** (0.75 g, yield 90.5%) as an off-white solid. ^1H NMR (600 MHz, $CDCl_3$): 3.57 (m, 16H), 3.83 (t, *J* = 5.1, 4H), 3.85 (s, 6H), 4.51 (t, *J* = 4.9, 4H), 5.30 (s, 4H), 6.28 (d, *J* = 15.9, 2H), 7.04 (m, 6H), 7.64 (d, *J* = 15.8, 2H), 7.84 (s, 2H). MS (ESI): *m/z* 819.3 (M + Na$^+$). ^1H NMR (600 MHz, D_2O-NaOD): Figure 6.

2.1.10. (*E*)-3-(4-((1-(17-Azido-3,6,9,12,15-Pentaoxaheptadecyl)-1*H*-1,2,3-Triazol-4-Yl)Methoxy)-3-Methoxyphenyl)Acrylic Acid (**4**)

To a solution of compound **7** (0.13 g, 0.22 mmol) in ethanol (5.0 mL), a 2 N NaOH solution (2.0 mL) was added, and the resulting mixture was heated under reflux for 2 h. Then, the reaction mixture was cooled to 0 °C and 3 N HCl was added dropwise until pH 2, and the crude was extracted with CH_2Cl_2. The organic layer was dried over sodium sulfate and evaporated under reduced pressure to give us compound **4** (0.12 g, yield 97%) as an off-white solid. ^1H NMR (600 MHz, $CDCl_3$): 3.36 (t, *J* = 5.1, 2H), 3.51–3.69 (m, 20H), 3.86 (t, *J* = 5.1, 2H), 3.88 (s, 3H), 4.53 (t, *J* = 5.0, 2H), 5.33 (s, 2H), 6.30 (d, *J* = 15.9, 1H), 7.05–7.09 (m, 3H), 7.67 (d, *J* = 15.9, 1H), 7.86 (s, 1H). MS (ESI): *m/z* 587.2 (M + Na$^+$).

2.2. SEC-MALS

The characterization of the molecular weight distribution (MWD) was performed by a multi-angle laser light scattering (MALS) detector on-line to a size exclusion chromatography (SEC or GPC) system. The SEC-MALS multi-detector system consisted of an Alliance 2695 chromatograph from Waters (USA) with two on-line detectors: a MALS Dawn DSP-F photometer from Wyatt (USA) and a 410 differential refractometer (DRI) from Waters as a concentration detector.

SEC experimental conditions were the following: two Shodex OHpak SB (806 HQ–805 HQ, 13 μm of particle size) columns from Showa Denko (J), 35 °C of temperature, 0.8 mL/min of flow rate, and about 2 mg/mL of a sample concentration. Two solvents (0.2 M NaCl + 0.1 M phosphate buffer pH 7.4 and 0.1 M carbonate buffer pH 10) were used as a mobile phase to try to overcome the solubility decrease produced by the grafting increase.

The MALS calibration constant was calculated using toluene as a standard by assuming a Rayleigh Factor of $1.406 \cdot 10^{-5}$ cm^{-1}. MALS angular normalization was performed by measuring the scattering intensity of a BSA globular protein (M = 66.4 kg/mol, R_g = 2.9 nm) assumed to act as an isotropic scatterer. It is known that the on-line MALS detector measures—for each polymeric fraction eluted from the SEC columns—the molecular weight (M), and when the angular dependence of the scattered light is experimentally measurable, the molecular size is also generally known as the radius of gyration (Rg). The SEC-MALS system was described in detail elsewhere [22,23]. The differential refractive index increment of the polymer with respect to the solvent (dn/dc = 0.140 mL/g) was calculated from the area of the DRI concentration detector after accurate calibration.

2.3. Swelling Performance

2.3.1. Swelling Kinetics

5 mg of each hydrogel (dry state) were positioned on a cell culture strainer and immersed in bidistilled water at 37 °C. The weight of each sample was monitored until it reached the swelling equilibrium, and the water uptake (WU) was calculated using Formula (1):

$$WU = [(Ws - Wd/Wd)] \cdot 100 \tag{1}$$

The water content of the hydrogel was calculated using the Formula (2):

$$WC = [(Ws - Wd)/Ws] \cdot 100 \tag{2}$$

where the Ws and Wd are the weight of swollen and dried hydrogel, respectively.

2.3.2. Total Water

Swollen samples (15–20 mg) were put in a platinum crucible and heated from 30 °C to 250 °C with a rate of 10 °C/min under nitrogen purge gas using a Q600 analyzer (TA Instruments-Waters, New Castle, DE, USA). The percent weight loss in the temperature range 30–120 °C permits quantifying the total water (WH).

2.3.3. Free and Bound Water

Swollen samples (5 mg) were sealed in anodized aluminium pans, cooled to −40 °C, and then heated up (2 °C/min) to 40 °C using a DSC-TA Q 2000 to obtain the percentages of freezable water (free and bound water) following the procedure reported by Li et al. [24]. Briefly, the total weight of water (WH), obtained by TGA, is the sum of freezing (WfH) and non-freezing (WnfH) water weights (3):

$$WH = WfH + WnfH \tag{3}$$

DSC thermograms of frozen hydrogels and of bidistilled water (from which the latent heat ΔH was obtained) permit quantifying latent heat ΔH of the freezing water (ΔHm). The freezing water (WfH) was derived using Equation (4):

$$WfH/Ws = \Delta Hm/\Delta H \tag{4}$$

where Ws is the weight of the swollen hydrogel.

By the difference non-freezing (WnfH), water weight can be obtained (Equation (3)).

2.4. Rheological Analysis

All rheological analyses were carried out on swollen samples at 37 °C using a Discovery HR-2 Rheometer (TA Instruments) equipped with a Peltier steel plate environmental system. Preliminary strain sweep tests were run to identify the Linear Viscoelasticity Region (LVR) recording elastic modulus of the materials at fixed oscillation frequencies (i.e., 0.1 Hz, 1 Hz, and 10 Hz) while varying the strain % from 0.1 to 10% [25].

Elastic (G') and viscous (G'') moduli of samples (shear strain: 0.25%) were measured as a function of oscillation frequency in the range of 0.1–10 Hz using a plate–plate geometry (Ø = 4 cm).

Viscosity measurements were performed by shear rate experiments (shear ramp from 0.01 to 250 s^{-1}) using a 1° cone-plate stainless steel geometry (40 mm, truncation 28.0 μm).

2.5. Thermal Behavior

Thermogravimetric Analysis was conducted using a Q600 thermogravimetric analyzer (TA Instruments-Waters, New Castle, DE, USA). Samples (15–20 mg) at the dry state were inserted into a platinum crucible and heated from room temperature to 600 °C (heating ramp 10 °C/min) under nitrogen gas. Samples were set up in three replicates.

101

2.6. Cell Culture and Cytotoxicity Test

In order to evaluate the in vitro cytotoxicity of **HA-FA-HEG-CL** materials, the direct contact tests, proposed by ISO 10995-5, Biological evaluation of medical devices–Part 5: Tests for cytotoxicity: in vitro methods was used [26]. This test is suitable for samples with various shapes, sizes, or physical status (i.e., liquids or solids). The evaluation of in vitro acute toxicity does not depend on the final use for which the product is intended, and the document ISO 10995-5:2009 recommends many cell lines from the American Type Collection. Among them, to test **HA-FA-HEG-CL** cytotoxicity, NIH3T3 mouse fibroblasts were chosen (American Type Culture Collection (USA). Fibroblasts NIH3T3 were propagated in DMEM supplemented with 10% fetal calf serum, 1% L-glutamine-penicillin-streptomycin solution, and 1% MEM non-essential amino acid solution, and then incubated at 37 °C in a humidified atmosphere containing 5% CO_2. Once at confluence, the cells were washed with 0.1 M PBS, separated with trypsin-EDTA solution, and centrifuged at 1000 r.p.m. for 5 min. The pellet was re-suspended in complete medium (dilution 1:15).

Cells (1.5×10^4) suspended in 1 mL of complete medium were seeded in each well of a 24 well round multidish and incubated at 37 °C in an atmosphere of 5% CO_2. After 24 h of culture, the culture medium was discharged and the swelled hydrogel (3 mg) was added to each well. The samples were set up in three replicates. Low density polyethylene (LDPE) (U.S. Pharmacopeia (Rockville, MD, USA) was used as the negative control and organo-tin stabilized polyurethane as the positive control (Gradko International Limited, Winchester, UK).

Cell viability was evaluated by Neutral Red uptake after 24, 48, and 72 h of incubation with 3T3 following the procedure previously reported [27].

The analysis of cell morphology after 24 h of incubation was performed via the optical microscopy observation of cells in contact with the test samples by using an inverted, phase-contrast microscope (Olympus IX50) equipped with a video camera (Optika). Reactivity of the test sample was indicated by malformation, degeneration, and the lysis of cells.

3. Results and Discussion

3.1. Synthesis of HA(270)-FA-Pg and HA-FA-HEG-CL Derivatives

HA(270)-FA-Pg graft copolymers were synthesized by reaction of medium molar mass (i.e., Mw = 270 Kda) **HA** with imidazolide derivative **2** [16], as depicted in Scheme 1.

The grafting procedure was performed in the presence of triethylamine (TEA) as the base in formamide as the solvent to obtain the corresponding graft copolymers **HA(270)-FA-Pg**. The stoichiometric ratio between **2** and **HA** (i.e., **2**/**HA** ratio, Table 1) varied from 12.5 to 50%, and the isolation of the copolymers from the reaction mixture was carried out via precipitation with acetone to obtain samples as white solids.

Table 1. Reaction parameters in the grafting of **HA(270)** to **HA(270)-FA-Pg** graft copolymers with imidazolide derivative **2**.

Copolymer	HA (g)	HA (mmol)	2/HA Ratio (%)	Grafting Degree [a] (%)	Convers. [b] (%)
HA(270)-FA-Pg-10	1.0	2.49	12.5	10	80
HA(270)-FA-Pg-20	1.0	2.49	25	20	80
HA(270)-FA-Pg-40	1.0	2.49	50	40	80

[a] The determination of the grafting degree was made by ^{1}H NMR spectroscopy after hydrolysis with NaOD in D_2O as described in ref. [14]. [b] The conversion into ferulate was calculated from the substitution degree and stoichiometric ratio **2**/**HA**.
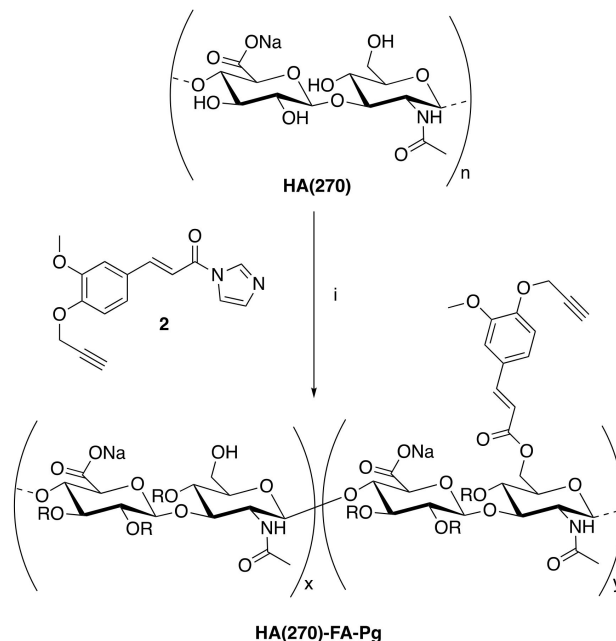
Scheme 1. The grafting reaction of medium molar mass **HA**(270) with imidazolide derivative **2** for the preparation of the **HA(270)-FA-Pg** graft copolymers. **Reagents**: (i) $HCONH_2$, TEA. **Substituents**: R = H or $C_{13}H_{11}O_3$.

The data shown in Table 1 suggested that the GD value could be adjusted in the range of 10–40% by employing the correct **2**/**HA** stoichiometric ratios with high conversion values (i.e., 80%).

HA(270)-FA-Pg graft copolymers were then submitted to the CuAAC dimerization reaction with divalent azide derivative **1** (Scheme 2) to obtain cross-linked **HA(270)** derivatives (i.e., **HA(270)-FA-HEG-CL**).

The dimerization reaction was performed by employing the three **HA(270)-FA-Pg** samples showing grafting degree values of 10, 20, and 40% in the aim of obtaining **HA(270)-FA-HEG-CL** derivatives bearing different densities of cross-linking groups affecting the mobility of the **HA(270)** backbone in **HA(270)-FA-HEG-CL-10**, **HA(270)-FA-HEG-CL-20**, and **HA(270)-FA-HEG-CL-40** materials. Thus, the amounts of divalent azide derivative **1** were calculated in order to induce the exhaustive dimerization of the propargylated ferulate residues grafting the **HA** backbones of **HA-FA-Pg** graft copolymers. As described previously, the catalytic species copper(I) was generated in situ from $CuSO_4$ with sodium ascorbate to perform the CuAAC dimerization reaction under very mild conditions.

In order to explore the role of the backbone length, the dimerization reaction was also applied to the previously published **HA-FA-Pg** graft copolymer showing a low molar mass value (i.e., Mw = 8.7 KDa) and a grafting degree of 20% (i.e., **HA-FA-Pg-3F**) to obtain **HA(8.7)-FA-HEG-CL-20** material.

Finally, compounds **3** and **4** were synthesized as described in Scheme 3 to be used as standard compounds in hydrolysis studies.
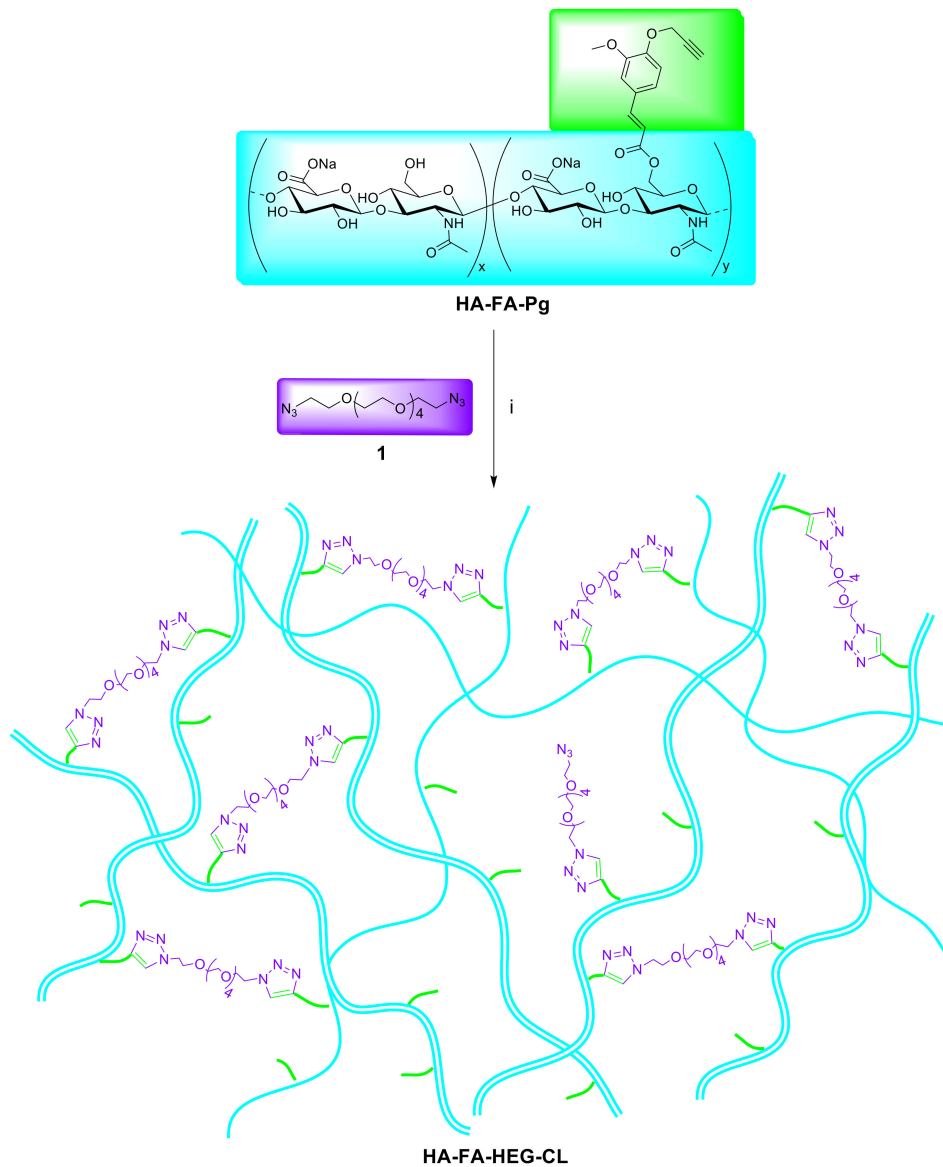
Scheme 2. The click chemistry dimerization of **HA-FA-Pg** with divalent azide derivative **1**, leading to **HA-FA-HEG-CL** materials. **Reagents**: (i) CuSO$_4$, sodium ascorbate, tert-BuOH, H$_2$O.
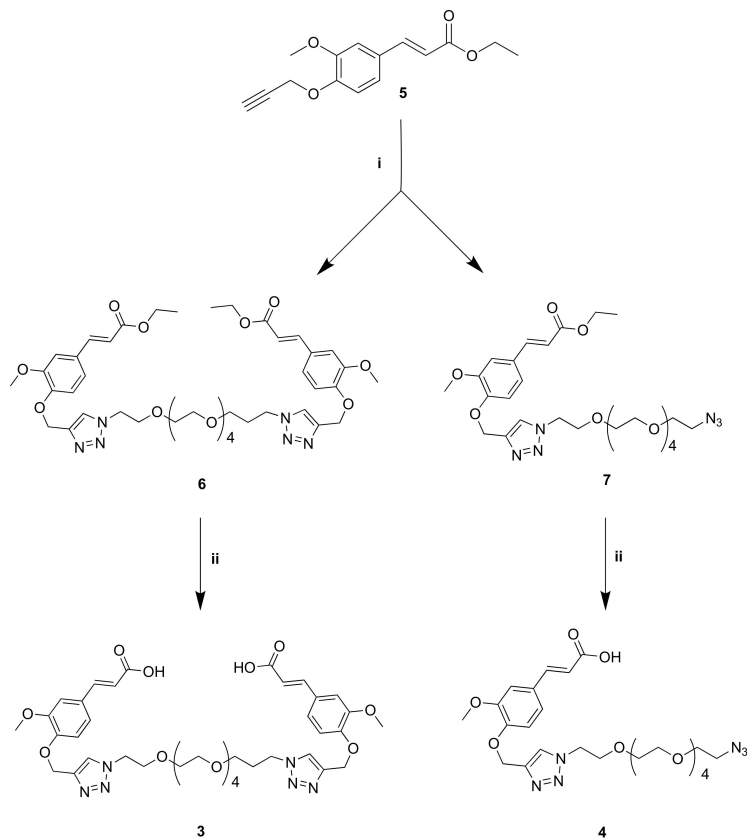
Scheme 3. The synthesis of standard compounds **3** and **4**. **Reagents:** (i) compound **1**, CuBr, DIPEA, THF; (ii) 2N NaOH, H$_2$O, C$_2$H$_5$OH.

Compounds **3** and **4** and their respective ethyl ester precursors **6** and **7** were synthesized from the intermediate ferulate **5** bearing a propargyl group [28] and an hexa(ethylene glycol) derivative terminated with azide groups at both ends (compound **1**, azido-**HEG-**azido) [20]. In particular, a copper(I)-catalyzed azide alkyne 1,3-dipolar cycloaddition (CuAAC) reaction was performed using copper(I) bromide as a catalyst in the presence of *N,N*-diisopropylethylamine (DIPEA) as the base in THF. The stoichiometric ratio of the reaction between propargylated ferulate **5** and compound **1** was optimized in order to obtain the divalent derivative **6** and the monovalent derivative **7** with different yields. Nevertheless, while the former was achieved with good conversion value (i.e., 80%), the latter was obtained with low yield (i.e., 11%) due to the fact that the reaction mainly evolved towards the formation of the divalent derivative **6**. Then, it was necessary to hydrolyze the ester group of compounds **6** and **7** with 2 N NaOH solution in ethanol to obtain the respective compounds **3** and **4** with very good yields to be used as standards in hydrolysis studies.

3.2. Structure of *HA-FA-Pg* and *HA-FA-HEG-CL* Derivatives

The structure of newly prepared **HA-FA-Pg** and **HA-FA-HEG-CL** derivatives was researched by ^{1}H NMR spectroscopic studies using D_2O as the solvent. The comparative analysis of the ^{1}H NMR spectra obtained with the three **HA(270)-FA-Pg** graft copolymers (Figure 3) substantiated the efficacious link between **HA** and **1** in the conditions used in the grafting reaction.
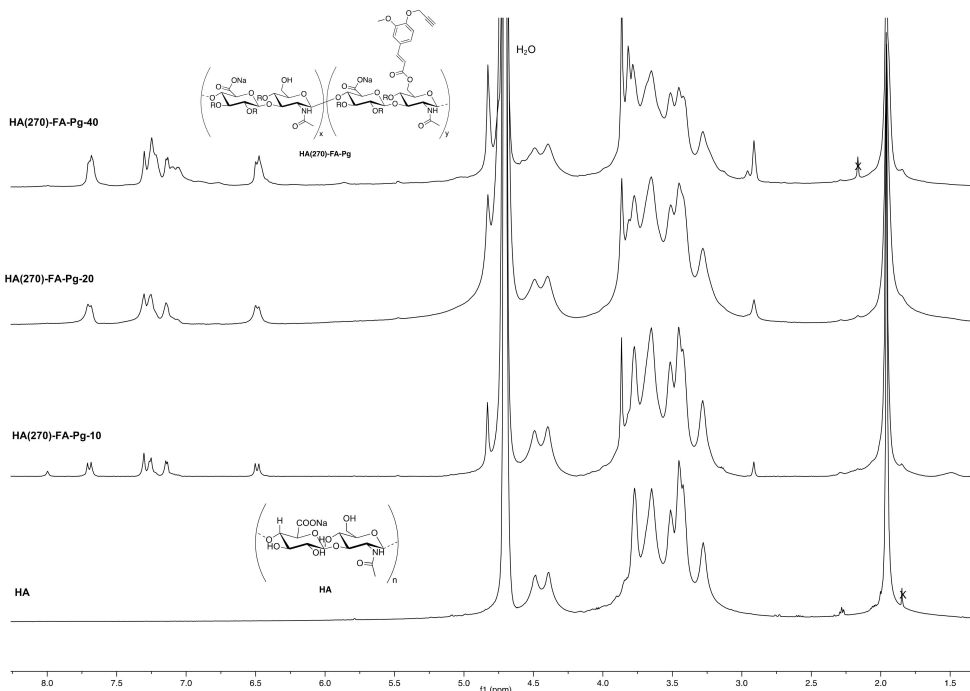
Figure 3. ^{1}H NMR spectra obtained with the three newly synthesized **HA(270)-FA-Pg** graft copolymers (D_2O, 600 MHz) compared with that obtained with a starting **HA** sample.

As expected, the ^{1}H NMR spectra of the graft copolymers showed, in their down-field region, signals attributed to the propargylated **FA** residues. The relative intensity of these signals increased from **HA(270)-FA-Pg-10** (grafting degree around 10%) to **HA(270)-FA-Pg-20** (grafting degree around 20%) and **HA(270)-FA-Pg-40** (grafting degree around 40%), paralleling the increase of the grafting degree. Furthermore, the broadness of the signal pattern appearing in the aromatic region was considered to be a further support of the effective coupling. The comparative analysis of the aromatic peaks at around 7.2 ppm suggested the presence of structural inhomogeneities, which appeared to increase with the increase in grafting degree. This observation was interpreted in terms of different sites of functionalization in addition to the most accessible primary OH groups. Moreover, the presence of a very small singlet at around 8.0 ppm may be related to the presence of formyl groups deriving from the formamide used as the reaction solvent.

In order to evaluate the occurrence of the click chemistry cross-linking of **HA(270)-FA-Pg** graft copolymers (i.e., **HA(270)-FA-Pg-10**, **HA(270)-FA-Pg-20**, and **HA(270)-FA-Pg-40**) leading **HA(270)-FA-HEG-CL** derivatives (i.e., **HA(270)-FA-HEG-CL-10**, **HA(270)-FA-HEG-CL-20**, and **HA(270)-FA-HEG-CL-40**, respectively), the ^{1}H NMR spectrum of

HA(270)-FA-HEG-CL-10 was analyzed in comparison to that of its corresponding synthetic precursor, the graft copolymer **HA(270)-FA-Pg-10** (Figure 4).
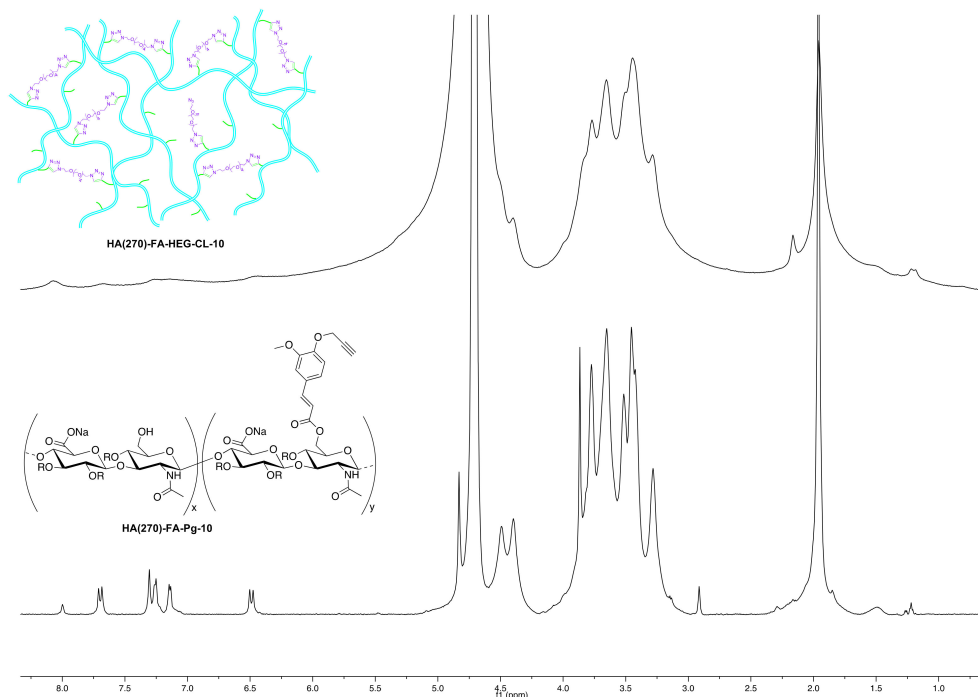
Figure 4. Comparison of the ^{1}H NMR spectrum obtained with the cross-linked **HA(270)-FA-HEG-CL-10** material (D$_2$O, 600 MHz) to that obtained with its corresponding synthetic precursor, the graft copolymer **HA(270)-FA-Pg-10**.

As expected, the disappearance of the singlet signal at around 2.91 ppm assigned to the alkyne hydrogen atom of **HA(270)-FA-Pg-10** graft copolymer and the presence of a new singlet at around 8.1 ppm in the spectrum of **HA(270)-FA-HEG-CL-10** material supported the conversion of the alkyne portion into the triazole one, as it usually happens in a CuAAC coupling reaction. Thus, this observation was taken into account as a strong structural evidence concerning **HA(270)-FA-HEG-CL-10** material. Moreover, the remarkable line broadening affecting all the peaks in the spectrum of **HA(270)-FA-HEG-CL-10** material is strongly suggestive of the reduced mobility in the cross-linked macromolecules of this material.

With the aim of identifying the actual cross-linking species, a gel dispersion of **HA(270)-FA-HEG-CL-10** material in (deuterated) water was treated with sodium hydroxide at room temperature, and a rather rapid gel–sol transition was observed. When the same experiment was performed in an NMR tube and ^{1}H NMR spectra were registered at regular time intervals, we obtained the results summarized in Figure 5.
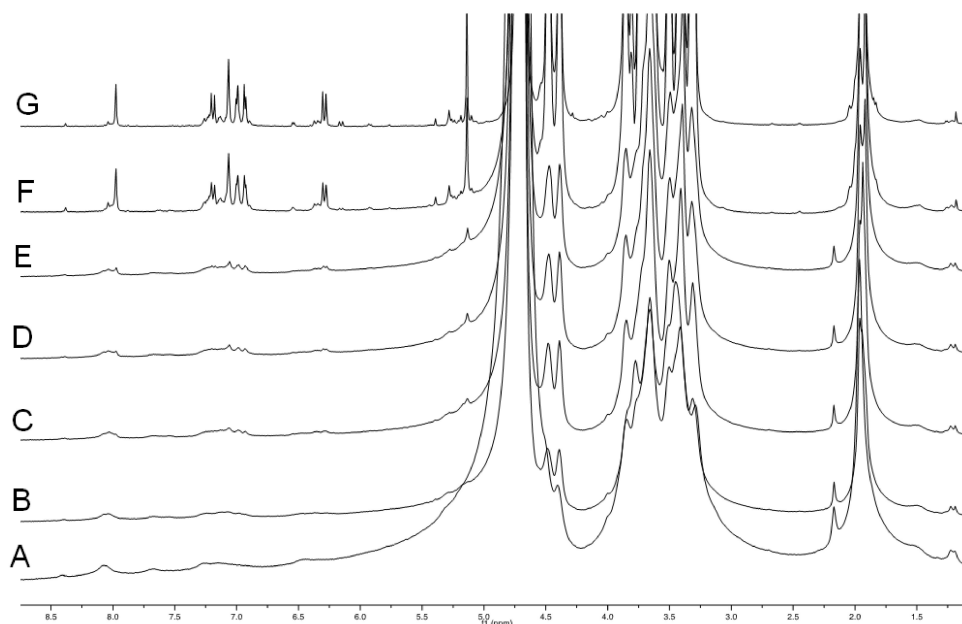
Figure 5. The comparison of ^{1}H NMR spectra obtained when a gel dispersion of **HA(270)-FA-HEG-CL-10** material in deuterated water was treated with NaOD at room temperature in an NMR tube, and ^{1}H NMR spectra were registered at regular time intervals. A: before the sodium hydroxide addition; B: immediately after the sodium hydroxide addition; C: after 10 min at room temperature; D: after 20 min at room temperature; E: after 30 min at room temperature; F: after 90 min at room temperature; G: after 24 h at room temperature.

The results shown in Figure 5 suggest that the presence of sodium hydroxide is capable of promoting the cleavage of the ester bond linking ferulate residues to the **HA** backbone with the formation of a major ferulate derivative and 2–3 minor products.

In order to identify the major product of the hydrolysis, dimeric compound **3** was added to the hydrolysis mixture, the result of which is shown in Figure 6.

Figure 6 shows that dimeric compound **3** is the major product of hydrolysis, and as expected, this compound is responsible for the cross-linking in **HA(270)-FA-HEG-CL-10** when covalently bound to **HA** hydroxy groups. In fact, when compound **3** was added to the hydrolysis mixture in the NMR tube, a significant increase was observed in the intensity of the signals attributed to the major product. Very similar results were obtained with **HA(270)-FA-HEG-CL-20** material, but the ^{1}H NMR hydrolysis experiments performed with **HA(270)-FA-HEG-CL-40** material suggested that the cross-linking of the highly grafted **HA(270)-FA-Pg-40** copolymer was not exhaustive (Figure S2). We assumed that during the cross-linking process, the increasing rigidity of the partially cross-linked material prevents the exhaustive combination of all the clickable groups present in the highly grafted copolymer. Thus, with the progress of the cross-linking process leading to **HA(270)-FA-HEG-CL-40** material and the increase in rigidity, divalent azide derivative **1** is capable of performing only the first CuAAC reaction, but not the complete dimerization.
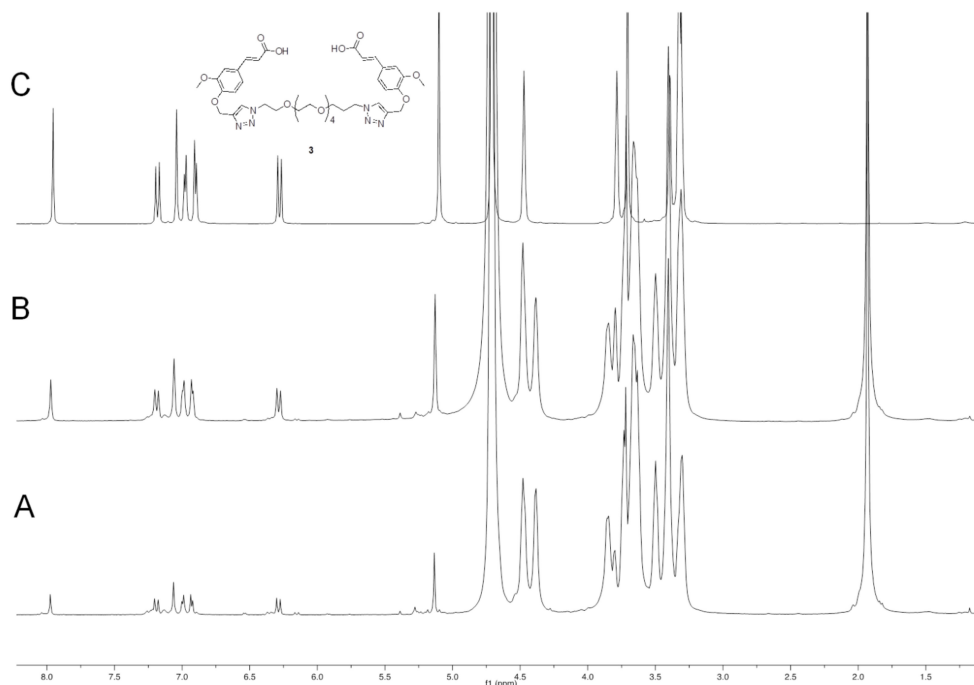
Figure 6. The comparison of ^{1}H NMR spectra obtained when a gel dispersion of **HA(270)-FA-HEG-CL-10** material in deuterated water was treated with sodium hydroxide at room temperature in an NMR tube for 24 h. (**A**): before the addition of compound **3**; (**B**): immediately after addition of compound **3**; (**C**): ^{1}H NMR spectrum of a solution of reference compound **3** in deuterated water containing NaOD.

3.3. Molecular Characterization of *HA(270)-FA-Pg* Derivatives

The characterization of the macromolecular features of **HA(270)-FA-Pg** graft copolymers was performed in comparison of the starting **HA** by means of a multi-angle laser light scattering (MALS) absolute detector on-line to a size exclusion chromatography (SEC) system. Two solvent systems (i.e., 0.2 M NaCl + 0.1 M phosphate buffer pH 7.4 or 0.1 M carbonate buffer pH 10) were employed as the mobile phases to circumvent the solubility decrease produced by the increase in the grafting degree. Comparable results were obtained for **HA(270)-FA-Pg-10** and **HA(270)-FA-Pg-20** in the two solvent systems, and **HA(270)-FA-Pg-40** was difficult to be analyzed at both pH values. The best results were obtained by using carbonate buffer at pH 10, and SEC-MALS results such as the molecular weight of the peak of the chromatogram (M_p), the weight-average of the molecular weight (M_w), and the polydispersity index M_w/M_n (where M_n denotes the numeric-average of the molecular weight) are summarized in Table 2.

Table 2. Macromolecular features of **HA(270)-FA-Pg** graft copolymers compared to those of starting **HA(270)**.

Sample	dn/dc (mL/g)	M_p (kg/mol)	M_w (kg/mol)	M_w/M_n	Rec. Mass [a] (%)	Grafting [b] (%)
HA(270) [c]	0.150	188	274	3.89	94	0
HA(270)-FA-Pg-10 [d]	0.140	278	330	2.09	80	10
HA(270)-FA-Pg-20 [d]	0.140	359	387	2.21	68	20
HA(270)-FA-Pg-40 [d]	0.140	347	288	2.49	21	40

[a] Recovered Mass: the fraction of the polymeric sample eluting from the SEC columns. [b] The determination of the grafting degree was made by ^{1}H NMR spectroscopy after hydrolysis with NaOD in D_2O as described in ref [14]. [c] The values of native **HA(270)** reported in the table were obtained with 0.2 M NaCl + 0.1 M phosphate buffer pH 7.4. [d] The values of the graft copolymers were obtained with 0.1 M carbonate buffer pH 10.

The molecular weight of the starting **HA(270)** sample was in the expected range, and the molecular weight distribution was substantially broad (M_w/M_n about 3.9). The Recovered Mass values of the samples showing low grafting degrees were relatively high and adequate for estimating the molecular weight distribution of those graft copolymers after the derivatization reactions.

Thus, the grafting reaction leading to **HA(270)-FA-Pg-10** and **HA(270)-FA-Pg-20** derivatives produced only small increases in molar weight of the macromolecules (i.e., the M_w average increased from 274 kg/mol of the starting **HA(270)** to 330 kg/mol of the **HA(270)-FA-Pg-10** derivative showing 10% of grafting or to 387 kg/mol of the **HA(270)-FA-Pg-20** derivative showing 20% of grafting).

The derivatization reaction can be assumed to produce two different effects on molecular weight distributions that can work simultaneously in opposite ways. The most obvious effect is the molecular weight increase produced by the grafting, while the less obvious, but however possible effect, is the molecular weight decrease produced by an eventual degradation. The results summarized in Table 2 suggest that the degradation of the starting **HA(270)** biopolymer is also very low for a high level of grafting.

Unfortunately, the molecular weight data (Table 2) are influenced by the insolubility increases when the grafting degree increases. Specifically, the low Recovered Mass value of the **HA(270)-FA-Pg-40** sample ($\approx$21%) means that the molecular weight of this sample is probably underestimated because the higher molecular weight fractions are not soluble.

3.4. Swelling Performance

The swelling performance of a polymeric hydrogel is strictly related to its capability to bind water molecules. Water content (WC) and water uptake (WU) were quantified. All hydrogels reached the swelling equilibrium within 24 h. The water uptake decreased from 8600 recorded for **HA(270)-FA-HEG-CL-10** to 2600 for **HA(270)-FA-HEG-CL-40,** with sample **HA(270)-FA-HEG-CL-20** showing an intermediate WU value of 2800. The obtained values highlighted a significant difference between sample **HA(270)-FA-HEG-CL-10** and the two samples with a higher grafting degree, whereas no significant difference was found in terms of WU between **HA(270)-FA-HEG-CL-20** and **HA(270)-FA-HEG-CL-40**. WC showed the same trend. This observation supported the assumption that **HA(270)-FA-HEG-CL-20** and **HA(270)-FA-HEG-CL-40** have a similar crosslinking degree despite the different grafting degree. **HA(8.7)-FA-HEG-CL-20** showed the highest values of WU and WC, reaching 9780 and 99%, respectively, thus suggesting a very soft matrix.

The swelling process can be schematized as a three-step process. During the first phase, water molecules strictly bind to the hydrophilic sites of the polymer. These water molecules that show a limited mobility are uniformly distributed along the polymer skeleton (non freezing water: nfw). After the formation of this first hydration layer, other water molecules layered above the first water layer to form the maximum amount of hydrogen bonds. This second layer showing a larger mobility can be frozen (freezing bound water: fbw). Finally, during the third step, all of the network is fulfilled by water (bulk water, i.e., free freezing

water: ffw) [29]. Consequently, the quantification of the three species into which water can be subdivided is of outmost importance.

The presence of a double peak for totally swollen hydrogels (Figure 7) permitted subdividing the freezable water into bound freezing water (Wbf) and free freezing water (Wff), respectively. All the data are reported in Table 3.
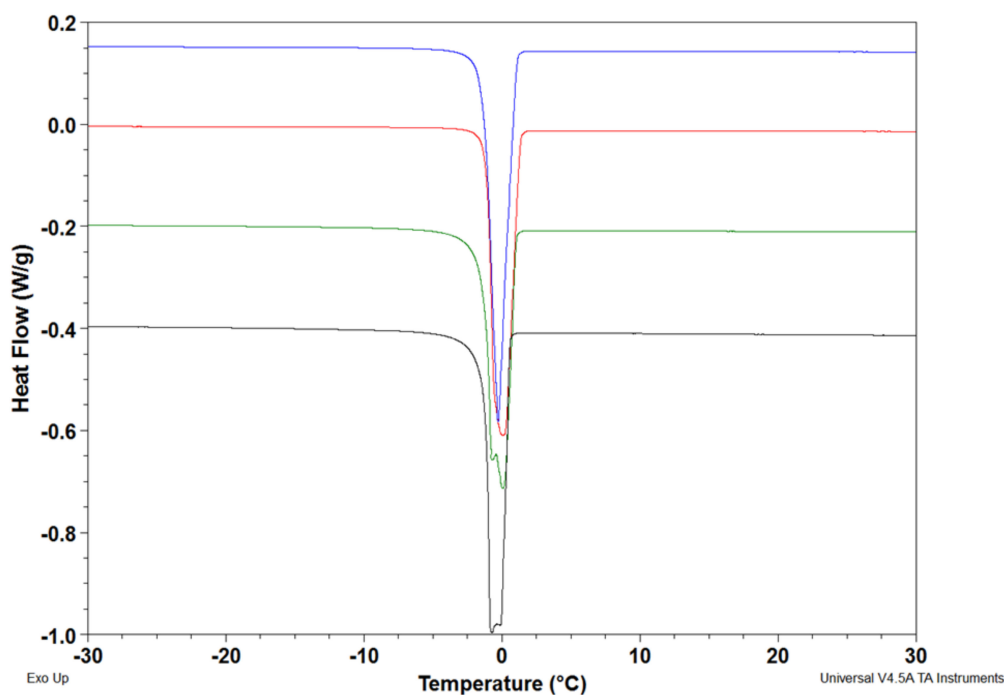
Figure 7. The DSC endothermic melting profile of frozen completely swollen hydrogels obtained with **HA(270)-FA-HEG-CL-20** (green), **HA(270)-FA-HEG-CL-40** (black), **HA(270)-FA-HEG-CL-10** (red), and **HA(8.7)-FA-HEG-CL-20** (blue).

Table 3. WC % (% water content by TGA), Wtot (total water by TGA), Wnf (not freezing Water by DSC), and Wf (freezing Water by DSC) % fW: percentage of freezing water. The subdivision of freezing water in free freezable water (Wff) and bound freezable water (Wbf) expressed as percentage.

Sample	30–120 °C WC (%)	Wsg (mg)	Wtot (mg)	Wf (mg)	Wff-Wbf (%)	Wnf (mg)
HA(270)-FA-HEG-CL-10	98	17.8	17.4 (100%)	16.2 (93%)	98-2	1.2 (7%)
HA(270)-FA-HEG-CL-20	97	13.8	13.4 (100%)	11.5 (87%)	82-18	1.8 (13%)
HA(270)-FA-HEG-CL-40	93	8.37	7.78 (100%)	6.95 (90%)	88-12	0.82 (10%)
HA(8.7)-FA-HEG-CL-20	97	19.4	18.8 (100%)	18.0 (95%)	97-3	0.88 (8%)

The used protocol, as reported in the experimental section, permits quantifying the freezing water and by difference with the total water, quantified by TGA, obtaining the not freezing water (Wnf). As shown by data summarized in Table 3, no significant differences can be observed among the samples in terms of water type distribution. Indeed, the highest percentage is represented by the free freezing water which ranges from 87% found for

HA(270)-FA-HEG-CL-20 to 95% found for **HA(8.7)-FA-HEG-CL-20**. Among the 270 kDa series, accordingly with the WC and WU measurements, **HA(270)-FA-HEG-CL-10** shows the highest percentage of Wf and consequently the lowest percentage of not freezable water or the water strictly bound to the matrix polymeric chains (7% against 10–13% found for the hydrogels with a higher grafting degree). Despite the lower grafting degree, **HA(270)-FA-HEG-CL-20** showed a lower amount of Wf, and consequently a higher percentage of not freezable water, in comparison with **HA(270)-FA-HEG-CL-40.** This phenomenon can be due to a higher crosslinking density in **HA(270)-FA-HEG-CL-20** with respect to **HA(270)-FA-HEG-CL-40** despite the lower grafting degree. Indeed, as also suggested by ^{1}H NMR hydrolysis experiments (Figure S2), a higher grafting degree does not guarantee a higher crosslinking density, since the achievement of an efficient crosslinking degree is possible according to an adequate chain mobility.

3.5. Rheological Analysis

The mechanical properties of **HA(270)-FA-HEG-CL** and **HA(8.7)-FA-HEG-CL-20** samples were studied by measuring the storage (G′) and the loss (G″) moduli as a function of frequency. The samples were allowed to relax before starting with a shear test. The frequency sweep test evidenced a "gel-like" behavior for all the tested materials since all of them showed that the storage modulus (G′) was greater than the loss modulus (G″). Moreover, **HA(270)-FA-HEG-CL** series can be defined as strong gels since both moduli are independent from frequency. Among the **HA(270)** series, no significant differences were recorded between **HA(270)-FA-HEG-CL-20** and **HA(270)-FA-HEG-CL-40**, whereas **HA(270)-FA-HEG-CL-10** showed significant lower mechanical properties (Figure 8). Nevertheless, the strongest effect is noted to be molecular weight. Indeed, **HA(8.7)** derivative showed about two orders of magnitude lower moduli values. Moreover, a higher dependence of moduli from frequency could be observed, thus highlighting a lower stiffness for the 8.7 kDa sample in comparison with the 270 kDa series. The stiffness of a material is strictly related to its crosslinking degree, and the mechanical analysis can be used to calculate the average mesh size (ξ) or the crosslinking density.

The average mesh size (ξ), defined as the distance between valid crosslinking points [30], was calculated using the elastic modulus value (G′). The higher the mesh size, the lower the crosslinking density. The hydrogels obtained with **HA(270)-FA-HEG-CL-20** and **HA(270)-FA-HEG-CL-40** samples showed superimposable mesh size values (i.e., 16 ± 1 nm, 18 ± 2 nm, respectively), whereas for **HA(270)-FA-HEG-CL-10** a value of 23 ± 1 nm was found. Finally, sample **HA(8.7)-FA-HEG-CL-20** showed a significantly different value of mesh size reaching 68 nm, thus confirming the swelling behavior results.

The obtained results appeared to confirm a slightly higher crosslinking density for **HA(270)-FA-HEG-CL-20** in comparison to **HA(270)-FA-HEG-CL-40,** which represented a heterogeneous material characterized by a non-exhaustive crosslinking, as suggested by ^{1}H NMR hydrolysis experiments (see Figure S2).

In Figure 9, viscosity curves of all the swollen hydrogels are depicted. Similar to swelling performance and viscoelastic properties, the highest effect is molecular weight, in opposition to crosslinking density, as has been already observed for other polymer based hydrogels [31]. Samples **HA(270)-FA-HEG-CL-20** and **HA(270)-FA-HEG-CL-40** showed a superimposable behavior which was slightly different from **HA(270)-FA-HEG-CL-10.** Viscosity curves were consistent with the different stiffness of analyzed materials. Indeed, the higher the crosslinking degree, the lower the resilience of the materials or resistance to shear rate; thus, viscosity can change more abruptly.
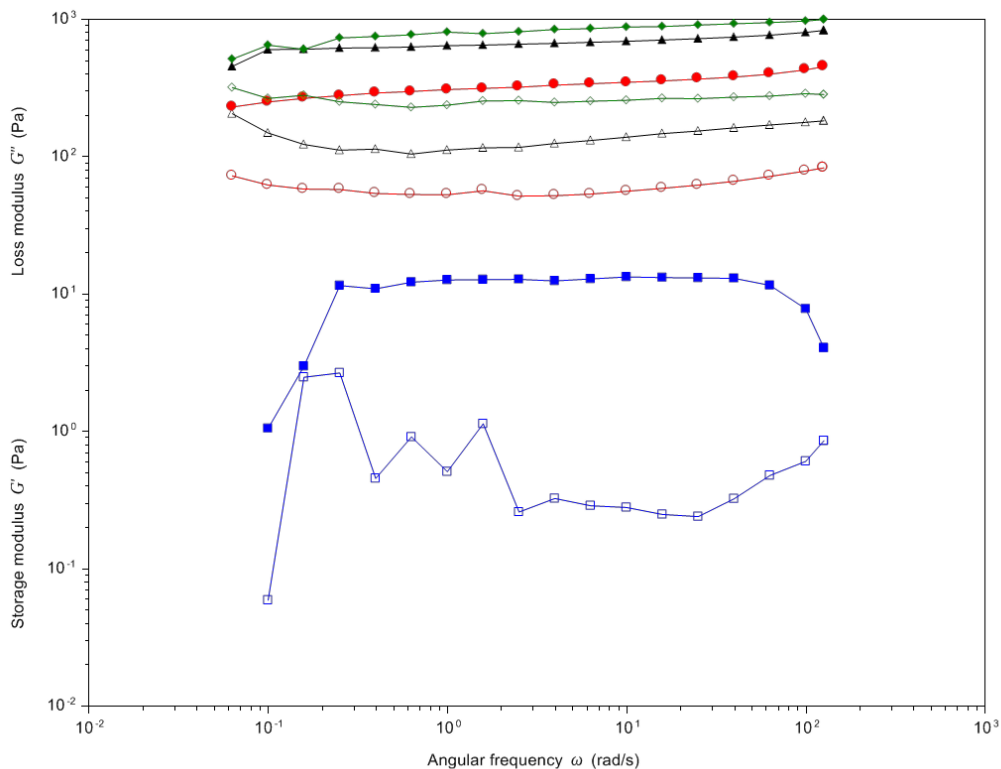
Figure 8. The storage (G′: full symbols) and loss (G″: empty symbols) moduli trend in the angular frequency range of 0.1–100 rad/s of the hydrogels obtained with **HA(270)-FA-HEG-CL-20** (green), **HA(270)-FA-HEG-CL-40** (black), **HA(270)-FA-HEG-CL-10** (red), and **HA(8.7)-FA-HEG-CL-20** (blue).

The zero shear viscosity was approximated by applying a Cross model that perfectly fit with experimental data (1.6×10^6 Pa·s, R^2 = 1.000 for **HA(270)-FA-HEG-CL-10**; 694 Pa·s, R^2 = 0.99 for **HA(270)-FA-HEG-CL-20**; 410 Pa·s, R^2 0.98 for **HA(270)-FA-HEG-CL-40**; 1.8×10^6 Pa·s, R^2 = 0.93 for **HA(8.7)-FA-HEG-CL-20**). Viscosity values of the three **HA(270)-FA-Pg** graft copolymers are summarized in Table S1. The major mechanical parameters of the hydrogels are summarized in Table 4.
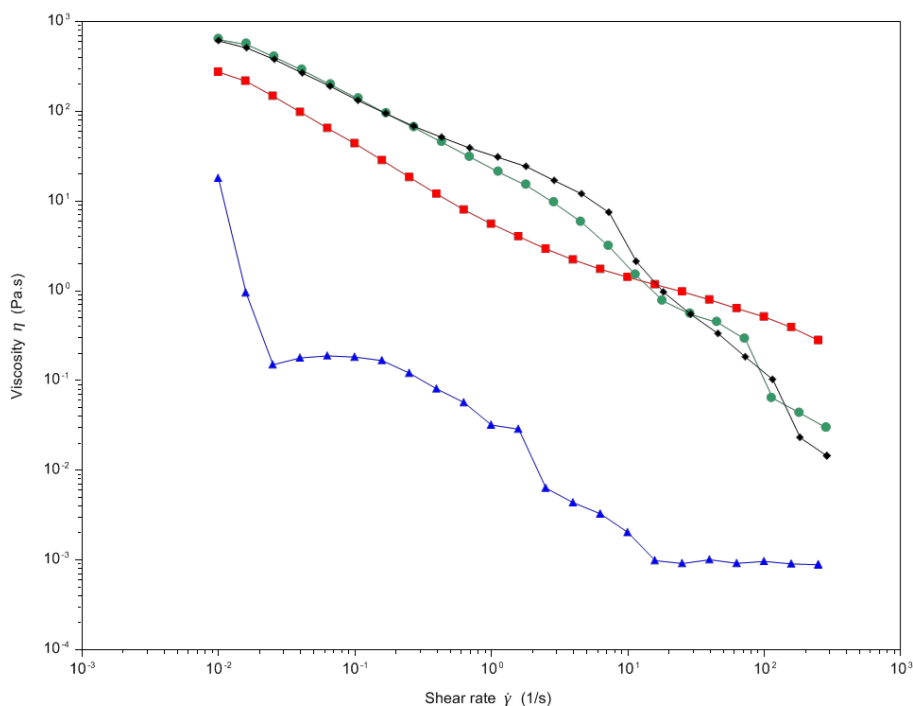
Figure 9. The viscosity curve of the swollen hydrogels obtained with **HA(270)-FA-HEG-CL-20** (green), **HA(270)-FA-HEG-CL-40** (black), **HA(270)-FA-HEG-CL-10** (red), and **HA(8.7)-FA-HEG-CL-20** (blue).

Table 4. The major mechanical parameters of the hydrogels obtained with **HA(270)-FA-HEG-CL-10**, **HA(270)-FA-HEG-CL-20**, **HA(270)-FA-HEG-CL-40**, and **HA(8.7)-FA-HEG-CL-20** materials.

Sample	G′ (2.5 Hz) (Pa)	G″ (2.5 Hz) (Pa)	η 0.1 (Pa.s)	Shear Thinning Ratio (η0.1/η250)
HA(270)-FA-HEG-CL-10	356 ± 9	59 ± 24	44 ± 11	156 ± 26
HA(270)-FA-HEG-CL-20	887 ± 11	266 ± 18	136 ± 48	4690 ± 154
HA(270)-FA-HEG-CL-40	708 ± 14	147 ± 39	138 ± 52	9428 ± 269
HA(8.7)-FA-HEG-CL-20	13 ± 2	0.25 ± 0.09	0.47 ± 0.05	390 ± 16

3.6. Thermal Behavior

Thermographs of all analyzed samples are reported in (Figure S2). Thermographs were obtained by plotting the derivative of weight versus temperature (Figure 10). Three regions of weight loss can be analyzed. The first region that ranges from 30 to 200 °C is related to the evaporation of water bound to the material. The second region spans from 200 °C to 400 °C and can be related to the degradation of free carbon chains. Finally, the third region (400–600 °C) is related to the backbone cleavage (carbonation phase). All weight percent losses are summarized in Table 5. No significant differences were observed among the 270 kDa series. Sample **HA(8.7)-FA-HEG-CL-20** shows a similar thermal behavior. Nevertheless, it shows a higher capability to bind water, as pointed out by the high weight per cent loss in the first range of heating. This phenomenon can be explained by considering

the very large mesh size of **HA(8.7)-FA-HEG-CL-20** in comparison to the hydrogel obtained by the 270 kDa series. The higher the mesh size, the higher the percentage of absorbed water, as also verified by swelling measurements.

Table 5. The TGA/DTG analysis of samples. Data were reported as percent mean value $\pm$ SD (n = 3).

Sample	30–200 °C (%)	200–400 °C (%)	400–600 °C (%)
HA(270)-FA-HEG-CL-10	13 $\pm$ 1	43 $\pm$ 3	7 $\pm$ 1
HA(270)-FA-HEG-CL-20	15 $\pm$ 2	43 $\pm$ 3	7 $\pm$ 1
HA(270)-FA-HEG-CL-40	18 $\pm$ 2	46 $\pm$ 2	7 $\pm$ 2
HA(8.7)-FA-HEG-CL-20	22 $\pm$ 3	43 $\pm$ 2	8 $\pm$ 2
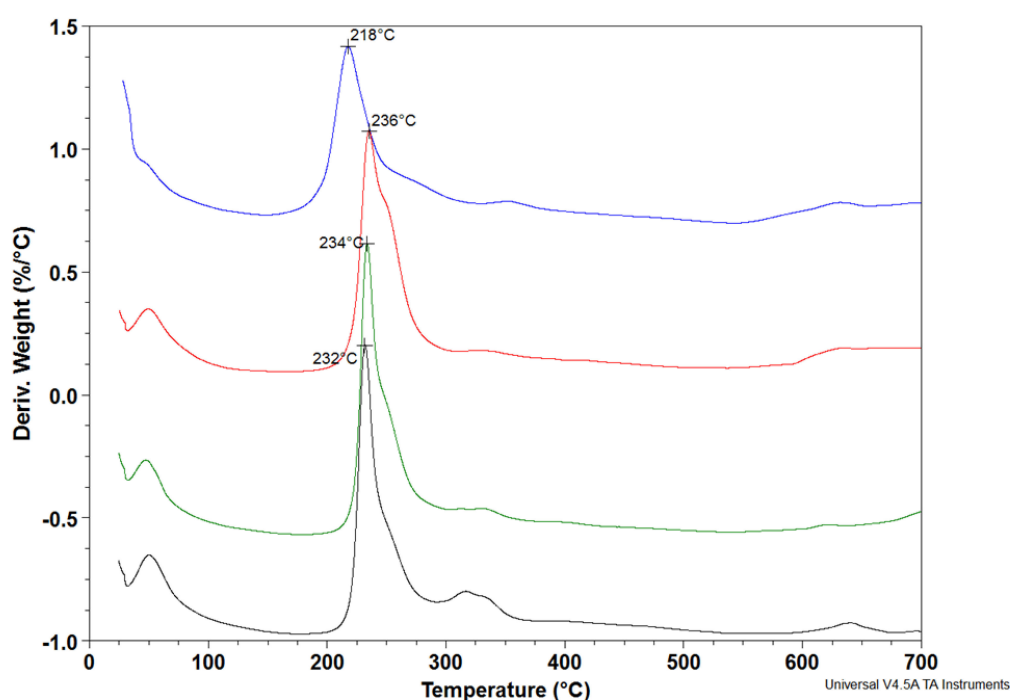
Figure 10. Thermographs obtained plotting the derivative of weight versus temperature (30–600 °C) of the hydrogels obtained with **HA(270)-FA-HEG-CL-20** (green), **HA(270)-FA-HEG-CL-40** (black), **HA(270)-FA-HEG-CL-10** (red), and **HA(8.7)-FA-HEG-CL-20** (blue).

HA-FA-HEG-CL derivatives obtained by crosslinking with CuAAC click chemistry reaction showed a significant decrease of the temperature (about 10 °C) at which the main weight loss occurred in comparison with the native polymers (data not shown). 270 kDa series shows a similar thermal behavior with the main weight loss recorded at about 230 °C despite the crosslinking density. A contrary sample **HA(8.7)-FA-HEG-CL-20** degrades at significantly lower temperatures (i.e., 218 °C), according to its lower structuring.

3.7. In Vitro Cytotoxicity: Cell Viability and Morphology

Non-confluent adhered fibroblasts were incubated with a concentration of 0.6 mg/cm^2 of each test sample. Cells viability and morphology were determined after 24 h of contact, the results of which are reported in Figures 11 and 12.
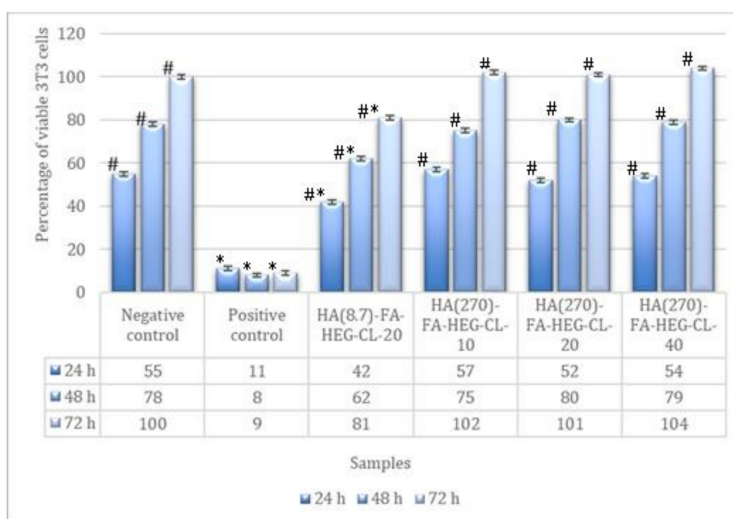
**Figure 11.** The percentage of viable NIH3T3 fibroblasts evaluated by the neutral red assay after 24, 48, and 72 h of contact with the tested samples (samples concentration = 0.6 mg/cm^2). Data are means ± SD of one experiment run in triplicate. * Value is statistically different in comparison to negative control LDPE, $p < 0.05$. # Values are statistically different in comparison to positive control PVC-org. Sn, $p < 0.05$.

As shown in Figure 11, **HA(270)-FA-HEG-CL-10**, **HA(270)-FA-HEG-CL-20**, and **HA(270)-FA-HEG-CL-40** demonstrated no toxic effect toward fibroblasts for all three incubation times as the percentage of cells in contact with the test materials was not statistically different ($p < 0.05$) in comparison to the negative control (LDPE), but differed significantly from those of the positive control which had a strong cytotoxic effect. On the contrary, fibroblasts in contact with **HA(8.7)-FA-HEG-CL-20** demonstrated a reduction of cell viability of about 20% in comparison to the negative control for all the incubation times.

Concerning the cytotoxicity, the standard ISO 10993-5 claims that a material can be considered as not cytotoxic if the solid material allows for a cell viability of over 70% after an exposure for 24 h. So, although the **HA(8.7)-FA-HEG-CL-20** sample affected the percentage of cell viability in comparison to the negative control, it cannot be considered cytotoxic, as well as all the other tested samples (i.e., **HA(270)-FA-HEG-CL-10**, **HA(270)-FA-HEG-CL-20**, and **HA(270)-FA-HEG-CL-40**).

As cell shape is closely related to cell function [32], the analysis of cell morphology is an important index of materials cytotoxicity. Optical microscopy images of fibroblasts 3T3 after 24 h of contact with positive control, negative control, and with the tested samples are reported in Figure 12. Cells in contact with the LDPE (Figure 12B) and with all the four tested samples showed the same shape and appeared to be flattened, elongated with a spindle-shaped morphology, confirming the good compatibility of all the materials toward fibroblasts 3T3 (Figure 12c–f).
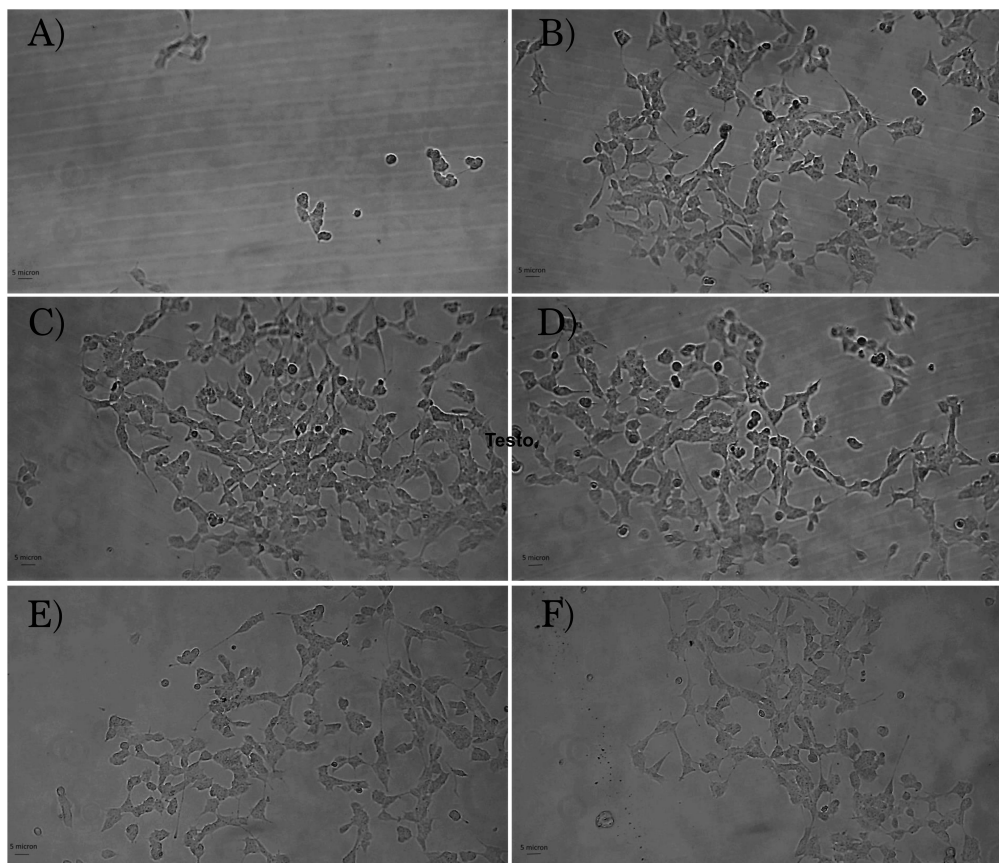
Figure 12. Optical microscope images of NIH3T3 mouse fibroblasts after 24 h of contact with: (**A**) positive control; (**B**) negative control (LDPE); (**C**) **HA(270)-FA-HEG-CL-10**; (**D**) **HA(270)-FA-HEG-CL-20**; (**E**) **HA(270)-FA-HEG-CL-40**; (**F**) **HA(8.7)-FA-HEG-CL-20**. Databar 5 μm. Magnification: 20×.

4. Conclusions

In conclusion, a click-chemistry crosslinking (click-crosslinking) procedure was developed to obtain cross-linked **HA** derivatives to be used in the formation of hydrogels. In particular, the clickable propargyl groups of **HA-FA-Pg** graft copolymers showing low and medium molecular weight values were employed in crosslinking by click-chemistry through a biocompatible hexa(ethylene glycol) spacer as an example of another possible application of our technology platform based on **HA-FA-Pg** graft copolymers. A short series of medium weight **HA-FA-Pg** graft copolymers was synthesized, characterized, and used in a CuAAC dimerization reaction under very mild conditions in the presence of very low amounts of copper(I) catalyst. The dimerization reaction was also applied to the previously published **HA-FA-Pg-3F** graft copolymer showing a low molar mass value, and hydrolysis studies confirmed the importance of the dimerization reaction in the formation of cross-linked **HA-FA-HEG-CL** materials. The interaction of the resulting **HA-FA-HEG-CL** materials with water led to the formation of hydrogels showing a wide

range of gelation features thanks to the possibility of tuning the crosslinking degree. As a consequence of that, different rheological behaviours have been observed. The tuneable rheological behaviour of **HA-FA-HEG-CL** materials led to their applicability in different biomedical fields. In particular, **HA(270)-FA-HEG-CL-10** seems to be a good candidate for potential application in the treatment of osteoarticular diseases since its shear-thinning ratio perfectly falls in the range of a healthy synovial fluid shear-thinning ratio (70–250). Moreover, the obtained results allow us to also conjecture their suitability as viscosity enhancers for eye drops. Finally, the data of both qualitative and quantitative cytotoxicity resulting from the experiments (performed according to the UNI EN ISO 10993-5 standards) demonstrates that our click-chemistry cross-linking procedure of **HA(270)-FA-Pg** graft copolymers is fully biocompatible since the resulting **HA(270)-FA-HEG-CL-10**, **HA(270)-FA-HEG-CL-20**, and **HA(270)-FA-HEG-CL-40** materials resulted in the avoidance of any in vitro cytotoxic effects.

References

1. Dicker, K.T.; Gurski, L.A.; Pradhan-Bhatt, S.; Witt, R.L.; Farach-Carson, M.C.; Jia, X. Hyaluronan: A simple polysaccharide with diverse biological functions. *Acta Biomater.* **2014**, *10*, 1558–1570. [CrossRef] [PubMed]
2. Fallacara, A.; Baldini, E.; Manfredini, S.; Vertuani, S. Hyaluronic Acid in the Third Millennium. *Polymers* **2018**, *10*, 701. [CrossRef]
3. Cohen, M.; Joester, D.; Geiger, B.; Addadi, L. Spatial and Temporal Sequence of Events in Cell Adhesion: From Molecular Recognition to Focal Adhesion Assembly. *ChemBioChem* **2004**, *5*, 1393–1399. [CrossRef]
4. Vasvani, S.; Kulkarni, P.; Rawtani, D. Hyaluronic acid: A review on its biology, aspects of drug delivery, route of administrations and a special emphasis on its approved marketed products and recent clinical studies. *Int. J. Biol. Macromol.* **2020**, *151*, 1012–1029. [CrossRef] [PubMed]
5. Trombino, S.; Servidio, C.; Curcio, F.; Cassano, R. Strategies for Hyaluronic Acid-Based Hydrogel Design in Drug Delivery. *Pharmaceutics* **2019**, *11*, 407. [CrossRef] [PubMed]
6. Gilarska, A.; Lewandowska-Łańcucka, J.; Horak, W.; Nowakowska, M. Collagen/chitosan/hyaluronic acid–based injectable hydrogels for tissue engineering applications–design, physicochemical and biological characterization. *Colloids Surf. B Biointerfaces* **2018**, *170*, 152–162. [CrossRef] [PubMed]
7. Khunmanee, S.; Jeong, Y.; Park, H. Crosslinking method of hyaluronic-based hydrogel for biomedical applications. *J. Tissue Eng.* **2017**, *8*, 2041731417726464. [CrossRef]
8. de O. Buanafina, M.M. Feruloylation in Grasses: Current and Future Perspectives. *Mol. Plant* **2009**, *2*, 861–872.
9. Grabber, J.H.; Ralph, J.; Hatfield, R.D. Cross-Linking of Maize Walls by Ferulate Dimerization and Incorporation into Lignin. *J. Agric. Food Chem.* **2000**, *48*, 6106–6113. [CrossRef]
10. Wallace, G.; Fry, S.C. *Phenolic Components of the Plant Cell Wall*; Kwang, W., Jeon, J.J., Eds.; Academic Press: Cambridge, MA, USA, 1994; Volume 151, pp. 229–267. ISBN 0074-7696.

11. Mathew, S.; Abraham, T.E. Ferulic Acid: An Antioxidant Found Naturally in Plant Cell Walls and Feruloyl Esterases Involved in its Release and Their Applications. *Crit. Rev. Biotechnol.* **2004**, *24*, 59–83. [CrossRef]

12. Bramanti, E.; Fulgentini, L.; Bizzarri, R.; Lenci, F.; Sgarbossa, A. β-Amyloid Amorphous Aggregates Induced by the Small Natural Molecule Ferulic Acid. *J. Phys. Chem. B* **2013**, *117*, 13816–13821. [CrossRef] [PubMed]

13. Noel, A.; Borguet, Y.P.; Raymond, J.E.; Wooley, K.L. Poly(carbonate–amide)s Derived from Bio-Based Resources: Poly(ferulic acid-co-tyrosine). *Macromolecules* **2014**, *47*, 2974–2983. [CrossRef] [PubMed]

14. Cappelli, A.; Grisci, G.; Paolino, M.; Giuliani, G.; Donati, A.; Mendichi, R.; Artusi, R.; Demiranda, M.; Zanardi, A.; Giorgi, G.; et al. Hyaluronan derivatives bearing variable densities of ferulic acid residues. *J. Mater. Chem. B* **2014**, *2*, 4489–4499. [CrossRef] [PubMed]

15. Valacchi, G.; Grisci, G.; Sticozzi, C.; Lim, Y.; Paolino, M.; Giuliani, G.; Mendichi, R.; Belmonte, G.; Artusi, R.; Zanardi, A.; et al. Wound healing properties of hyaluronan derivatives bearing ferulate residues. *J. Mater. Chem. B* **2015**, *3*, 7037–7045. [CrossRef] [PubMed]

16. Cappelli, A.; Paolino, M.; Grisci, G.; Razzano, V.; Giuliani, G.; Donati, A.; Bonechi, C.; Mendichi, R.; Battiato, S.; Samperi, F.; et al. Hyaluronan-coated polybenzofulvene brushes as biomimetic materials. *Polym. Chem.* **2016**, *7*, 6529–6544. [CrossRef]

17. Licciardi, M.; Scialabba, C.; Giammona, G.; Paolino, M.; Cappelli, A. Design and development of hyaluronan-functionalized polybenzofulvene nanoparticles as CD44 receptor mediated drug delivery system. *J. Nanopart. Res.* **2017**, *19*, 197. [CrossRef]

18. Razzano, V.; Paolino, M.; Reale, A.; Giuliani, G.; Artusi, R.; Caselli, G.; Visintin, M.; Makovec, F.; Donati, A.; Villafiorita-Monteleone, F.; et al. Development of Imidazole-Reactive Molecules Leading to a New Aggregation-Induced Emission Fluorophore Based on the Cinnamic Scaffold. *ACS Omega* **2017**, *2*, 5453–5459. [CrossRef]

19. Cappelli, A.; Paolino, M.; Reale, A.; Razzano, V.; Grisci, G.; Giuliani, G.; Donati, A.; Bonechi, C.; Lamponi, S.; Mendichi, R.; et al. Hyaluronan-based graft copolymers bearing aggregation-induced emission fluorogens. *RSC Adv.* **2018**, *8*, 5864–5881. [CrossRef]

20. Paolino, M.; Licciardi, M.; Savoca, C.; Giammona, G.; Modica De Mohac, L.; Reale, A.; Giuliani, G.; Komber, H.; Donati, A.; Leone, G.; et al. Hyaluronan Graft Copolymers Bearing Fatty-Acid Residues as Self-Assembling Nanoparticles for Olanzapine Delivery. *Pharmaceutics* **2019**, *11*, 675. [CrossRef]

21. Atrei, A.; Innocenti, C.; Lamponi, S.; Paesano, S.; Leone, G.; Reale, A.; Paolino, M.; Cappelli, A. Covalent hyaluronic-based coating of magnetite nanoparticles: Preparation, physicochemical and biological characterization. *Mater. Sci. Eng. C* **2020**, *107*, 110271. [CrossRef]

22. Mendichi, R.; Giacometti Schieroni, A. Use of a multi-detector size exclusion chromatography system for the characterization of complex polymers. *Curr. Trends Polym. Sci.* **2001**, *6*, 17–32.

23. Wyatt, P.J. Light scattering and the absolute characterization of macromolecules. *Anal. Chim. Acta* **1993**, *272*, 1–40. [CrossRef]

24. Li, W.; Xue, F.; Cheng, R. States of water in partially swollen poly(vinyl alcohol) hydrogels. *Polymer* **2005**, *46*, 12026–12031. [CrossRef]

25. Leone, G.; Consumi, M.; Pepi, S.; Pardini, A.; Bonechi, C.; Tamasi, G.; Donati, A.; Lamponi, S.; Rossi, C.; Magnani, A. Enriched Gellan Gum hydrogel as visco-supplement. *Carbohydr. Polym.* **2020**, *227*, 115347. [CrossRef] [PubMed]

26. *ISO 10995-5:2009*; Biological Evaluation of Medical Devices—Part 5: Tests for Cytotoxicity: In Vitro Methods. ISO: Geneva, Switzerland, 2009.

27. Lamponi, S.; Baratto, M.C.; Miraldi, E.; Baini, G.; Biagi, M. Chemical Profile, Antioxidant, Anti-Proliferative, Anticoagulant and Mutagenic Effects of a Hydroalcoholic Extract of Tuscan Rosmarinus officinalis. *Plants* **2021**, *10*, 97. [CrossRef] [PubMed]

28. Joram Mendoza, D.; Mouterde, L.M.M.; Browne, C.; Singh Raghuwanshi, V.; Simon, G.P.; Garnier, G.; Allais, F. Grafting Nature-Inspired and Bio-Based Phenolic Esters onto Cellulose Nanocrystals Gives Biomaterials with Photostable Anti-UV Properties. *ChemSusChem* **2020**, *13*, 6552–6561. [CrossRef]

29. Leone, G.; Bidini, A.; Lamponi, S.; Magnani, A. States of water, surface and rheological characterisation of a new biohydrogel as articular cartilage substitute. *Polym. Adv. Technol.* **2013**, *24*, 824–833. [CrossRef]

30. Gan, Y.; Li, P.; Wang, L.; Mo, X.; Song, L.; Xu, Y.; Zhao, C.; Ouyang, B.; Tu, B.; Luo, L.; et al. An interpenetrating network-strengthened and toughened hydrogel that supports cell-based nucleus pulposus regeneration. *Biomaterials* **2017**, *136*, 12–28. [CrossRef]

31. Leone, G.; Consumi, M.; Pepi, S.; Pardini, A.; Bonechi, C.; Tamasi, G.; Donati, A.; Rossi, C.; Magnani, A. Poly-vinyl alcohol (PVA) crosslinked by trisodium trimetaphosphate (STMP) and sodium hexametaphosphate (SHMP): Effect of molecular weight, pH and phosphorylating agent on length of spacing arms, crosslinking density and water interaction. *J. Mol. Struct.* **2020**, *1202*, 127264. [CrossRef]

32. Lamponi, S.; Leone, G.; Consumi, M.; Greco, G.; Magnani, A. In Vitro Biocompatibility of New PVA-Based Hydrogels as Vitreous Body Substitutes. *J. Biomater. Sci. Polym. Ed.* **2012**, *23*, 555–575. [CrossRef]

Chapter 5

Medicinal Chemistry: novel COX-2 inhibitors containing a Nitric Oxide (NO) donor moiety endowed with vasorelaxant properties

5.1. The Cyclooxygenase (COX) enzymes.

Prostaglandin G/H synthase enzymes (PGHS), usually known as cyclooxygenases (COX), are responsible for the formation of prostanoids, important biological mediators which play a critical role in several biological processes.[1] Arachidonic acid (AA) is a 20-carbon unsaturated fatty acid distributed throughout the phospholipidic bilayer of the cell membranes. Phospholipase A2 (PLA_2) enzymes cleave membrane-bound arachidonate for conversion into bioactive precursors. AA can be metabolized through the COX pathway via a two-step process: the first one involves the conversion of AA to prostaglandin G2 (PGG_2), a 9,11-endoperoxide-15-hydroperoxide, and in the second step peroxidase reduces PGG_2 to prostaglandin H_2 (PGH_2). Specific PG synthases further metabolize PGH_2 to give structurally related bioactive lipids, including PGs PGE_2, PGD_2, $PGF_{2\alpha}$, prostacyclin PGI_2, and thromboxane A_2 (TxA_2),[2] as shown in Figure 5.1.
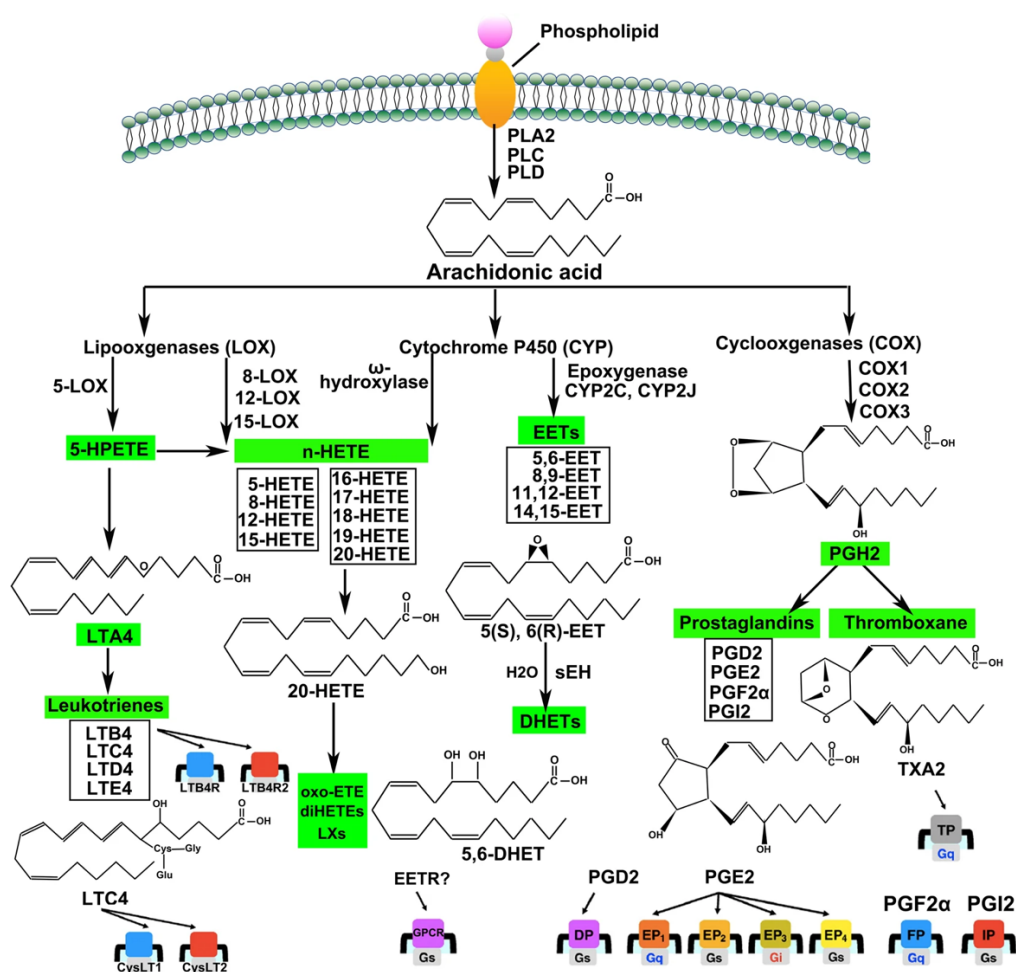
Figure 5.1. Metabolism pathways of arachidonic acid.[3]

Human COX enzymes exist in two enzymatic isoforms: the constitutive Cyclooxygenase-1 (COX-1) and the inducible isoform Cyclooxygenase-2 (COX-2). Concerning their chemical structure, COX-1 (Figure 5.2) and COX-2 are homodimers made up of 576 and 581 amino acids, respectively, with a molecular mass of approximately 70 kDa per monomer. The homodimers contain three high mannose oligosaccharides, one of which facilitates protein folding.
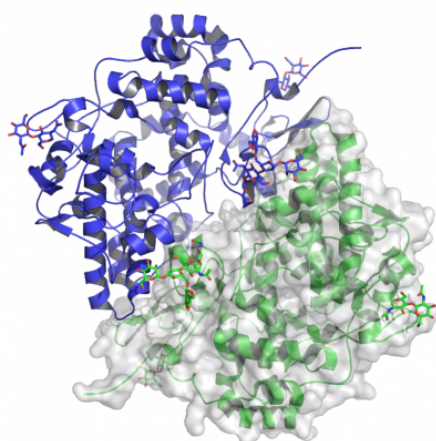
Figure 5.2. Homodimeric structure of the enzymatic isoform of human COX-2.

Each subunit of the dimer consists of three domains, the epidermal growth factor domain, the membrane binding domain, and the catalytic domain, which contains the cyclooxygenase and peroxidase active sites on either side of the heme prosthetic group. The cyclooxygenase active site lies on the opposite side of the heme from the peroxidase active site at the top of an L-shaped channel that originates in the membrane binding domain.[4] Considering the 60% identity in sequence between COX-1 and COX-2, it is not surprising that their three-dimensional configurations are nearly structurally superimposable. Nevertheless, the volume of the COX-2 active site is approximately 20% larger than that of the COX-1 active site, due to the substitution of three amino acids in the side-pocket. Furthermore, the presence of a smaller amino acid at position 523 in COX-2, such as Valine in COX-2 rather than Isoleucine in COX-1, results in a marked difference in the size and shape of the side-pocket, as shown in Figure 5.3.
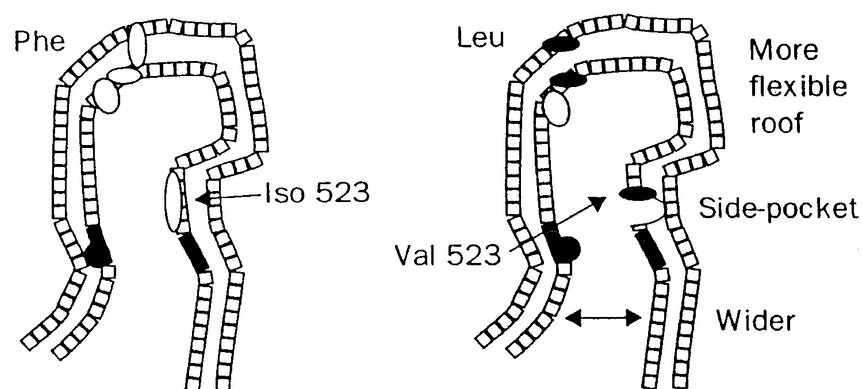
Figure 5.3. Comparison between the active site of COX-1 (left panel) and COX-2 (right panel). The Ile523 in COX-1 is replaced by a Val523 in COX-2. This substitution creates differences in the active binding site's side-pocket volume.[5]

Moreover, the switch of Valine (Val434) in the COX-2 for Isoleucine (Ile434) in the COX-1 reduces the space in the pocket by forcing the adjacent Phenylalanine (Phe518) to occupy the space for ligand binding.[6] Consequently, overcrowded molecules cannot enter the hydrophobic pocket of COX-1, unlike COX-2. A further exchange of Arginine (Arg513) in the COX-2 instead of a Histidine (His513) also plays a *key role*. The side chain of Arg guarantees the formation of stable bonds with selective COX-2 inhibitors and participates with amino acids Arginine (Arg120), Tyrosine (Tyr355), and Glutamic acid (Glu524) in the formation of H-bonds at the end of the AA binding site.[7] In this context, the side-pocket of the COX-2 is defined as the "*selectivity pocket*",[6] and the chemical-structural differences between the two enzymatic isoforms of COX enzymes have stimulated the rapid development of selective COX-2 inhibitors.

Regarding the human implications, COX-1 is expressed throughout the body and performs several homeostatic functions such as maintaining normal gastric mucosa and influencing renal blood flow and thrombocytes aggregation, a physiological process where platelets adhere to each other at sites of vascular injury and form a hemostatic plug. In contrast, the COX-2 inducible isoform is expressed in response to physiological stimuli, growth factors, and inflammatory diseases, such as rheumatoid arthritis (RA) and osteoarthritis (OA), producing the prostaglandins that mediate pain and support the inflammatory process.[8] In RA disorder, an inflammatory joint disease that most frequently affects the anatomical components of articular and juxta-articular tissues of

diarthrodial joints (Figure 5.4), COX-2 is involved in the chondrocyte response to high shear stress, associated with decreased antioxidant capacity and increased apoptosis.[9]
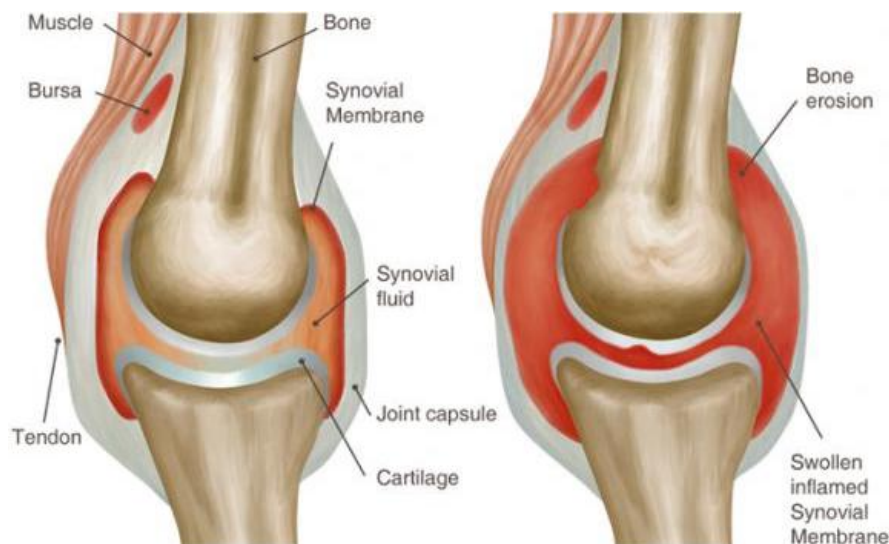
Figure 5.4. Comparison between healthy joint (left panel) and joint affected by rheumatoid arthritis (right panel).

Concerning the implication of COX-2 in cancer, it has been evidenced by pharmacological analysis of PGs in different epithelial cancer, including those originating in the colon and rectum, stomach, breast, prostate, and lung,[10] where COX-2 is up-regulated. Particularly, PGE_2 exerts carcinogenic effects on the human body. It has been found that premalignant lesions and cancers produce excessive quantities of PGE_2, and this enhances tumor cell growth and increases tumor invasiveness.[1] In cutaneous tissues, increased expression of COX-2 and production of primary PGE_2 have been reported to increase cell growth and decrease apoptosis. PGE_2 is also supposed to be responsible for different skin cancers, such as squamous cell and basal cell carcinoma.[11]

5.2. From traditional non-steroidal anti-inflammatory drugs (tNSAIDs) to selective COX-2-inhibiting Nitric Oxide Donors (CINODs).

Among the analgesic/anti-inflammatory agents, the traditional non-steroidal anti-inflammatory drugs (*t*NSAIDs) represent a class of therapeutic molecules commonly used in the treatment of various inflammatory diseases. *t*NSAIDs perform their therapeutic action *via* the inhibition of both isoforms of cyclooxygenases (COX), often with a preference for COX-1. Therefore, especially in prolonged use, this poor selectivity leads to inhibition of the synthesis of prostanoids that are essential for the maintenance of physiological functions of the gastric mucosa and of renal homeostasis, giving rise to severe gastrointestinal (GI) complications such as mucosal damage, bleeding, and renal damage.[12] It has been recently discovered that the clinical use of selective COX-2 inhibitors, also called Coxib, significantly reduces the gastric toxicity associated with *t*NSAIDs. Several clinical studies have shown that selective COX-2 inhibition gives rise to anti-inflammatories and analgesics with a safer GI profile.[13] On the contrary, the long-term use of selective COX-2 inhibitors is associated with a higher incidence of side effects relating to the cardiovascular system, with an increased incidence of myocardial infarction, angina pectoris, and temporary ischemic attacks.[14] The cause of this cardiovascular toxicity arises from the fact that the COX-2 isoform, constitutively expressed in the vascular epithelium, is fundamental to the synthesis of prostaglandin (PG)-I, a potent vasodilator. The high selectivity in the inhibition of COX-2 leads to the prevalence of the pro-aggregative and vasoconstrictive stimulus exerted by thromboxane (TxA$_2$) no longer counterbalanced by the vasodilator effect of prostacyclin (PGI$_2$), producing myocardial infarction and thrombotic events.[15] For these reasons, two vicinal diaryl-substituted heterocycles (VDHs), namely Rofecoxib and Valdecoxib (Figure 5.5) were withdrawn from the global pharmaceutical market in 2004 and 2005.[16]

Chapter 5. Medicinal Chemistry: novel COX-2 inhibitors containing a Nitric Oxide (NO) donor moiety endowed with vasorelaxant properties

Rofecoxib   **Valdecoxib**
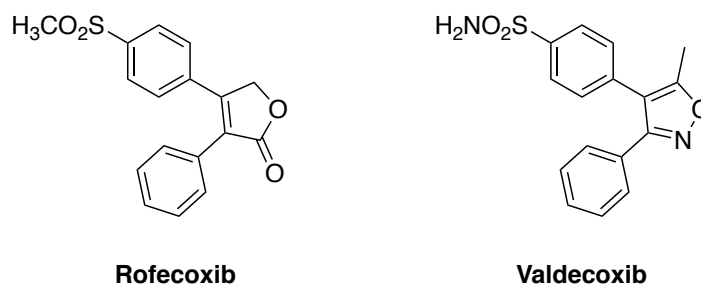
Figure 5.5. The two vicinal diaryl-substituted heterocycles (VDHs) drugs removed from the market.

VDHs represent topic scaffolds, bearing two phenyl rings on adjacent atoms of a five- or six-membered heterocyclic system. In the last few years, they have stimulated enormous interest in their clinical applications.[17] Highly substituted diarylpyrrole, including 1,2-, 2,3-, 3,4-, 4,5-, and 1,5-diarylpyrrole heterocycles, have caught the research attention due to their promising biological profiles. Interestingly, new chemical entities based on the 1,5-diarylpyrrole scaffold have been developed as anti-inflammatory, anticancer, antimycobacterial, analgesic, anticoccidial, antinociceptive, antimicrobial, antihyperlipidemic agents, and EP1-receptor antagonist.[18]

The GI side effects related to the use of *t*NSAIDs and the cardiovascular toxicity involving selective COX-2 inhibitors have created the requisite for developing novel analgesic and anti-inflammatory agents with a better profile of tolerability. In this context, the synthesis of hybrid molecules capable of selectively inhibiting COX-2 and at the same time of releasing Nitric Oxide (NO) appropriately, referred to as CINOD,[19] has encouraged the research of new anti-inflammatory and analgesic drugs, devoid of the gastrointestinal and cardiovascular side effects. Anzini and coworkers have developed a novel class of compounds, based on vicinal diarylpyrroles able to combine the selective inhibition of cyclooxygenase-2 (COX-2) with the release of NO[20,21,22] to achieve anti-inflammatory agents endowed with an overall safer profile. Similarly to PGI_2, NO has an important role in maintaining appropriate functionality of the cardiovascular system at low concentrations.[23] Through the activation of guanylate cyclase (sGC), NO gives rise to an increase in cyclic guanosine monophosphate (cGMP), which leads to vasodilation in smooth muscles, inhibits adhesion of leukocytes to the vessel wall, and inhibits platelet aggregation, producing an overall anti-thrombotic action (Figure 5.6).[24]
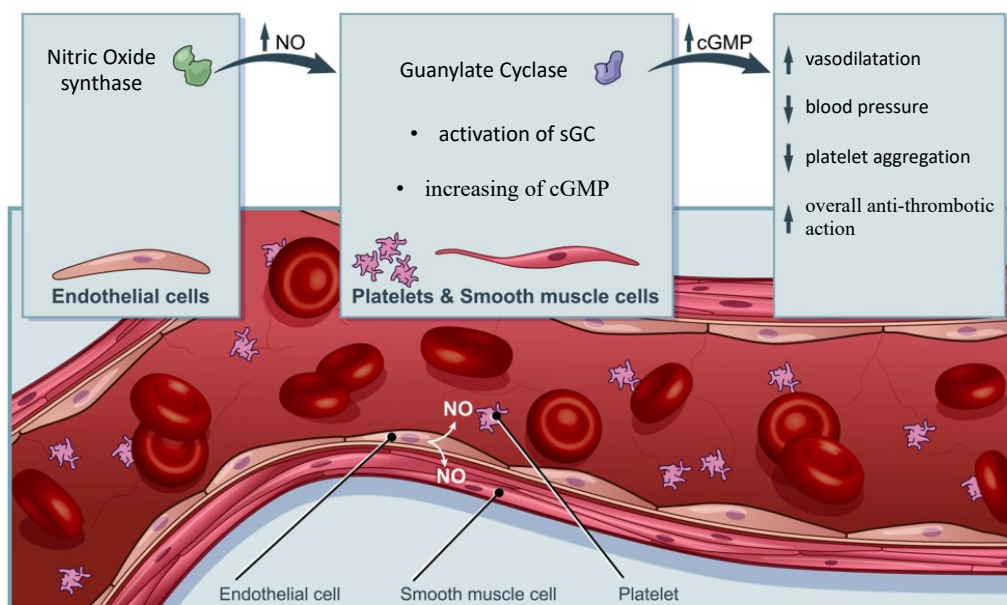
Figure 5.6. Nitric Oxide (NO) signaling pathway.[25]

Furthermore, NO is now widely recognized as a critical mediator of gastrointestinal mucosal defense, mimicking many of the same actions as PGs in the GI tract. NO-releasing drugs imitate the well-known physiological process of endothelium-dependent relaxation of blood vessels, resulting in NO-mediated activation of sGC and accumulation of cGMP in adjacent vascular smooth muscle cells.

5.3. References.

1. Grosser, T.; Fries, S.; FitzGerald, G.A. *J Clin Invest*. **2006**, *116*, 4-15.

2. Khan, M. N.; Lee, Y.S. *Med Res Rev*. **2011**, *31*, 161-201.

3. Wang, B.; Wu, L.; Chen, J. Dong, L.; Chen, C.; Wen, Z.; Hu, J.; Fleming, I.; Wang, D. W. *Sig Transduct Target Ther*. **2021**, *6* (1), 94.

4. Garavito, R. M.; Malkowski, M. G.; DeWitt, D. L. *Prostaglandins Other Lipid Mediat*. **2002**, 129-152.

5. Mengle-Gaw, L. J.; Schwartz, B. D. *Mediators of Inflammation*, **2002**, 275-286.

6. Van Ryn J.; Trummlitz G.; Pairet M. *Current Med. Chem*. **2000**, *7*, 1145-1169.

7. Kurumbail R. G.; Kiefer J. R.; Marnett L. J. *Curr. Op. Struc. Biol*. **2001**, *11*, 752-757.

8. Dannhardt, G.; Kiefer, W. *Eur. J. Med. Chem*. **2001**, *36*, 109-126.

9. Otero, M.; Goldring, M. B. *Arthritis Research & Therapy* **2007**, *9* (5), 220.

10. Lee, J. L.; Mukhtar, H.; Bickers, D. R.; Kopelovich, L.; Athar, M. *Toxicol Appl Pharmacol*. **2003**, *192*, 294-306.

11. Sticozzi, C.; Belmonte, G.; Cervellati, F.; Di Capua, A.; Maioli, E.; Cappelli, A.; Giordani, A.; Biava, M.; Anzini, M.; Valacchi. G. *Eur J Pharm Sci*. **2013**, *49*, 133-141.

12. Kauffman, G. *Gastroenterology* **1989**, *96*, 606-614.

13. Hashemi Goradel, N.; Najafi, M.; Salehi, E.; Farhood, B.; Mortezaee, K. *J. Cell. Physiol*. **2019**, *234*, 5683-5699.

14. McGettigan, P.; Henry, D. *JAMA* **2006**, *296* (13), 1633.

15. Dogńe, J. -M.; Supuran, C. T.; Pratico, D. *J. Med. Chem*. **2005**, *48*, 2251-2257.

16. Sun, S. X.; Lee, K. Y.; Bertram, C. T.; Goldstein, J. L. *Curr. Med. Res. Opin*. **2007**, *23*, 1859-1866.

17. Barmade, M. A.; Ghuge, R. B. *Vicinal Diaryl Substituted Heterocycles, Elsevier* **2018**, 1-20.

18. Ghuge, R. B.; Khadse, A. N. *Vicinal Diaryl Pyrroles: Synthesis and Biological Aspects, Vicinal Diaryl Substituted Heterocycles, Elsevier* **2018**, 47-82.

19. Geusens, P. *Expet Opin. Biol. Ther*. **2009**, *9*, 649-657.

20. Biava, M.; Porretta, G. C.; Poce, G.; Battilocchio, C.; Alfonso, S.; Rovini, M.; Valenti, S.; Giorgi, G.; Calderone, V.; Martelli, A.; Testai, L.; Sautebin, L.; Rossi,

A.; Papa, G.; Ghelardini, C.; di Cesare Mannelli, L.; Giordani, A.; Anzellotti, P.; Bruno, A.; Patrignani, P.; Anzini, M. *J. Med. Chem*. **2011**, *54*, 7759-7771.

21. Anzini, M.; Di Capua, A.; Valenti, S.; Brogi, S.; Rovini, M.; Giuliani, G.; Cappelli, A.; Vomero, S.; Chiasserini, L.; Sega, A.; Poce, G.; Giorgi, G.; Calderone, V.; Martelli, A.; Testai, L.; Sautebin, L.; Rossi, A.; Pace, S.; Ghelardini, C.; di Cesare Mannelli, L.; Benetti, V.; Giordani, A.; Anzellotti, P.; Dovizio, M.; Patrignani, P.; Biava, M. *J. Med. Chem*. **2013**, *56*, 3191-3206.

22. Martelli, A.; Testai, L.; Anzini, M.; Cappelli, A.; Di Capua, A.; Biava, M.; Poce, G.; Consalvi, S.; Giordani, A.; Caselli, G.; Rovati, L.; Ghelardini, C.; Patrignani, P.; Sautebin, L.; Breschi, M. C.; Calderone, V. *Pharmacol. Res*. **2013**, *78*, 1-9.

23. Kerwin, J. F.; Lancaster, J. R.; Feldman, P.L. *J. Med. Chem*. **1995**, *38*, 4343-4362.

24. Ignarro, L.J. *J. Physiol. Pharmacol*. **2002**, *53*, 503-514.

25. *Circulation*, 2018, *138* (3).

5.4. Research article: "Novel analgesic/anti-inflammatory agents: 1,5-Diarylpyrrole nitrooxyethyl sulfides and related compounds as Cyclooxygenase-2 inhibitors containing a nitric oxide donor moiety endowed with vasorelaxant properties".

Authors: **Mario Saletti**, Samuele Maramai, Annalisa Reale, Marco Paolino, Simone Brogi, Angela Di Capua, Andrea Cappelli, Gianluca Giorgi, Danilo D'Avino, Antonietta Rossi, Carla Ghelardini, Lorenzo Di Cesare Mannelli, Roccaldo Sardella, Andrea Carotti, Gerald Woelkart, Burkhard Klosch, Chiara Bigogno, Giulio Dondio, Maurizio Anzini.

Contribution: The Ph.D. candidate's contribution to this work refers to the design, synthesis, and preliminary NMR analysis of compounds, as well as the writing of the introduction, experimental section, and the original draft.

In this research article, a novel class of CINOD compounds has been proposed and synthesized. In this context, the design of target molecules able to combine the selective inhibition of cyclooxygenase-2 (COX-2) with the release of nitric oxide (NO) is a promising strategy to achieve potent anti-inflammatory agents endowed with an overall safer profile and reduced toxicity in gastrointestinal and cardiovascular systems. Particularly, the attention of the current work has been focused on the synthesis of nitrooxy- and hydroxy ethyl sulfides along with their oxidation products nitrooxy- and hydroxyethyl sulfoxides, also referred to as thio-CINOD. Curiously, it has been observed that the oxidation state of the sulfur atom and the presence of the additional oxygen atom

in the nitrooxy- and hydroxyethyl sulfoxides play a substantial role in increasing compounds' activity and vasorelaxation. In addition, the novel thio-CINODs have been tested *in vivo*. The resulting screening proved significantly efficacious in mouse models of inflammation and nociception at 20 mg/kg.

Chapter 5. Medicinal Chemistry: novel COX-2 inhibitors containing a Nitric Oxide (NO) donor moiety endowed with vasorelaxant properties

Novel analgesic/anti-inflammatory agents: 1,5-Diarylpyrrole nitrooxyethyl sulfides and related compounds as Cyclooxygenase-2 inhibitors containing a nitric oxide donor moiety endowed with vasorelaxant properties☆

Mario Saletti [a,†], Samuele Maramai [a,†], Annalisa Reale [a], Marco Paolino [a], Simone Brogi [b], Angela Di Capua [a,1], Andrea Cappelli [a], Gianluca Giorgi [a], Danilo D'Avino [c], Antonietta Rossi [c], Carla Ghelardini [d], Lorenzo Di Cesare Mannelli [d], Roccaldo Sardella [e], Andrea Carotti [e], Gerald Woelkart [f], Burkhard Klösch [g], Chiara Bigogno [h], Giulio Dondio [h], Maurizio Anzini [a,*]

[a] *Dipartimento di Biotecnologie, Chimica e Farmacia (Dipartimento di Eccellenza 2018-2022), Università degli Studi di Siena, Via Aldo Moro 2, 53100, Siena, Italy*
[b] *Dipartimento di Farmacia, Università di Pisa, Via Bonanno, 6, 56126, Pisa, Italy*
[c] *Dipartimento di Farmacia (Dipartimento d'Eccellenza 2018-2022), Università di Napoli "Federico II", Via D. Montesano 49, I-80131, Napoli, Italy*
[d] *Dipartimento di Neuroscienze, Area del Farmaco e Salute del Bambino (NEUROFARBA), Università di Firenze, Viale G. Pieraccini 6, I-50139, Firenze, Italy*
[e] *Dipartimento di Scienze Farmaceutiche, Università di Perugia, Via Fabretti 48, 06123, Perugia, Italy*
[f] *Department of Pharmacology and Toxicology, Institute of Pharmaceutical Sciences, University of Graz, Humboldtstraße 46, A-8010, Graz, Austria*
[g] *Ludwig Boltzmann Institute for Arthritis and Rehabilitation, Humboldtstrasse 46, 8010, Graz, Austria*
[h] *Aphad SrL, Via della Resistenza, 65, 20090, Buccinasco, Italy*

ARTICLE INFO

ABSTRACT

The design of compounds able to combine the selective inhibition of cyclooxygenase-2 (COX-2) with the release of nitric oxide (NO) is a promising strategy to achieve potent anti-inflammatory agents endowed with an overall safer profile and reduced toxicity upon gastrointestinal and cardiovascular systems. With the aim of generating novel and selective COX-2 inhibiting NO-donors (CINOD) and encouraged by the promising results obtained with our nitrooxy- and hydroxyethyl ethers **11** and **12** reported in previous works, we shifted our attention on the synthesis of isosteric thioanalogs nitrooxy- and hydroxy ethyl sulfides **13a-c** and **14a-c,** respectively, along with their oxidation products nitrooxy- and hydroxyethyl sulfoxides **15a-c** and **16a-c,** respectively, also referred to as thio-CINOD. Preliminary data and metabolic analysis highlighted how the isosteric substitution of the ethereal oxygen atom of **11a-c** with sulfur in compounds **13a-c**, independently from the presence and the number of fluorine atoms in N_1-phenyl ring, leads to new selective and highly potent COX-2 inhibitors, capable to induce vasorelaxant responses *in vivo*. The same behavior is observed with their oxidized counterparts nitrooxyethyl sulfoxides **15a-c**, in which the oxidation state of the sulfur atom and the presence of the additional oxygen atom play a substantial role in enhancing compounds activity and vasorelaxation. In addition, the screened compounds proved significantly efficacious in mouse models of inflammation and nociception at the dose of 20 mg/kg.

1. Introduction

The traditional non-steroidal anti-inflammatory drugs (*t*NSAIDs) represent a class of therapeutic agents widely used in the treatment of various pathologies [1]. Up to now, treatment with *t*NSAIDs is the best therapy for pain caused by rheumatoid arthritis (RA) and osteoarthritis (OA) [2]. Other examples of common applications are in the treatment of intestinal bowel disease (IBD) inflammation [3], urogenital tract [4] and respiratory system [5] inflammation, dysmenorrhea [6], lupus erythematosus [7] and fibromyalgia [8]. Although the analgesic action of *t*NSAIDs does not match in potency that of the opiates, their co-administration with usual narcotics has found wide application for

---

Chapter 5. Medicinal Chemistry: novel COX-2 inhibitors containing a Nitric Oxide (NO) donor moiety endowed with vasorelaxant properties

the treatment of both post-operative pain and of chronic pain induced by various pathologies, including cancer pathologies [9,10]. *t*NSAIDs perform their anti-inflammatory and analgesic action *via* inhibition of cyclooxygenases (COX) [11]. At least two isoforms of COX are known: COX-1, expressed constitutively, and COX-2, which is absent from most tissues in physiological conditions and is expressed as a result of pro-inflammatory stimuli (e.g.: cytokines) [11]. As *t*NSAIDs are not selective, they inhibit both isoforms often with a preference for COX-1 [12]. This poor selectivity leads, with concomitant inhibition of COX-1, to inhibition of the synthesis of prostanoids that are essential for maintenance of the functions of the gastric mucosa and of renal homeostasis, giving rise, especially in prolonged use, to severe gastrointestinal (GI) complications (mucosal damage, bleeding) and renal damage [12]. Clinical use of selective COX-2 inhibitors also referred to as Coxib has recently shown that the gastric toxicity associated with the use of *t*NSAIDs can be reduced considerably [13]. Several recent clinical studies have shown that selective COX-2 inhibition, as well as giving rise to anti-inflammatories and analgesics with a safer GI profile, prove effective in the treatment of various pre-cancerous and cancerous forms [14]. In fact, COX-2 is overexpressed in gastric, hepatic, pancreatic, esophageal, colon, breast, bladder, and lung tumors [15]. However, various clinical and epidemiological studies have shown that long-term use of selective COX-2 inhibitors is associated with a higher incidence of adverse effects relating to the cardiovascular system, and in particular with an increased incidence of myocardial infarction, angina pectoris and transient ischemic attacks [16,17]. The cause of this toxicity for cardiovascular system, which is also found with some *t*NSAIDs that are rather selective in inhibiting COX-2, arises from the fact that this isoform, constitutively expressed in the vascular epithelium, is fundamental to the synthesis of prostaglandin (PG)-I, a potent vasodilator [18,19]. Thus, high selectivity in inhibition of COX-2 leads, in the cardiovascular system, to prevalence of the pro-aggregative and vasoconstrictive stimulus exerted by thromboxane (TxA_2) no longer counterbalanced by the vasodilator effect of prostacyclin (PGI_2) [18]. Such a pharmacological effect caused well-known dramatic consequences: following the results of clinical studies (VIGOR and APPROVe) [19], demonstrating increased incidence of myocardial infarction and thrombotic events, two vicinal diaryl-substituted heterocycles (VDHs), namely rofecoxib and valdecoxib (Fig. 1) were withdrawn from the global pharmaceutical market in 2004 and 2005, respectively [20].

The GI side effects associated with the use of *t*NSAIDs and those relating to the use of selective COX-2 inhibitors created the need for new analgesics and anti-inflammatories agents that have a better profile of tolerability.

Similarly to PGI_2, nitric oxide (NO) at low concentrations has an important role in maintaining appropriate functionality of the cardiovascular system [21]. Through the activation of guanylate cyclase (sGC), NO gives rise to an increase in cGMP, which leads to vasodilation in smooth muscles, inhibits adhesion of leukocytes to the vessel wall and inhibits platelet aggregation, eliciting an overall anti-thrombotic action [22]. Furthermore, NO is now widely recognized as a critical mediator of gastrointestinal mucosal defense, exerting many of the same actions as PGs in the GI tract [23]. It was also demonstrated that NO was able to reduce the severity of gastric injury in experimental models [24,25]. As
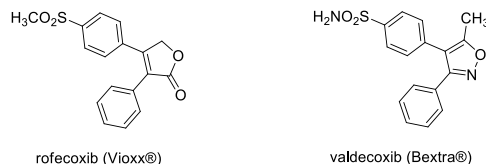
a consequence, it was proposed that linking of a NO-releasing moiety to a *t*NSAID might reduce the toxicity of the latter [26]. NO-releasing drugs mimic the well-known physiological process of endothelium-dependent relaxation of blood vessels, resulting in NO-mediated activation of sGC and accumulation of cGMP in adjacent vascular smooth muscle cells. In different animal studies, NO-releasing derivatives of a wide array of *t*NSAIDs (Fig. 2), including NO-aspirin (**1**), NO-naproxen (**2**), NO-flurbiprofen (**3**), NO-diclofenac (**4**), and NO-indomethacin (**5**) have shown to spare the GI tract, even though they suppressed PG synthesis as effectively as the parent drug [27,28]. The synthesis of this kind of hybrid molecules capable of selectively inhibiting COX-2 and at the same time of releasing NO (or NO-donors) appropriately, also referred to as CINOD [29], boosted the search of new anti-inflammatory and analgesic drugs, devoid of the cardiovascular and renal side effects, especially those associated with the use of VDHs rofecoxib and valdecoxib [20], (Fig. 1) cited above and known as Viooxx® and Bextra®, respectively.

VDHs represent a family of privileged scaffolds, bearing two phenyl rings on adjacent atoms of a five- or six-membered heterocyclic system, that in the last few decades elicited enormous interest for their clinical applications [30].

Among VDHs, vicinal diarylpyrroles came out as promising building blocks for the discovery of novel drug molecules. In fact, highly substituted diarylpyrrole, including 1,2-, 2,3-, 3,4-, 4,5-, and 1,5-diarylpyrrole heterocycles, have been reported along with their various and promising biological profiles [31]. In particular, new chemical entities based on the 1,5-diarylpyrrole scaffold have been developed as anti-inflammatory, anticancer, antimycobacterial, analgesic, anticoccidial, antinociceptive, antimicrobial, antihyperlipidemic agents, and EP1-receptor antagonist [31].

As only a few number of drugs with vicinal diarylpyrrole scaffold were available on the market, since 2005 extensive research work has been reported by our research group on the development of 3-substituted 1,5-diarylpyrrole derivatives having carboxylic acids and esters (**6**) [32] alkoxy ethers (**7a,b**) [33], alkyl sulfides (**8a,b**) and sulfoxides (**9a,b**) [34] along with nitric oxide-releasing moieties as
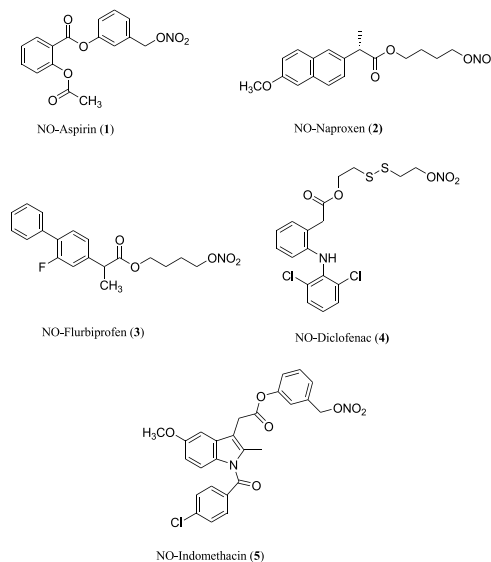

Fig. 1. The two vicinal diaryl-substituted heterocycles (VDHs) drugs withdrawn from the market.

Fig. 2. Chemical structures of NO-*t*NSAIDs.

2

nitrooxyalkyl esters (**10a,b**) [35], and ethers (**11a-c**) [36] for their anti-inflammatory and selective COX-2 inhibitory activities [37]. Most of these compounds exhibited potent biological activities, which were comparable to the standard selective COX-2 inhibitors (e.g. celecoxib) in *in vitro*, *in vivo*, and *ex vivo* studies [32–36]. The discovery of nitrooxy analogs (**10a** and **11a-c**) has laid the foundation for the development of novel dual COX-2 inhibitors/NO-donors with NO-dependent vaso-relaxant property [38], thus facilitating gastrointestinal and cardiovascular safety. Both nitrooxyalkyl inverse ethers (**11a-c**) and their metabolites, hydroxyethyl derivatives (**12a-c**), displayed very potent COX-2 inhibitory activity in the nanomolar range [36] (Fig. 3).

As an extension of our previous work focused on novel COX-2 inhibiting NO-donors and encouraged by the promising results of previously reported nitrooxy- and hydroxyethyl ethers **11** and **12** [36], we shifted our attention on the synthesis of nitrooxy- and hydroxy ethyl sulfides **13a-c** and **14a-c** respectively, as thio-analogs of **11a-c** and **12a-c** along with their oxidation products nitrooxy- and hydroxyethyl sulfoxides **15a-c** and **16a-c**, respectively (Fig. 4).

In fact, as recently reported by some of us, the transformation of 1,5-diarylpyrrole-3-alkoxyethyl ethers (**7**) into the corresponding alkyl sulfides (thioethers) (**8a,b**) and respective alkyl sulfoxides (**9a,b**), still lead to selective and active compounds endowed with COX-2 inhibitory activity in the low nanomolar range [34]. The synthetic procedure and the biological evaluation of target compounds **13a-c** and **15a-c**, along with that of their metabolites **14a-c** and **16a-c**, as highly selective COX-2

inhibitors and efficacious vasorelaxant agents is the object of the present study. Our findings also suggested that our best compounds caused vasorelaxation through NO-generation and activation of the sCG/cGMP/PKG pathway.

2. Chemistry

2.1. Synthesis of target compounds

The synthesis of hydroxyethyl sulfides **14a-c** and hydroxyethyl sulfoxides **16a-c** as synthetic precursors of nitrooxyethyl sulfides **13a-c** and nitrooxyethyl sulfoxides **15a-c** was achieved as reported in Scheme 1. Briefly, hydroxyethyl derivatives **17a-c** were prepared in gram-scale according to the previously-reported procedure [36,39]. The activation of the suitable alcohol **17a-c** by means of tosyl chloride (TsCl) in the presence of *N,N*-diisopropylenethylamine (DIPEA) and 4-(dimethylamino)pyridine (DMAP) gave the corresponding O-tosyl derivatives **18a-c** which by reaction with ethyl 2-mercaptoacetate in dry THF and in the presence of 1,8-diazabicyclo[5.4.0]undec-7-ene (DBU) at room temperature (r.t.) were smoothly transformed into ethylthioacetate derivatives **19a-c** [40]. The reduction of **19a-c** using 1 M LiAlH$_4$ in dry tetrahydrofuran (THF) at r.t. provided the expected hydroxyethyl sulfides **14a-c**, also referred to as hydroxyethyl thioethers, in satisfactory yields. The transformation of compounds **14a-c** into the corresponding sulfoxides **16a-c**, requested the preventive protection the alcoholic function of hydroxyethyl sulfides by reaction with *tert*-butyldimethylsilyl chloride (TBDMSiCl) [41] in the presence of imidazole at r.t. to give silyloxy derivatives **20a-c**. Then oxidation of **20a-c** by means of *m*-chloroperbenzoic acid (*m*-CPBA) [42] in dichloromethane (DCM) at r.t. afforded protected sulfoxides **21a-c**, which were in turn deprotected by treatment with tetrabutylammonium fluoride (TBAF) in dry THF at r.t. to yield hydroxyethyl sulfoxides **16a-c.**

In order to overcome the difficulty in obtaining nitrooxyethyl sulfides **13a-c** directly from hydroxyethyl derivatives **14a-c**, by following the procedure previously reported for the synthesis of nitrooxyethyl ethers **11** [33], an alternative procedure was run as sketched in Scheme 2. Accordingly, compounds **16a-c** were converted into the corresponding nitrooxyethyl sulfoxides **15a-c**, by means of previous activation via tosyl chloride in the same conditions reported above to give compounds **22a-c**. These compounds were then reacted with tetrabutylammonium nitrate in dry THF to yield nitrooxyethyl sulfoxides **15a-c** which, by reaction with Lawesson's reagent [43], were easily reduced to the expected nitrooxyethyl sulfides **13a-c** in satisfactory yields.

2.2. Enantioseparation of chiral sulfoxides 15b,c and 16b,c

In view of potential extensions of the present work, such as the enantioselective synthesis of the chiral sulfoxides here reported, we embarked with the enantiomeric separation of compounds **15b,c** and **16b,c**. To this aim, an efficient enantioselective liquid chromatography method has been recently developed by some of us [44].

Accordingly, two cellulose tris(3,5-dichlorophenylcarbamate)-based chiral stationary phases (CSPs), one with a coated (CSP 1) and the other with an immobilized (CSP 2) chiral selector, have been successfully used (enantioseparation and enantioresolution values up to 1.94 and 6.32, respectively), in combination with an ethanol/2-propanol (80:20, v/v) containing mobile phase. In the study, the coupling of electronic circular dichroism studies to *ab initio* time-dependent density functional theory simulations has allowed us to establish the enantiomer elution order for three out of four compounds (namely **15c** and **16b,c**). (S) < (R) for the two hydroxyethyl derivatives (**16b,c**) with both CSPs; while, for compound **15c**, an opposite elution order has been determined, depending on the coated or immobilized nature of the chiral selector, that is, (S) < (R) with CSP 1 and (R) < (S) with CSP 2 (see Supporting Information).
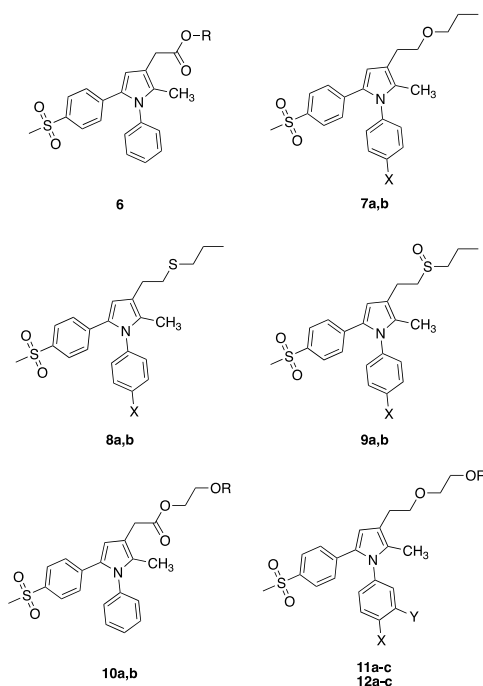
Fig. 3. Evolution of 3-substitued-1,5-diarylpyrroles: from COX-2 inhibitors (COXIB) (**6–9**) to dual COX-2 inhibiting NO-donors (CINOD) (**10a, 11a-c**) and their respectively active metabolites (**10b, 12a-c**). Substituents: **7a, 8a, 9a**, X = H; **7b, 8b, 9b**, X = F; **10a**, R = NO$_2$; **10b**, R = H; **11a**, X = Y = H, R = NO$_2$; **11b**, X = F, Y = H, R = NO$_2$; **11c**, X = Y = F, R = NO$_2$; **12a**, X = Y = R = H; **12b**, X = F, Y = R = H; **12c**, X = Y = F, R = H.
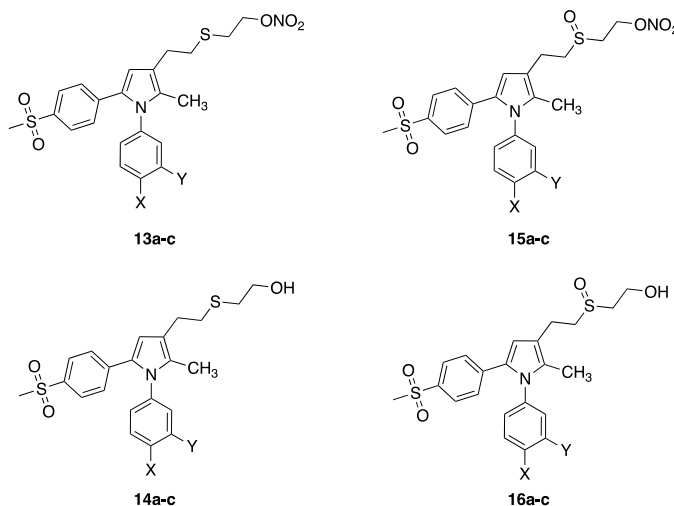
Fig. 4. Chemical structures of target compounds **13–16**. Substituents: **13a, 14a, 15a, 16a**, X = Y = H; **13b, 14b, 15b, 16b**, X = F, Y = H; **13c, 14c, 15c, 16c**, X = Y = F.

3. Results and discussion

3.1. In vitro COX-2 inhibitory activity and selectivity

Target compounds **13–16** were subjected to an *in vitro* cell culture (J774 murine macrophage) assay to evaluate their inhibitory potency and selectivity on both COX isoforms. The results were summarized in Table 1 and compared with previously reported isosteric nitrooxyethyl- and hydroxyethyl ethers **11a-c** and **12a-c** [36].

On the basis of their IC$_{50}$ values, nitrooxyethyl sulfides **13a** (IC$_{50}$ = 0.029 μM) and **13c** (IC$_{50}$ = 0.016 μM), resulted equally or much more active than corresponding nitrooxyethyl ethers **11a** (IC$_{50}$ = 0.017 μM) and **11c** (IC$_{50}$ = 0.920 μM). Similarly, 4′-F derivative **13b** showed an activity that appeared slightly increased with respect to **11b**, being their IC$_{50}$ values 0.009 μM and 0.014 μM, respectively. These data clearly indicate that the isosteric substitution of the ethereal oxygen atom of **11a-c** with sulfur as in compounds **13a-c**, independently from the presence and the number of fluorine atoms in N$_1$-phenyl ring, un-equivocally leads to selective and highly potent COX-2 inhibitors. The same behavior is paralleled by nitrooxyethyl sulfoxides **15a-c** which showed IC$_{50}$ values of 0.074, 0.005, and 0.003 μM, respectively. Remarkable is the fact that in these compounds the oxidation state of the sulfur atom and the presence of the additional oxygen atom play an important role, confirming the elevated COX-2 inhibitory activity of nitrooxyethyl sulfides **13a-c** which is improved in 4′-F derivative **15b** (0.005 μM) and even more in 3′,4′-diF compound **15c** (0.003 μM), while in non-halogenated compound **15a** the activity drops to 0.074 μM with respect to that of **13a** (0.029 μM). Furthermore, among hydroxyethyl sulfides and sulfoxides **14a-c** and **16a-c**, which could be regarded as the metabolites of compounds **13a-c** and **15a-c** after these latter have released NO, all hydroxyethyl sulfides **14a-c** showed an efficacious and selective COX-2 inhibitory activity, spanning from 0.008 to 0.025 μM, respectively. Even if it appears not surprising that the isosteric non-halogenated hydroxyethyl thioether **14a** shows a COX-2 inhibition (0.025 μM) equal to that of the corresponding hydroxyethyl ether **12a** (0.027 μM), it is noteworthy that both 4′-F and 3′,4′-diF derivative **14b** and **14c** resulted 11- and 25-fold more active than **12b** (0.008 vs 0.089

μM) and **12c** (0.017 vs 0.420 μM), respectively. The same behavior does not apply to hydroxyethyl sulfoxides **16a-c** in which the S═O moiety along with the presence or not of fluorine atoms in the N$_1$-phenyl ring induce a dramatic decrease in COX-2 inhibitory activity dropping from low nanomolar values of sulfides **14a-c** to micromolar ones of their oxidation products.

An intriguing aspect of the structure-activity relationships (SARs), when hydroxy- and nitrooxyethyl sulfides **14a-c** and **13a-c** are taken into account, deals with the overlapping IC$_{50}$ values of both series of compounds all of which show a COX-2 inhibitory activity comprised between 0.008 and 0.029 μM, respectively. Differently from previously reported nitrooxyehtyl ethers **11a-c** [36], where an efficacious electronic interaction of the nitrate group at the inner hydrophobic channel of the enzyme strongly contributed to the inhibitory activity, in the case of thio-analogs **13a-c**, this seems not to be the unique requisite to assess the low nanomolar values that result equipotent with those of hydroxyethyl thioethers **14a-c**. Probably, the elevated inhibitory activity of hydroxyethyl sulfides **14a-c** is due to a different electronic interaction of the alcoholic oxygen of the side chain at the active site of the enzyme in which the presence, the number, and the position of fluorine atoms in N$_1$-phenyl ring of the 1,5-diarylpyrrole scaffold are able, as for compounds **12a-c**, to fine tuning the enzymatic inhibition.

3.2. Molecular modelling studies

Computational studies helped us to rationalize the influence of the lateral chain on the inhibitory potency against *h*COX-2 enzyme showed by compounds, as experimentally determined. In particular, we employed compounds **13b**, **14b**, **15b**, and **16b** that present the same scaffold and differ on the lateral side chain. The results of this computational experiment are illustrated in Fig. 5.

Briefly, for all selected compounds the diarylpyrrole moiety established the same contacts within the *h*COX-2 binding site. In fact, compounds targeted the backbone of F518 and the side chain of R513 by H-bonds, while they can form a cation-π stacking with R120. Interestingly, analyzing the accommodation of the lateral chain we observed some slight difference among the selected compounds that can support the

M. Saletti et al.
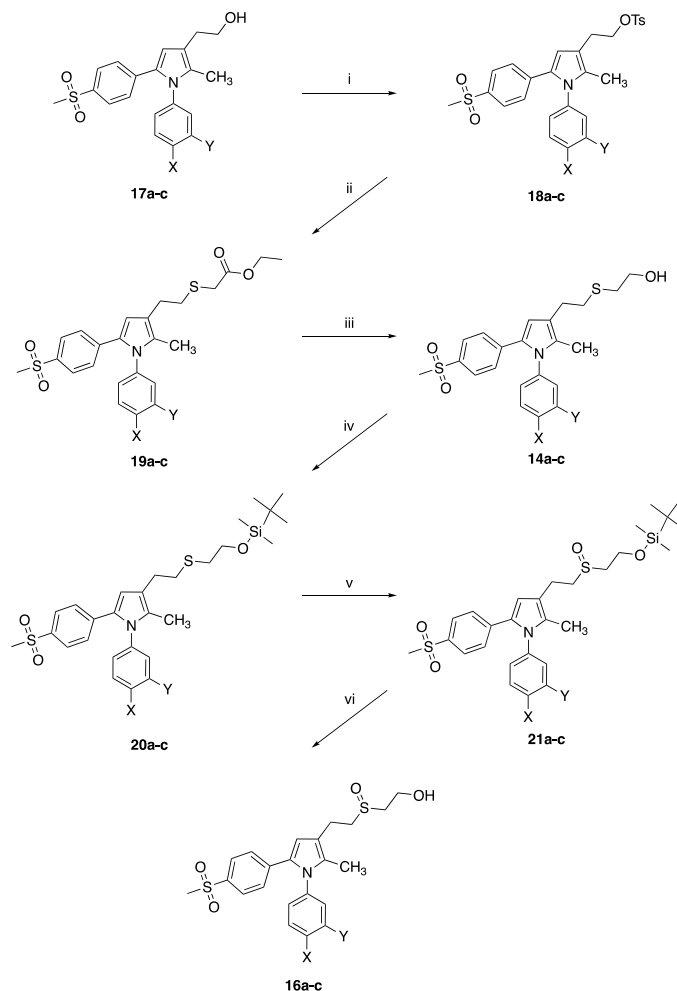
Scheme 1. Synthesis of target compounds **14a-c** and **16a-c**.
Reagents and Conditions: (i) TsCl, DIPEA, DMAP, dry DCM, r.t., 30 min; (ii) HSCH$_2$COOEt, DBU, dry THF, r.t., 4 h; (iii) LiAlH$_4$, dry THF, r.t., 1 h; (iv) TBDMSiCl, imidazole, dry DCM, r.t., 4 h; (v) *m*-CPBA, dry DCM, r.t., 1 h; (vi) TBAF, dry THF, r.t., 1 h. Substituents: **14a, 16a, 17a, 18a, 19a, 20a, 21a**, X = Y = H; **14b, 16b, 17b, 18b, 19b, 20b, 21b**, X = F, Y = H; **14c, 16c, 17c, 18c, 19c, 20c, 21c**, X = Y = F.

small difference in biological activity. Compound **13b** showing a IC$_{50}$ of 0.009 μM can accommodate the lateral chain in a favorable position allowing the maximization of contacts within the binding site. In particular, the end of the chain H-binds the side chain of R120 and the negative oxygen of the nitro-group can form a salt bridge with R120 (Fig. 5A). This binding mode accounted for a docking score of −10.32 kcal/mol. Replacing the nitro-group with a terminal OH did not change the activity of the resulting compound. In fact, compound **14b** showed an IC$_{50}$ of 0.008 μM. In this case the end of the lateral chain is involved in a strong network of contacts with R120 and with the side chain of Y355 (Fig. 5B). This slightly different binding mode with respect to that found for **13b**, is well tolerated by the enzyme and also the docking score is very similar (docking score −10.25 kcal/mol). The replacement of sulfur with a sulfoxide in the lateral chain of compound **13b** and **14b** led to compounds **15b** and **16b**. In this case the different arrangement of the

lateral chain is reflected to a different potency observed for **15b** and **16b**. In fact, **15b** showed an increased network of polar contacts with R120 in which also the sulfoxide participates establishing a H-bond with the sidechain of R120, in addition to the H-bonds/salt bridge observed between the nitro-terminal region and R120 (Fig. 5C). This binding mode accounted for a slight increase in affinity denoted by the observed docking score of −11.04 kcal/mol that is reflected by an increase in potency since **15b** showed an IC$_{50}$ of 0.005 μM. Finally, the introduction of sulfoxide in the lateral chain containing a terminal OH appeared to be deleterious for the activity. Although the resulting compound **16b** showed an IC$_{50}$ of 0.916 μM, we observed a decrease in the number of contacts established by the lateral chain of **16b** within the *h*COX-2 binding site with respect to the previously discussed compounds. In fact, also the sulfoxide moiety of **16b** is able to interact with R120, while the accommodation of the rest of the lateral chain did not produce any
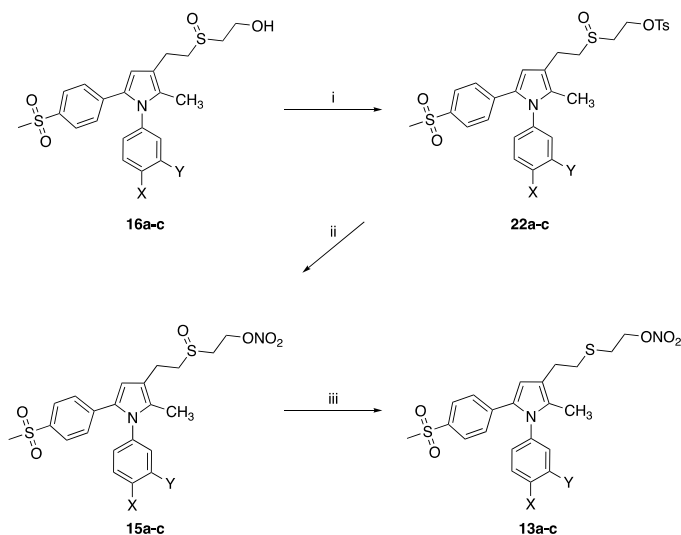
Scheme 2. Synthesis of target compounds **13a-c** and **15a-c.**
Reagents and conditions: (i) TsCl, DIPEA, DMAP, dry DCM, r.t., 30 min; (ii) (Bu₄N)⁺NO₃⁻, dry THF, reflux, 1 h; (iii) Lawesson's Reagent, dry THF, 0 °C, 1 h.
Substituents: **13a, 15a, 16a, 22a,** X = Y = H; **13b, 15b, 16b, 22b,** X = F, Y = H; **13c, 15c, 16c, 22c,** X = Y = F.

observable contacts (Fig. 5D). Accordingly, the reduced number of contacts within the binding site is reflected, as already mentioned in a decrease in activity and consequently in a reduction of docking score that for this compound was found to be −9.83 kcal/mol.

3.3. In vitro metabolism of compounds 13b, 14b, 15b, and 16b

The pharmacological properties of target compounds **13**–**16** may be preliminarily explained when a putative metabolic pathway is taken into consideration (Fig. 6). It is possible to suppose that the biotransformation involving nitrooxyethyl sulfides **13a-c** starts with the NO release to give the corresponding hydroxyethyl sulfides **14a-c** as active metabolites that by means of cytochrome Cyp450 are successively oxidized to hydroxyethyl sulfoxides **16a-c** showing to be much less active with respect to parent compounds. Alternatively, compounds **13a-c** may be firstly transformed into nitrooxyethyl sulfoxides **15a-c** which in turn release NO to give hydroxyethyl sulfoxides **16a-c** as the final products even if a further oxidation of compounds **15a-c** and **16a-c** to the corresponding sulfone derivatives **23a-c** and **24a-c** may be considered the real final metabolic destination of nitrooxyethyl sulfides **13a-c**.

In this way, compounds **13b, 14b, 15b,** and **16b** were selected to assess their metabolic stability to phase I oxidative metabolism using mouse and human liver microsomes (Table 2). As predicted, compound **13b** was highly metabolized after incubation with human and mouse liver microsomes, showing very high intrinsic clearance value of 61.2 and 131.7 μL/min/mg protein, respectively. However, the two potential metabolites **14b** and **15b** resulted more metabolically stable than the corresponding nitrooxyethyl sulfide **13b,** especially in the human species, and with compound **14b** showing a little propensity to be more unstable in the mouse species (73.2 *vs.* 39.2 μL/min/mg protein in the mouse and human, respectively). This behavior might guarantee a significant duration of action as anti-inflammatory and antinociceptive agent in view of the *in vitro* COX-2 inhibitory and vasorelaxant activity of the parent **13b** and its potential metabolites **14b** and **15b**. Compound **16b**, as expected, was very stable to the phase I oxidative conditions,

displaying a very low intrinsic clearance in both species (3.2 and 9.7 μL/min/mg protein in human and mouse, respectively) (see Supporting Information).

3.4. Vasorelaxant activity of compounds 13a-c and 15a-c

Agents that selectively inhibit COX-2 and additionally release NO might improve the safety profile of anti-inflammatory drugs. A well-established model of measuring isometric tension of rat aortic rings pre-contracted with L-phenylephrine (PE) was used to evaluate the vascular effects of compounds **13a-c** and **15a-c** at varying concentrations. To demonstrate that the observed vasodilation could be ascribed to the release of NO, experiments were performed in the absence and presence of the GC inhibitor 1*H*- [1,2,4]oxadiazolo[4,3-*a*]quinoxalin-1-one (ODQ). Remarkably, all tested compounds, with the exception of **15b**, promoted relaxation in a dose-dependent manner, as shown in Fig. 7A, with efficacy parameters ranging from 59% to 78%.

Among the active compounds, the sulfoxides **15a** and **15c** exerted considerable relaxation at quite low concentrations, which could be easily achieved *in vivo*, and are definitely more active than their sulfide counterparties. All the tested analogs are slightly or significantly more efficacious than the ethereal compound **11b**, taken as reference. [36] The presence and the position of the fluorine atom(s) in the N₁-phenyl ring resulted less influent for the activity, especially in the sulfides series, while the oxidation state of the sulfur atom strongly contributed to the vasorelaxation. The only outlier is represented by compounds **15b**, which showed negligible levels of vasorelaxant efficacy. The experiments carried out in the presence of ODQ confirmed that the vasorelaxant effects could be attributed to the release of NO, as the GC inhibitor significantly antagonized the vasodilator responses evoked by derivatives **13a-c**, **15a** and **15c** (Fig. 7B). Moreover, we know from our previous experiments that the corresponding hydroxyalkyl derivatives **12a-c** (and related compounds here not shown) were devoid of remarkable vasorelaxant effects [38]. This result further indicated that such a pharmacodynamic feature of the tested compounds is due to the

6

137

Table 1

In vitro COX-1 and COX-2 inhibitory activity (J774 Murine Macrophage Assay) of compounds **11–16**.

Compound	R	X	Y	COX-1 IC_{50} (µM)[a]	COX-2 IC_{50} (µM)[a]	COX-1/COX-2 (SI)[b]
11a[c]	NO_2	H	H	>10	0.017	>588.2
11b[c]	NO_2	F	H	>10	0.014	>714.3
11c[c]	NO_2	F	F	>10	0.920	>10.9
12a[c]	H	H	H	>10	0.027	>370.4
12b[c]	H	F	H	>10	0.089	>112.3
12c[c]	H	F	F	>10	0.420	>23.8
13a	NO_2	H	H	>10	0.029	>344.8
13b	NO_2	F	H	>10	0.009	>1111.1
13c	NO_2	F	F	>10	0.016	>625.0
14a	H	H	H	>10	0.025	>400.0
14b	H	F	H	>10	0.008	>1250.0
14c	H	F	F	>10	0.017	>588.2
15a	NO_2	H	H	>10	0.074	>135.1
15b	NO_2	F	H	>10	0.005	>2000.0
15c	NO_2	F	F	>10	0.003	>3333.3
16a	H	H	H	>10	0.320	>31.2
16b	H	F	H	>10	0.916	>11.0
16c	H	F	F	>10	0.140	>71.4
Celecoxib[d]	–	–	–	3.84	0.061	>63.0

[a] Results are expressed as the mean (n = 3 experiments) of the % inhibition of PGE2 production by test compounds with respect to control samples. The IC_{50} values were calculated by the GraphPad Instat program. Data fit was obtained by means of the sigmoidal dose-response equation (variable slope) (GraphPad software).
[b] *In vitro* COX-2 selectivity index [IC_{50}(COX-1/IC_{50}(COX-2)].
[c] See ref. [36].
[d] See ref [35].

nitrooxy group and to its expected biotransformation to NO. However, in specific circumstances, NO can also have damaging effects, like collapse due to severe hypotension. Whether NO is useful or harmful depends on the rate and location of its production and on its chemical fate, necessitating comprehensive elaboration of the effects of new developed NO-releasing drugs. By observing the curves in Fig. 7A at increasing concentrations of tested compounds, we could see a slow increment of vasorelaxation, which is preferred to avoid possible side effect and imputable to a controlled rate of NO release. Taken together, these pieces of evidence confirmed that the modifications brought to the reference compound **11b** modulated the relaxing capacity of the new analogs, leading to the discovery of promising hybrid agents that can induce desired vasodilation at physiological relevant concentrations.

3.5. In vivo anti-inflammatory and antinociceptive studies

On the basis of their interesting COX-2 inhibitory activity observed in the *in vitro* test, compounds **13b,c**, **14b,c**, and **15b,c** were selected and assayed in *in vivo* anti-inflammatory and antinociceptive tests. (Tables 3 and 4). In the abdominal constriction test, compounds **13b,c**, **14b,c**, and **15b,c** induced a reduction of the number of writhes in a statistically significant manner at the minimum dose of 20 mg/kg *per os* (p.o.), while at the dose of 10 mg/kg p.o., they were devoid of any antinociceptive efficacy (Table 3). The activity of the compounds mentioned above, all administered at a dose of 20 mg/kg p.o., in the presence of an inflammatory stimulus induced by intraplantar administration of carrageenan in the rat paw can be observed in Table 4. In these experiments, the behavioral effect of the compounds, as the response to the algic agent in the paw pressure test and in the volume of the paw, were measured and

compared to celecoxib as the reference drug. All the compounds showed a good activity against carrageenan-induced hyperalgesia 30 min after administration, disappearing completely at 1 h after treatment (Table 4). Moreover, a very good activity was demonstrated against carrageenan induced edema in the rat paw (Table 4), with a substantial complete remission 30 min after the administration of all the compounds at the same dose of 20 mg/kg p.o. The antinociceptive/anti-inflammatory and anti-edema profile of all the compounds evaluated is practically superimposable, so demonstrating that no difference in potency or efficacy exists between them.

4. Conclusion

In this research work, we designed and synthesized novel nitro-oxyethyl sulfides and sulfoxides based on the 1,5-diarylpyrrole scaffold, endowed with nanomolar potency in inhibiting COX-2 enzyme, and high selectivity over COX-1 isoform. Computational analysis helped us to rationalize the contribution of the side chains to the potency of inhibition of COX-2 and confirmed the SAR trends observed with the new analogs, especially for those bearing a 4-F-phenyl ring connected to the nitrogen atom of the pyrrole system (i. e. compounds **13b**, **14b**, **15b**, and **16b**). After the *in vitro* evaluation of the metabolic stability and formation of potential metabolites, we determined the vasorelaxant effect of compounds **13a-c** and **15a-c**, where the presence of a NO-donating moiety was able to induce a significant concentrations-dependent vasodilation for almost all the tested agents. In addition, the *in vivo* evaluation in animal models of inflammation and nociception, confirmed the analgesic and anti-inflammatory activity of the target compounds at the concentration of 20 mg/kg, which achieved
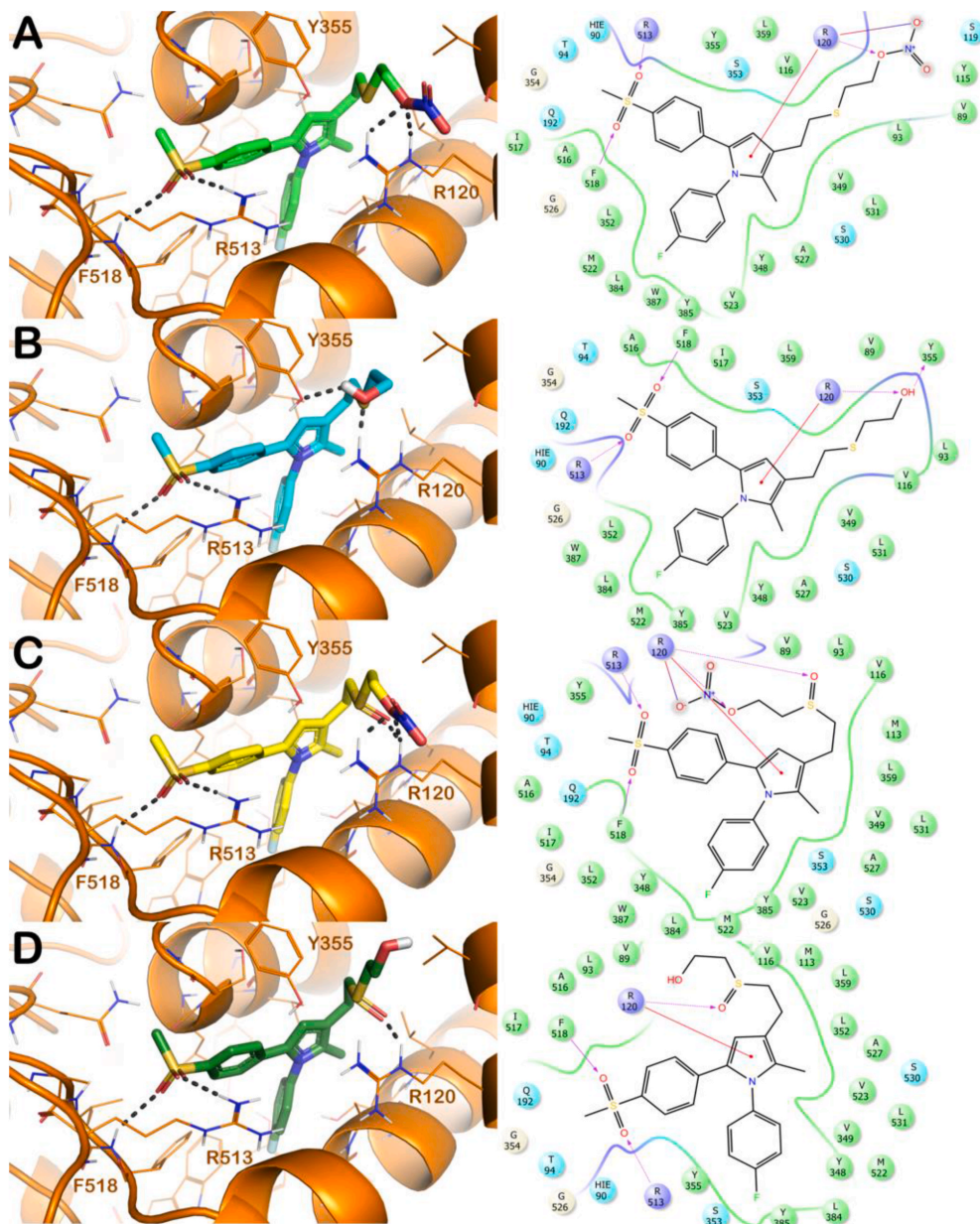
Fig. 5. Proposed binding mode of compounds **13b** (light green sticks, panel A), **14b** (cyan sticks, panel B), **15b** (yellow sticks, panel C), and **16b** (dark green sticks, panel D) within the *h*COX-2 binding site (orange cartoon, PDB ID 5KIR). Key interacting residues are represented by lines. H-bonds are indicated as gray dotted lines. Nonpolar hydrogens were omitted for the sake of clarity. Pictures were generated by PyMOL (The PyMOL Molecular Graphics System, version 1.8.4.0, Schrödinger, LLC, New York, 2018), while ligand-interaction diagrams were generated by Maestro (Maestro, release 2015-1, Schrödinger, LLC, New York, 2015).

Fig. 6. Putative metabolic pathway of nitrooxyethyl sulfides **13a-c** and related compounds. Substituents: **13a, 14a, 15a, 16a, 23a, 24a**, X = Y = H; **13b, 14b, 15b, 16b, 23b, 24b**, X = F, Y = H; **13c, 14c, 15c, 16c, 23c, 24c**, X = Y = F.

Table 2
In vitro determination of the metabolic stability after incubation with mouse and human liver microsomes.

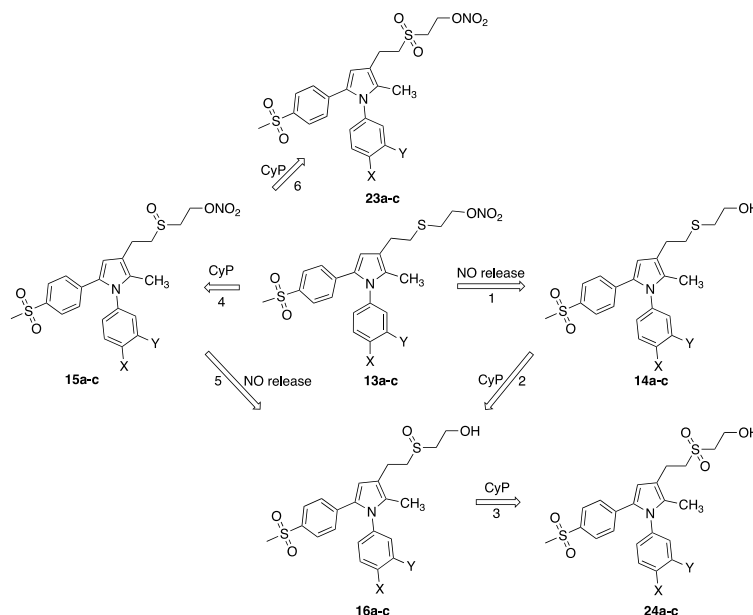| Compound	Human liver microsomes (HLM)				Mouse liver microsomes (MLM)			
	Cli	SD	$t_{1/2}$	SD	Cli	SD	$t_{1/2}$	SD
	μL/min/mg protein		min		μL/min/mg protein		min	
13b	131.7	5.8	10.5	0.5	61.2	7.8	22.8	2.9
14b	39.2	8.4	36.2	7.8	73.2	12.8	19.2	3.4
15b	39.9	1.5	34.7	1.3	40.3	8.3	35.1	7.3
16b	3.2	1.3	469.8	189.0	9.7	0.2	142.5	3.6
7-EC[a]	113.0	24.3	12.6	2.7	296.8	4.7	4.7	0.1
Propranolol	25.2	0.1	55.0	0.1	47.5	1.3	29.2	0.8

[a] 7-ethoxycoumarin.

remarkable results in comparison to celecoxib as the reference drug. The simultaneous effect against pain and inflammation, coupled with the presence of an appropriate NO-donor moiety and vasorelaxant capability at physiological relevant concentration, highlighted the potential of these hybrid compounds to be useful tools for the development of strong antinociceptive and anti-inflammatory drugs, exhibiting promising features for a possible safer profile. As a further development of the current work, we are seeking to explore more in deep the release of NO and related effects induced by the most promising compounds, along with the additional pharmacological evaluation in cancer therapy.

5. Experimental section

5.1. General procedures for the synthesis of target compounds

5.1.1. Materials and methods

All reagents and solvents were purchased from Sigma-Aldrich and were used as received. Merck silica gel 60 (230–400 mesh) was used for column chromatography. Merck TLC aluminum sheets, silica gel 60 F254 were used for TLC. ^{1}H and ^{13}C NMR spectra were recorded with either a Bruker DRX 600 AVANCE or a Bruker DRX 400 spectrometer in the indicated solvent (the residual solvent peaks were used as the internal standard). The values of the chemical shifts (δ) are reported in ppm, and the H–H coupling constants (J) are expressed in Hz. An Agilent 1100 LC/MSD running with an electrospray source (ESI) was used in mass spectrometry measurements. A Bruker Tims-TOF instrument with an ESI source was used to measure the high-resolution mass values. Melting points were determined in open capillaries on a Gallenkamp apparatus and are uncorrected. Purity of compounds **13a-c**, **14a-c**, **15a-c**, and **16a-c** was assessed by RP-HPLC and was found to be higher than 95%. Agilent Zorbax® Eclipse XDB-C8 column was used in the HPLC analysis with water-methanol (20:80) as the mobile phase at a flow rate of 0.600 mL/min. UV detection was achieved at 228 nm.

5.1.2. Preparation of 1,5-diaryl-3-(2-hydroxyethyl)pyrroles **17a-c**

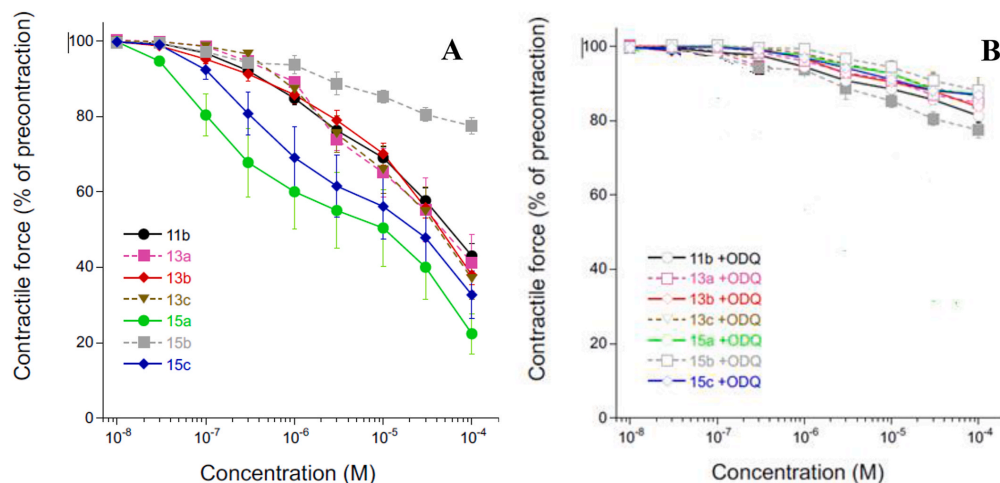Compounds **17a-c** were re-synthesized according to previously

9

Fig. 7. Effects of experimental compounds on vascular tone. Rat aortic rings were precontracted with ʟ-phenylephrine (10 μM) and cumulative concentration-response curves to various experimental compounds were established in the absence (**A**) and presence (**B**) of ODQ (10 μM). Data are expressed as mean values ± s.e.m. obtained from 7 (**11b**, **13b**), 5 (**13a**, **13c**, **15a**, **15c**) or 3 (**15b** and all ODQ) rings.

Table 3
Effect of compounds **13b-c**, **14b-c**, and **15b-c** in the mouse abdominal constriction test (acetic acid 0.6%).

Treatment	dose p.o. (mg Kg^{-1})	n. writhes
CMC		30.3 ± 4.2
13b	10	$24.2 \pm 3.0^\circ$
13b	20	$20.5 \pm 2.8^*$
13b	30	$20.6 \pm 2.2^*$
13c	10	$22.5 \pm 3.4^*$
13c	20	$19.0 \pm 2.7^*$
13c	30	$20.7 \pm 4.1^*$
14b	10	26.5 ± 3.6
14b	20	$23.1 \pm 3.2^*$
14b	30	$21.5 \pm 3.0^*$
14c	10	$23.8 \pm 2.5^*$
14c	20	$19.6 \pm 3.5^*$
14c	30	$17.4 \pm 4.4^*$
15b	10	29.2 ± 2.1
15b	20	$21.8 \pm 3.3^*$
15b	30	$18.0 \pm 3.1^*$
15c	10	$25.9 \pm 2.6^\circ$
15c	20	$20.1 \pm 3.4^*$
15c	30	$21.3 \pm 3.3^*$

All compounds were administered 30 min before test. $^*P < 0.01$, $^\circ P < 0.05$ versus vehicle-treated mice. For each group were used at least 5 mice.

reported procedure starting from the suitable acetate esters and their spectroscopic and analytical data were consistent with those we have already reported [33,36].

5.1.3. General procedure for the synthesis of tosyl ester derivatives 18a-c
To a solution of the suitable alcohol (**17a-c**, 5.0 mmol, 1 equivalent) in dry DCM (50 mL), 4-(dimethylamino)pyridine (DMAP) (1.5 equivalents) and *N,N*-diisopropylethylamine (DIPEA) (1.5 equivalents) were added in sequence. The solution was cooled at 0 °C, and tosyl chloride (1.5 equivalents) was added. After stirring for 30 min at room temperature, the reaction mixture was treated with water and the organic layer was washed with water, dried over anhydrous Na$_2$SO$_4$, filtered and evaporated in vacuo. The residue was purified by flash chromatography

with the indicated eluent to obtain the expected tosyl derivative **18a-c**.

5.1.3.1. 2-(2-Methyl-5-(4-(methylsulfonyl)phenyl)-1-phenyl-1H-pyrrol-3-yl)ethyl-4-methylbenzenesulfonate (18a). This compound was obtained in 74% yield by following the general procedure and the analytical data were in agreement with those already reported [34].

5.1.3.2. 2-(1-(4-Fluorophenyl)-2-methyl-5-(4-(methylsulfonyl)phenyl)-1H-pyrrol-3-yl)ethyl-4-methylbenzenesulfonate (18b). This compound was obtained in 86% yield by following the general procedure and the analytical data were in agreement with those already reported [34].

5.1.3.3. 2-(1-(3,4-Difluorophenyl)-2-methyl-5-(4-(methylsulfonyl) phenyl)-1H-pyrrol-3-yl)ethyl-4-methylbenzenesulfonate (18c). The title compound was obtained starting from the hydroxyl derivative **17c** as a white powder (yield 73%) using petroleum ether-ethyl acetate (4:6 v/v) as the eluting mixture. Mp: 151–152.2 °C. ^{1}H NMR (400 MHz, CDCl$_3$): 1.99 (s, 3H), 2.42 (s, 3H), 2.84 (t, $J = 7.7$, 2H), 3.01 (s, 3H), 4.18 (t, $J = 7.0$, 2H), 6.30 (s, 1H), 6.87 (d, $J = 8.3$, 1H), 6.96 (t, $J = 8.6$, 1H), 7.12 (d, $J = 8.2$, 2H), 7.20 (m, 1H), 7.31 (d, $J = 7.9$, 2H), 7.70 (d, $J = 8.2$, 2H), 7.77 (d, $J = 8.0$, 2H). MS (ESI) m/z: [M + Na]$^+$ Calcd for C$_{27}$H$_{25}$F$_2$NNaO$_5$S$_2^+$ 568.1; Found 568.2.

5.1.4. General procedure for the synthesis of ethylthioacetic esters 19a-c
To a cooled (0 °C) solution of the proper tosyl ester derivative (**18a-c**, 3.0 mmol, 1 equivalent) in dry THF (10 mL) 1,5-diazabicyclo[5.4.0] undec-5-ene (DBU) (3 equivalents) and ethylthioglicolate (3 equivalents) were added. The reaction mixture, after being stirred at r.t. for 4h under a nitrogen atmosphere, was treated with a 2 N HCl solution (20 mL). The organic layer was then extracted with EtOAc and the combined organic extracts were washed to neutrality, dried over anhydrous Na$_2$SO$_4$, filtered, and concentrated under reduced pressure. The residue so obtained was purified by means of flash chromatography using petroleum ether/EtOAc (8:2 v/v) as the eluent to give the expected ethylthioacetic ester **19a-c**.

Table 4

Effect of compounds **13b-c**, **14b-c**, and **15b-c** in comparison with Celecoxib on hyperalgesia and paw edema induced by carrageenan in the rat paw-pressure test.

Pre-treatment i.pl.	Treatment p.o.	Dose (mg Kg^{-1})	Paw-pressure (g)					Volume (mL)
			Before treatment	After treatment				
				15 min	30 min	45 min	60 min	30 min
Saline	CMC		65.4 ± 3.4	61.3 ± 4.1	58.6 ± 3.5	60.5 ± 4.2	62.5 ± 3.9	1.44 ± 0.05
carrageenan	CMC		33.6 ± 3.9	31.9 ± 3.0	32.6 ± 4.1	33.3 ± 3.0	31.7 ± 3.5	2.68 ± 0.04
carrageenan	13b	20	33.2 ± 3.4	39.9 ± 3.5	45.9 ± 2.2^	44.7 ± 3.1^	37.5 ± 3.3	2.18 ± 0.05^
carrageenan	13c	20	33.1 ± 3.0	40.6 ± 3.7	46.1 ± 4.1^	45.7 ± 4.0^	37.1 ± 3.9	2.31 ± 0.04^
carrageenan	14b	20	30.9 ± 3.5	41.5 ± 4.7	48.2 ± 4.5^	48.7 ± 3.9^	38.2 ± 3.5	2.22 ± 0.04^
carrageenan	14c	20	31.8 ± 2.5	37.8 ± 4.3	46.6 ± 4.1^	45.3 ± 5.0^	39.6 ± 4.9	2.09 ± 0.06^
carrageenan	15b	20	32.6 ± 2.9	42.3 ± 3.1	47.2 ± 3.7^	46.1 ± 4.3^	36.3 ± 4.3	2.25 ± 0.04^
carrageenan	15c	20	34.6 ± 3.7	39.8 ± 4.5	48.2 ± 3.9^	44.2 ± 5.6^	38.3 ± 3.8	2.20 ± 0.04^
carrageenan	Celecoxib	10	32.7 ± 2.9	48.5 ± 4.0*	51.3 ± 3.8*	54.0 ± 3.6*	46.7 ± 3.1*	1.56 ± 0.04*

All compounds were administered at the dose of 20 mg Kg^{-1} p.o. Carrageenan (100 μL- 1%- i.pl. 2 h before test). Test was performed 30 min after the compound injection. There were 4–5 rats per group. *P < 0.01, ^P < 0.05 versus the corresponding carrageenan-treated rat.

5.1.4.1. Ethyl 2-(2-(2-Methyl-5-(4-(methylsulfonyl)phenyl)-1-phenyl-1H-pyrrol-3-yl)ethylthio)acetate (19a). Light yellow oil (yield 72%). ^{1}H NMR (400 MHz, CDCl$_3$): 1.28 (t, J = 7.1, 3H), 2.05 (s, 3H), 2.78 (t, J = 7.4, 2H), 2.89 (t, J = 7.6, 2H), 3.01 (s, 3H), 3.26 (s, 2H), 4.20 (q, J = 7.2, 2H), 6.43 (s, 1H), 7.11–7.13 (m, 4H), 7.37–7.39 (m, 3H), 7.69 (d, J = 8.6, 2H). MS (ESI) *m/z*: [M + Na]$^+$ Calcd for C$_{24}$H$_{27}$NNaO$_4$S$_2^+$ 480.1; Found 480.2.

5.1.4.2. Ethyl 2-(2-(1-(4-Fluorophenyl)-2-methyl-5-(4-(methylsulfonyl)phenyl)-1H-pyrrol-3-yl)ethylthio) acetate (19b). Light yellow oil (yield 94%). ^{1}H NMR (400 MHz, CDCl$_3$): 1.28 (t, J = 7.2, 3H), 2.04 (s, 3H), 2.78 (t, J = 7.4, 2H), 2.89 (t, J = 7.6, 2H), 2.99 (s, 3H), 3.26 (s, 2H), 4.19 (q, J = 7.1, 2H), 6.43 (s, 1H), 7.07–7.16 (m, 6H), 7.76 (d, J = 8.4, 2H). MS (ESI) *m/z*: [M + H]$^+$ Calcd for C$_{24}$H$_{27}$FNO$_4$S$_2^+$ 476.1; Found 476.3.

5.1.4.3. Ethyl 2-(2-(1-(3,4-Difluorophenyl)-2-methyl-5-(4-(methylsulfonyl)phenyl)-1H-pyrrol-3-yl)ethylthio) acetate (19c). Yellow oil (yield 90%). ^{1}H NMR (400 MHz, CDCl$_3$): 1.28 (t, J = 7.1, 3H), 2.07 (s, 3H), 2.77 (m, 2H), 2.88 (m, 2H), 3.01 (s, 3H), 3.26 (s, 2H), 4.20 (q, J = 7.2, 2H), 6.42 (s, 1H), 6.90 (d, J = 8.8, 1H), 7.01 (m, 1H), 7.13–7.23 (m, 3H), 7.69 (d, J = 8.6, 2H). MS (ESI) *m/z*: [M + H]$^+$ Calcd for C$_{24}$H$_{26}$F$_2$NO$_4$S$_2^+$ 494.1; Found 494.2.

5.1.5. General procedure for the synthesis of 1,5-diarylpyrrol-3-((2-hydroxyethyl)thioethyl)-ethers 14a-c

To a solution of the suitable ethylthioacetic ester (19a-c, 3.0 mmol, 1 equivalent) in dry THF (12 mL) a solution of lithium aluminum hydride 1 M in THF (2.2 equivalents) was added dropwise. After stirring for 1h at r.t. under a nitrogen atmosphere, the excess of the reducing agent was decomposed by careful addition of H$_2$O (2.0 mL). The inorganic material was filtered off and washed with THF. The filtrate was dried (Na$_2$SO$_4$) and evaporated under reduced pressure. The residue, purified by flash-chromatography using petroleum ether/EtOAc (3:7 v/v) as the eluting mixture, gave the expected compound **14a-c**.

5.1.5.1. 2-(2-(2-Methyl-5-(4-(methylsulfonyl)phenyl)-1-phenyl-1H-pyrrol-3-yl)ethylthio)ethan-1-ol (14a). Colorless needles (yield 61%), Mp: 153–153.7 °C. ^{1}H NMR (400 MHz, CDCl$_3$): 2.05 (s, 3H), 2.75–2.80 (m, 6H), 2.98 (s, 3H), 3.74 (t, J = 5.9, 2H), 6.43 (s, 1H), 7.11–7.14 (m, 4H), 7.36–7.41 (m, 3H), 7.63 (d, J = 8.4, 2H). ^{13}C NMR (101 MHz, CDCl$_3$): 11.0, 27.0, 33.0, 35.7, 44.5, 60.3, 111.7, 119.9, 127.1, 127.2, 128.1, 128.4, 129.4, 130.7, 131.1, 136.5, 138.5, 138.9. MS (ESI) *m/z*: [M + H]$^+$ Calcd for C$_{22}$H$_{26}$NO$_3$S$_2^+$ 416.1; Found 416.4. HRMS (ESI) *m/z*: [M + H]$^+$ Calcd for C$_{22}$H$_{26}$NO$_3$S$_2^+$ 416.13486, found 416.128367; [M + Na]$^+$ Calcd for C$_{22}$H$_{25}$NNaO$_3$S$_2^+$ 438.11681, found 438.110033; [M + K]$^+$ Calcd for C$_{22}$H$_{25}$KNO$_3$S$_2^+$ 454.09074, found 454.083834; [2 M + Na]$^+$ Calcd for C$_{44}$H$_{50}$N$_2$NaO$_6$S$_4^+$ 853.24439, found 853.231833. X-Ray crystallography (see Supporting Information, Fig. S1): a single crystal of

14a was submitted to X-Ray data collection on an Oxford-Diffraction Xcalibur Sapphire 3 diffractometer with a graphite monochromated Mo-Kα radiation (λ = 0.71073 Å) at 293 K. The structure was solved by direct methods implemented in SHELXS-97 program [45]. The refinements was carried out by full-matrix anisotropic least squares on F^2 for all reflections for non-H atoms by means of the SHELXL program [46]. The compound crystalizes in the Triclinic crystal system, space group P-1 (n. 2). Bond lengths and angles have normal values. The dihedral angles formed by pyrrole ring with the phenyl bound to N1 and with that bound to C2 are 67.84° and 29.36°, respectively, while the dihedral angle between the two phenyl rings is 63.51°. There is an intermolecular hydrogen bonding interaction:

O(3)-H (x,y,z)··· ···O(2) *(1-x,1-y,1-z)* with a distance H··· ···O(2) of 2.11 Å

During the refinement, a statistical disorder was found for atoms S2, C21, C22 with two different positions, with 0.62(1) being the highest site occupation factor shown by S2A, C21A and C22A. The torsion angles C19–C20–S2A-C21A and C19–C20–S2B–C21B are 77.7(4)° and 129.4 (6)°, respectively. Crystallographic data have been deposited with the Cambridge Crystallographic Data Centre as supplementary publication no. CCDC 2162091. Copies of the data can be obtained, free of charge, on application to CCDC, 12 Union Road, Cambridge CB2 1EZ, UK; (fax: +44(0) 1223 336 033; or e-mail: deposit@ccdc.cam.ac.uk).

5.1.5.2. 2-(2-(1-(4-Fluorophenyl)-2-methyl-5-(4-(methylsulfonyl)phenyl)-1H-pyrrol-3-yl)ethylthio)ethan-1-ol (14b). White powder (yield 90%), Mp 86.7–87.2 °C. ^{1}H NMR (400 MHz, CDCl$_3$): 2.04 (s, 3H), 2.76–2.78 (m, 6H), 2.99 (s, 3H), 3.73 (t, J = 5.8, 2H), 6.42 (s, 1H), 7.07–7.17 (m, 6H), 7.66 (d, J = 8.4, 2H). ^{13}C NMR (101 MHz, CDCl$_3$): 11.0, 27.0, 33.0, 35.6, 44.5, 60.5, 111.9, 116.4 (t, J = 23.3) 120.0, 127.3, 130.0 (d, J = 13.5) 130.1, 130.7, 131.2, 134.98 (d, J = 3.0), 136.7, 138.3, 161.90 (d, J = 248.7). MS (ESI) *m/z*: [M + H]$^+$ Calcd for C$_{22}$H$_{25}$FNO$_3$S$_2^+$ 434.1; Found 434.2. HRMS (ESI) *m/z*: [M + Na]$^+$ Calcd for C$_{22}$H$_{24}$FNNaO$_3$S$_2^+$ 456.10738, found 456.100007; [M + K]$^+$ Calcd for C$_{22}$H$_{24}$FKNO$_3$S$_2^+$ 472.08132, found 472.073765; [2 M + Na]$^+$ Calcd for C$_{44}$H$_{48}$F$_2$N$_2$NaO$_6$S$_4^+$ 889.22555, found 889.211760.

5.1.5.3. 2-(2-(1-(3,4-Difluorophenyl)-2-methyl-5-(4-(methylsulfonyl)-phenyl)-1H-pyrrol-3-yl)ethylthio)ethan-1-ol (14c). White powder (yield 87%), Mp: 130.6–131 °C. ^{1}H NMR (600 MHz, CDCl$_3$): 2.06 (s, 3H), 2.71–2.82 (m, 6H), 3.01 (s, 3H), 3.74 (t, J = 5.9, 2H), 6.41 (s, 1H), 6.91 (d, J = 8.5, 1H), 7.01 (t, J = 7.5, 1H), 7.17 (d, J = 8.3, 2H), 7.22 (q, J = 8.9, 1H), 7.71 (d, J = 8.3, 2H). ^{13}C NMR (151 MHz, CDCl$_3$): 11.0, 26.9, 32.9, 35.6, 44.5, 60.2, 112.3, 117.8 (d, J = 11.7), 117.9 (d, J = 11.7), 120.3, 124.8, 127.4 (2 C), 130.6, 131.3, 135.3 (dd, J = 7.6, 2.5), 137.1, 138.0, 149.9 (dd, J = 251.4, 12.0), 151.2 (dd, J = 252.4, 13.1). MS (ESI) *m/z*: [M + Na]$^+$ Calcd for C$_{22}$H$_{23}$F$_2$NNaO$_3$S$_2^+$ 474.1; Found 474.0. HRMS (ESI) *m/z*: [M + H]$^+$ Calcd for C$_{22}$H$_{24}$F$_2$NO$_3$S$_2^+$ 452.11602, found

11

452.108562; [M + Na]$^+$ Calcd for C$_{22}$H$_{23}$F$_2$NNaO$_3$S$_2^+$ 474.09796, found 474.090116; [M + K]$^+$ Calcd for C$_{22}$H$_{23}$F$_2$KNO$_3$S$_2^+$ 490.07190, found 490.063962; [2 M + Na]$^+$ Calcd for C$_{44}$H$_{46}$F$_4$N$_2$NaO$_6$S$_4^+$ 925.20670, found 925.191991.

5.1.6. General procedure for the synthesis of compounds 20a-c
To a cooled (0 °C) solution of the suitable hydroxyethylthio ether (**19a-c**, 2.0 mmol, 1 equivalent) in dry DCM (20 mL), imidazole (3.32 equivalents), and TBDMSiCl (1.66 equivalents) were added in sequence and the reaction was stirred at r.t. for 4 h. The reaction mixture was then treated with a saturated solution of NH$_4$Cl and the organic layer extracted with DCM. The usual workup of the organic phase gave a residue, which was purified by flash chromatography using petroleum ether/EtOAc (8:2 v/v) as the eluting mixture gave the expected compound **20a-c**.

5.1.6.1. 3-(2-(2-((tert-Butyldimethylsilyl)oxy)ethylthio)ethyl)-2-methyl-5-(4-(methylsulfonyl)phenyl)-1-phenyl-1H-pyrrole (20a). Light yellow oil (yield 95%). ^{1}H NMR (400 MHz, CDCl$_3$): 0.06 (s, 6H), 0.88 (s, 9H), 2.04 (s, 3H), 2.67–2.71 (t, J = 8.0, 2H), 2.75–2.80 (m, 4H), 2.97 (s, 3H), 3.76–3.80 (m, 2H), 6.42 (s, 1H), 7.11–7.13 (m, 4H), 7.37–7.38 (m, 3H), 7.61 (d, J = 8.0, 2H). MS (ESI) *m/z*: [M + Na]$^+$ Calcd for C$_{28}$H$_{39}$NNaO$_3$S$_2$Si$^+$ 552.2; Found 552.3.

5.1.6.2. 3-(2-(2-((tert-Butyldimethylsilyl)oxy)ethylthio)ethyl)-1-(4-fluorophenyl)2-methyl-5-(4-(methylsulfonyl)phenyl)-1H-pyrrole (20b). Yellow oil (yield 80%). ^{1}H NMR (400 MHz, CDCl$_3$): 0.07 (s, 6H), 0.90 (s, 9H), 2.04 (s, 3H), 2.70 (t, J = 7.1, 2H), 2.73–2.82 (m, 4H), 2.99 (s, 3H), 3.79 (t, J = 7.2, 2H), 6.42 (s, 1H), 7.08–7.16 (m, 6H), 7.66 (d, J = 8.4, 2H). MS (ESI) *m/z*: [M + Na]$^+$ Calcd for C$_{28}$H$_{38}$FNNaO$_3$S$_2$Si$^+$ 570.2; Found 570.4.

5.1.6.3. 3-(2-(2-((tert-Butyldimethylsilyl)oxy)ethylthio)ethyl)-1-(3,4-difluorophenyl)-2-methyl-5-(4-(methylsulfonyl)phenyl)-1H-pyrrole (20c). Pale yellow oil (yield 56%). ^{1}H NMR (400 MHz, CDCl$_3$): 0.07 (s, 6H), 0.88 (s, 9H), 2.04 (s, 3H), 2.70 (t, J = 7.1, 2H), 2.74–2.91 (m, 4H), 3.01 (s, 3H), 3.71 (t, J = 7.1, 2H), 6.41 (s, 1H), 6.90 (m, 1H), 7.00 (m, 1H), 7.15 (d, J = 8.5, 2H), 7.20 (d, J = 8.9, 1H), 7.69 (d, J = 8.5, 2H). MS (ESI) *m/z*: [M + Na]$^+$ Calcd for C$_{28}$H$_{37}$F$_2$NNaO$_3$S$_2$Si$^+$ 588.2; Found 588.2.

5.1.7. General procedure for the synthesis of compounds 21a-c
To a cooled (0 °C) solution of the proper protected hydroxyethylthioether derivative (**20a-c**, 1.5 mmol, 1 equivalent) in dry DCM (6 mL), a solution of *m*-chloroperbenzoic acid (1.5 equivalents) was added dropwise and the resulting mixture was stirred for 1 h at r.t. under a nitrogen atmosphere. The reaction mixture was then treated with a saturated solution of NaHCO$_3$ and the organic layer extracted with DCM. The usual workup of the organic phase gave a residue which was purified by flash chromatography using petroleum ether/EtOAc (3:7 v/v) as the eluting mixture to give the expected compound (**21a-c**).

5.1.7.1. 3-(2-(2-((tert-Butyldimethylsilyl)oxy)ethylsulfinyl)ethyl)-2-methyl-5-(4-(methylsulfonyl)phenyl)-1-phenyl-1H-pyrrole (21a). Light yellow oil (yield 80%). ^{1}H NMR (400 MHz, CDCl$_3$): 0.07 (s, 6H), 0.87 (s, 9H), 2.06 (s, 3H), 2.84–3.04 (m, 9H), 4.00–4.09 (m, 2H), 6.42 (s, 1H), 7.11–7.13 (m, 4H), 7.37–7.39 (m, 3H), 7.62 (d, J = 8.0, 2H). MS (ESI) *m/z*: [M + Na]$^+$ Calcd for C$_{28}$H$_{39}$NNaO$_4$S$_2$Si$^+$ 568.2; Found 568.2.

5.1.7.2. 3-(2-(2-((tert-Butyldimethylsilyl)oxy)ethylsulfinyl)ethyl)-1-(4-fluorophenyl)2-methyl-5-(4-(methylsulfonyl)phenyl)-1H-pyrrole (21b). Yellow oil (yield 70%). ^{1}H NMR (400 MHz, MeOD): 0.08 (s, 6H), 0.87 (s, 9H), 2.06 (s, 3H), 2.89–3.00 (m, 2H), 3.02–3.16 (m, 7H), 4.03–4.10 (m, 2H), 6.52 (s, 1H), 7.19 (m, 4H), 7.23 (d, J = 8.4, 2H), 7.67 (d, J = 8.4, 2H). MS (ESI) *m/z*: [M + Na]$^+$ Calcd for C$_{28}$H$_{38}$FNNaO$_4$S$_2$Si$^+$ 586.2; Found 586.3.

5.1.7.3. 3-(2-(2-((tert-Butyldimethylsilyl)oxy)ethylsulfinyl)ethyl)-1-(3,4-difluorophenyl)-2-methyl-5-(4-(methylsulfonyl)phenyl)-1H-pyrrole (21c). Pale yellow oil (yield 89%). ^{1}H NMR (400 MHz, CDCl$_3$): 0.09 (s, 6H), 0.88 (s, 9H), 2.08 (s, 3H), 2.76–3.20 (m, 7H), 3.99–4.35 (m, 4H), 6.42 (s, 1H), 6.91 (m, 1H), 7.00 (m, 1H), 7.08–7.24 (m, 3H), 7.71 (d, J = 8.4, 2H). MS (ESI) *m/z*: [M + Na]$^+$ Calcd for C$_{28}$H$_{37}$F$_2$NNaO$_4$S$_2$Si$^+$ 604.2; Found 604.5.

5.1.8. General procedure for the synthesis of hydroxyethylsulfinyl derivatives 16a-c
To a cooled (0 °C) solution of the suitable protected alcohol (**21a-c**, 0.5 mmol, 1 equivalent) in dry THF (1 mL), a 1 M solution of tetrabutylammonium fluoride (TBAF) in THF (3 equivalents) was added dropwise and the reaction stirred for 1 h at r.t. under a nitrogen atmosphere. The reaction mixture was then treated with water and the organic phase extracted with DCM. The usual workup of the organic phase gave a residue, which was purified by flash chromatography using firstly petroleum ether/EtOAc (1:1 v/v) and then EtOAc/MeOH (9:1 v/v) as the eluting mixtures to give the expected compounds **16a-c**.

5.1.8.1. 2-(2-(2-Methyl-5-(4-(methylsulfonyl)phenyl)-1-phenyl-1H-pyrrol-3-yl)ethylsulfinyl)ethanol (16a). Pale yellow oil (yield 75%). ^{1}H NMR (400 MHz, CDCl$_3$): 2.07 (s, 3H), 2.88–3.16 (m, 9H), 4.20–4.22 (m, 2H), 6.42 (s, 1H), 7.12–7.14 (m, 4H), 7.38–7.40 (m, 3H), 7.63 (d, J = 8.0, 2H). ^{13}C NMR (101 MHz, CDCl$_3$): 10.9, 19.6, 44.5, 53.4, 53.9, 56.2, 111.6, 118.1, 127.1, 127.2, 128.2, 128.3, 129.5, 130.9, 131.3, 136.6, 138.3, 138.7. MS (ESI) *m/z*: [M + Na]$^+$ Calcd for C$_{22}$H$_{25}$NNaO$_4$S$_2^+$ 454.1; Found 454.6. HRMS (ESI) *m/z*: [M + Na]$^+$ Calcd for C$_{22}$H$_{26}$NNaO$_4$S$_2^+$ 454.11172, found 454.108891; [2 M + Na]$^+$ Calcd for C$_{44}$H$_{50}$N$_2$NaO$_8$S$_4^+$ 885.23422, found 885.230986.

5.1.8.2. 2-(2-(1-(4-Fluorophenyl)-2-methyl-5-(4-(methylsulfonyl)phenyl)-1H-pyrrol-3-yl)ethylsulfinyl)ethanol (16b). White solid (yield 75%). Mp: 146.0–147.2 °C. ^{1}H NMR (600 MHz, CDCl$_3$): 2.07 (s, 3H), 2.95–3.07 (m, 7H), 3.16 (br s, 1H), 3.21–3.29 (m, 2H), 4.14–4.25 (m, 2H), 6.44 (s, 1H), 7.07–7.20 (m, 6H), 7.68 (d, J = 8.0, 2H). ^{13}C NMR (151 MHz, CDCl$_3$): 11.0, 19.6, 44.5, 53.4, 53.9, 56.8, 111.6, 116.5 (d, J = 22.7), 118.0, 127.3, 127.4, 130.0 (d, J = 8.6), 131.6, 134.8 (d, J = 3.1), 137.0, 138.1, 161.9 (d, J = 248.9). MS (ESI) *m/z*: [M + Na]$^+$ Calcd for C$_{22}$H$_{24}$FNNaO$_4$S$_2^+$ 472.1; Found 472.3. HRMS (ESI) *m/z*: [M + Na]$^+$ Calcd for C$_{22}$H$_{24}$FNNaO$_4$S$_2^+$ 472.10230, found 472.094670; [2 M + Na]$^+$ Calcd for C$_{44}$H$_{48}$F$_2$N$_2$NaO$_8$S$_4^+$ 921.21538, found 921.200050.

5.1.8.3. 2-(2-(1-(3,4-Difluorophenyl)-2-methyl-5-(4-(methylsulfonyl)phenyl)-1H-pyrrol-3-yl)ethylsulfinyl)ethanol (16c). White solid (yield 80%), Mp: 131.4–132.6 °C. ^{1}H NMR (600 MHz, CDCl$_3$): 2.09 (s, 3H), 2.72–3.24 (m, 8H), 4.22 (m, 2H), 6.42 (s, 1H), 6.91 (m, 1H), 7.00 (m, 1H), 7.16 (d, J = 8.5, 2H), 7.21 (q, J = 8.9, 1H), 7.71 (d, J = 8.5, 2H). ^{13}C NMR (151 MHz, CDCl$_3$): 11.0, 19.6, 44.5, 53.6, 53.9, 56.7, 112.1, 117.9 (dd, J = 21.3, 18.6, 2 C), 118.1, 124.8 (dd, J = 5.3, 3.0), 127.4, 127.5, 130.9, 131.6, 135.1 (m), 137.2, 137.8, 150.0 (dd, J = 251.5, 12.5), 150.2 (dd, J = 252.3, 13.2). MS (ESI) *m/z*: [M + Na]$^+$ Calcd for C$_{22}$H$_{23}$F$_2$NNaO$_4$S$_2^+$ 490.1; Found 490.2. HRMS (ESI) *m/z*: [M + Na]$^+$ Calcd for C$_{22}$H$_{23}$F$_2$NNaO$_4$S$_2^+$ 490.09288, found 490.084417; [M + K]$^+$ Calcd for C$_{22}$H$_{23}$F$_2$KNO$_4$S$_2^+$ 506.06681, found 506.058210; [2 M + Na]$^+$ Calcd for C$_{44}$H$_{46}$F$_4$N$_2$NaO$_8$S$_4^+$ 957.19653, found 957.180217.

5.1.9. General procedure for the synthesis of compounds 22a-c
Tosyl-protected/activated alcohols **22a-c** were prepared using the same procedure reported for the synthesis of tosyl ester derivatives **18a-c** cited above.

Chapter 5. Medicinal Chemistry: novel COX-2 inhibitors containing a Nitric Oxide (NO) donor moiety endowed with vasorelaxant properties

5.1.9.1. 2-(2-(2-Methyl-5-(4-(methylsulfonyl)phenyl)-1-phenyl-1H-pyr-rol-3-yl)ethylsulfinyl)ethyl 4-methylbenzenesulfonate (22a). The title compound was obtained starting from alcohol **16a** as a yellow oil (yield 68%). ^{1}H NMR (400 MHz, CDCl$_3$): 2.06 (s, 3H), 2.41 (s, 3H), 2.90–3.15 (m, 9H), 4.38–4.52 (m, 2H), 6.41 (s, 1H), 7.15 (d, J = 8.4, 4H), 7.34 (d, J = 8.4, 2H), 7.39–7.42 (m, 3H), 7.65 (d, J = 8.4, 2H), 7.79 (d, J = 7.6, 2H). MS (ESI) *m/z*: [M + Na]$^+$ Calcd for C$_{29}$H$_{31}$NNaO$_6$S$_3^+$ 608.1; Found 608.1.

5.1.9.2. 2-(2-(1-(4-Fluorophenyl)-2-methyl-5-(4-(methylsulfonyl)phenyl)-1H-pyrrol-3-yl)ethylsulfinyl) ethyl 4-methylbenzenesulfonate (22b). The title compound was obtained starting from alcohol **16b** as a pale-yellow oil (yield 80%). ^{1}H NMR (400 MHz, CDCl$_3$): 2.03 (s, 3H), 2.44 (s, 3H), 2.91–3.13 (m, 9H), 4.37–4.61 (m, 2H), 6.41 (s, 1H), 7.09–7.17 (m, 6H), 7.34 (d, J = 7.6, 2H), 7.68 (d, J = 8.4, 2H), 7.78 (d, J = 8.2, 2H). MS (ESI) *m/z*: [M + Na]$^+$ Calcd for C$_{29}$H$_{30}$FNNaO$_6$S$_3^+$ 626.1; Found 626.3.

5.1.9.3. 2-(2-(1-(3,4-Difluorophenyl)-2-methyl-5-(4-(methylsulfonyl)phenyl)-1H-pyrrol-3-yl)ethylsulfinyl) ethyl 4-methylbenzenesulfonate (22c). The title compound was obtained starting from alcohol **16c** as a yellow oil (yield 80%). ^{1}H NMR (400 MHz, CDCl$_3$): 2.16 (s, 3H), 2.49 (s, 3H), 2.89–3.17 (m, 9H), 4.36–4.45 (m, 2H), 6.41 (s, 1H), 6.93 (m, 1H), 7.02 (m, 1H), 7.13–7.37 (m, 5H), 7.71 (d, J = 8.6, 2H), 7.78 (d, J = 8.1, 2H). MS (ESI) *m/z*: [M + Na]$^+$ Calcd for C$_{29}$H$_{29}$F$_2$NNaO$_6$S$_3^+$ 644.1; Found 644.2.

5.1.10. General procedure for the synthesis of nitrooxyethylsulfinyl derivatives 15a-c

To a 0.05 M solution of the appropriate tosyl ester derivative (**22a-c**, 0.5 mmol, 1 equivalent) in dry THF (10 mL), tetrabutylammonium nitrate (4 equivalents) was added and the mixture stirred to reflux for 1 h. Water was added, and the mixture extracted with EtOAc. The organic layer was then washed with brine and H$_2$O, dried over Na$_2$SO$_4$, filtered and the solvent evaporated in vacuo. The crude product was purified by flash chromatography on silica gel with EtOAc/methanol (1:9 v/v) as eluent to give the expected compound.

5.1.10.1. 2-(2-(2-Methyl-5-(4-(methylsulfonyl)phenyl)-1-phenyl-1H-pyr-rol-3-yl)ethylsulfinyl)ethyl nitrate (15a). Amber oil (yield 88%). ^{1}H NMR (400 MHz, CDCl$_3$): 2.06 (s, 3H), 2.98–3.12 (m, 9H), 4.90 (t, J = 5.8, 2H), 6.42 (s, 1H), 7.15 (d, J = 8.0, 2H), 7.38–7.42 (m, 5H), 7.65 (d, J = 8.0, 2H). ^{13}C NMR (101 MHz, CDCl$_3$): 10.9, 26.9, 28.8, 33.9, 44.5, 72.0, 111.7, 119.6, 127.1, 127.3, 128.1, 128.4, 129.4, 130.7, 131.1, 136.6, 138.4, 138.9. MS (ESI) *m/z*: [M + Na]$^+$ Calcd for C$_{22}$H$_{24}$N$_2$NaO$_6$S$_2^+$ 499.1; Found 499.0. HRMS (ESI) *m/z*: [M + H]$^+$ Calcd for C$_{22}$H$_{25}$N$_2$O$_6$S$_2^+$ 477.11485, found 477.109965; [M + Na]$^+$ Calcd for C$_{22}$H$_{24}$N$_2$NaO$_6$S$_2^+$ 499.09680, found 499.091710; [2 M + Na]$^+$ Calcd for C$_{44}$H$_{48}$N$_4$NaO$_{12}$S$_4^+$ 975.20438, found 957.201338.

5.1.10.2. 2-(2-(1-(4-Fluorophenyl)-2-methyl-5-(4-(methylsulfonyl)phenyl)-1H-pyrrol-3-yl)ethylsulfinyl)ethyl nitrate (15b). Pale yellow solid (yield 93%), Mp: 171.6–172.2 °C. ^{1}H NMR (400 MHz, CDCl$_3$): 2.03 (s, 3H), 2.94–3.12 (m, 9H), 4.92 (t, J = 5.8, 2H), 6.42 (s, 1H), 7.10–7.16 (m, 6H), 7.67 (d, J = 8.4, 2H). ^{13}C NMR (101 MHz, CDCl$_3$): 10.9, 19.6, 44.5, 49.1, 54.6, 65.2, 111.5, 116.5 (d, J = 22.6), 117.8, 127.3, 127.4, 130.0 (d, J = 8.5), 131.0, 131.5, 134.8 (d, J = 3.2), 137.1, 138.0, 162.0 (d, J = 249.2). MS (ESI) *m/z*: [M + Na]$^+$ Calcd for C$_{22}$H$_{23}$FN$_2$NaO$_6$S$_2^+$ 517.1; Found 517.6. HRMS (ESI) *m/z*: [M + Na]$^+$ Calcd for C$_{22}$H$_{23}$FN$_2$NaO$_6$S$_2^+$ 517.08738, found 517.080908; [M + K]$^+$ Calcd for C$_{22}$H$_{23}$FKN$_2$O$_6$S$_2^+$ 533.06131, found 533.060023; [2 M + Na]$^+$ Calcd for C$_{44}$H$_{46}$F$_2$N$_4$NaO$_{12}$S$_4^+$ 1011.18553, found 1011.179365.

5.1.10.3. 2-(2-(1-(3,4-Difluorophenyl)-2-methyl-5-(4-(methylsulfonyl)phenyl)-1H-pyrrol-3-yl)ethylsulfinyl) ethyl nitrate (15c). Straw-yellow oil (yield 65%). ^{1}H NMR (600 MHz, CDCl$_3$): 2.08 (s, 3H), 2.88–3.22 (m,

9H), 4.92 (t, J = 5.9, 2H), 6.41 (s, 1H), 6.92 (d, J = 6.9, 1H), 7.02 (t, J = 7.0, 1H), 7.17 (d, J = 8.2, 1H), 7.22 (q, J = 8.8, 2H), 7.72 (d, J = 8.2, 2H). ^{13}C NMR (151 MHz, CDCl$_3$): 11.0, 26.7, 28.9, 34.0, 44.5, 72.0, 112.0, 117.9 (d, J = 18.7, 2 C), 118.4, 124.8, 127.5 (2 C), 130.9, 131.8, 135.1, 137.4, 137.8, 150.0 (dd, J = 250.0, 11.6), 151.1 (dd, J = 252.3, 13.5). MS (ESI) *m/z*: [M + Na]$^+$ Calcd for C$_{22}$H$_{22}$F$_2$N$_2$NaO$_6$S$_2^+$ 535.1; Found 535.1. HRMS (ESI) *m/z*: [M + Na]$^+$ Calcd for C$_{22}$H$_{22}$F$_2$N$_2$NaO$_6$S$_2^+$ 535.07796, found 535.069504; [M + K]$^+$ Calcd for C$_{22}$H$_{22}$F$_2$KN$_2$O$_6$S$_2^+$ 551.05189, found 551.043263.

5.1.11. General procedure for the synthesis of nitrooxyethyl thioethers 13a-c

To a cooled (0 °C) solution of the suitable nitrooxy ethylsulfinyl derivative (**15a-c**, 1.0 mmol, 1 equivalent) in dry THF (2 mL), Lawesson's reagent (1 equivalent) was added, and the reaction was maintained under stirring for 1 h at the same temperature. The reaction mixture was then treated with water and the organic phase extracted with EtOAc. The combined extracts were dried over dry Na$_2$SO$_4$, filtered and the solvent removed in vacuo to give a residue, which after purification by flash chromatography using EtOAc/methanol (9:1 v/v) as eluent yielded the target compound (**13a-c**).

5.1.11.1. 2-(2-(2-Methyl-5-(4-(methylsulfonyl)phenyl)-1-phenyl-1H-pyr-rol-3-yl)ethylthio)ethyl nitrate (13a). Yellow oil (yield 55%). ^{1}H NMR (400 MHz, CDCl$_3$): 2.04 (s, 3H), 2.75–2.86 (m, 6H), 2.97 (s, 3H), 4.58 (t, J = 6.5, 2H), 6.42 (s, 1H), 7.12–7.14 (m, 4H), 7.37–7.39 (m, 3H), 7.62 (d, J = 8.0, 2H). ^{13}C NMR (101 MHz, CDCl$_3$): 10.9, 26.9, 28.8, 33.9, 44.5, 72.0, 111.7, 119.6, 127.1, 127.3, 128.1, 128.4, 129.4, 130.7, 131.1, 136.6, 138.4, 138.9. MS (ESI) *m/z*: [M + Na]$^+$ Calcd for C$_{22}$H$_{24}$N$_2$NaO$_5$S$_2^+$ 483.1; Found 483.3. HRMS (ESI) *m/z*: [M + H]$^+$ Calcd for C$_{22}$H$_{25}$NO$_5$S$_2^+$ 461.11994, found 461.112459; [M + Na]$^+$ Calcd for C$_{22}$H$_{24}$N$_2$NaO$_5$S$_2^+$ 483.10188, found 483.098389; [M + K]$^+$ Calcd for C$_{22}$H$_{24}$KN$_2$O$_5$S$_2^+$ 499.07582, found 499.070728; [2 M + Na]$^+$ Calcd for C$_{44}$H$_{48}$N$_4$NaO$_{10}$S$_4^+$ 943.21455, found 943.210458.

5.1.11.2. 2-(2-(1-(4-Fluorophenyl)-2-methyl-5-(4-(methylsulfonyl)-phenyl)-1H-pyrrol-3-yl)ethylthio)ethyl nitrate (13b). White solid (yield 70%), Mp: 150.5–151.4 °C. ^{1}H NMR (400 MHz, CDCl$_3$): 2.07 (s, 3H), 2.74–2.89 (m, 6H), 2.99 (s, 3H), 4.59 (t, J = 6.4, 2H), 6.42 (s, 1H), 7.10–7.16 (m, 6H), 7.66 (d, J = 8.4, 2H). ^{13}C NMR (101 MHz, CDCl$_3$): 11.1, 26.9, 28.8, 33.9, 44.5, 72.0, 111.8, 116.5 (d, J = 22.7), 119.6, 124.9, 127.4 (2C), 130.1 (d, J = 8.9), 131.3, 134.8 (d, J = 3.1), 136.8, 138.2, 151.8 (d, J = 247.9). MS (ESI) *m/z*: [M + Na]$^+$ Calcd for C$_{22}$H$_{23}$FN$_2$NaO$_5$S$_2^+$ 501.1; Found 501.2. HRMS (ESI) *m/z*: [M + Na]$^+$ Calcd for C$_{22}$H$_{23}$FN$_2$NaO$_5$S$_2^+$ 501.09246, found 501.084317; [M + K]$^+$ Calcd for C$_{22}$H$_{23}$FKN$_2$O$_5$S$_2^+$ 517.06640, found 517.058102; [2 M + Na]$^+$ Calcd for C$_{44}$H$_{46}$F$_2$N$_4$NaO$_{10}$S$_4^+$ 979.19570, found 979.180140.

5.1.11.3. 2-(2-(1-(3,4-Difluorophenyl)-2-methyl-5-(4-(methylsulfonyl)phenyl)-1H-pyrrol-3-yl)ethylthio)ethyl nitrate (13c). Straw-yellow oil (yield 72%). ^{1}H NMR (600 MHz, CDCl$_3$): 2.06 (s, 3H), 2.70–2.94 (m, 6H), 3.01 (s, 3H), 4.59 (t, J = 7.0, 2H), 6.43 (s, 1H), 6.92 (d, J = 7.8, 1H), 7.03 (d, J = 7.4, 1H), 7.15–7.23 (m, 3H), 7.72 (d, J = 8.2. 2H). ^{13}C NMR (151 MHz, CDCl$_3$): 11.0, 27.0, 28.9, 34.6, 44.5, 72.1, 112.2, 117.9 (dd, J = 17.7, 13.5, 2 C), 120.2, 124.8, 127.4 (2 C), 130.6, 131.4, 135.1 (m), 137.1, 137.9, 149.9 (dd, J = 250.0, 11.6), 151.1 (dd, J = 252.3, 13.5). MS (ESI) *m/z*: [M + H]$^+$ Calcd for C$_{22}$H$_{23}$F$_2$N$_2$O$_5$S$_2^+$ 497.1; Found 497.1. HRMS (ESI) *m/z*: [M + H]$^+$ Calcd for C$_{22}$H$_{23}$F$_2$N$_2$O$_5$S$_2^+$ 497.10110, found 497.098109; [M + Na]$^+$ Calcd for C$_{22}$H$_{22}$F$_2$N$_2$NaO$_5$S$_2^+$ 519.08304, found 519.078053; [2 M + Na]$^+$ Calcd for C$_{44}$H$_{44}$F$_4$N$_4$NaO$_{10}$S$_4^+$ 1015.17686, found 1015.170694.

5.2. In vitro inhibition of COX-1 and COX-2 enzymes

The *in vitro* COX-1 and COX-2 inhibition of target compounds **13–16**

was evaluated through cell-based assay employing murine monocyte/macrophage J774 cell lines. The cell line was grown in DMEM supplemented with 2 mM glutamine, 25 mM HEPES, 100 units/mL penicillin, 100 μg/mL streptomycin, 10% fetal bovine serum (FBS), and 1.2% sodium pyruvate. Cells were plated in 24-well culture plates at a density of 2.5×10^5 cells/mL and allowed to adhere at 37 °C in 5% CO_2 for 2 h. Immediately before the experiments, culture medium was replaced with fresh medium and cells were stimulated as described previously [47]. The evaluation of COX-1 inhibitory activity was achieved pretreating cells with test compounds (10 μM) for 15 min and then incubating them at 37 °C for 30 min with 15 μM arachidonic acid to activate the constitutive COX. At the end of the incubation, the supernatants were collected for the measurement of PGE_2 levels by an enzyme immunoassay (EIA). To evaluate COX-2 activity, cells were stimulated for 24 h with Escherichia coli lipopolysaccharide (LPS, 10 μg/mL) to induce COX-2, in the absence or presence of test compounds (0.001–10 μM). The supernatants were collected for the measurement of PGE_2 by means of EIA. Celecoxib was utilized as a reference compound for the selectivity index. Triplicate wells were used for the various conditions of the treatment in the cell culture assay throughout the experiments. Results are expressed as the mean of three experiments of the % inhibition of PGE_2 production by test compounds with respect to control samples. Data fit was obtained using the sigmoidal dose-response equation (variable slope) (GraphPad software). The IC_{50} values were calculated by the GraphPad Instat program (GraphPad software).

5.3. Computational details

Molecular docking experiments were conducted using Glide software (Glide, Schrödinger, LLC, New York, NY, release 2015-1) using Maestro Drug Discovery suite release 2015 as graphical interface as previously reported [34,39]. The crystal structure of *h*COX-2 (PDB ID 5KIR (10.1107/S2053230X16014230)) was downloaded from Protein Data Bank (PDB, https://www.rcsb.org/) and treated by Protein Preparation Wizard application available in Maestro in order to obtain a suitable structure for further *in silico* investigation. Drawing tools available in Maestro were adopted for building the structure of the ligands. MacroModel software was used for compounds energy minimization employing with OPLS-2005 force field. The resulting molecules were submitted to LigPrep application (LigPrep, Schrödinger, LLC, New York, NY, release 2017) for generating the most plausible ionization state at physiological pH (7.4 ± 0.2). Glide calculations were conducted using extra precision (XP) as scoring function. Default values were used for preparing the energy grids (protein atom scaling factor 1.0 Å, within a cubic box centered on crystallized ligands). The number of poses entered to post-docking minimization was set to 50.

5.4. In vitro oxidative metabolic stability

5.4.1. Intrinsic clearance in microsomes [48]

Mouse (Sigma Aldrich, CD-1 male, pooled) and human microsomes (Sigma Aldrich, human, pooled), at the final concentration of 0.5 mg/mL, were preincubated with the test compounds **13b**, **14b**, **15b**, and **16b** dissolved in DMSO at the final concentration of 1 μM in phosphate buffer 50 mM, pH 7.4, 3 mM $MgCl_2$ for 10 min at 37 °C. Reaction was then started by adding the cofactor mixture solution (NADP, glucose-6-phosphate, glucose-6-phosphate dehydrogenase in 2% $NaHCO_3$). Samples were taken at 0, 10, 30, 45, and 60 min and added to acetonitrile to stop the reaction. Samples were then centrifuged, and the supernatant was analyzed by LC-MS/MS to quantify the amount of compound. A control sample without cofactor was always added to check the chemical stability of test compound. Two reference compounds of known metabolic stability, 7-ethoxycoumarin (7-EC) and propranolol, were present in every experiment. A fixed concentration of verapamil was added in every sample as internal standard for LC-MS/MS analyses. The percentage of the area of the test compound remaining at the various

incubation times was calculated with respect to the area of the compound at time 0 min. The rate constant, k (min^{-1}) derived for the exponential decay equation (peak area/IS vs time) was used to calculate the rate of intrinsic clearance (Cli) of the compounds using the following equation:

Cli (μL/min/mg) = k/microsomal conc. x 1000

Where k is the rate constant (min^{-1}) and microsomal protein conc. = 0.5 mg protein/mL. The classification of the *in vitro* stability is reported as Supplementary Material in Table S1.

5.4.2. LC–MS/MS analytical method

Samples were analyzed under the following conditions: UFLC (Shimadzu) AC20 coupled with an API 3200 triple-quadrupole (ABSciex); eluents, (phase A) 95% water, 5% acetonitrile + 0.1% HCOOH, (phase B) 5% water, 95% acetonitrile + 0.1% HCOOH; flow rate, 0.3 mL/min; column, Gemini-Nx 5 μm C18 110Å (50 × 2.00 mm) at 35 °C; injection volume, 5 μL. LC-MS/MS analyses were carried out using an ESI-(+) interface in multiple reaction monitoring mode (MRM). Source conditions ESI positive: T = 450 °C, Gas 1 = 45, Gas 2 = 35, CUR = 40, IS = 4500, CAD 2. Compounds retention times and MRM transitions and conditions are reported as supplementary material in Tables S2 and S3.

5.5. Vasorelaxant activity determination

5.5.1. Animals and tissue preparation [49]

All animal experiments were performed in compliance with the Austrian law on experimentation with laboratory animals (last amendment 2013) based on the European Union guidelines for the Care and the Use of Laboratory Animals (European Union Directive 2010/63/EU). Thoracic aortas were harvested from unsexed Sprague-Dawley rats (obtained from Charles River, Sulzfeld, Germany) that were housed at the local animal facility in approved cages. They were fed standard chow (Altromin 3023; obtained from Königshofer Futtermittel, Ebergassing, Austria) and received water *ad libitum*. Animals were euthanized in a box that was gradually filled with CO_2 until no more vital signs (cessation of respiration and circulation) were noticed. Subsequently, the thorax of the animals was opened, the thoracic aorta removed, cleaned from connective tissue, and used for assessment of vessel function. The killing of animals solely for the use of their organs or tissues is explicitly excluded in Article 3 (page L276/39) of EU Directive 2010/63/EU on protection of animals used for scientific purposes.

5.5.2. Isometric tension vasomotor studies

For isometric tension measurements, vessel rings with intact endothelium were suspended in 5-mL organ baths containing oxygenated Krebs-Henseleit buffer (concentrations in mM: NaCl 118.4, $NaHCO_3$ 25, KCl 4.7, KH_2PO_4 1.2, $CaCl_2$ 2.5, $MgCl_2$ 1.2, D-Glucose 11; pH 7.4), as previously described in detail [50]. After equilibration for 60 min at the optimal resting tension of 20 mN, maximal contractile activity was determined with a depolarizing solution containing 60 mM K^+. Rings that did not elicit adequate and stable contraction to high K^+ were considered damaged and omitted from the study. After washout, tissues were precontracted with L-phenylephrine (PE 10 μM; Sigma-Aldrich, Vienna, Austria) to an equivalent level (i. e. ~90% of maximal contraction obtained with high K^+). When contraction had reached a stable plateau (~after 20 min) cumulative concentration-response curves were established with experimental compounds (10 nM-100 μM). Where indicated, the effects of the compounds on vascular tone were tested in the presence of the guanylate cyclase inhibitor 1*H*- [1,2,4] oxadiazolo-[4,3-*a*]quinoxalin-1-one (ODQ 10 μM; Enzo Life Sciences, Lausen, Switzerland). The contractile force corresponding to each agonist concentration was recorded and expressed as percent of pre-contraction. When applicable, concentration-response curves were fitted to a Hill-type model giving estimates of agonist potency (EC_{50}) and

efficacy (E_{max}).

5.6. In vivo studies

5.6.1. Animals

For all the experiments described below, male CD1 albino mice (23–25 g) or male Sprague–Dawley rats (Harlan, Varese, Italy) weighing approximately 200–250 g at the beginning of the experimental procedure, were used. Animals were housed in CeSAL (Centro Stabulazione Animali da Laboratorio, University of Florence) and used at least one week after their arrival. Four rats were housed per cage (size 26 × 41 cm); animals were fed a standard laboratory diet and tap water *ad libitum*, and kept at 23 ± 1 °C with a 12 h light/dark cycle, light at 7 a.m. All animal manipulations were carried out according to the European Community guidelines for animal care (DL 116/92, application of the European Communities Council Directive of November 24, 1986 (86/609/EEC). The ethical policy of the University of Florence complies with the Guide for the Care and Use of Laboratory Animals of the US National Institutes of Health (NIH Publication No. 85-23, revised 1996; University of Florence assurance number: A5278-01). Formal approval to conduct the experiments described was obtained from the Italian Ministry of Health (N° 54/2014-B) and from the Animal Subjects Review Board of the University of Florence. Experiments involving animals have been reported according to ARRIVE guideline. All efforts were made to minimize animal suffering and to reduce the number of animals used.

5.6.2. Carrageenan-induced acute inflammatory pain

One hundred μL of carrageenan solution (Sigma–Aldrich; 1% in saline) was injected intraplantarly into the rat left hind paw. 2 h after carrageen injection, compounds were administered (p.o.) and their anti-hypersensitive effect was measured over time by the paw pressure test. Control rats received 100 μL of vehicle (saline) solution intraplantarly and saline i.p..

5.6.3. Abdominal contraction pain

At predetermined time intervals (30 and 60 min) after drug administration, mice were injected intraperitoneally with a 0.6% (w/w) solution of acetic acid (10 mL kg^{-1}), to induce pain sensation evident from typical abdominal contractions of animals named 'writhing'. The number of induced writhings was counted for 10 min, starting 5 min after acetic acid injection [51].

5.6.4. Paw pressure test

The pain threshold in the rat was determined with an analgesimeter (Ugo Basile, Varese, Italy) as described [52]. Briefly, a constantly increasing pressure was applied to a small area of the dorsal surface of the paw using a blunt conical probe. Pressure was increased until a vocalization or a withdrawal reflex occurred. The withdrawal threshold was expressed in grams, the test was repeated twice, and the mean was considered as the value for each paw.

5.6.5. Edema volume measurement

Rat paw volumes were measured using a plethysmometer. Sixty min after the injection of carrageenan, the paw volume of the ipsilateral hind paw was measured and compared with carrageenan + vehicle-treated controls. The results are reported as paw volume expressed in mL.

5.6.6. Statistical analysis of behavioral measurements

Results were expressed as means ± s.e.m. and the analysis of variance was performed by one way ANOVA. A Bonferroni's significant difference procedure was used as post-hoc comparison. P values of less than 0.05 or 0.01 were considered significant. Data were analyzed by means of the "Origin 9" software (OriginLab, Northampton, USA).

Author contributions

The manuscript was written through contributions of all authors. All authors have given approval to the final version of the manuscript.

Declaration of competing interest

The authors declare that they have no known competing financial interests or personal relationships that could have appeared to influence the work reported in this paper.

Data availability

Data will be made available on request.

Appendix A. Supplementary data

Supplementary data to this article can be found online at https://doi.org/10.1016/j.ejmech.2022.114615.

References

[1] T. Grosser, E.M. Smyth, G.A. FitzGerald, Antiinfiammatori, antipiretici, e analgesici; farmacoterapia della gotta, in: L. Brunton, B.A. Chabner, B.C. Knollmann (Eds.), Le Basi Farmacologiche Della Terapia, twelfth ed., Zanichelli Editore, Bologna, 2012, pp. 45–80.

[2] J.-Y. Reginster, O. Bruyère, P.G. Conaghan, T. McAlindon, C. Cooper, Importance of safety in the management of osteoarthritis and the need for updated meta-analyses and recommendations for reporting of harms, Drugs Aging 36 (2019) 3–6, https://doi.org/10.1007/s40266-019-00659-8.

[3] X.-P. Miao, J.-S. Li, Q. Ouyang, R.-W. Hu, Y. Zhang, H.-Y. Li, Tolerability of selective cyclooxygenase 2 inhibitors used for the treatment of rheumatological manifestations of inflammatory bowel disease, Cochrane Database Syst. Rev. 10 (2014) CD007744, https://doi.org/10.1002/14651858.CD007744.pub2.

[4] A. Kahokehr, R. Vather, A. Nixon, A.G. Hill, Non-steroidal anti-inflammatory drugs for lower urinary tract symptoms in benign prostatic hyperplasia: systematic review and meta-analysis of randomized controlled trials, BJU Int. 111 (2013) 304–311, https://doi.org/10.1111/j.1464-410X.2012.11559.x.

[5] C. Warren-Gash, J.A. Udell, Respiratory tract infections, nonsteroidal anti-inflammatory drugs and acute myocardial infarction: is understanding interaction between risk factors the key to personalizing prevention? J. Infect. Dis. 215 (2017) 497–499, https://doi.org/10.1093/infdis/jiw604.

[6] S.L. Corson, R.J. Bolognese, Ibuprofen therapy for dysmenorrhea, J. Reprod. Med. 20 (1978) 246–252.

[7] Johns Hopkins Lupus Center, Treating Lupus with NSAIDs, (n.d.).

[8] S. Derry, P.J. Wiffen, W. Häuser, M. Mücke, T.R. Tölle, R.F. Bell, R.A. Moore, Oral nonsteroidal anti-inflammatory drugs for fibromyalgia in adults, Cochrane Database Syst. Rev. 3 (2017) CD012332, https://doi.org/10.1002/14651858.CD012332.pub2.

[9] M.N.A. Khan, Y.S. Lee, Cyclooxygenase inhibitors: scope of their use and development in cancer chemotherapy, Med. Res. Rev. 31 (2011) 161–201, https://doi.org/10.1002/med.20182.

[10] C. Sticozzi, G. Belmonte, F. Cervellati, A. Di Capua, E. Maioli, A. Cappelli, A. Giordani, M. Biava, M. Anzini, G. Valacchi, Antiproliferative effect of two novel COX-2 inhibitors on human keratinocytes, Eur. J. Pharmaceut. Sci. 49 (2013) 133–141, https://doi.org/10.1016/j.ejps.2013.02.009.

[11] J.R. Vane, R.M. Botting, Mechanism of action of nonsteroidal anti-inflammatory drugs, Am. J. Med. 104 (1998) 2S–8S, https://doi.org/10.1016/S0002-9343(97)00203-9.

[12] G. Kauffman, Aspirin-induced gastric mucosal injury: lessons learned from animal models, Gastroenterology 96 (1989) 606–614, https://doi.org/10.1016/S0016-5085(89)80056-3.

[13] D.L. DeWitt, COX-2-Selective inhibitors: the new super aspirins, Mol. Pharmacol. 55 (1999) 625. http://molpharm.aspetjournals.org/content/55/4/625.abstract.

[14] N. Hashemi Goradel, M. Najafi, E. Salehi, B. Farhood, K. Mortezaee, Cyclooxygenase-2 in cancer: a review, J. Cell. Physiol. 234 (2019) 5683–5699, https://doi.org/10.1002/jcp.27411.

[15] D. Wang, R.N. DuBois, Eicosanoids and cancer, Nat. Rev. Cancer 10 (2010) 181–193, https://doi.org/10.1038/nrc2809.

[16] P. McGettigan, D. Henry, Cardiovascular risk and inhibition of cyclooxygenase, JAMA 296 (2006) 1633, https://doi.org/10.1001/jama.296.13.jrv60011.

[17] L.A. Perry, C. Mosler, A. Atkins, M. Minehart, Cardiovascular Risk Associated with NSAIDs and COX-2 Inhibitors, 2014, pp. 35–38. https://Www.Uspharmacist.Com/Article/Cardiovascular-Risk-Associated-with-Nsaids-and-Cox2-Inhibitors.

[18] J.-M. Dogné, C.T. Supuran, D. Pratico, Adverse cardiovascular effects of the coxibs, J. Med. Chem. 48 (2005) 2251–2257, https://doi.org/10.1021/jm0402059.

[19] J.A. Baron, R.S. Sandler, R.S. Bresalier, A. Lanas, D.G. Morton, R. Riddell, E.R. Iverson, D.L. DeMets, Cardiovascular events associated with rofecoxib: final

analysis of the APPROVe trial, Lancet 372 (2008) 1756–1764, https://doi.org/10.1016/S0140-6736(08)61490-7.

[20] S.X. Sun, K.Y. Lee, C.T. Bertram, J.L. Goldstein, Withdrawal of COX-2 selective inhibitors rofecoxib and valdecoxib: impact on NSAID and gastroprotective drug prescribing and utilization, Curr. Med. Res. Opin. 23 (2007) 1859–1866, https://doi.org/10.1185/030079907X210561.

[21] J.F. Kerwin, J.R. Lancaster, P.L. Feldman, Nitric oxide: a new paradigm for second messengers, J. Med. Chem. 38 (1995) 4343–4362, https://doi.org/10.1021/jm00022a001.

[22] L.J. Ignarro, Nitric oxide as a unique signaling molecule in the vascular system: a historical overview, J. Physiol. Pharmacol. 53 (2002) 503–514.

[23] J.L. Wallace, P. del Soldato, The therapeutic potential of NO-NSAIDs, Fundam. Clin. Pharmacol. 17 (2003) 11–20, https://doi.org/10.1046/j.1472-8206.2003.00125.x.

[24] W.K. MacNaughton, G. Cirino, J.L. Wallace, Endothelium-derived relaxing factor (nitric oxide) has protective actions in the stomach, Life Sci. 45 (1989) 1869–1876, https://doi.org/10.1016/0024-3205(89)90540-7.

[25] H. Kitagawa, F. Takeda, H. Kohei, Effect of endothelium-derived relaxing factor on the gastric lesion induced by HCl in rats, J. Pharmacol. Exp. Therapeut. 253 (1990) 1133–1137.

[26] J.L. Wallace, B. Reuter, C. Cicala, W. McKnight, M.B. Grisham, G. Cirino, Novel nonsterodial anti-inflammatory drug derivatives with markedly reduced ulcerogenic properties in the rat, Gastroenterology 107 (1994) 173–179, https://doi.org/10.1016/0016-5085(94)90074-4.

[27] C. Velázquez, P.N. Praveen Rao, E.E. Knaus, Novel nonsteroidal antiinflammatory drugs possessing a nitric oxide donor diazen-1-ium-1,2-diolate moiety: design, synthesis, biological evaluation, and nitric oxide release studies, J. Med. Chem. 48 (2005) 4061–4067, https://doi.org/10.1021/jm050211k.

[28] C. Pereira-Leite, C. Nunes, J.C. Bozelli, S. Schreier, C.S. Kamma-Lorger, I. M. Cuccovia, S. Reis, Can NO-indomethacin counteract the topical gastric toxicity induced by indomethacin interactions with phospholipid bilayers? Colloids Surf., B 169 (2018) 375–383, https://doi.org/10.1016/j.colsurfb.2018.05.019.

[29] P. Geusens, Naproxcinod, a new cyclooxygenase-inhibiting nitric oxide donor (CINOD), Expet Opin. Biol. Ther. 9 (2009) 649–657, https://doi.org/10.1517/14712590902926071.

[30] M.A. Barmade, R.B. Ghuge, Vicinal Diaryl Heterocyclic System: A Privileged Scaffold in the Discovery of Potential Therapeutic Agents, Vicinal Diaryl Substituted Heterocycles, Elsevier, 2018, pp. 1–20, https://doi.org/10.1016/B978-0-08-102237-5.00001-8.

[31] R.B. Ghuge, A.N. Khadse, Vicinal Diaryl Pyrroles: Synthesis and Biological Aspects, Vicinal Diaryl Substituted Heterocycles, Elsevier, 2018, pp. 47–82, https://doi.org/10.1016/B978-0-08-102237-5.00003-1.

[32] M. Biava, G.C. Porretta, A. Cappelli, S. Vomero, F. Manetti, M. Botta, L. Sautebin, A. Rossi, F. Makovec, M. Anzini, 1,5-Diarylpyrrole-3-acetic acids and esters as novel classes of potent and highly selective cyclooxygenase-2 inhibitors, J. Med. Chem. 48 (2005) 3428–3432, https://doi.org/10.1021/jm049121q.

[33] M. Anzini, M. Rovini, A. Cappelli, S. Vomero, F. Manetti, M. Botta, L. Sautebin, A. Rossi, C. Pergola, G. Ghelardini, M. Norcini, A. Giordani, F. Makovec, P. Anzellotti, P. Patrignani, M. Biava, Synthesis, biological evaluation, and enzyme docking simulations of 1,5-diarylpyrrole-3-alkoxyethyl ethers as selective cyclooxygenase-2 inhibitors endowed with anti-inflammatory and antinociceptive activity, J. Med. Chem. 51 (2008) 4476–4481, https://doi.org/10.1021/jm800084s.

[34] A. Reale, S. Brogi, A. Chelini, M. Paolino, A. Di Capua, G. Giuliani, A. Cappelli, G. Giorgi, G. Chemi, A. Grillo, M. Valoti, L. Sautebin, A. Rossi, S. Pace, C. la Motta, L. di Cesare Mannelli, E. Lucarini, C. Ghelardini, M. Anzini, Synthesis, biological evaluation and molecular modeling of novel selective COX-2 inhibitors: sulfide, sulfoxide, and sulfone derivatives of 1,5-diarylpyrrol-3-substituted scaffold, Bio 27 (2019), 115045, https://doi.org/10.1016/j.bmc.2019.115045.

[35] M. Biava, G.C. Porretta, G. Poce, C. Battilocchio, S. Alfonso, M. Rovini, S. Valenti, G. Giorgi, V. Calderone, A. Martelli, L. Testai, L. Sautebin, A. Rossi, G. Papa, C. Ghelardini, L. di Cesare Mannelli, A. Giordani, P. Anzellotti, A. Bruno, P. Patrignani, M. Anzini, Novel analgesic/anti-inflammatory agents: diarylpyrrole acetic esters endowed with nitric oxide releasing properties, J. Med. Chem. 54 (2011) 7759–7771, https://doi.org/10.1021/jm200715n.

[36] M. Anzini, A. Di Capua, S. Valenti, S. Brogi, M. Rovini, G. Giuliani, A. Cappelli, S. Vomero, L. Chiasserini, A. Sega, G. Poce, G. Giorgi, V. Calderone, A. Martelli,

L. Testai, L. Sautebin, A. Rossi, S. Pace, C. Ghelardini, L. di Cesare Mannelli, V. Benetti, A. Giordani, P. Anzellotti, M. Dovizio, P. Patrignani, M. Biava, Novel analgesic/anti-inflammatory agents: 1,5-diarylpyrrole nitrooxyalkyl ethers and related compounds as cyclooxygenase-2 inhibiting nitric oxide donors, J. Med. Chem. 56 (2013) 3191–3206, https://doi.org/10.1021/jm301370e.

[37] A. Giordani, M. Biava, M. Anzini, V. Calderone, L.C. Rovati, Diaryl-2-alkylpyrrole-3-substituted Nitro Esters, Selective COX-2 Inhibitors and Nitric Oxide Donors, vol. 1, WO2012032479A1, 2012, p. 5.

[38] A. Martelli, L. Testai, M. Anzini, A. Cappelli, A. Di Capua, M. Biava, G. Poce, S. Consalvi, A. Giordani, G. Caselli, L. Rovati, C. Ghelardini, P. Patrignani, L. Sautebin, M.C. Breschi, V. Calderone, The novel anti-inflammatory agent VA694, endowed with both NO-releasing and COX2-selective inhibiting properties, exhibits NO-mediated positive effects on blood pressure, coronary flow and endothelium in an experimental model of hypertension and endothelial dysfunction, Pharmacol. Res. 78 (2013) 1–9, https://doi.org/10.1016/j.phrs.2013.09.008.

[39] A. Di Capua, C. Sticozzi, S. Brogi, M. Brindisi, A. Cappelli, L. Sautebin, A. Rossi, S. Pace, C. Ghelardini, L. di Cesare Mannelli, G. Valacchi, G. Giorgi, A. Giordani, G. Poce, M. Biava, M. Anzini, Synthesis and biological evaluation of fluorinated 1,5-diarylpyrrole-3-alkoxyethyl ether derivatives as selective COX-2 inhibitors endowed with anti-inflammatory activity, Eur. J. Med. Chem. 109 (2016) 99–106, https://doi.org/10.1016/j.ejmech.2015.12.044.

[40] H.S. Broadbent, W.S. Burnham, R.K. Olsen, R.M. Sheeley, Sterically-crowded pyrroles, J. Heterocycl. Chem. 5 (1968) 757–767, https://doi.org/10.1002/jhet.5570050604.

[41] S.K. Chaudhary, O. Hernandez, 4-dimethylaminopyridine: an efficient and selective catalyst for the silylation of alcohols, Tetrahedron Lett. 20 (1979) 99–102, https://doi.org/10.1016/S0040-4039(01)85893-7.

[42] W.K. Slusarek, X. Yang, M.E. Irving, D.H. Levy, J.B. Mooberry, J.J. Seifert, J. H. Reynolds, L.M. Irving, Z.R. Owczarczyk, D.K. Southby, Color Photothermographic Elements Comprising Blocked Developing Agents, US6537712B1, 2003.

[43] H. Bartsch, T. Erker, The Lawesson reagent as selective reducing agent for sulfoxides, Tetrahedron Lett. 33 (1992) 199–200, https://doi.org/10.1016/0040-4039(92)88049-B.

[44] I. Varfaj, A. di Michele, F. Ianni, M. Saletti, M. Anzini, C. Barola, B. Chankvetadze, R. Sardella, A. Carotti, Enantioseparation of novel anti-inflammatory chiral sulfoxides with two cellulose dichlorophenylcarbamate-based chiral stationary phases and polar-organic mobile phase(s), J. Chromatogr. A 1 (2021), 100022, https://doi.org/10.1016/j.jcoa.2021.100022.

[45] G.M. Sheldrick, Acta Crystallogr. A 64 (1) (2008) 112, https://doi.org/10.1107/S0108767307043930.

[46] G.M. Sheldrick, Acta Crystallogr. C 71 (1) (2015) 3, https://doi.org/10.1107/S2053229614024218.

[47] A. Rossi, A. Ligresti, R. Longo, A. Russo, F. Borrelli, L. Sautebin, The inhibitory effect of propolis and caffeic acid phenethyl ester on cyclooxygenase activity in J774 macrophages, Phytomedicine 9 (6) (2002) 530–535, https://doi.org/10.1078/09447110260573164.

[48] S.E. Clarke, P. Jeffrey, Utility of metabolic stability screening: comparison of *in vitro* and *in vivo* clearance, Xenobiotica 31 (2001) 591–598, https://doi.org/10.1080/00498250110057350.

[49] G. Wölkart, A. Schrammel, C.N. Kovani, S. Scherübel, K. Zorn-Pauly, E. Malle, B. Pelzmann, M. Andrä, A. Ortner, B. Mayer, Br. J. Pharmacol. 174 (20) (2017) 3640–3653, https://doi.org/10.1111/bph.13967.

[50] G. Wölkart, A. Kollau, H. Stessel, M. Russwurm, D. Koesling, A. Schrammel, K. Schmidt, B. Mayer, Effects of flavoring compounds used in electronic cigarette refill liquids on endothelial and vascular function, PLoS One 14 (2019), e0222152, https://doi.org/10.1371/journal.pone.0222152.

[51] N. Mennini, S. Furlanetto, M. Bragagni, C. Ghelardini, L. di Cesare Mannelli, P. Mura, Development of a chitosan-derivative micellar formulation to improve celecoxib solubility and bioavailability, Drug Dev. Ind. Pharm. 40 (2014) 1494–1502, https://doi.org/10.3109/03639045.2013.831440.

[52] G.E. Leighton, R.E. Rodriguez, R.G. Hill, J. Hughes, κ-Opioid agonists produce antinociception after i.v. and i.c.v. but not intrathecal administration in the rat, Br. J. Pharmacol. 93 (1988) 553–560, https://doi.org/10.1111/j.1476-5381.1988.tb10310.x.

16

5.5. Research article: "Enantioseparation of novel anti-inflammatory chiral sulfoxides with two cellulose dichlorophenylcarbamate-based chiral stationary phases and polar-organic mobile phase(s)".

Contribution: The Ph.D. candidate's contribution to this work includes synthesizing and preliminary NMR characterization of analyzed compounds and reviewing the manuscript.

The current work has reported the enantioresolution of two nitrooxyethyl sulfoxides along with their metabolites, hydroxyethyl derivatives, with two cellulose tris(3,5-dichlorophenylcarbamate)-based chiral stationary phases (CSPs) one with a coated (CSP 1) and the other (CSP 2) with an immobilized chiral selector. The immobilized selector in CSP 2 produced comparable-to-better performances than the coated one in CSP 1 running the analysis with a polar-organic mobile phase. Interestingly, for the two hydroxyethyl derivatives, the same enantiomeric elution order was obtained with both CSPs, while the compounds containing the NO group, such as nitrooxyethyl sulfoxides, provided a different elution order depending on the coated or immobilized nature of the chiral selector. In addition, a molecular modeling study based on docking simulations has been performed to gain a deeper insight into the enantioseparation mechanism of the hydroxyethyl derivatives on both CSPs.

Enantioseparation of novel anti-inflammatory chiral sulfoxides with two cellulose dichlorophenylcarbamate-based chiral stationary phases and polar-organic mobile phase(s)

Ina Varfaj [a,1], Alessandro Di Michele [b,1], Federica Ianni [a], Mario Saletti [c], Maurizio Anzini [c], Carolina Barola [d], Bazan Chankvetadze [e], Roccaldo Sardella [a,*], Andrea Carotti [a,*]

[a] *Department of Pharmaceutical Sciences, University of Perugia, Via Fabritius 48, 06123 Perugia, Italy*
[b] *Department of Physics and Geology, University of Perugia, Via Pascoli 1, 06123 Perugia, Italy*
[c] *Department of Biotechnology, Chemistry and Pharmacy, University of Siena, Via A. Moro, 53100 Siena, Italy*
[d] *Istituto Zooprofilattico Sperimentale dell'Umbria e delle Marche "Togo Rosati", Via G. Salvemini 1, 06126 Perugia, Italy*
[e] *Institute of Physical and Analytical Chemistry, School of Exact and Natural Sciences, Tbilisi State University, Chavchavadze Ave 3, 0179 Tbilisi, Georgia*

ARTICLE INFO

ABSTRACT

Chiral sulfoxides represent a class of substances of great importance in many fields, including medicinal chemistry dealing with the synthesis of novel cyclooxygenase-2 (COX-2) inhibiting/NO donors. In the present study, two nitrooxyethyl sulfoxides along with their metabolites, hydroxyethyl derivatives have been successfully enantioresolved with two cellulose *tris*(3,5-dichlorophenylcarbamate)-based chiral stationary phases (CSPs), one with a coated (CSP 1) and the other (CSP 2) with an immobilized chiral selector. The immobilized selector in CSP 2 produced comparable-to-better performances than the coated one in CSP 1 (with α and R_S values up to 1.94 and 6.32, respectively) running the analysis with a polar-organic phase made up with an ethanol/2-propanol (80:20, v/v) mobile phase. Electronic circular dichroism studies coupled to *ab initio* time-dependent density functional theory simulations allowed us to determine the elution order of three out of four compounds. For the two hydroxyethyl derivatives the same enantiomeric elution order [(*S*)<(*R*)] was obtained with both CSPs, while the compounds containing the −ONO$_2$ group experienced a different elution order depending on the coated or immobilized nature of the chiral selector [(*S*)<(*R*) with CSP 1 and (*R*)<(*S*) with CSP 2]. A molecular modeling study based on docking simulations was performed to gain a deeper insight into the enantioseparation mechanism of the hydroxyethyl derivatives on both CSPs.

1. Introduction

Chiral stationary phases (CSPs) based on derivatized cellulose and amylose chiral selectors are recognized as the most versatile materials for the successful enantioseparation of analytes belonging to different chemical classes [1–5]. In this framework, the polysaccharide phenylcarbamates have demonstrated relevant chiral recognition abilities towards chiral sulfoxides in all the most relevant elution modes: normal phase (NP) [6–8], reversed-phase (RP) [9,10], and polar-organic (PO) conditions [11–14].

Chiral sulfoxides represent a class of substances of great importance in many fields, including the synthesis of active pharmaceutical ingredients (APIs) contained in some major blockbuster drugs, such as omeprazole, lansoprazole, pantoprazole as well as of chiral pesticides, whose fipronil is an interesting example. It is worth to be highlighted that some of the drugs for human use containing chiral sulfoxide APIs (such as, omeprazole and lansoprazol) are available also in enantiomerically pure forms in some formulations.

Over the last decades, the widespread interest towards chiral sulfoxides (either as racemates or enantiomerically pure forms, the latter underlying the importance to develop enantioselective chromatography methods) has inspired several medicinal chemistry projects, including those focused on the synthesis of nonsteroidal anti-inflammatory drugs (NSAIDs) endowed with selective cyclooxygenase-2 (COX-2) inhibition activity [15–18].

Suppression of Prostaglandin I2 (PGI2) formation due to the inhibition of vascular COX-2 has been found to be sufficient to account for the cardiovascular (CV) hazard from traditional NSAIDs (*t*NSAID) and selective ones for COX-2 [15]. These findings justify the need to develop NSAIDs with NO-releasing properties in order to mitigate their gastroin-

---

Chapter 5. Medicinal Chemistry: novel COX-2 inhibitors containing a Nitric Oxide (NO) donor moiety endowed with vasorelaxant properties

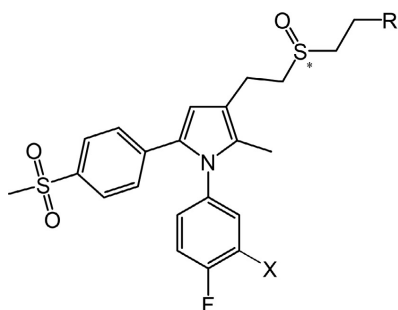I. Varfaj, A.D. Michele, F. Ianni et al.

Fig. 1. Structure of the investigated compounds.

1: X=H, R=ONO₂
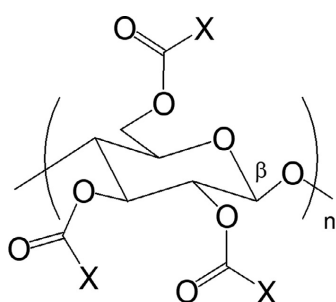**2**: X=F, R=ONO₂
3: X=H, R=OH
4: X=F, R=OH

Fig. 2. Structure of the employed chiral stationary phases.

X=

CSP 1: coated chiral selector
CSP 2: immobilized chiral selector

testinal (GI) and CV hazard. Indeed, the novel class of anti-inflammatory agents, named COX-inhibiting nitric oxide donors (CINODs), developed by linking a NO-releasing moiety to a *t*NSAID, has been shown to have a more favourable clinical profile than the parent traditional NSAIDs in randomized clinical trials [16,17].

In this scenario, as an extension of our previous work focused on novel COX-2 inhibiting/NO donors and encouraged by the promising results of previously reported nitrooxy- and hydroxyethyl ethers [18], we shifted our attention on the synthesis of the nitrooxyethyl sulfoxides **1** and **2** (Fig. 1) along with that of their metabolites hydroxyethyl derivatives **3** and **4** (Fig. 1).

In a previous work [14], we successfully used a CSP based on a coated cellulose *tris*(3,5-dichlorophenylbarbamate) chiral selector (CSP 1, Fig. 2) for the PO enantioseparation of two chiral sulfoxides sharing structural characteristics with compounds **1–4** (Fig. 1). In the present study, the profitable use of CSP 1 under the same mass spectrometry (MS) fully compatible elution regime is demonstrated also for compounds **1–4**. A comparative study with the immobilized version of CSP 1, that is CSP 2, is also illustrated. Moreover, the appraisal of the enantiomeric elution order (EEO) through the combination of electronic circular dichroism (ECD) analyses along with *in-silico* time-dependent density functional theory (TD-DFT) simulations is discussed. Furthermore, a molecular modeling study based on docking simulations was performed to gain a deeper insight into the enantioseparation mechanism of the hydroxyethyl derivatives **3** and **4** on both CSPs.

2. Materials and methods

2.1. Chemicals

Analytical grade methanol (MeOH), ethanol (EtOH), and 2-propanol (2-PrOH), as well as 1,3,5-tri-*tert*-butylbenzene used as the unretained marker, were purchased from Merck Life Science (Merck KGaA, Darmstadt, Germany). Water for HPLC analysis was purified with a New Human Power I Scholar water purification system (Human Corporation, Seoul, Korea). Compounds **1–4** were synthesized at the University of Siena in the laboratory of Professor Maurizio Anzini. The synthetic procedures will be described in a manuscript under preparation.

All the binary mobile phases employed were degassed by sonication for 10 min before use. Samples for HPLC analysis were dissolved in the selected mobile phase and injected at the approximate concentration of 0.5–1.0 mg/mL. Samples for ECD were solubilized in MeOH.

2.2. Instrumentation

The HPLC analyses were performed on a Shimadzu (Kyoto, Japan) LC-20A Prominence, equipped with a CBM-20A communication bus module, two LC-20AD dual piston pumps, a SPD-M20A photodiode array detector, and a Rheodyne 7725i injector (Rheodyne Inc., Cotati, CA, USA) with a 20 μL stainless steel loop. Column temperature was controlled through a Grace (Sedriano, Italy) heater/chiller (Model 7956R) thermostat.

2

150

CSP 1 was a prototype of the Sepapak 5 column (250 mm x 4.6 mm I.D., containing a cellulose *tris*(3,5-dichlorophenylcarbamate)-based chiral selector adsorbed onto a 5 µm silica gel) kindly provided by Sepaserve GmbH (Münster, Germany). CSP 2 was a prototype of the commercially available Lux i-Cellulose-5 from Phenomenex (Torrance, CA, USA), incorporating the cellulose *tris*(3,5-dichlorophenylcarbamate) as the chiral selector (250×4.6 mm ID, 5 µm), covalently bonded to 1000 Å pore size silica support.

The columns were conditioned with the selected mobile phase at a 1.0 mL/min flow rate for at least 40 min before use. All the analyses were carried out at a 0.7 mL/min flow rate and with a 25 °C column temperature, unless otherwise stated.

The ECD spectra were recorded by means of a Jasco J-810 Spectropolarimeter (Jasco Corporation, Tokyo, Japan) at 25 °C, using 10 mm quartz cell. The samples were solubilised in MeOH and analysed in the global spectral range of 200–400 nm.

2.3. Theoretical chiroptical spectroscopy

The theoretical chiroptical properties of compounds **1, 3**, and **4** were determined according to an *in house* developed protocol for stereochemical characterization by TD-DFT calculations, already applied to a series of chiral sulfoxides [14,19]. The molecules were built by the Maestro graphical interface (version 12.9, Schrödinger, LLC, New York, NY, 2021) of the Schrödinger Suite 2021–3. The correct protonation state was assigned by the "Ligprep Protocol" using the default options.

Because conformers of a molecule have significantly different ECD spectra conformational search was performed with MacroModel (version 13.3, Schrödinger, LLC, New York, NY, 2021); then, the geometries of each conformer were refined with Jaguar (version 11.3, Schrödinger, LLC, New York, NY, 2021), and finally, the high-lying or redundant conformers were eliminated.

The conformational analysis was performed using the MMFFs force field and the "Mixed torsional/Low-mode sampling", executing 200 steps, retaining at most 50 conformers per each molecule, lying in a window of 5.0 kcal/mol from the global minimum and using methanol as the solvent. The resulting conformers were submitted to a quantum mechanical energy optimization by means of B3LYP [20] as DFT and the TZVP Ahlrichs-type triple-valence plus polarization basis set and the Poisson-Boltzmann Solvation solver [21] to take into account the chloroform environment, and finally the level of accuracy set to Ultrafine (iacc=1).

Conformational clustering was performed with a RMSD threshold value of 0.01 Å for heavy atoms. TD-DFT calculations were carried out using the ORCA 4.1.2 software [22]. The PBE0 functional [23] was used in combination with the TZVP basis set and the calculations were performed on all the optimized conformers.

Theoretical values of oscillator strength (fj), rotational strength in dipole velocity formalism (Rj) and excitation energy (expressed as wavelength, λj) were calculated for the 50 lowest energy electronic transitions of each optimized conformer. The theoretical spectra of the optimized conformers were then derived by approximation of fj and Rj values to Gaussian bands with a ΔS value of 0.25 Ev [24]. The theoretical ECD spectra of the two compounds were finally derived as the weighted average of the contribution of all conformers according to their Boltzmann equilibrium populations at 298.15 K and 1 atm, based on free energy values (χ_G), and compared to the experimental spectra. This last step was performed using the SpecDis software [25].

2.4. Induced fit docking and prime/MMGBSA calculation

The Induced fit docking and prime/MMGBSA calculation study for the enantiomers of compounds **3** and **4** were determined using a previously published model [26] in order to reflect the nonameric structure of the CSP employed in this work [27].

The induced fit docking (IFD) was performed using the Schrödinger suite 2021–3. The grid box was centered on the monomer number 5 of the chiral selector. The IFD stage 1 applies a vdW scaling of 0.7/0.5 to the receptor/ligand vdW radii, respectively. The resulting top 20 poses for each enantiomer were considered for the subsequent step. In stage 2, residues within 5.0 Å of ligand pose are kept free to move, and the side chains are further optimized. Poses falling in a range of 30 kcal/mol from the minimum energy recorded in the previous step are then finally re-docked using Glide SP (single precision mode). The IFD Score obtained for each output is the result of the sum of energy terms coming from the refinement calculation and the Glide scoring function. All the docked poses for both the enantiomers were further submitted to a Molecular Mechanics Generalized Born Surface Area (MMGBSA) calculation to estimate the binding free energy (ΔGbind) of the enantiomers to the chiral selector model using the Prime/MMGBSA method. The monomers falling within a range of 6 Å of the ligand were set free to relax and minimize. All the other settings not specified herein were kept at default values.

3. Results and discussion

3.1. Enantioselective liquid-chromatography analysis of compounds 1–4 with two cellulose dichlorophenyl carbamate-based chiral stationary phases

In a previous work [14], we successfully used CSP 1 (Fig. 2) for the enantioseparation of two chiral sulfoxides sharing structural characteristics with compounds **1–4** (Fig. 1). In that case, the use of plain methanol produced good separation performances (with α and R$_S$ values up to 1.22 and 2.47, respectively) in less than 30 min of analysis.

The chiral selector in CSP 1 is soluble in *n*-hexane rich mobile phase for NP applications, while it is practically insoluble in all the solvents typical of PO and RP analysis [11]. Moreover, the chiral selector in CSP 1 holds a great number of free carbamate groups amenable for intermolecular interactions [12], which makes this phase highly performing for many enantioselective analyses.

Encouraged by this very positive result of the previous study, we decided to retain the use of a PO eluent in combination with the same CSP 1. However, for the compounds under investigation MeOH alone or with minor amounts of other solvents (up to 5% of water, acetonitrile, EtOH, and 2-PrOH in binary eluent systems) did not provide appreciable results mostly in terms of enantioresolution factors (data not shown), which stimulated us to test the greener EtOH. With only a few numbers of analyses, the eluent system composed of EtOH/2-PrOH (80:20, v/v) emerged as the best mobile phase, leading to the enantioresolution of three out of four compounds (that is, **2–4**) (Fig. 3 black bottom lines in all the entries; Table 1). Compared to a mobile phase made up with plain MeOH, the use of a EtOH/2-PrOH-based eluent intensified both the intramolecular and the intermolecular analyte-chiral selector H-bonding interactions. It is therefore likely that H-bonds seems to have a certain relevance for the enantiseparation of these compounds with CSP 1.

Since CSP 1 is a research-type non-commercial phase, we decided to test the commercially available column CSP 2 bearing the same chiral selector, but immobilized onto a silica-based support. The comparative evaluation was performed with the PO mobile phase composition previously optimized for CSP 1.

Data listed in Table 1 readily suggest that the coated polymer in CSP 1 is involved in a higher number of achiral interactions, leading to stronger retention of the enantiomers but with a negligible effect on the enantioselectivity extent. This retention behavior should not be regarded as universal since it was already described [28] that the relative binding strength of coated and immobilized phases strongly depends on the composition of the mobile phase employed.

As far as the enantioselectivities are concerned, the results obtained from the comparative analysis were somehow in contrast with the frequent observation that the enantiseparation capabilities of the immobilized selectors are lower than those by the corresponding coated vari-
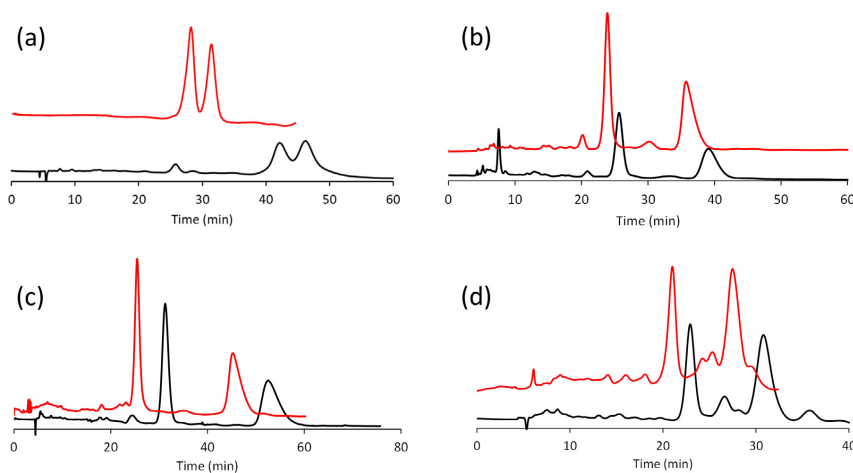
Fig. 3. Chromatograms of compounds (a) **1**, (b) **2**, (c) **3** and (d) **4**, obtained under the optimized PO conditions with CSP 1 (bottom - black - lines) and CSP 2 (upper – red - lines). Other experimental conditions: mobile phase, EtOH/2-PrOH (80:20, v/v); flow rate, 0.7 mL/min; column temperature, 25 ˚C. Note that the analysis of compound **4** was performed on a not purified sample, without compromising the quality of enantioseparation.

Table 1

Chromatographic performances obtained with the chiral stationary phases carrying the coated (CSP 1) and the immobilized (CSP 2) chiral selector.

Cpd	Column	Chromatographic parameters[a]					
		k_1	k_2	N_1	N_2	α	R_S
1	CSP 1	8.60 (S)	9.52 (R)	1290	1334	1.11	0.84
	CSP 2	5.58 (R)	6.38 (S)	2636	2981	1.15	1.54
2	CSP 1	4.22 (S)	6.01 (R)	2623	1605	1.42	3.24
	CSP 2	3.82 (S)	5.30 (R)	2832	2108	1.39	3.25
3	CSP 1	6.12 (S)	10.97 (R)	2647	1071	1.79	4.82
	CSP 2	4.80 (S)	9.31 (R)	3313	1616	1.94	6.32
4	CSP 1	4.84	7.90	2343	1326	1.63	4.23
	CSP 2	4.44	7.13	3461	1876	1.61	4.82

[a] All the analyses were performed at least thrice with CSP 1, while were repeated even more times with CSP 2 (in order to allow the enantiomer collection for the following ECD study). Only negligible differences were found in terms of both thermodynamic and kinetic parameters values. For compounds 1–4, the variations of the retention times (tR) among three consecutive injections performed with the two CSPs was always lower than 3.0%. Instead, as far as the number of theoretical plates, N, the variation was always lower than 10%.

ants under the same eluent conditions (actually, when "standard" eluent components are used [29–31]. Indeed, for the four compounds under investigation, the apparent reduction of the high-order stereospecific configuration of the polymer upon immobilization to the silica matrix (in CSP 2) did not cause a deterioration of its chiral recognition ability.

In fact, as readily evident from data listed in Table 1, the immobilized selector in CSP 2 produced resolution factor values comparable or higher than those from the coated version in CSP 1. The better result obtained with the immobilized selector for three out of four compounds (that is, **1**, **3** and **4**) is mostly ascribed to the higher efficiency exhibited by the former (higher N values, Table 1). The chromatograms obtained with CSP 2 are shown as red (upper) lines in Fig. 3.

Under the eluent conditions applied, only compound **1** was not resolved when analysed with CSP 1. The base-line separation (α=1.18,

R_S=1.64) was gained in less than 50 min of analysis, increasing the column temperature to 30 ˚C. Since in most cases the transfer of the analyte from the mobile phase to the stationary phase is an exothermic process, this change in experimental conditions caused an expected reduction of the retention times (data not shown). Still in line with our forecast, the improvement of R_S was the result of the enhanced kinetic effect upon increasing temperature. However, very unexpectedly α increased with increasing temperature. This is actually a rather unusual situation for LC applications [32] which can indicate an entropy-driven separation mechanism [33–35].

With both CSPs, monofluorinated compounds **1** and **3** were more retained than the corresponding difluorinated **2** and **4** variants. Some plausible explanations can be proposed to explain this chromatographic behavior, which needs to be verified through focused in-depth investigations. First of all, the higher steric demand in **2** and **4** can reduce to some extent the interaction with the chiral selector. On the other side, fluorine atoms are electronegative substituents that through an electron-withdrawing effect decrease the basicity of the close sites involved in analyte retention (both enantioselective and non-enantioselective) [36,37]. Also interestingly, with CSP 2 for both mono- and difluorinated compounds, the presence of the –OH group promoted always higher retentions than the –ONO_2 group (see **1** vs **3**, and **2** vs **4**). A single trend was instead missing with CSP 1.

It's worth highlighting that lower retention times can be conveniently achieved using a shorter column length. As a proof-of-concept, the chromatograms obtained for compounds **3** and **4** under the same conditions are shown as Supplementary Material (Fig. S1).

3.2. Assignment of the absolute configuration through ECD studies and ab-initio in-silico simulations

Due to the lack of pure enantiomeric standards of known stereochemistry, an indirect protocol was applied to establish the EEO with the two CSPs under optimized eluent conditions. Accordingly, based on a well-established procedure [19,38], ECD studies were coupled to *ab initio* TD-DFT simulations. Experimental off-line ECD spectra of the two enantiomers of compounds **1**, **3** and **4** were measured after their collection with CSP 2 under the optimized eluent conditions. Sample limita-
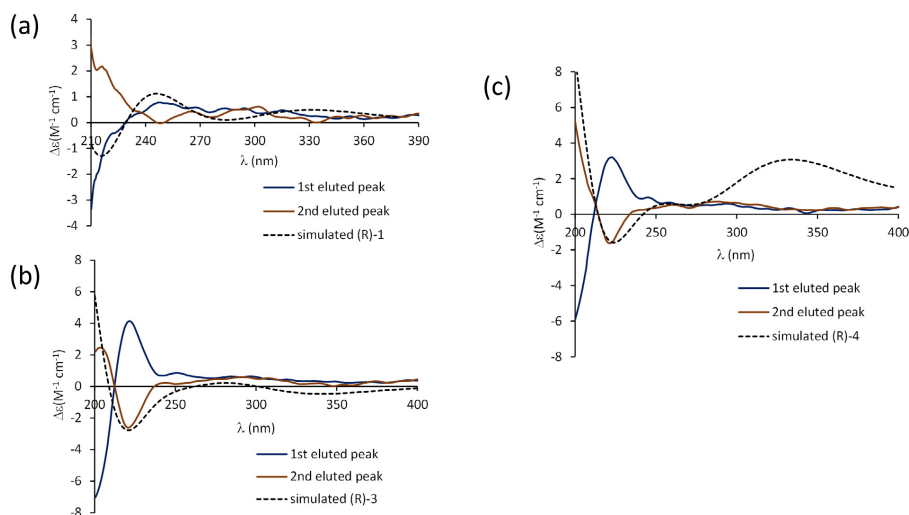
4

Fig. 4. Experimental ECD spectra of the first- (blue line) and second- (brown line) eluted enantiomer of (a) **1**, (b) **3** and (c) **4**. The theoretical spectra of the simulated (*R*) enantiomers is reported as dashed line.

tions did not enable to measure the ECD spectra for the enantiomers of compound **2** and hence to establish its EEO with the two CSPs. However, for compound **2**, the same elution order was produced by the two CSPs.

As far as compound **1** is concerned, the positive Cotton effect at around 250 nm, that is a signature of the ECD spectrum of the first eluted peak with CSP 2, is also evident in the theoretical spectrum of (*R*)−**1**, thereby leading to a ready conclusion about the EEO. Based on this result, the (*R*)−**1** < (*S*)−**1** EEO was established with CSP 2. For this compound, an opposite EEO was found with CSP 1 [that is, (*S*)<(*R*)]. Only one case of the reversal of the EEO on coated and immobilized polysaccharide-based CSPs with the same chiral selector is reported in literature [35] and mostly imputed to the peculiar morphology assumed by the chiral polymer upon its immobilization.

As readily evident from the ECD spectra displayed in Fig. 4, the isolated peaks of compounds **3** and compound **4** exhibit specular Cotton effects typical of enantiomeric compounds, with a common negative signal centered at around 230 nm. The ECD spectrum of the second eluted peak is well mimicked by the TD-DFT theoretical spectrum of the (*R*) enantiomers [EEO: (*S*)<(*R*)]. The same elution order was found also with CSP 1.

3.3. Enantiorecognition mechanism of compounds 3 and 4 on CSP 1 and CSP 2

As readily evident from data reported in Table 1 and the results of the ECD/TD-DFT study (Fig. 4), the enantiomers of compounds **3** and **4** exhibited a very similar chromatographic behavior on CSP 1 and CSP 2, along with a strongly comparable enantiorecognition mechanism. Indeed, it is likely that the way of anchoring of the chiral selector (either through coating or immobilization) to the silica support did not have a peculiar impact on the stereoselective recognition of the enantiomers of compounds **3** and **4**. Accordingly, it seemed that their chromatographic behavior was essentially ruled by the chemistry of the cellulosic chiral selector and the mobile phase composition. Based on those findings, we were stimulated to investigate the enantiorecognition mechanism of compounds **3** and **4** on the two CSPs. This was performed by a docking study which was set up on a system simulating the interaction between the chiral selector and the enantiomers of the analytes (the selectands). Accordingly, the chiral selector assumed the role of "receptor", while the enantiomers of compounds **3** and **4** of binders.

The nonameric structure of the chiral selector was derived from a model already built up by Dallocchio et al. [26] for the cellulose *tris*(3,5-dimethylphenylcarbamate) selector. This was made possible after a careful modification of the original cellulose structure. In order to give some flexibility to the cellulose-based polymer, and to refine and adapt the binding cavity upon the molecules binding, an induced fit docking (IFD) protocol was applied. The best-ranked result for the enantiomers of **3** identified a somewhat stronger binding for (*R*)−**3** with respect to (*S*)−**3** (with a score of −8.82 kcal/mol and −8.37 kcal/mol, respectively). As far as compound **4** is concerned, an opposite situation was found, being (*S*)−**4** more tightly bound to the polymer than (*R*)−**4** (with a score of −8.77 kcal/mol and −8.57 kcal/mol, respectively). In order to more detailed results, better supporting the experimental α values, a further computational step was added to the protocol. Indeed, to gain a deeper insight into the thermodynamic of the association process, the free energy of binding (ΔG_{bind}) was estimated for the two enantiomers of compounds **3** and **4** towards the polymer. All the 20 selector-selectand complexes generated by the IFD step were additionally submitted to a Prime/MMGBSA calculation. The calculated Molecular Mechanics Generalized Born Surface Area (MMGBSA) was useful to compare the binding energies of the most stable complex formed by each enantiomer and the chiral selector. As a result, a $\Delta\Delta G$ of about 20 kcal/mol (−103.6 and −83.7 kcal/mol for (*R*)−**3** and (*S*)−**3**, respectively) was recorded for compound **3** thus indicating the (*S*)−**3**<(*R*)−**3** EEO. The same protocol for the enantiomers of compound **4** displayed a $\Delta\Delta G$ of about 3 kcal/mol (−77.5 and −74.3 kcal/mol for (*R*)−**4** and (*S*)−**4**, respectively), thus indicating the (*S*)−**4**<(*R*)−**4** EEO. In order to better understand the enantiorecognition mechanism at the basis of the chromatographic separation, it is important to highlight some binding features revealed by the analyses of the most stable selector-selectand complexes (Fig. 5). (*R*)−**3** displayed the best interaction pattern with two π-π stacking interactions engaged by its pyrrole moiety and one phenyl group with two dichloro-substituted phenyl rings of the selector. Moreover, in the extended conformation adopted by (*R*)−**3**, it is
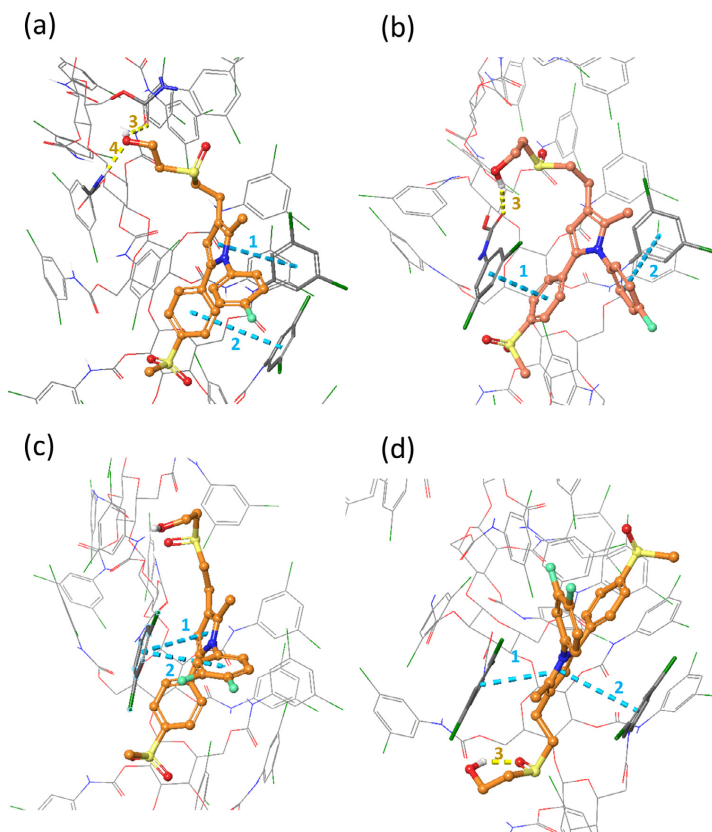
Fig. 5. Most stable complexes formed by (a) (*R*)−**3**, (b) (*S*)−**3**, (c) (*R*)−**4**, and (d) (*S*)−**4** and the chiral selector. All the enantiomers are shown in orange ball and stick; the π-π-stacking and H-bond interactions are shown **and** numbered in cyan and yellow dashed lines, respectively. The interacting selector moieties are shown in bolded lines.

able to engage two stabilizing hydrogen bonds with its hydroxyl group and two carbamate residues of the selector (Fig. 5a). Its antipode (*S*)−**3** shows a similar binding mode, with two π-π stacking interactions between its two phenyl rings and two different dichlorophenyl moieties of the chiral selector. Additionally, the hydroxyl group of (*S*)−**3** establishes a single H-bond with a carbamate group of the chiral selector (Fig. 5B). Notably, (*S*)−**3** adopts a more folded conformation with respect of the (*R*) enantiomer, thus spending a higher conformational cost to interact by this disposition. By counting the number of the selector atoms (excluding the hydrogens) surrounding the selectand in a range of 4 Å, it is possible to have a measure of the inclusion of compound **3** enantiomers in the binding cavity. It is worth noting that the (*R*) enantiomer is surrounded by 86 atoms while the (*S*) one by 70 atoms, thereby indicating a deeper inclusion by the former.

(*R*)−**4** engages with the selector two π-π stacking interactions established by the pyrrole moiety and one phenyl ring interacting with only one dichloro-substituted phenyl ring (Fig. 5c). Even in this case, the (*R*) enantiomer adopts an extended conformation, pointing the sulfoxide and the hydroxyl groups towards the -NH residue of a carbamate moiety of the selector. Differently from the (*R*)−**3**, it should be noted that no hydrogen bonds are observed in this binding pose because the atom angles and distances are not appropriate for this type of interaction to establish (Fig. 5c). The (*S*)−**4** pose is flipped (head to tail) with

respect of its antipode (Fig. 5d). Indeed, the sulfoxide and the hydroxyl groups are exposed towards the mobile phase. Two π-π stacking interactions are engaged by the pyrrole ring with two dichlorophenyl rings of the selector and no other interactions are observed. As already found for (*S*)−**3**, the molecule appears folded with an intramolecular H-bond taking place between the sulfoxide oxygen and the hydroxyl hydrogen (Fig. 5d). In this enantiomer pair, the number of atoms in contact with the selectand in both the poses is 57, thus not representing a discriminating aspect in the enantioseparation process. The centroid distances and the torsion angles formed by the planes of the aromatic rings in the stacking interactions are reported in Table 2 together with the H-bond donor and acceptor atoms distances and angles.

The head to tail flipping, the different enantiomer inclusion in the selector cavities and the importance of the π-π interactions are all aspects already emerged in an *in silico* study made by Alcaro et al. regarding the enantiorecognition process of asymmetric pyrazoles toward with a cellulose-based CSP [39].

4. Conclusion

Chiral sulfoxides are of outstanding importance in the fields of medicinal chemistry and drug discovery. In this paper we have developed an efficient HPLC method enabling the enantioresolution of four

Table 2
Distances, dihedrals and angles values of the interactions depicted and numbered in Fig. 5.

Cpd	Distance (Å)				Angle (°)			
	d1[a]	d2[a]	d3[b]	d4[b]	ϕ1[a]	ϕ2[a]	α3[b]	α4[b]
(R)−3	5.8	5.5	1.9	1.7	12.8	−22.0	142.4	106.0
(S)−3	4.1	5.8	2.2	–	23.8	−16.7	144.9	–
(R)−4	4.1	4.4	–	–	0.1	152.5	–	–
(S)−4	3.6	4.4	1.9	–	34.2	−14.2	144.1	–

[a] Centroid distance and dihedral angle formed by the planes defined by the aromatic rings in $\pi-\pi$ stacking interaction.
[b] H-bond donor and acceptor atoms distance and angle.

novel chiral sulfoxides endowed with promising COX-2 inhibition activity. The method is based on the use of a MS compatible PO eluent and two cellulose dichlorophenyl carbamate-based CSPs. The difference between the two CSPs is the coated or immobilized nature of the polymeric selector. The application of the optimized experimental conditions have revealed an almost comparable performance by the two CSPs, with only a marginal superiority by the one in which the chiral selector is immobilized onto the silica surface. On the contrary, the EEO derived through the combination of experimental analyses and *ab initio in silico* simulations revealed for two out of four compounds a strict dependence of the enantiorecognition mechanism from the type of anchoring of the chiral selector. Finally, the application of a IFD protocol enabled to establish the importance of π-π stacking interactions and enantiomer inclusion in the enantiorecognition mechanism of the two compounds experiencing the same EEO with the two CSPs.

Contributor role	Role definition
Conceptualization	Ideas; formulation or evolution of overarching research goals and aims.
Methodology	Development or design of methodology; creation of models
Software	Programming, software development; designing computer programs; implementation of the computer code and supporting algorithms; testing of existing code components.
Validation	Verification, whether as a part of the activity or separate, of the overall replication/reproducibility of results/experiments and other research outputs.
Formal analysis	Application of statistical, mathematical, computational, or other formal techniques to analyze or synthesize study data.
Investigation	Conducting a research and investigation process, specifically performing the experiments, or data/evidence collection.
Resources	Provision of study materials, reagents, materials, patients, laboratory samples, animals, instrumentation, computing resources, or other analysis tools.
Data Curation	Management activities to annotate (produce metadata), scrub data and maintain research data (including software code, where it is necessary for interpreting the data itself) for initial use and later reuse.
Writing – original draft preparation	Creation and/or presentation of the published work, specifically writing the initial draft (including substantive translation).
Writing – review and editing	Preparation, creation and/or presentation of the published work by those from the original research group, specifically critical review, commentary or revision – including pre- or post-publication stages.
Visualization	Preparation, creation and/or presentation of the published work, specifically visualization/data presentation.
Supervision	Oversight and leadership responsibility for the research activity planning and execution, including mentorship external to the core team.
Project administration	Management and coordination responsibility for the research activity planning and execution.
Funding acquisition	Acquisition of the financial support for the project leading to this publication.

Declaration of Competing Interest

We hereby confirm no conflict of interest.

Supplementary materials

Supplementary material associated with this article can be found, in the online version, at doi:10.1016/j.jcoa.2021.100022.

References

[1] B. Chankvetadze, Polysaccharide-Based Chiral Stationary Phases for Enantioseparations by High-Performance Liquid Chromatography: An Overview, in: G.K.E. Scriba (Ed.), Chiral separations, methods in molecular biology, vol 1985, Humana, New York, 2019, pp. 93–126.

[2] B. Chankvetadze, Recent developments on polysaccharide-based chiral stationary phases for liquid-phase separation of enantiomers, J Chromatogr A 1269 (2012) 26–51 https://doi:. https://doi.org/10.1016/j.chroma.2012.10.033.

[3] E. Yashima, Polysaccharide-based chiral stationary phases for high-performance liquid chromatographic enantioseparation, J Chromatogr A 906 (2001) 105–125 https://doi:. https://doi.org10.1016/s0021-9673(00)00501-x.

[4] Y. Okamoto, T. Ikai, Chiral HPLC for efficient resolution of enantiomers, Chem Soc Rev 37 (2008) 2593–2608 https://doi:. https://doi.org10.1039/B808881k.

[5] R. Sardella, S. Levent, F. Ianni, B. Çalişkan, J. Gerstmeier, C. Pergola, et al., Chromatographic separation and biological evaluation of benzimidazole derivative enantiomers as inhibitors of leukotriene biosynthesis, J Pharm Bio Anal 89 (2014) 88–92 https://doi:. https://doi.org10.1016/j.jpba.2013.10.039.

[6] S. Carradori, D. Secci, P. Guglielmi, M. Pierini, R. Cirilli, High-performance liquid chromatography enantioseparation of chiral 2-(benzylsulfinyl)benzamide derivatives on cellulose tris(3,5-dichlorophenylcarbamate) chiral stationary phase, J Chromatogr A 1610 (2020) 460572 https://doi.org/. https://doi.org/10.1016/j.chroma.2019.460572.

[7] T. Khatiashvili, R. Kakava, I. Matarashvili, H. Tabani, C. Fanali, A. Volonterio, et al., Separation of enantiomers of selected chiral sulfoxides with cellulose tris(4-chloro-3-methylphenylcarbamate)-based chiral columns in high-performance liquid chromatography with very high separation factor, J Chromatogr A (2018) 59–66 1545https://doi.org/. https://doi.org10.1016/j.chroma.2018.02.054.

[8] N. Kolderová, T. Neveselý, J. Šturala, M. Kuchař, R. Holakovský, M. Kohout, Enantioseparation of Chiral Sulfoxides on Amylose-Based Columns: Comparison of Normal Phase Liquid Chromatography and Supercritical Fluid Chromatography, Chromatographia 80 (2017) 547–557 https://doi.org/. https://doi.org10.1007/s10337-016-3234-6.

[9] Z. Shedania, R. Kakava, A. Volonterio, T. Farkas, B. Chankvetadze, Separation of enantiomers of chiral sulfoxides in high-performance liquid chromatography with cellulose-based chiral selectors using methanol and methanol-water mixtures as mobile phases, J Chromatogr A 1557 (2018) 62–74 https://doi.org/. https://doi.org10.1016/j.chroma.2018.05.002.

[10] Z. Shedania, R. Kakava, A. Volonterio, T. Farkas, B. Chankvetadze, Separation of enantiomers of chiral sulfoxides in high-performance liquid chromatography with cellulose-based chiral selectors using acetonitrile and acetonitrile-water mixtures as mobile phases, J Chromatogr A 1609 (2020) 460445 https://doi.org/. https://doi.org10.1016/j.chroma.2019.460445.

[11] B. Chankvetadze, C. Yamamoto, Y. Okamoto, Extremely high enantiomer recognition in HPLC separation of racemic 2-(benzylsulfinyl)benzamide using cellulose tris(3,5-dichlorophenylcarbamate) as a chiral stationary phase, Chem Lett 29 (2000) 1176–1177 https://doi.org/. https://doi.org/10.1246/cl.2000.1176.

[12] B. Chankvetadze, C. Yamamoto, Y. Okamoto, Enantioseparation of selected chiral sulfoxides using polysaccharide-type chiral stationary phases and polar organic, polar aqueous–organic and normal-phase eluents, J Chromatogr A 922 (2001) 127–137 https://doi.org/. https://doi.org10.1016/S0021-9673(01)00958-X.

[13] M. Gegenava, L. Chankvetadze, T. Farkas, B. Chankvetadze, Enantioseparation of selected chiral sulfoxides in high-performance liquid chromatography with polysaccharide-based chiral selectors in polar organic mobile phases with emphasis on enantiomer elution order, J Sep Sci 37 (2014) 1083–1088 https://doi.org/. https://doi.org10.1002/jssc.201301318.

[14] R. Sardella, F. Ianni, A. Di Michele, A. Di Capua, A. Carotti, M. Anzini, et al., Enantioresolution and stereochemical characterization of two chiral sulfoxides endowed with COX-2 inhibitory activity, Chirality 29 (2017) 536–540 https://doi.org/. https://doi.org10.1002/chir.22724.

[15] T. Grosser, S. Fries, G.A. FitzGerald, Biological basis for the cardiovascular consequences of COX-2 inhibition: therapeutic challenges and opportunities, J Clin Invest 116 (2006) 4–15 https://doi.org/. https://doi.org/10.1172/JCI27291.

[16] J.L. Wallace, M.J. Miller, Nitric Oxide in Mucosal Defence: A Little Goes a Long Way, Gastroenterology 119 (2000) 512–520 https://doi.org/. https://doi.org10.1053/gast.2000.9304.

[17] J.R. Whittle, Cicloxygenase and Nitric Oxide Systems in the Gut as Therapeutic Targets for Safer Anti-Inflammatory Drugs, Curr Opin Pharmacol 4 (2004) 538–545 https://doi.org/. https://doi.org/10.1016/j.coph.2004.08.003.

[18] M. Anzini, A. Di Capua, S. Valenti, S. Brogi, M. Rovini, G. Giuliani, et al., Novel analgesic/anti-inflammatory agents: 1,5-diarylpyrrole nitrooxyalkyl ethers and related compounds as cyclooxygenase-2 inhibiting nitric oxide donors, J Med Chem 56 (2013) 3191–3206 https://doi.org/. https://doi.org/10.1021/jm301370e.

[19] R. Sardella, A. Carotti, G. Manfroni, D. Tedesco, A. Martelli, C. Bertucci, et al., Enantioresolution, stereochemical characterization and biological activity of a chiral large-conductance calcium-activated potassium channel opener, J Chromatogr A 1363 (2014) 162–168 https://doi.org/. https://doi.org10.1016/j.chroma.2014.06.020.

[20] P.J. Stephens, F.J. Devlin, C.F. Chabalowski, M.J. Frisch, Ab initio calculation of vibrational absorption and circular dichroism spectra using density functional force fields, J Phys Chem 98 (1994) 11623–11627 https://doi.org/. https://doi.org10.1021/j100096a001.

[21] B. Marten, K. Kim, C. Cortis, R.A. Friesner, R.B. Murphy, M.N. Ringnalda, et al., New Model for calculation of solvation free energies: correction of self-consistent reaction field continuum dielectric theory for short-range hydrogen-bonding effects, J Phys Chem 100 (1996) 11775–11788 https://doi.org/. https://doi.org10.1021/jp953087x.

[22] F. Neese, The ORCA program system, WIREs Comput Mol Sci 2 (2012) 73–78 https://doi.org/. https://doi.org10.1002/wcms.81.

[23] J.P. Perdew, K. Burke, M. Ernzerhof, Generalized gradient approximation made simple, Phys Rev Lett 77 (1996) 3865–3868 https://doi.org/. https://doi.org10.1103/PhysRevLett.77.3865.

[24] P.J. Stephens, N. Harada, ECD cotton effect approximated by the Gaussian curve and other methods, Chirality 22 (2010) 229–233 https://doi.org/. https://doi.org10.1002/chir.20733.

[25] T. Bruhn, A. Schaumlöffel, Y. Hemberger, G. Bringmann, SpecDis: quantifying the comparison of calculated and experimental electronic circular dichroism spectra, Chirality 25 (2013) 243–249 https://doi.org/. https://doi.org10.1002/chir.22138.

[26] R. Dallocchio, A. Dessi, M. Solinas, A. Arras, S. Cossu, E. Aubert, et al., Halogen bond in high-performance liquid chromatography enantioseparations: description, features and modelling, J Chromatogr A 1563 (2018) 71–81.

[27] G. Floresta, A. Carotti, F. Ianni, V. Sorrenti, S. Intagliata, A. Rescifina, et al., Chromatograpic resolution of phenylethanolic-azole racemic compounds highlighted stereoselective inhibition of heme oxygenase-1 by (R)-enantiomers, Bioorg Chem 99 (2020) 103777.

[28] L. Thunberg, J. Hashemi, S. Andersson, Comparative study of coated and immobilized polysaccharide-based chiral stationary phases and their applicability in the resolution of enantiomers, J Chromatogr B 875 (2008) 72–80 https://doi.org/. https://doi.org10.1016/j.jchromb.2008.07.044.

[29] I. Ali, H.Y. Aboul-Enein, Impact of immobilized polysaccharide chiral stationary phases on enantiomeric separations, J Sep Sci 29 (2006) 762–769 https://doi.org/. https://doi.org10.1002/jssc.200500372.

[30] N. Enomoto, S. Furukawa, Y. Ogasawara, H. Akano, Y. Kawamura, E. Yashima, et al., Preparation of Silica Gel-Bonded Amylose through Enzyme-Catalyzed Polymerization and Chiral Recognition Ability of Its Phenylcarbamate Derivative in HPLC, Anal Chem 68 (1996) 2798–2804 https://doi.org/. https://doi.org10.1021/ac960002v.

[31] E. Yashima, H. Fukaya, Y. Okamoto, 3,5-Dimethylphenylcarbamates of cellulose and amylose regioselectively bonded to silica gel as chiral stationary phases for high-performance liquid chr, J Chromatogr A 677 (1994) 11–19 https://doi.org/. https://doi.org10.1016/0021-9673(94)80539-3.

[32] A. Bajtai, I. Ilisz, R. Berkecz, F. Fülöp, W. Lindner, A. Péter, Polysaccharide-based chiral stationary phases as efficient tools for diastereo- and enantioseparation of natural and synthetic Cinchona alkaloid analogs, J Pharma Biomed Anal 193 (2021) 113724 https://doi.org/. https://doi.org10.1016/j.jpba.2020.113724.

[33] I. Matarashvili, L. Chankvetadze, S. Fanali, T. Farkas, B. Chankvetadze, HPLC separation of enantiomers of chiral arylpropionic acid derivatives with emphasis on elution order using polysaccharide-based chiral columns and normal-phase eluents, J Sep Sci 36 (2013) 140–147 https://doi.org/. https://doi.org10.1002/jssc.201200885.

[34] I. Matarashvili, G. Kobidze, A. Chelidze, G. Dolidze, N. Beridze, T. Farkas, et al., The effect of temperature on separation of enantiomers with coated and covalently immobilized polysaccharide-based chiral stationary phases, J Chromatogr A 1599 (2019) 172–179 https://doi.org/. https://doi.org10.1016/j.chroma.2019.04.024.

[35] M. Maisuradze, G. Sheklashvili, A. Chokheli, I. Matarashvili, T. Gogatishvili, T. Farkas, et al., Chromatographic and thermodynamic comparison of amylose tris(3-chloro-5-methylphenylcarbamate) coated or covalently immobilized on silica in high-performance liquid chromatographic separation of the enantiomers of select chiral weak acids, J Chromatogr A 1602 (2019) 228–236 https://doi.org/. https://doi.org10.1016/j.chroma.2019.05.026.

[36] P. Peluso, V. Mamane, S. Cossu, Liquid Chromatography Enantioseparations of Halogenated Compounds on Polysaccharide-Based Chiral Stationary Phases: Role of Halogen Substituents in Molecular Recognition, Chirality 27 (2015) 667–684 https://doi.org/. https://doi.org10.1002/chir.22485.

[37] P. Peluso, V. Mamane, R. Dallocchio, A. Dessì, S. Cossu, Noncovalent interactions in high-performance liquid chromatography enantioseparations on polysaccharide-based chiral selectors, J Chromatogr A 1623 (2020) 461202 https://doi.org/. https://doi.org10.1016/j.chroma.2020.461202.

[38] B. Cerra, A. Carotti, D. Passer, R. Sardella, G. Moroni, A. Di Michele, et al., Exploiting chemical toolboxes for the expedited generation of tetracyclic quinolines as a novel class of PXR agonists, ACS Med Chem Lett 10 (2019) 677–681 https://doi.org/. https://doi.org10.1021/acsmedchemlett.8b00459.

[39] S. Alcaro, A. Bolasco, R. Cirilli, R. Ferretti, R. Fioravanti, F. Ortuso, Computer-Aided Molecular Design of Asymmetric Pyrazole Derivatives with Exceptional Enantioselective Recognition toward the Chiralcel OJ-H Stationary Phase, J Chem Inf Model 52 (2012) 649–654 https://doi.org/. https://doi.org10.1021/ci200592h.

Acknowledgments